



Aalborg Universitet

AALBORG UNIVERSITY
DENMARK

Deformation and Indentation Cracking in Borate-Based Glasses

Liu, Pengfei

DOI (link to publication from Publisher):
[10.54337/aau451026283](https://doi.org/10.54337/aau451026283)

Publication date:
2021

Document Version
Publisher's PDF, also known as Version of record

[Link to publication from Aalborg University](#)

Citation for published version (APA):
Liu, P. (2021). *Deformation and Indentation Cracking in Borate-Based Glasses*. Aalborg Universitetsforlag. <https://doi.org/10.54337/aau451026283>

General rights

Copyright and moral rights for the publications made accessible in the public portal are retained by the authors and/or other copyright owners and it is a condition of accessing publications that users recognise and abide by the legal requirements associated with these rights.

- Users may download and print one copy of any publication from the public portal for the purpose of private study or research.
- You may not further distribute the material or use it for any profit-making activity or commercial gain
- You may freely distribute the URL identifying the publication in the public portal -

Take down policy

If you believe that this document breaches copyright please contact us at vbn@aub.aau.dk providing details, and we will remove access to the work immediately and investigate your claim.

**DEFORMATION AND INDENTATION
CRACKING IN BORATE-BASED GLASSES**

**BY
PENGFEI LIU**

DISSERTATION SUBMITTED 2021



AALBORG UNIVERSITY
DENMARK

DEFORMATION AND INDENTATION CRACKING IN BORATE-BASED GLASSES

by

Pengfei Liu



AALBORG UNIVERSITY
DENMARK

Dissertation submitted 2021

Dissertation submitted: July 2021

PhD supervisor: Prof. Morten M. Smedskjær,
Aalborg University

PhD committee: Associate Professor Morten Lykkegaard Christensen
Aalborg University (chair)

Senior Scientist Stefan Karlsson
RISE - Research Institutes of Sweden

Professor Russell J. Hand
University of Sheffield

PhD Series: Faculty of Engineering and Science, Aalborg University

Department: Department of Chemistry and Bioscience

ISSN (online): 2446-1636
ISBN (online): 978-87-7210-970-1

Published by:
Aalborg University Press
Kroghstræde 3
DK – 9220 Aalborg Ø
Phone: +45 99407140
aauf@forlag.aau.dk
forlag.aau.dk

© Copyright: Pengfei Liu

Printed in Denmark by Rosendahls, 2021



CV

Mr. Pengfei Liu was born in Xingtai, Hebei, P. R. China in February 1991. He got his Bachelor's degree in Materials Science from Changan University, and Master's degree in Materials Engineering from Central South University, P. R. China in 2014 and 2018, respectively. He got the China Scholarship Council (CSC) scholarship in June 2018, and then started his PhD study at the Department of Chemistry and Bioscience in Aalborg University in September 2018. His research has been focused on deformation and indentation cracking in the borate-based glasses during the three-year PhD study at AAU.

ENGLISH SUMMARY

Glasses are inherently brittle materials due to their unstable shear deformation mechanism and limited crack propagation resistance. These limitations severely restrict the practical strength of glasses due to surface flaws and defects, which act to amplify local tensile stresses, and thus results in catastrophic failures. This greatly limits the future application of glasses in various fields. Glass scientists have made great efforts to overcome this limitation through various methods, such as optimized composition design, post-treatment etc. In order to design and prepare stronger and tougher glass, it is of great significance to understand the relationship between the chemical composition, post-treatment, network structure, and mechanical properties of glasses. In this thesis, we have studied the deformation and indentation cracking behavior of oxide glasses, specifically borate-based glasses, from the viewpoints of composition design and post-processing. The goal of this work is to provide insights into the composition/post-treatment-structure-properties relation in these glasses.

In this work, all oxide glasses are synthesized with a predetermined chemical composition through the traditional melt-quenching technique. The borate-based glass systems include: i) alkali aluminoborates glasses and ii) lithium borophosphate glasses. We also performed the hot-compression and humid-aging treatments on the alkali aluminoborates glasses to understand the effect of densification and water-incorporation on the structure and properties. We studied the short- and medium-range structure of those glasses mainly using micro-Raman spectroscopy and nuclear magnetic resonance (NMR) spectroscopy. Furthermore, we used the Fourier transform infrared spectroscopy to analyze the water content. Finally, the mechanical properties were investigated by indentation test to explore the deformation and cracking behavior upon sharp contact loading.

Firstly, we studied the composition-structure-property relations in borate-based glass systems. We find that the additions the addition of SiO_2 and P_2O_5 partially disturbs the borate network of aluminoborates glasses due to the formation of mainly Si-O-B and P-O-B units, thus increasing the average network rigidity but decreasing the atomic packing density. Consequently, we only observe a minor change in hardness, glass transition temperature, and Poisson's ratio. In lithium phosphoaluminoborate glasses, the P_2O_5 addition is found to result in a minor decrease in the coordination numbers of boron, but to no change in that of aluminum. The introduced phosphate species thus compete with boron for some of the alkali modifiers, leading to fewer alkali-B^{IV} interactions. We discussed these changes in relation to the mechanical properties. Overall these studies provide insights into the complex structural interactions in mixed network former glasses and their impact on the mechanical properties.

Secondly, we studied the structure and mechanical properties of densified aluminoborate glasses. We have found that the cation-oxygen coordination numbers of both boron and aluminum increase upon hot compression, whereas the number of bridging oxygens (Q^n) around phosphorus decreases in lithium phosphoaluminoborate glasses. Consequently, we observe a significant increase in density, atomic packing density, Young's modulus, hardness, and a remarkable decrease in the crack resistance due to the large reduction of densification ability during the indentation. The increases in bond constraint density (due to volume densification) and network rigidity (due to higher average coordination number) are responsible for the pressure-induced increase in hardness and Young's modulus. Finally, our work shows that the atomic self-adaptivity strongly depends on the openness extent of structure and the coordination change contribution to the overall volume densification, as well as the glass composition.

Finally, we studied the effects of the humid aging treatment on the structure and mechanical properties of alkali aluminoborate glasses. We find that this hydrolysis effect strongly depends on the composition and chemical durability of oxide glasses. We have shown that ultra-high resistance to sharp contact cracking can be achieved in a caesium aluminoborate glass by simply storing the glass under typical atmospheric humidity conditions. This is due to the formation of the micro-size surface hydration layer with a high freedom network and higher mobility Cs-OH groups, better protecting the glass from damage during indentation. In a word, our work provides guidelines for how to control the humid aging rate as a function of relative humidity and temperature to form a hydration layer and thus achieve ultrahigh crack resistance in such glasses.

DANSK RESUME

Glasser er sprøde materialer som følge af deres ustabile forskydningsdeformationsmekanisme og begrænsede modstandsevne mod revneudbredelse. Disse egenskaber begrænser kraftigt den reelle styrke af glas da overfladefejl og overfladedefekter forstærker den lokale trækspænding og derved fører til ødelæggende materialesvigt. Dette begrænser i stor grad den fremtidige anvendelse af glas inden for adskillige felter. Glasforskere har gjort store anstrengelser for at overkomme denne begrænsning med mange forskellige metoder, eksempelvis kompositionsoptimering, efterbehandling etc. For at kunne udvikle og producere stærke og seje glasser, er det af stor betydning at forstå sammenhængen mellem kemisk komposition, efterbehandling, struktur af glasnetværket og mekaniske egenskaber. I denne afhandling har vi for oxidglasser, specifikt boratbaserede glasser, undersøgt deformationen og revnedannelsen ved indentering med fokus på effekten af kompositionsoptimering og efterbehandlinger. Målet for dette arbejde er at belyse sammenhængene mellem komposition, efterbehandling, struktur og egenskaber for disse glasser.

I dette arbejde er alle oxidglaser fremstillet med den traditionelle smelteafkølingsteknik efter en forudbestemt kemisk komposition. De boratbaserede glassystemer omfatter a) alkali-aluminoborat-glasser og b) litium-borofosfat-glasser. Vi behandlede også alkali-aluminoborat-glassene med varm-kompression og aldring med fugt for at forstå effekten på struktur og egenskaber af henholdsvis komprimering and inkorporering af vand. Vi undersøgte den korttrækkende og mellemlangtrækkende struktur i disse glasser ved brug af primært mikro-Raman spektroskopi og kernemagnetisk resonans (NMR) spektroskopi. Derudover anvendte vi Fourier-transformeret infrarød spektroskopi til at måle vandindholdet. Ydermere blev de mekaniske egenskaber karakteriseret ved indenteringsforsøg for undersøgelse af hårdhed og revnedannelsen som følge af skarp punktbelastning.

Vi studerede først komposition-struktur-egenskaber relationen for boratbaserede glasser. Vi klarlagte at tilføjelse af SiO_2 and P_2O_5 påvirker boratnetværket i aluminoborat-glasser ved at danne hovedsageligt Si-O-B- og P-O-B-enheder, hvorved den gennemsnitlige rigiditet af netværket øges mens den atomare pakningsdensitet mindskes. Vi observerede som følge heraf en mindre ændring i hårdhed, glastranstempertur og Poissons ratio. I litium-fosfoaluminoborat-glassene resulterede tilføjelsen af P_2O_5 i et lille fald i bors koordinationsstal, men ingen ændring i aluminiums koordinationsstal. De dannede fosfatstrukturer konkurrerer dermed med bor om nogle af alkali netværksmodifikatorerne, førende til færre alkali- B^{IV} -interaktioner. Vi diskuterede disse ændringer og sammenhængen med mekaniske egenskaber. Disse studier giver generelt indsigt i de komplicerede strukturelle interaktioner i glasser med flere netværksmodifikatorer og deres påvirkning på de mekaniske egenskaber.

Vi har dernæst undersøgt strukturen og de mekaniske egenskaber af komprimerede aluminoborat-glasser. Vi har fundet at kation-oxygen-koordinationstallet for både bor and aluminium øges af varm-kompression, mens antallet af netværksforbindende oxygenatomer (Q^n) omkring fosforatomerne falder i litium-fosfoaluminoborat-glassene. Som følge heraf ser vi en signifikant stigning i densitet, atomar pakningsdensitet, Youngs modul og hårdhed, samt et bemærkelsesværdigt fald i modstandsevnen mod revnedannelse grundet den store reduktion i glasset mulighed for at fortætte under indentering. Stigningerne i densiteten af restriktive bindinger (som følge af volumenkomprimeringen) og netværksrigiditeten (grundet højere gennemsnitligt koordinationstal) er årsagen til den trykinducerede stigning i hårdhed og Youngs modul. Endeligt viser vi at den atomare selv-tilpasningsevne er stærkt afhængig af graden af åbenheden i strukturen, af bidraget fra koordinationsændringer til den samlede volumenkomprimering og af glaskompositionen.

Afslutningsvis har vi undersøgt effekterne af fugtig aldring på strukturen og de mekaniske egenskaber af alkali-aluminoborat-glasser. Vi har observeret at denne hydrolyseeffekt er stærkt afhængig af kompositionen og den kemiske resistens af oxidglasser. Vi har vist at ekstrem høj modstand mod revnedannelse ved skarp kontaktbelastning kan opnås i cæsium-aluminoborat-glas ved simpel opbevaring af glasset i typiske atmosfæriske fugtighedsforhold. Dette skyldes dannelsen af et mikrometer-tyndt hydreret overfladelag med en høj grad af frihed i netværket og indeholdende cæsium-hydroxyl-enheder med høj mobilitet, derved ydende beskyttelse af glasset bedre mod skader fra indentering. Kort sagt, vores arbejde angiver retningslinjer for hvordan man kan kontrollere hastigheden af fugtig aldring med relativ luftfugtighed og temperatur for at danne et hydreret overfladelag og derved at opnå en ultrahøj modstand mod revnedannelse i sådanne glas.

ACKNOWLEDGEMENTS

I would like to thank many people for helping me during my Ph.D. Without them, I can hardly imagine whether I can successfully complete my PhD study. First and foremost, I would like to thank my supervisor, Prof. Morten Matstrup Smedskjær. Three years ago, I met him for the first time through a Skype meeting. With his enthusiastic help, I won a CSC scholarship, and this allowed me to come to Denmark for pursuing my PhD degree with him in 2018. Afterwards, I was thrilled by his scientific knowledge and attitude, research creativity and working efficiency. With his guidance and support, I can easily complete my research projects independently. During these three years, I have also learned from the encouraging discussions and constructive criticisms how to better design experiments, write high-level scientific papers and overcome the challenge in the study. These are the great benefits of my life. I really appreciate his help.

I would like to thank all my collaborators, who made it possible to realize the goal of my studies through their excellent expertise and experience. I would like to thank our collaborators at Corning Inc.: Dr. Randall E. Youngman. Dr. Randall provided specific help and guidance on the tricky technique of solid-state NMR spectroscopy. He has furthermore been involved with scientific discussions and the writing of manuscripts. I would like to thank our collaborators at UCLA: Prof. Mathieu Bauchy. He often gave me some scientific discussions and constructive criticisms at our weekly group meetings. I would like to thank our collaborators in Warsaw, Poland: Profs. Sylwester Rzoska and Michal Bockowski. Both provided compression experiments and participated in scientific discussions and manuscript reviews. I would like to thank our collaborator at Aalborg University: Associate Prof. Lars R. Jensen. He provided ever-present helpfulness and assistance with Raman spectroscopy and mechanical testing. Furthermore, he also participated in scientific discussions and manuscript reviews.

I also appreciate Professor Zhuan Li from Central South University in China, who made the recommendation for me to come to Denmark for the PhD degree. In addition, he gave me great help in the application of CSC scholarship, and led me into the scientific world. I really appreciate his help.

It is a marvellous experience to work with all my colleagues in the chemistry section. They helped me so much in conducting my experiments, reviewing my paper as well as other leisure activities, like coffee breaks and cake sharing. I would like to thank everyone to express my gratitude: Prof. Yuanzheng Yue, Assoc. Prof. Donghong Yu, Assoc. Prof. Morten Christensen, Assoc. Prof. Vittorio Boffa, Assoc. Prof. Wanmin Liu, Assoc. Prof. Thorbjørn Nielsen, Assoc. Prof. Mads Jørgensen, Assoc. Prof. Cejna Quist-Jensen, Dr. Ang Qiao, Dr. Chao Zhou, Dr. Yang Shen, Dr. Tobias Bechgaard, Dr. Martin Østergaard, Dr. Rasmus Peterson, Dr. Usuma Naknikham, Dr. Katie

Kedwell, Dr. Kacper Januchta, Dr. Malwina Stępniewska, Dr. Qiang Tao, Dr. Ming Liu, Dr. Theany To, Dr. Anil Kumar Suri, Dr. Qi Zhang, Dr. Tao Du, Mikkel Bødker, Katarzyna Janowska, Rasmus Madsen, Søren Sørensen, Anne Sophie Jødal, Johan Christensen, Rasmus Christensen, Chengwei Gao, Sheng Li, Zhencai Li, Xianzheng Ma, Wei Fan, Xiangting Ren, Wei Xu, Jiajia Yan, Xinxin Chen, Annemarie Davidsen, Anne Flensburg, Lisbeth Wybrandt, Timo Kirwa. I also appreciate Assoc. Prof. Deyong Wang for his scientific assistance and helpful discussions.

Furthermore, I would personally give my tremendous appreciation to my lovely friends: Juan, Miaomiao, Jinfeng, Wenfu, Na, Bin, Kaiqi, Da, Yanqi, Yichen, Xu, Guanyi, Congyi, Fu, Lan, Qian. This list goes on. It is lovely to have them around.

My great thanks belong to all members of my family. I could continue my study to pursue the PhD degree and come abroad owing to their endless love, encouragement and support. The biggest thanks go to my dear wife, Xiaoguang, mainly for her understanding, unconditional support and faith in my abilities. I love all of you forever!

TABLE OF CONTENTS

Chapter 1. Introduction.....	11
1.1. Background and Challenges.....	11
1.2. Objectives.....	12
1.3. Thesis Content.....	13
Chapter 2. Fundamentals of Indentation Deformation and Cracking	15
2.1. Deformation Mechanism.....	15
2.2. Indentation Cracking.....	21
2.3. Summary.....	24
Chapter 3. Structure and Mechanical Properties of Borate-based Glasses	25
3.1. Structure of Borate-based Glasses.....	25
3.1.1. Borate Glass.....	26
3.1.2. Aluminoborate Glass.....	26
3.1.3. Borophosphate Glasses.....	29
3.2. Structure-Property Relations.....	29
3.3. Summary.....	30
Chapter 4. Structure and Mechanical Properties of Densified Aluminoborate Glasses.....	31
4.1. Hot Compression.....	31
4.2. Densification Effect on Structure.....	32
4.2.1. Short-Range Structure.....	33
4.2.2. Medium-Range Structure.....	34
4.3. Composition Effect on Densification Behaviour.....	36
4.4. Densification Effect on Mechanical Property.....	38
4.4.1. Density.....	38
4.4.2. Young's Modulus and Hardness.....	39
4.4.3. Crack Initiation Resistance.....	39
4.5. Relations of Atomic Self-Adaptivity and Cracking Behaviour.....	40
4.6. Summary.....	43

Chapter 5. Structure and Mechanical Properties of Hydrated Aluminoborate Glasses	45
5.1. Humid Aging Post-treatment	45
5.2. Chemical Durability	46
5.3. Content and Form of Water in Glass	47
5.4. Water Effect on the Structure of Aluminoborate Glass	48
5.5. Hydration Layer Depth	50
5.6. Hydration Effect on Deformation/Cracking Behavior	51
5.6.1. Indent Size Length Recovery	51
5.6.2. Elastic Recovery.....	52
5.6.3. Crack Initiation Resistance.....	53
5.7. Summary	55
Chapter 6. Conclusions and Perspectives	57
6.1. Conclusion	57
6.2. Perspective	58
Biography	59
List of publications	69

CHAPTER 1. INTRODUCTION

1.1. BACKGROUND AND CHALLENGES

Glasses are one of the most important families of man-made materials due to their many excellent properties(1)(2)(3), and have been widely used in various application fields, from automotive window glass and architectural window glass to protective screens for electronic devices and optical fibres in high-speed internet cables etc. As we know, defect-free amorphous oxide materials can have very high ultimate strength and ductility(4)(5). However, Almost all oxide glasses are inherently brittle due to the unstable shear deformation mechanism and limited crack propagation resistance(6)(7)(8). Due to surface flaws and defects, the practical application strength of glasses is much lower than the theoretical value. In addition, the impact or scratching events may lead to the formation of cracks on the glass surface, thereby amplifying local tensile stresses, leading to catastrophic failures. These obviously have severely restricted the future application of oxide glass in various fields, including energy, information technology and communications, defense, consumer electronics, and medicine. In order to meet the higher requirements for glasses in future applications, glass scientists have been interested in finding and designing stronger glass. In addition, it is necessary to develop a new type of glass with higher crack resistance and fracture toughness to minimize the possibility of crack initiation and flow propagation. In the past many years, glass scientists have done a lot of research to tried to improve the surface damage resistance of glass through precise composition design and more effective surface treatment. The chemical composition design(9)(10)(11)(12), heat treatment (13) and chemical surface strengthening (14)(15) are the most commonly used methods. The purpose of heat treatment and chemical surface strengthening is to increase the strength of the glass surface, thereby increasing the critical stress required for crack initiation on the surface. However, these methods will not only increase the extra cost of manufacturing glass, but are also limited by the thickness of the glass (heat treatment) and the glass containing movable ions (chemical surface strengthening), etc.

Among the different oxide glasses, modified borate-based glasses have been widely used in various industrial fields (such as batteries, metal seals, biomedical components etc(16)(17)(18). because of their excellent properties(1)(2)(3), such as good transparency, low melting temperature, similar thermal expansion coefficient with many metals/ceramics and corrosion resistance to alkali-metals. Furthermore, borate-based glass has some interesting features in terms of structure, mainly includes: i) Rich medium and short-range structure(19)(20)(21), and ii) The network structure is sensitive to external conditions such as temperature(22), humidity(23)(24) and pressure/stress(25)(26)(27). In some borate-based glasses, the network structure cannot accommodate more tetrahedral boron units, and then form non-bridging oxygen (NBO), which in turn depolymerizes the glassy network structure. These

structural differences will affect the mechanical properties of the glass. In addition, various superstructure units exist in the borate-based glass. These complex superstructures significantly affect their various properties(28)(29)(30), such as density, glass transition temperature, thermal expansion coefficient, ionic conductivity, etc. In particular, we found in aluminoborate glasses(24)(31) that the glass network structure is very sensitive to the applied pressure/stress due to the increase of the coordination number of boron or aluminum under pressure/stress, which is beneficial to improve the crack initiation ability. These special structural characteristics will lead to the discovery of some glass families with high damage resistance, including alkali aluminoborate glasses as well as boroaluminosilicate glasses. These studies on the composition design of borate-based glass are of great significance for understanding the deformation mechanism of oxide glass and the structural origin of high damage resistance.

Due to the non-equilibrium nature and non-crystalline structure of oxide glasses, knowledge of the relation between chemical composition, atomic-scale structure, and mechanical properties remains challenging(32)(33). Therefore, it is important to understand the structural origins of the high crack resistance of oxide glasses(34)(35). This thesis will be devoted to understanding the structural origins of indentation deformation and cracking behaviour and the underlying material properties, which is beneficial to improve the crack resistance of oxide glass. In addition to obtaining fundamental understanding, we will search for more damage resilient glass compositions, which are prone to self-adapt by changing their chemical bonding environment when subjected to an external force. Furthermore, the dependence of crack resistance and indentation recovery on aging under a humid atmosphere will be studied. The dependence of crack resistance on chemical composition, structural features, deformation mechanism, indentation recovery, and other mechanical properties will be also the focus of our investigation.

1.2. OBJECTIVES

The overall goal of this Ph.D. project is to strengthen the current understanding of composition-structure-mechanical property relations in oxide glasses. More specifically, this thesis focuses on studying the correlation between the chemical composition and deformation and cracking behavior of borate-based glasses. Furthermore, this thesis also attempts to study the effects of humid aging on the structure and performance of glasses. In short, this thesis focuses on studying how to adjust the glass chemical composition and post-processing conditions to achieve better mechanical properties for oxide glasses. The thesis only describes the study on modified borate-based glass systems, especially aluminoborate glasses. In summary, the thesis attempts to shed light on the following aspects:

1. Fundamentals of indentation deformation and cracking.

2. Structure and mechanical properties of borate-based glasses.
3. Structure and mechanical properties of densified aluminoborate glasses.
4. Structure and mechanical properties of hydrated aluminoborate glasses

1.3. THESIS CONTENT

The main experiments of this thesis are conducted at Aalborg University. This thesis consists of six papers, of which four have been published in peer-reviewed journals, one submitted for publication, and one in preparation. These papers constitute the main body of the thesis, and will be cited by their roman numerals throughout the thesis:

I. **P.F. Liu**, K. Januchta, L.R. Jensen, M. Bauchy, M.M. Smedskjaer, “Competitive Effects of Free Volume, Rigidity, and Self-Adaptivity on Indentation Response of Silicoaluminoborate Glasses”. *Journal of American Ceramic Society*. 103 (2020) 944-954

II. K. Januchta, **P.F. Liu**, S.R. Hansen, T. To, M.M. Smedskjaer, “Indentation cracking and deformation mechanism of sodium aluminoborosilicate glasses”. *Journal of American Ceramic Society*. 103 (2020) 1656-1665

III. **P.F. Liu**, A.L.S. Søndergaard, R.E. Youngman, S.J. Rzoska, M. Bockowski, L.R. Jensen, M.M. Smedskjaer, “Structural densification of lithium phosphoaluminoborate glasses”. *Journal of American Ceramic Society*. 104 (2021) 1345-1359

IV. **P.F. Liu**, R.E. Youngman, L.R. Jensen, M. Bockowski, M.M. Smedskjaer, “Achieving Ultrahigh Crack Resistance in Glass through Humid Aging”. *Physical Review Materials*. 4 (2020) 63606

V. **P.F. Liu**, L.R. Jensen, C.W. Gao, M.M. Smedskjaer, “Indentation deformation and cracking behavior of hydrated aluminoborate glasses”. Manuscript submitted to *Journal of American Ceramic Society*

VI. **P.F. Liu**, R.E. Youngman, L.R. Jensen, M.M. Smedskjaer, “Structural Transition in Lithium Borophosphate Glasses Explains the Variation in their Mechanical Properties” (to be submitted).

CHAPTER 2. FUNDAMENTALS OF INDENTATION DEFORMATION AND CRACKING

In daily life, glass products always fail due to breakage, which mainly consists of three stages, namely deformation, cracks initiation and fracture (crack growth). Specifically, when the surface of the glass comes into contact with a hard object, the glass may undergo deformation (elastic and plastic) first, because the stress generated during this process does not reach the yield stress condition(36). As the contact load becomes larger, cracks will occur in the contact deformation area after reaching the yield stress condition. Over time, this may cause cracks to grow, which leads to the failure of glass products. In addition, the contacting objects can have different material properties, shapes and speeds, which complicates the analysis of failure events. In this chapter, we mainly introduced the deformation and cracking behavior caused by the sharp contact load. To better understand the deformation and cracking mechanism of oxide glass, indentation experiments are used to understand the deformation and cracking behaviour and its structural origin in this thesis.

2.1. DEFORMATION MECHANISM

In the indentation experiments, the response of glasses to a sharp contact load is not only related to their hardness, but also the strength, ductility or brittleness. During the indentation experiment, the initial response of the glass material is elastic deformation. As the applied load continues to increase, plastic deformation will occur in the contact area of the glass surface with the indenter. The different types of deformation have been schematically shown in Figure 2-1b. A lot of previous work(37)(38)(39)(40) has shown that the permanent deformation (plastic) in the indentation process stems from two different processes, namely densification and shear flow, which largely depend on the glass composition and experimental conditions (loading/unloading rate, dwell time, temperature and humidity, etc). Shear flow is the main reason for inducing material to accumulate around the indents, and this process mainly involves the long-distance displacement of structural units and atoms. While the densification process mainly involves small relative displacements of atoms and limited deformation of structural units (such as changes in bond angles). Through many studies on glass composition, Peter(37) provide the scanning electron microscopy (SEM) images of Vickers indented alkali silicate glasses (Figure 2-1a) to prove the existence of the densification in the indentation-induced deformation. Furthermore, we found the observations of shear flow during indentation from our study regarding the indentation deformation and cracking behavior of hydrated aluminoborate glasses (Paper V). We can obviously find the pile-up around the indentation imprint above the glass

surface (Figure 2-1c), as well as shear bands (also called slip lines) inside the indent (Figure 2-1c), suggesting that the hydrated caesium aluminoborate glasses are indeed subject to shear flow during indentation (41). Shear bands are visible as parallel lines or waves moving outward from the point of contact, indicating a flow-like material deformation (42). Some studies (38)(43) have shown that the deformation mode strongly depends on the chemical composition, especially the content of the network modifier. In other words, glass with high modifier concentration tends to deform by shear flow during indentation, while glass with lower modifier content is deformed mainly by densification during indentation.

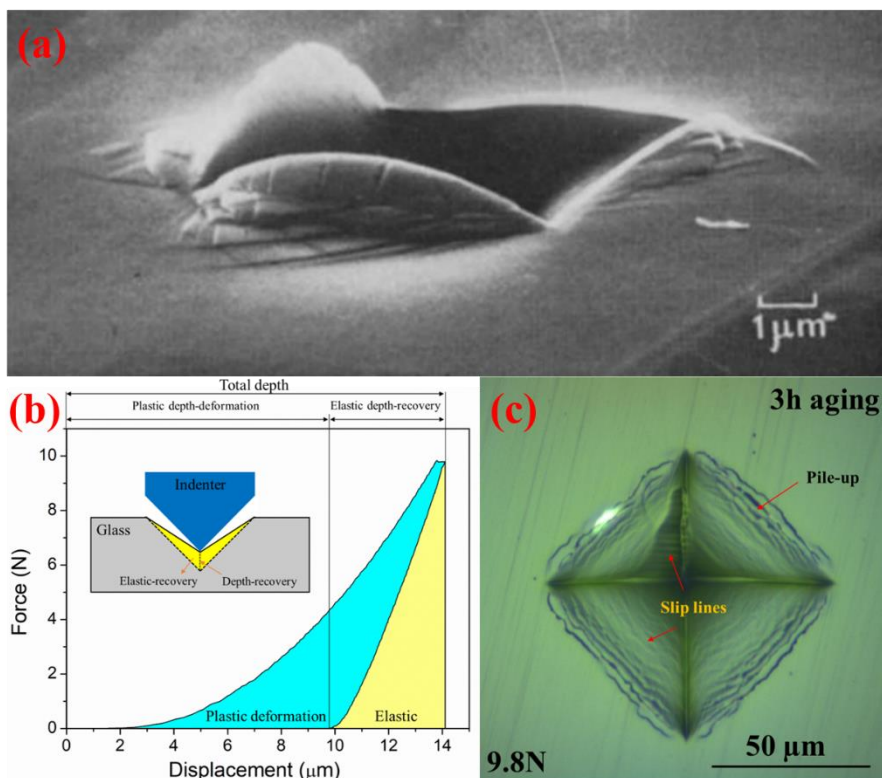


Figure 2-1. (a) Scanning electron microscope image of a Vickers-70° indentation impression on the surface of an alkali silicate glass. Figure reproduced from ref. (37). (b) The force-displacement curve has been obtained at 9.8 N. Figure adapted from Paper V. (c) Optical images of Vickers-136° indents on the surface of the Cs-aluminoborate glass before and after humid aging at 60% RH after 3 hours aging. Figure adapted from Paper V.

From the above analysis, we know that the indentation process mainly involves reversible (elastic) and irreversible (plastic) deformation processes. This elastic contribution can be estimated from the elastic recovery accompanying the unloading process (see Figure 2-1a). However, understanding the contribution of permanent

deformation to the indentation process is relatively complicated. Since it is meaningful to understand the residual stress stored in the permanent deformation during the indentation process, Yoshida and Rouxel et al (38)(44) quantified the deformation mechanism by using atomic force microscopy (AFM). This method takes advantage of the different characteristics of dense substances and replacement substances. The dense glass network structure can be recovered by annealing below T_g , and the recoverable volume increases with the increase of annealing temperature. While, the volume change caused by the shear flow is not affected by the annealing at $0.9 T_g$, because the viscosity is too high and there will not be any significant viscous flow in the experimental time (2 hours). Therefore, this method (see Figure 2-2) quantifies the recording topographic images of the indent size before and after the annealing at $0.9 T_g$ to measure the shrinkage extent of the indentation cavity during annealing. Since densification can affect both the inside of indent and the immediate neighborhood of the indent side, we can estimate the densification volume through the post-annealing indentation and pile-up volumes. The densification volume (V_d) can be estimated as:

$$V_d = (V_i^- - V_a^-) + (V_a^+ - V_i^+) \quad (2-1)$$

where V is the volume of the indent site, the superscripts - and + relate to the volume below and above the surface of the glass, while the subscripts i and a are related to the initial state and annealed state of the indent.

Due to geometric constraints and residual stress fields, the densification volume may not be completely recovered after annealing. As such, the relative extent of densification can be expressed as the volume recovery ratio (V_R), and the calculation formula is further defined as follows:

$$V_R = \frac{V_d}{V_i^-} \quad (2-2)$$

where V is the volume of the indent site, the superscripts - and + relate to the volume below and above the surface of the glass, while the subscripts i and a are related to the initial state and annealed state of the indent.

The $V_a^+ - V_i^+$ shows the contribution of densification to the pile-up, while the $V_i^+ - (V_a^+ - V_i^+)$ can be attributed to shear flow. Hence the pile-up ratio (V_p) representative of volume-conservative flow is estimated as:

$$V_p = \frac{(2V_i^+ - V_a^+)}{V_i^-} \quad (2-3)$$

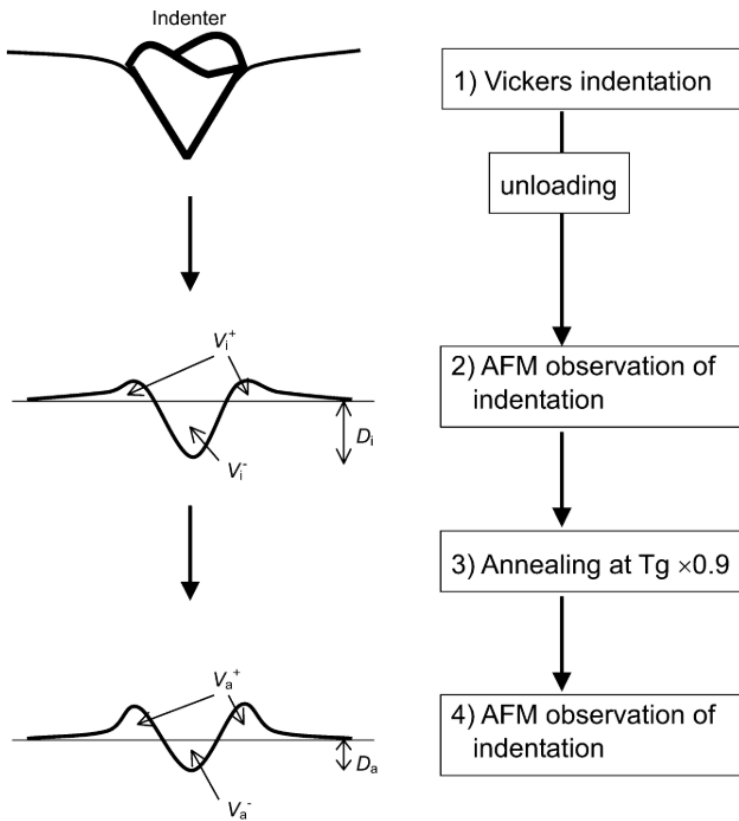


Figure 2-2. Schematic diagram of the process for measuring changes in indentation volume before and after annealing. Figure reproduced from ref (38).

However, since AFM measurement is time-consuming and resource-intensive, this hinders the effective collection of oxide glass densification data. In addition, we can obtain similar information from optical microscopes. The shape and size of the indent will change after the annealing at $0.9 T_g$, which can be easily observed by an optical microscope, as shown in Figure 2-3.

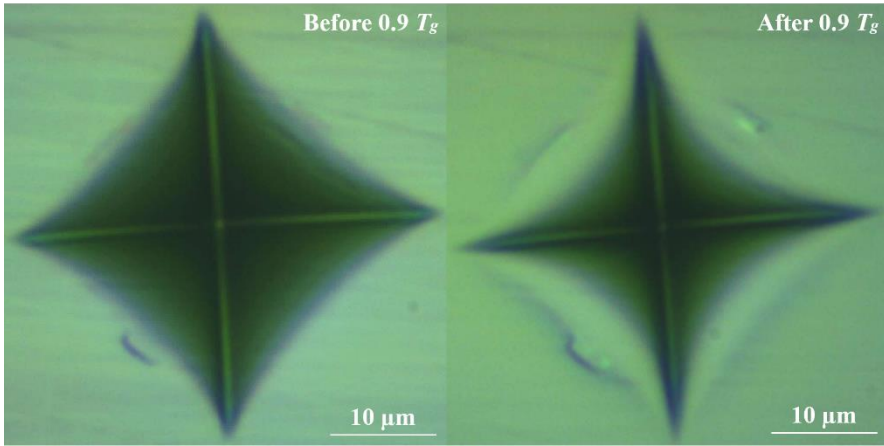


Figure 2-3. Optical images of Vickers-136° indents produced at 4 N on the surface of the 20SiO₂-35B₂O₃-25Li₂O-20Al₂O₃ glass before and after re-annealing at 0.9T_g for 2h. Figure adapted from Paper I.

In particular, we can find from Fig. 2-3 that the side length of the indentation shrinks significantly, while the recovery of the diagonal length is close to zero. In this work, a parameter similar to V_R has been proposed, namely the side length recovery (L_{SR}), which can be calculated from the indentation side length recovery before and after annealing (Figure 2-4):

$$L_{SR} = \frac{L_{S,i} - L_{S,a}}{L_{S,i}} \quad (2-4)$$

where L_S is the indent side length (edge to edge), and subscripts i and a are related to initial and annealed states, respectively.

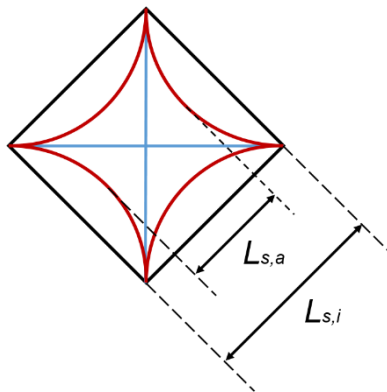


Figure 2-4. Schematic representation of the analysis method for the side length recovery (L_{SR}).

To further evaluate the possibility of using L_{SR} as a substitute for V_R calculated from AFM measurements, we determined the L_{SR} values of a series of oxide glasses with known V_R values (Paper II). Figure 2-5 shows the obvious positive correlation between L_{SR} and V_R , showing that L_{SR} seems to be a satisfactory alternative to V_R . This paves the way for a more effective quantitative study of the indentation deformation mechanism in the future.

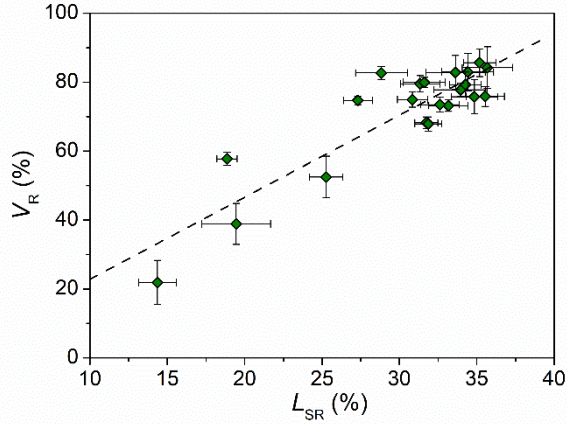


Figure 2-5. Volume recovery ratio (V_R) as a function of side length recovery ratio (L_{SR}). Figure adapted from Paper II.

Moreover, we can obtain similar information from optical microscopes of aluminoborate glasses before and after hydration (Paper IV). The shape and size of the indent will change after humid aging, which can be easily observed by an optical microscope, as shown in Figure 2-6. Besides, we can find from Fig. 2-6 that the side length of the indentation shrinks significantly than the diagonal length. In order to evaluate the effect of humid aging on the indentation deformation of the aluminoborate glasses, we used similarly to the recovery of indentation volume following this method to calculate the aging-induced side length recovery (L_{AR}),

$$L_{AR} = \frac{L_{S,i} - L_{S,a}}{L_{S,i}} \quad (2-5)$$

Where L_S is the indent side length (edge to edge), and subscripts i and a are related to initial and aged states, respectively.

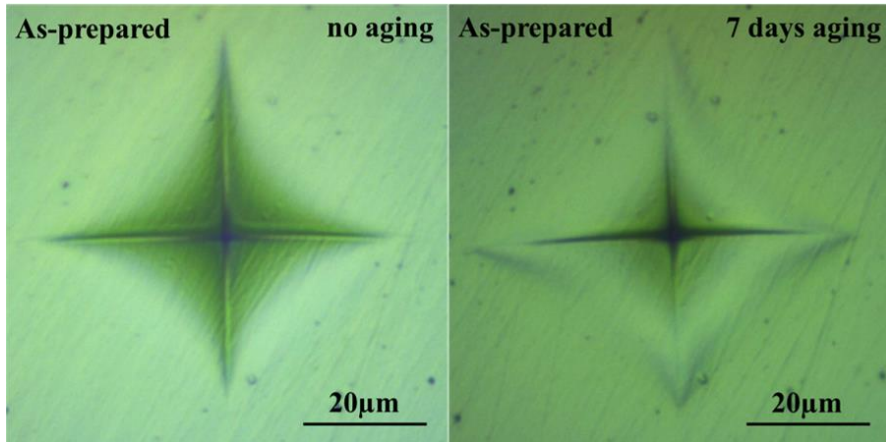


Figure 2-6. Optical images of Vickers-136° indents produced at 4.9 N on the surface of the Cs-aluminoborate glass before and after aging at 23 °C and 45 %RH for 7 days. Figure adapted from Paper IV.

2.2. INDENTATION CRACKING

Accompanied by the unloading process, the glass in the elastic-strain zone attempts to recover, but it is hindered by the permanently deformed glass in the plastic zone. This process will lead to the storage of residual stresses, which may initiate the formation of cracks if they are tensile and of sufficient magnitude. Therefore, the cracking behaviour of oxide glass depends on the magnitude of the residual stress stored in and around the deformed area. Some studies have shown that the indentation crack mode has a strong correlation with the chemical composition of the glass(45)(46). For example, it is known that amorphous silica will form annular cracks around the indentation(47)(48), while soda-lime-silica glass is more prone to form long radial cracks which started from the corners of the indents(49). Figure 2-7 shows the different cracking systems found in oxide glass through the Lee et al study. These cracks are median, radial, half-penny, cone and lateral, respectively. In the thesis, we focus on the corner cracking systems including the radial and half-penny.

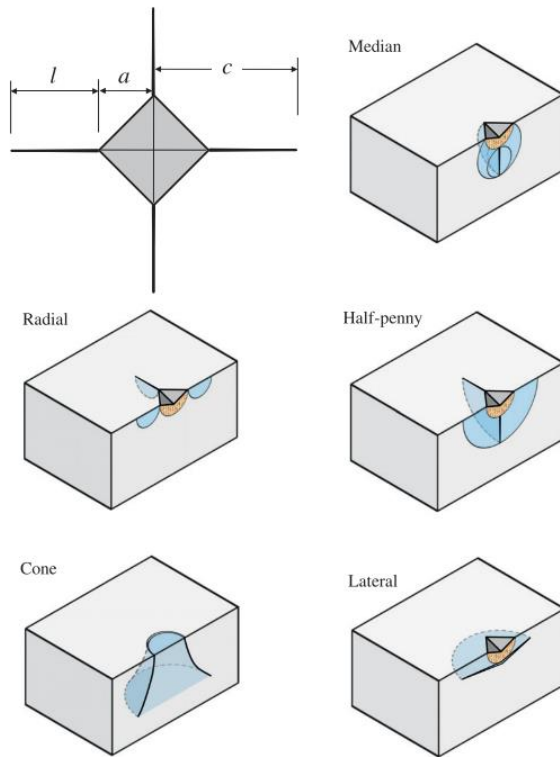


Figure 2-7. Schematic diagram of different crack systems caused by Vickers indentation in oxide glass. Figure reproduced from ref (49).

From the deformation mechanism analysis, we can find that part of the energy provided by the indenter is consumed in plastic deformation, while the remaining part is used for elastic recovery during unloading. The crack initiation comes from the difference in stress matching at the elastoplastic boundary(50). This is because the plastic deformation area is under compressive stress from the indenter, while the elastic deformation area is under tensile stress from the indenter. Now, the common solution to the indentation crack problem is the elastic stress field proposed by Yoffe (50). This model deals with axisymmetric loads in an infinite half-space from the indenter tip, and shows the distribution of elastic stress outside the plastic zone. The elastic stress in Yoffe's field defines the probability of crack Initiation in a given position and direction. From this model, we know that the stress of the crack system strongly depends on the loading condition, material properties and the distance from the contact point. Moreover, Arora et al. (47) found that the indentation crack mode and indentation deformation mechanism are also related to the classification of normal and abnormal chemical compositions. That is, glasses with low Poisson's ratio values tend to be easy to densify and show cone cracking, which is "abnormal" behavior. While the glass with a higher Poisson's ratio value also undergoes extensive shear

during the indentation process and exhibits median and/or radial cracking, which is “normal” behavior. According to the basic characteristics of glass, Sellappan and Rouxel et al. proposed the boundary of different microcrack mechanisms in the representation of E/H and ν (see Figure 2-8), which opened the way for some basic principles about the compositional dependence of cracking behavior. All studied glasses in this thesis are mainly distributed in the median and/or radial cracking area, which is conducive to study their crack resistance (see next).

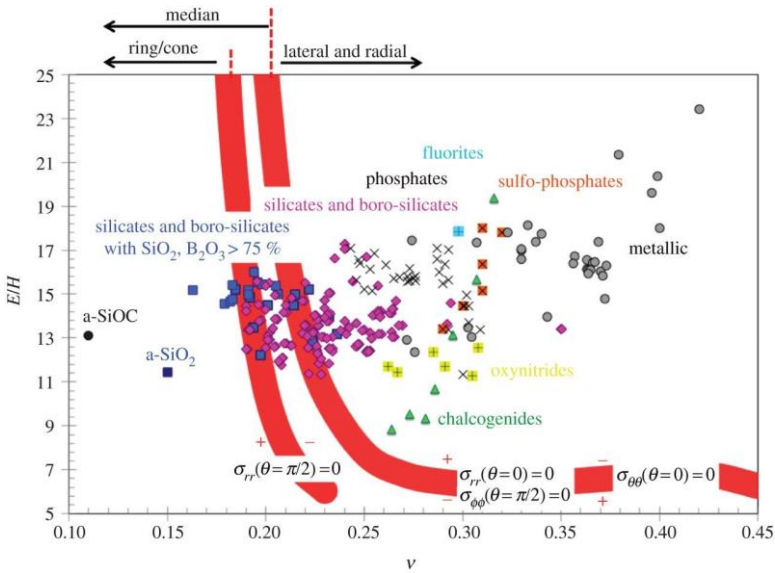


Figure 2-8. Dependence of the critical Poisson's ratio values for the transitions from cone/median to median cracking and from median to lateral/radial cracking on the glass composition in the case of loading. Figure reproduced from ref (51).

According to the composition and characteristics of the glasses, the cracking mode in the oxide glass can be reasonably predicted by the above-mentioned method or model. However, it is still very challenging to predict the critical load of crack initiation. At present, indentation experiments are usually used to quantify the crack initiation ability of glasses. Especially for glass that can produce corner cracks (radial and half-penny in Figure 2-7), we usually use the method of Wada et al. (52) to evaluate the crack initiation ability of the glass surface. That is, we first use the Vickers indenter to produce a series of indents on the glass surface under different loads, and then evaluate the crack initiation ability by recording the number of corner cracks of each indentation imprint. According to this method, the probability of crack initiation (PCI) at each load was derived as the ratio between the number of corners with a corner crack and the total number of corners. The crack resistance is defined as the load at which an average of 2 cracks for Vickers ($PCI = 50\%$) occurred. This is performed under different loads, from low loads that cause no corner cracks (i.e. 0%) to high

loads that cause extensive corner cracks (i.e. 100%). Then we fit the data using appropriate mathematical functions (solid lines in Figure 2-9). As shown in Figure 2-9, the load corresponding to a 50% crack probability is defined as the indentation crack initiation resistance, or simply crack resistance (CR). In this thesis, we use this parameter (CR) to characterize the crack initiation ability of glass under various conditions (different components, densification and hydration).

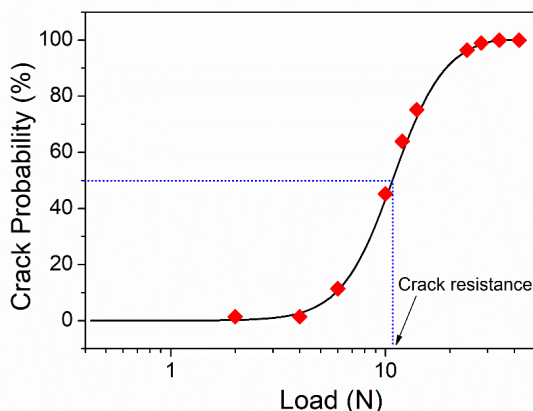


Figure 2-9. Crack probability as a function of applied indentation load for lithium silicoaluminoborate glasses. The experimental data was fit to a sigmoidal function of the form $y = A_2 + (A_1 - A_2) / \left[1 + \left(\frac{x}{x_0} \right)^p \right]$ (solid lines), and the crack resistance (dashed line) was derived from the load at which an average of two radial cracks ($CP = 50\%$) formed at the corners of the residual Vickers hardness imprints. Figure adapted from Paper I.

2.3. SUMMARY

As mentioned in Section 1.2, the focus of this thesis is to understand the deformation and cracking behavior of boron-based glass. In this chapter, we mainly introduce the deformation mechanism and cracking behavior of glass under contact load. From this chapter, we know that understanding the critical load for cracking (crack initiation ability) is one of the important factors in the design of super-strong glass. This is because the surface of the glass with low crack resistance is susceptible to continuous damage, thus leads to the appearance of a large number of defects, thereby increases the probability of failure for the glass material. Furthermore, the crack initiation ability of glass strongly depends on the glass composition, as well as some post-treatment includes surface chemical enhancement, densification, hydration, etc. However, to further understand the relationship between these factors and crack initiation of glasses, we must start with understanding the network structure of glass, which is the content of the next chapter.

CHAPTER 3. STRUCTURE AND MECHANICAL PROPERTIES OF BORATE-BASED GLASSES

Glasses with different compositions have different network structure arrangements and macroscopic properties. From Section 2.2, we know that depending on the glass composition, different micro-crack patterns are observed, and the indentation cracking may be formed during the loading and unloading stages. Therefore, when studying the deformation and cracking behaviour of glass, we must consider the composition of the glass to understand the structural origin of deformation and cracking for glasses. The structural arrangement of glass changes significantly with the composition, so we first need to understand the network structure of glass with different composition systems, such as silicate glass, borate glass and phosphate glass. Therefore, this chapter mainly introduces the structure and performance of different glass systems.

3.1. STRUCTURE OF BORATE-BASED GLASSES

Generally, we first need to melt the oxide mixture at a high temperature, and then quickly cool the molten liquid into a glass state to obtain the oxide glass. During the cooling process, a random three-dimensional network composed of interconnected oxygen ions and metal or semi-metal cations is formed in the glass. This random network (see Figure 3-1) was proposed by Zachariassen(53) in 1932 and was subsequently confirmed(54)(55). However, since the bond angle distribution is larger than their crystalline counterparts, there is no long-range order in this random network (56). These random networks include network formers, intermediates and network modifiers. Some elements (such as B and Si) form tightly constrained coordination polyhedrons, which form the framework of the glass (network formers). Other types of elements (such as Li and Na) occupy the voids in the glass network, thereby affecting the characteristics of the structure (modifier). According to different glass structures and chemical properties, the last type of elements (such as Al) can be used as network formers and network modifiers (intermediates). Oxygen atoms in oxide glass can act as bridging (BO) or non-bridging (NBO) units. The form of bonding with oxygen atoms mainly depends on whether they connect two network-forming cations together or depolymerize the network by connecting the network-forming cation with a modified cation. The distribution of these oxygen species has an impact on the flexibility of the glassy network, which in turn affects the mechanical properties. With the development of glass structure theory, in 1985, Greaves' study(57) suggested to modify the random network theory, and showed that the modifier would not be randomly distributed in the glass network, but aggregated in the channel-like structure.

Next, the glass structure in the composition related to this thesis will be firstly introduced.

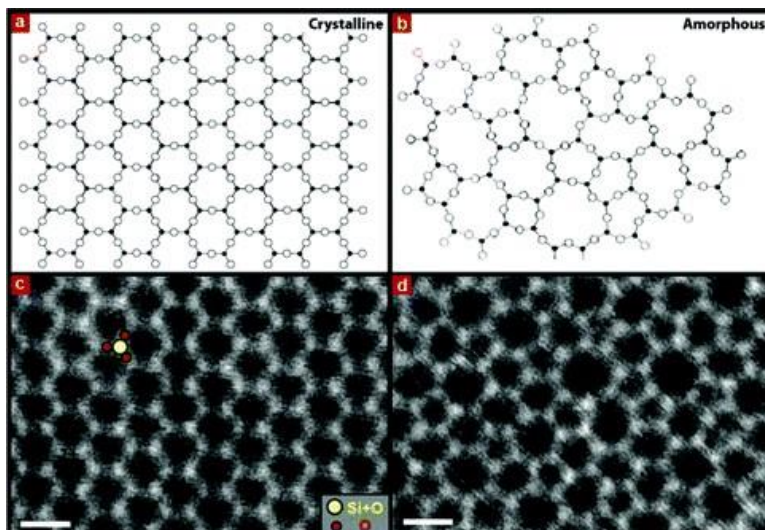


Figure 3-1. Annular dark-field scanning transmission electron microscopy images of crystalline (left) and amorphous (right) silica. The images were acquired on two-dimensional silica structures supported on graphene. The crystalline silica structures appears much more ordered compared to the amorphous network. The images are compared to schematic representations of structural configurations. Figure reproduced from ref. (54).

3.1.1. BORATE GLASS

The glassy B_2O_3 is formed by connecting boron atoms with three oxygen atoms in a planar triangular structure(58). These triangular boron units form a six-membered ring composed of three B atoms and three O atoms. After the introduction of modifiers in borate glass, a series of non-monotonic changes in properties will be observed, which is called “boron anomaly”(29). These modifiers can cause coordination changes from B^{III} to B^{IV} , where the B^{IV} can be charged by the modifier cation(59). However, when the modifier reaches the critical content, the boron-containing network structure cannot form more tetrahedral units, but forms depolymerized triangular units with NBO(58)(19).

3.1.2. ALUMINOBORATE GLASS

Aluminum is an intermediate, so it can be used as a network former and modifier, depending on the glass structure and chemical properties. Aluminum can enter the glass network in the coordination of Al^{IV} , Al^V or Al^{VI} . Four-coordination aluminum requires modifier or oxygen to ensure charge balance. When Al_2O_3 is introduced into the alkali borate glass, the aluminum cation has a higher affinity for the modifier

cation, which causes the aluminum cation to tend to enter the tetrahedral structure of the borate network. This indicates that in aluminoborate glass, there is a competition between the B atoms and the Al atoms for the modified cation, which usually moves in the direction favoring the Al atom(59)(60).

Taking hydrated caesium aluminoborate glass ($25\text{Cs}_2\text{O}-25\text{Al}_2\text{O}_3-50\text{B}_2\text{O}_3$, in Paper IV) as an example, we will introduce the short- and medium-range structure of aluminoborate glass in detail. From Figure 3-2, the expected band assignments are outlined in the following. The lowest frequency band region, ranging from ~ 280 to 625 cm^{-1} , is expected to contain contributions from B-O-B, Al-O-Al, and B-O-Al stretching vibrations(61), in addition to vibrations due to superstructural units such as penta-borates. The second region, ranging from ~ 625 to 815 cm^{-1} , is characteristic for B_2O_3 -rich glasses(61), since peaks in this frequency range are typically assigned to borate superstructures such as chain and ring metaborates(62)(63), di-triborates, and penta-, tetra-, or triborates(20)(64), as well as boroxol rings(62)(58). In addition, B-O-Al stretching and aluminate network vibrations may be found in this region. The third region, ranging from ~ 815 to 1000 cm^{-1} , is expected to result from vibrations of AlO_4 units ($\sim 900\text{ cm}^{-1}$)(65)(66), Al-B network ($\sim 980\text{ cm}^{-1}$)(67), and borate superstructures ($\sim 930\text{ cm}^{-1}$)(61)(63). The fourth region, ranging from ~ 1000 to 1200 cm^{-1} , is usually assigned to other borate superstructural units such as diborates. The fifth region, ranging from ~ 1150 to 1600 cm^{-1} , is expected to be dominated by signal contributions from vibrations of superstructural units such as pyroborate units and chain and ring metaborate units(68). The sixth region (containing two small bands), ranging from ~ 2300 to 2400 cm^{-1} , are from the Raman measurements process. The last region, ranging from ~ 2850 to 3800 cm^{-1} , is expected to be associated with hydroxyl groups attached to the glass network due to hydration(69)(13).

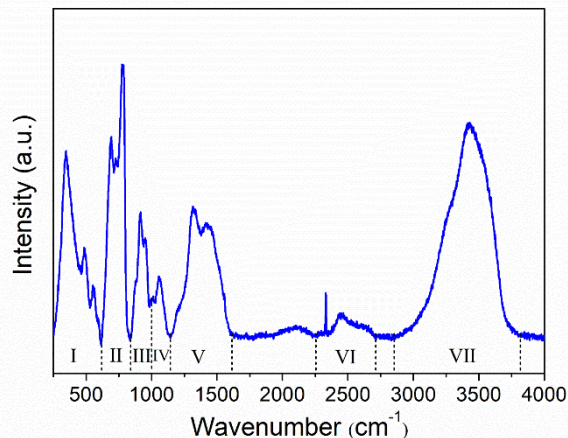


Figure 3-2. Micro-Raman spectrum of the caesium aluminoborate glass that has been aged for 7 days at 45% RH. The spectrum is divided into seven main band regions. Figure adapted from Paper IV.

SiO_2 is a common glass network former, and its structure and properties have received extensive attention from glass scientists(70). The SiO_2 glass network structure is a tetrahedral structure formed by one silicon atom and four oxygen atoms, where each Si-O-Si angle is around 144° (71) and the number of bridging oxygen (BO) is usually described by Q^n (n is the number of bridging oxygen). After adding the network modifier, non-bridging oxygen (NBO) is formed, which connects the network former to the network modifier. When silica is added to aluminoborate glass, this will cause the silica to mix with boron and aluminum polyhedrons, thereby forming Si-O-B and Si-O-Al bonds. Taking lithium silicoaluminoborate glass (in Paper I) as an example, we found that the introduction of SiO_2 will form the network of Si-O-Si, Si-O-B and Si-O-Al, as well as the stretching Si-O vibration in Q^2 and Q^3 species. However, this addition of SiO_2 will result in the removal of B_2O_3 , thereby reducing the formation probability of a medium-range order borate superstructure.

Glassy P_2O_5 is composed of PO_4 tetrahedrons, each of which has a different π bond ($\text{P}=\text{O}$). The number of bridging oxygens (BO) on the PO_4 tetrahedra can be described using the Q^n , where n is the number of BO atoms per PO_4 tetrahedra. Taking lithium phosphoaluminoborate glass (in Paper III) as an example, We can found that the addition of P_2O_5 will form the network of P-O-P and P-O-B, as well as and PO_2^- , $\text{P}_2\text{O}_7^{4-}$, PO_3^{2-} units. This addition of P_2O_5 will result in the removal of B_2O_3 and Al_2O_3 , thereby reducing the formation probability of AlO_4 units and medium-range order borate superstructures. As shown in Figure 3-3, we find from the ^{11}B NMR spectra that the addition of P_2O_5 is beneficial for the conversion of B^{IV} to B^{III} . This could be because the introduced phosphate competes with boron for some of the Li modifiers, leading to fewer Li- B^{IV} interactions and thus a lower level of modification of the borate polyhedra. Furthermore, the ^{27}Al NMR data indicates that Al^{IV} , Al^{V} and Al^{VI} groups are all affected by neighbouring phosphate groups, and thus these glasses contain a substantial amount of mixing between aluminate and phosphate polyhedra. Finally, we find that the addition of P_2O_5 has no effect on the aluminum coordinations, while has a slight effect on the boron coordinations.

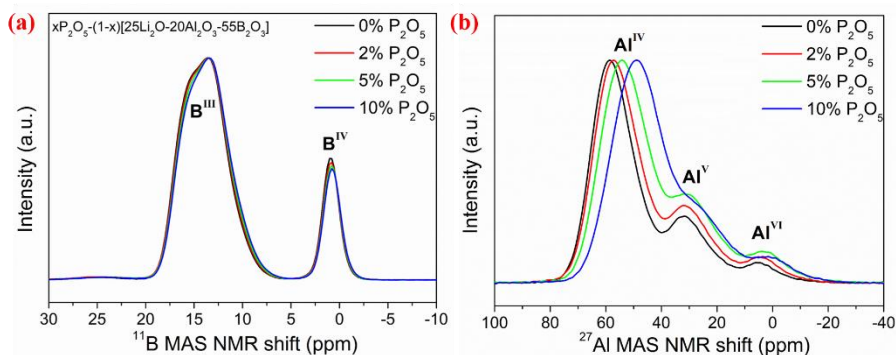


Figure 3-3. All NMR spectra results for the as-prepared lithium phosphoaluminoborate glasses. Figure adapted from Paper III.

3.1.3. BOROPHOSPHATE GLASSES

The addition of B_2O_3 to the glassy P_2O_5 will cause the mixing of P_2O_5 and boron polyhedrons, thereby forming the P-O-B bond. If the network modifier is introduced, NBO and BO_4 can be formed. Taking lithium borophosphate glass (in Paper VI) as an example, we find from the Raman spectroscopy data that the B_2O_3 addition disturbed the phosphate network, with the NMR data showing consumption of NBOs and formation of new rigid P-O-B bonds at higher boron content. Overall this increases the average network rigidity and also the density, Vickers hardness, glass transition temperature and Young's modulus, while a decrease in Poisson's ratio is found. In addition, we find that the phosphate groups are partially depolymerized from Q^3/Q^2 units to Q^1 units upon B_2O_3 addition, suggesting the number of bridging oxygens around phosphorous decreases.

3.2. STRUCTURE-PROPERTY RELATIONS

Due to the non-equilibrium nature and non-crystalline structure of oxide glasses, knowledge of the relation between chemical composition, atomic-scale structure, and mechanical properties remains challenging. Normally, the number of bonds of each atom and their strength have a significant impact on the properties of the glasses. In addition, the packing density of the atoms and NBOs also affect the properties of the glasses. Taking lithium borophosphate glass ($45Li_2O-(55-x)P_2O_5-xB_2O_3$, in Paper VI) as an example, we can find from Figure 3-4a that Young's modulus, Poisson's ratio and glass transition temperature are strongly dependent on the NBOs content. That is because that the consumption of NBOs can increase the average network rigidity of glasses. In addition, in Figure 3-4b, the hardness shows a monotonous correlation with the atomic packing density (C_g) and bond strength (the formation of P-O-B bonds). Therefore, enhancing the understanding of structure and structure-performance relations of glasses is essential for obtaining glass with excellent performance.

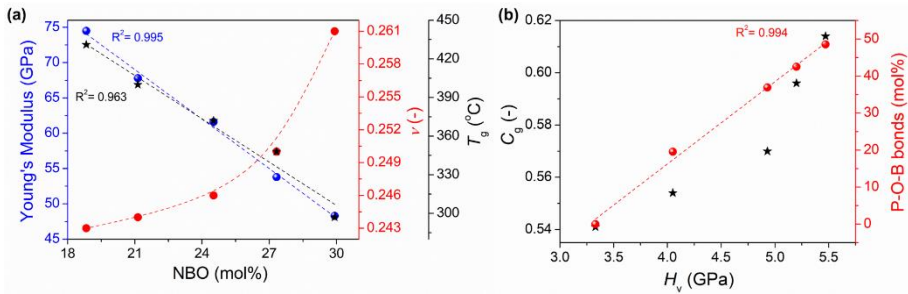


Figure 3-4. (a) The effect of NBOs on Young's modulus (E), Poisson's ratio (ν) and glass transition temperature (T_g). (b) The dependence of hardness on atomic packing density (C_g) and bond strength (P-O-B bonds). Figure adapted from Paper VI.

With the development of science, material researchers have developed a keen interest in how the structure affects the properties of materials and how to predict their properties based on the structure of materials. For glass materials, in 2009, Gupta and Mauro (15) used the topological constraints theory to successfully predict the glass transition temperature. The model predicts the glass transition temperature of a given glass by predicting its viscosity. That is because the number of bonds per atom determines the number of constraints, thereby determining the level of rigidity of a given glass composition at a given temperature. Subsequently, this topological method was applied to predict the mechanical properties of oxide glasses, such as hardness and elastic modulus(72)(73). Chemical bonds and bond angles constrain atoms in network glasses, with the strengths of the constraints depending on the local topology and the chemical nature of elements. In Paper I, we first calculated the number of bond constraints per atom (n_c) and constraint density (n') (see Figure 3-5a), then used the hardness model of Zheng et al (3-1) to predict the hardness of lithium silicoaluminoborate glasses (see Figure 3-5b).

$$H_V = \frac{dH_V}{dn'} \times n' \quad (3-1)$$

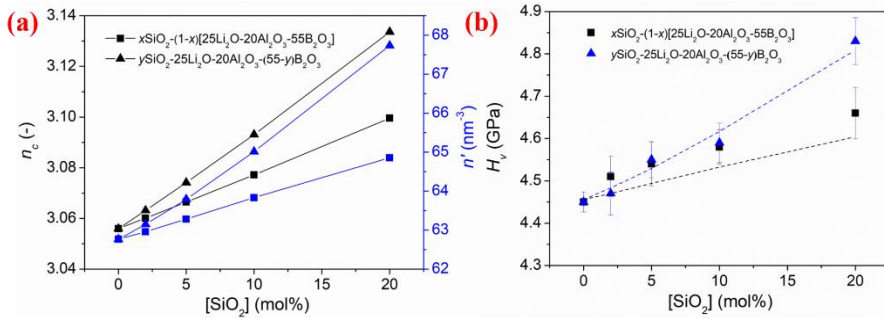


Figure 3-5. (a) Composition dependence of n_c and n' for lithium silicoaluminoborate glasses. (b) Composition dependence of indentation hardness for lithium silicoaluminoborate glasses. Figure adapted from Paper I.

3.3. SUMMARY

The structure of oxide glass is disordered, but the short- and medium-range structure is ordered and has abundant structural units. Therefore, we can easily change the short- and medium-range structure of the glass by adjusting the chemical composition (such as network formers, network modifiers and intermediates) to adjust the performance of the glass. Furthermore, we can use the network topology model to successfully predict the mechanical properties of the glass within a specific composition range. Therefore, the optimization of glass performance in the future requires a further understanding of the glass structure and structure-property relations.

CHAPTER 4. STRUCTURE AND MECHANICAL PROPERTIES OF DENSIFIED ALUMINOBORATE GLASSES

According to the analysis of the deformation mechanism in Chapter 2, we know that densification is one of the key factors affecting its deformation and cracking behavior in glasses. Therefore, understanding the densification mechanism of glass under high pressure is very important for designing a new type of damage-resistant glass(74). In addition, the compression process can balance the different characteristics of composition-temperature-pressure by adjusting the extent of freedom of the network structure. Under pressure, the changes in glass properties are related to the extent of volume densification and the corresponding structural changes in the short and medium-length scales(75). Therefore, the study on the compression of glasses can also improve our understanding of the structural origin for the deformation behavior of glasses, which is conducive to the design of glasses with excellent mechanical properties.

4.1. HOT COMPRESSION

Normally, glass is produced by cooling the melt at a sufficient cooling rate. Due to the different cooling rates of glass components, the network structure of the glass will undergo different extents of relaxation during the cooling process (from the supercooled liquid through the glass transition zone), resulting in different glass densities. Glass can be made dense by various methods, such as sub- T_g annealing, cold compression and hot compression. In addition, we can also obtain local densification of the glass through the indentation process. Next, we will focus on the hot compression method.

The compression experiment is mainly controlled by temperature and pressure test conditions. The hot compression experiment (high temperature) can achieve permanent densification of the glass at a pressure much lower than the pressure required for cold compression (room temperature)(70)(76)(77). In addition, in the cold compression experiment, when the pressure is lower than 5-10 GPa(78), the glass structure changes caused by most pressures are still reversible during the pressure reduction process. This is not conducive to studying the effect of densification on the structure and performance of the glass. Therefore, glasses are densified through the hot compression experiments (especially at the glass transition temperature (T_g), which has many advantages: i) Hot compression (at T_g) has less structural relaxation

problems due to the instantaneous pressure drop during cooling. ii) The glass can be compressed at a constant viscosity (i.e. 10^{-12} Pa•sec) at T_g . iii) Hot compression at T_g , the density of the glass increases linearly with the pressure (lower than 1 GPa)(79)(80). iv) Hot compression experiments can prepare large samples (cm^2 scale), allowing more comprehensive structural characterization and mechanical testing. Therefore, in this thesis, we mainly focused on the hot compression experiments at the ambient pressure (1-2 GPa) and glass transition temperature (T_g) of the glasses.

All studied glass samples were cut into a specific size and then optically polished. In our hot compression experiments, firstly the polished glass samples are placed in an Al_2O_3 crucible (see Figure 4-1). Subsequently, the pressure of the gas pressure chamber rises to slightly below the final target pressure. Then the gas pressure chamber is heated up to the target glass transition temperature at a constant heating rate of 600 K/h, which causes the internal pressure to increase up to the final target pressure. This gas pressure chamber will be kept at the target pressure (1-2 GPa) at T_g for 30 min. The gas pressure chamber will be then cooled down to room temperature at a constant rate of 60 K/min, and then depressurized to atmospheric pressure at a rate of 30 MPa/min. The pressure and temperature of these hot compression experiments were controlled with an accuracy of 1 MPa and 0.1 K, respectively.

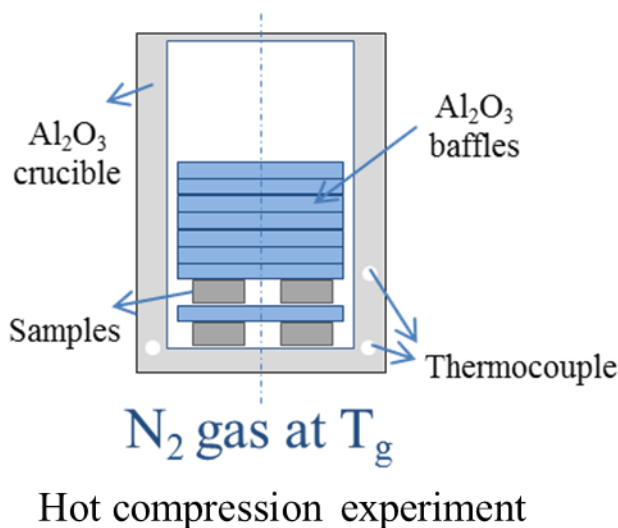


Figure 4-1. Schematic diagram of the gas pressure chamber used in our hot compression experiments. Figure reproduced from ref (81).

4.2. DENSIFICATION EFFECT ON STRUCTURE

Lee et al.(82) have proposed some mechanisms for structural changes caused by pressure. However, our current understanding of the relationship between the glass

structure changes by pressure and its performance is still very limited. Now, the continuous development of advanced material structure characterization techniques (such as Raman spectroscopy, and solid-state nuclear magnetic resonance (NMR) spectroscopy) provide the possibility to further understand this correlation.

4.2.1. SHORT-RANGE STRUCTURE

The short-range structure of glass is usually defined by the first coordination sphere of a given element. These elements include network modifiers (Li, Na, etc.) and network formers (B, Al and Si etc). Therefore, the impact of densification on the short-range structure is mainly reflected in the changes in the environment of the network modifiers and in the coordination numbers of the network formers. Next, we will introduce in detail the influence of compression on the short-range structure of glass based on our research.

The pressure-induced changes in modifier environments have previously been studied in situ during cold compression using diffraction techniques(83), and ex-situ after hot compression using NMR spectroscopy(31)(79)(84)(85). In addition, we found that it is relatively easy to use NMR spectroscopy to study the environmental changes of network modifiers in compressed glass. These studies indicate that the resonance frequency of the network modifier shifts to a higher frequency after hot compression.

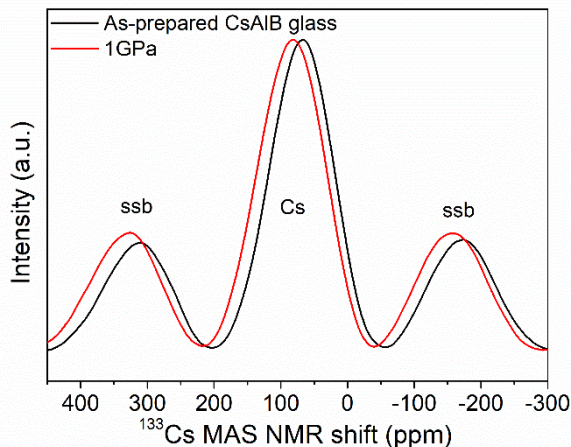


Figure 4-2. ^{133}Cs MAS NMR spectra for Cs-aluminoborate glass. Spinning sidebands (ssb) are indicated. Figure adapted from Paper IV.

In this thesis, we performed ^{133}Cs MAS NMR measurements on hot-compressed (1 GPa) Cs-aluminoborate glass ($25\text{Cs}_2\text{O}-25\text{Al}_2\text{O}_3-50\text{B}_2\text{O}_3$, in Paper IV), which expands the research scope of glass network modifiers. In this study, the ^{133}Cs MAS NMR shift increases from 79 to 87 ppm upon 1 GPa hot compression (see Figure 4-2). That is

because the pressure strengthens the interaction between oxygen and cesium ions in the network, resulting in a reduction in the average distance between oxygen and modified cations (Cs^+).

As we know, the network former is an important factor in the formation of the glass network structure. Therefore, understanding the effect of hot compression on the network former is very important for studying the densification mechanism of glass. In this thesis, we performed ^{11}B MAS NMR and ^{27}Al MAS NMR measurements on hot-compressed caesium aluminoborate glass ($25\text{Cs}_2\text{O}-25\text{Al}_2\text{O}_3-50\text{B}_2\text{O}_3$, in Paper IV) and lithium phosphoaluminoborate glasses ($x\text{P}_2\text{O}_5-(1-x)[25\text{Li}_2\text{O}-20\text{Al}_2\text{O}_3-55\text{B}_2\text{O}_3]$, in Paper III). Take lithium phosphoaluminoborate glasses as an example, we can find from Figure 4-3 that these local boron and aluminum environments are very sensitive to densification. That is, boron and aluminum will increase their average coordination number upon compression. The increase in the coordination number of boron is related to the presence of non-bridging oxygen (NBO), that is, $\text{B}^{\text{III}} + \text{NBO} \rightarrow \text{B}^{\text{IV}}$. The formation of high coordinated aluminum is for the charge-stabilised NBOs.

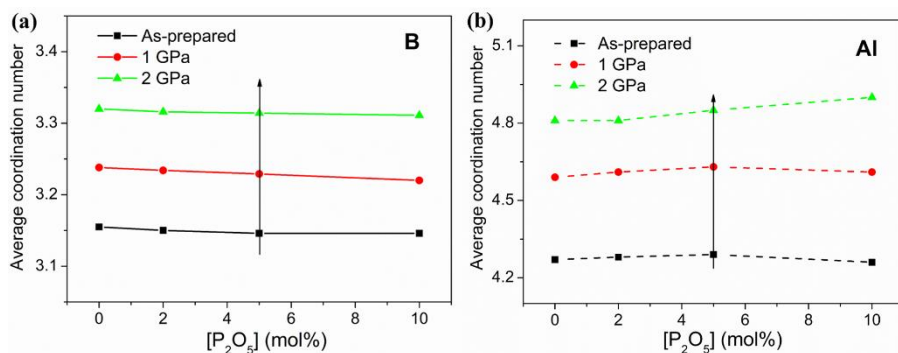


Figure 4-3. Composition and pressure dependence of the average coordination number (CN) of boron and aluminum. Figure adapted from Paper III.

4.2.2. MEDIUM-RANGE STRUCTURE

Previous studies have shown that for hot compressed SiO_2 glass, compression lead to an increase in the content of small rings(70). While in borate glass, we found that the compression causes the ring structure to break(31)(74)(86). Therefore, in the borate-based glass, the medium-range order consists of ring structures with well-defined bond angles. In this thesis, we used Raman spectroscopy and NMR spectroscopy to study the changes in the medium-range structure of aluminoborate glass before and after hot compression. Take lithium phosphoaluminoborate glasses (in Paper III) as an example, we can find from Figure 4-4a that the area fractions of bands I and II decrease with increasing pressure, while the area fractions of bands III and IV increase with pressure. These changes indicate that some some superstructural borate units and aluminoborate units are broken under presure. In addition, the high-frequency band

IIIc (related to PO_2^- , $\text{P}_2\text{O}_7^{4-}$, PO_3^{2-} units(87)) becomes wider and more intense upon the hot compression, which is result from the P-O-P bond angle distortion.

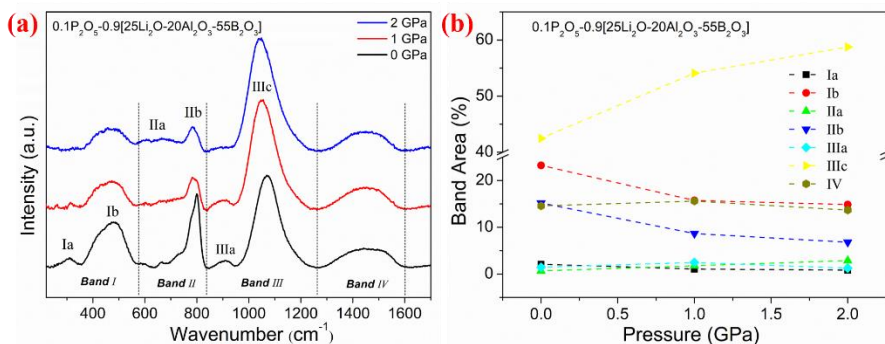


Figure 4-4. (a) Micro-Raman spectra of the as-prepared and compressed lithium phosphoaluminoborate glasses with 10 mol% P_2O_5 . (b) Pressure dependence of the relative fractions of the Raman bands. Figure adapted from Paper III.

In order to better understand the structural origin of the densification part in the deformation process, we used Raman spectroscopy to analyze the changes in the local structure of the caesium aluminoborate glass ($25\text{Cs}_2\text{O}-25\text{Al}_2\text{O}_3-50\text{B}_2\text{O}_3$, in Paper IV) before and after the indentation deformation. Figure 4-5 shows the structural changes induced by indentation deformation in the Cs-aluminoborate glass. From this figure, we can find that the Cs-aluminoborate glass in the center of the indent has obviously undergone changes in its network structure, which can be found from the increase in relative intensity of bands I, II and III. These changes could be associated with the consumption of NBOs on pyroborate units and the formation of B^{IV} units in diborate species. During the indentation process, some energy is fast transferred into the glass upon the applied external force, such as sharp contact loading. Glass attempts to dissipate this energy through local densification (decrease in bond angles and length) and structural changes (structural rearrangements, increase in coordination numbers and bond swapping etc.) under the contact surface. This indicates that the densification ability and structural pressure sensitivity of glass are of great significance to its deformation and cracking behavior.

By comparing the effects of these two densification methods on the glass structure, we found that there are some differences between the structural changes caused by pressure and the structural changes caused by indentation deformation. But the structural changes under these two types of densification are similar in some cases. This indicates that we can better understand the structural origin of the local deformation caused by external force in daily life through the structural changes caused by the hot compression.

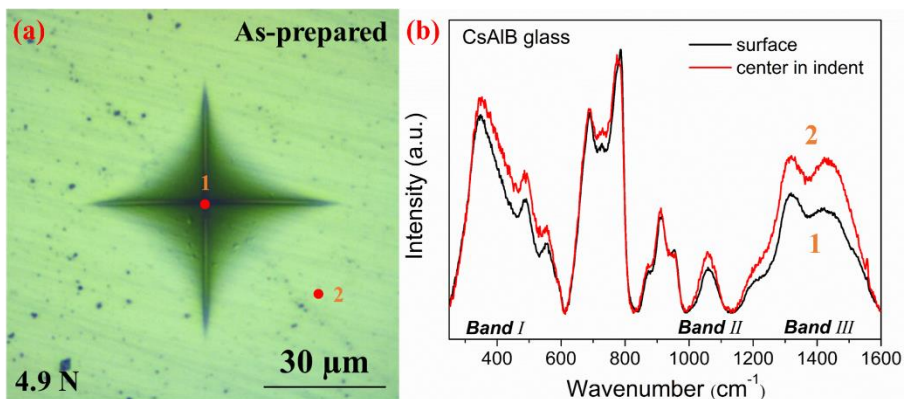


Figure 4-5. Structural changes induced by indentation deformation in the caesium aluminoborate glass. Figure adapted from Paper IV.

4.3. COMPOSITION EFFECT ON DENSIFICATION BEHAVIOUR

Following section 4.2.1, we continue to study the glass composition effect on the extent of structural changes caused by hot compression (densification). Take lithium phosphoaluminoborate glasses (in Paper III) as an example, we find From figure 4-6 that there is no effect of P_2O_5 on the changes in the coordination number of boron upon compression. While the addition of P_2O_5 has a significant effect on the changes in the coordination numbers of aluminum upon compression. We can find from Figure 4-3b that the addition of P_2O_5 is beneficial to the increase in Al coordination number caused by pressure.

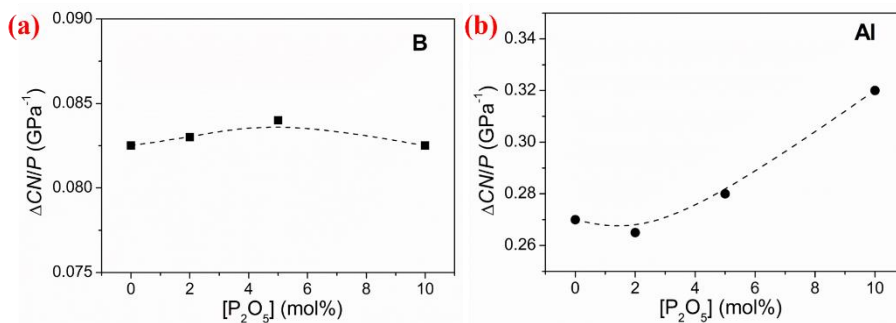


Figure 4-6. Composition dependence of the change in boron and aluminum coordination number with pressure ($\Delta CN/P$). Figure adapted from Paper III.

In fact, compared with other oxide glasses(75)(88), Al speciation of this series of glasses has the largest extent of pressure-induced changes under similar experimental conditions (pressure and temperature). These results indicate the addition of P_2O_5

positively influences the pressure-induced conversion of Al^{IV} to Al^V and Al^{VI}, in turn suggesting a link between aluminum and phosphate units as suggested by the formation of Al-O-P bonding. Therefore, understanding the effect of the changes in the coordination numbers of the network former on the extent of densification is very important for studying the structural origin of the densification.

To better quantify the contribution of the network former coordination changes to the overall pressure-induced volume densification ($\Delta V_{m(\text{Al+B})}/\Delta V_m$), we follow the approach of Wu et al.(25) to calculate the pressure-induced molar volume change only due to boron and aluminum coordination changes ($\Delta V_{m(\text{Al+B})}$) and the measured pressure-induced molar volume change (ΔV_m). $\Delta V_{m(\text{Al+B})}$ is calculated as,

$$V_{m(\text{Al+B})} = [X_{\text{Al}_2\text{O}_3} \sum x_i V_{([i]\text{Al})}] + [X_{\text{B}_2\text{O}_3} \sum x_i V_{([i]\text{B})}] \quad (4-1)$$

where $X_{(\text{Al}_2\text{O}_3)}$ and $X_{(\text{B}_2\text{O}_3)}$ are molar fractions of Al₂O₃ and B₂O₃ in the glass, x_i is the fraction of Al or B in each coordination state, $V_{([i]\text{Al})}$ and $V_{([i]\text{B})}$ are partial molar volumes of Al₂O₃ and B₂O₃ in each coordination state i . The detailed information is shown in Paper III.

Take lithium phosphoaluminoborate glasses as an example (in Table 4-1), we can find that there is a smaller change from 1 to 2 GPa than from ambient to 1 GPa for both the molar volume (V_m) and $V_{m(\text{Al+B})}$ upon hot compression. The ratio of $\Delta V_{m(\text{Al+B})}/\Delta V_m$ is above 50% at 2 GPa (Table 4-1). This is a large proportion of the pressure-induced volume densification compared to that found for calcium aluminoborosilicate glasses (9-36% at 2 GPa)(25). This is likely because the present glasses have more pronounced coordination number changes of Al and B upon compression. That is, reassociation of charge-balancing modifier cations from Al^{IV} to B^{IV} sites is required upon compression, which is promoted by the mobility of small lithium cations. As shown in Table 4-1, we also find that the $V_{m(\text{Al+B})}$ contribution to the overall change in measured V_m becomes smaller with the increasing content of P₂O₅.

Table 4-1. The value of molar volume changes(ΔV_m), Volume changes ($\Delta V_{m(\text{Al+B})}$) and the ratio of ($\Delta V_{m(\text{Al+B})}/\Delta V_m$) calculated by Eq. (4-1) in lithium phosphoaluminoborate glasses. Table adapted from Paper III.

Glass	P0 Glass	P2 Glass	P5 Glass	P10 Glass
ΔV_m at 1 GPa (cm ³ /mol)	2.40	2.38	2.38	2.38
ΔV_m at 2 GPa (cm ³ /mol)	3.79	3.73	3.82	3.91
$\Delta V_{m(\text{Al+B})}$ at 1 GPa (cm ³ /mol)	1.05	1.04	1.03	0.88
$\Delta V_{m(\text{Al+B})}$ at 2 GPa (cm ³ /mol)	2.02	1.97	2.01	1.88
$\Delta V_{m(\text{Al+B})}/\Delta V_m$ at 1 GPa	43.8%	43.7%	43.3%	37.0%
$\Delta V_{m(\text{Al+B})}/\Delta V_m$ at 2 GPa	53.3%	52.8%	52.6%	48.1%

4.4. DENSIFICATION EFFECT ON MECHANICAL PROPERTY

The key strategy to expand the future application of glasses is to improve their mechanical properties, especially the inherent brittleness. However, the understanding of the structural origin of mechanical properties such as hardness and crack resistance is still limited. As we know, the mechanical properties of glass can be adjusted through the compression process, but the understanding of the structural origin of this change is not very clear. Therefore, it is necessary to have an in-depth understanding of the changes in glass mechanical properties upon compression.

4.4.1. DENSITY

Many previous studies(89)(90)(91) have shown that properties related to free volume (especially atomic packing density) have a great influence on elastic modulus, hardness, deformation mechanism and fracture toughness. Therefore, studying the effect of hot compression on the density and atomic packing density is helpful to understand the changes of related mechanical properties caused by densification. Take lithium phosphoaluminoborate glasses (in Paper III) as an example, we can find from Figure 4-7 that the addition of P_2O_5 has only a slight effect on the density, while the density increases dramatically upon hot compression. Since there are also changes in the size of the atoms upon the addition of P_2O_5 , we calculate the atomic packing density (C_g) to further understand differences in free volume. We can also find that C_g decreases with the content of P_2O_5 for all studied glasses, showing that the network becomes gradually more open with P_2O_5 addition. While the C_g increases dramatically upon hot compression, indicating that the network becomes gradually more rigidity.

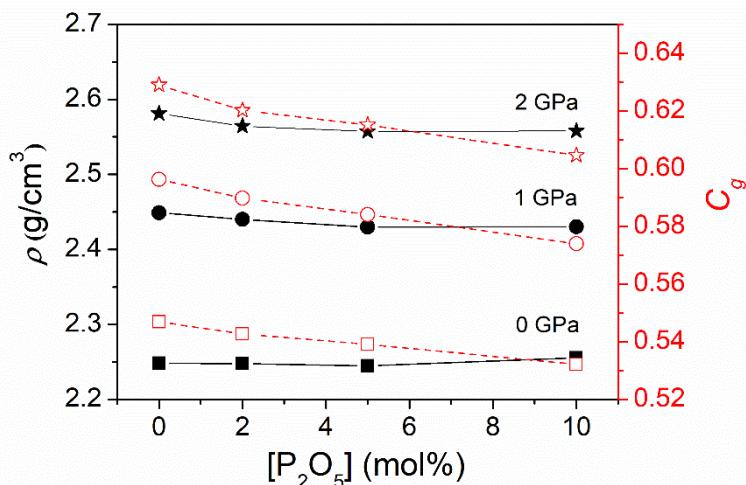


Figure 4-7. Compositional and pressure dependence of density (ρ) and atomic packing density (C_g). Figure adapted from Paper III.

4.4.2. YOUNG'S MODULUS AND HARDNESS

Young's modulus is important for glass design with special properties. In this thesis, the elastic properties of all glasses were measured by ultrasonic echography using an ultrasonic thickness gauge (38DL Plus, Olympus) equipped with 20 MHz delay line transducers. Generally speaking, Young's modulus depends on the bond energy between the atoms and atomic packing density. Take lithium phosphoaluminoborate glasses (in Paper III) as an example, we can find from Figure 4-8a that atomic packing density scales positively with E across pressures and compositions, showing that the role of packing density on elastic moduli is also seen from the pressure-induced increase in all Young's modulus. Although the elastic moduli are thus easily changed by compression, hardness is even more sensitive to the pressure treatment. The hardness of glass is the result of the combined effect of elastic deformation, plastic deformation (volume densification and shear flow). However, the hardness measured by the indents mainly depends on plastic deformation. In this thesis, we used indentation experiments to measure the hardness of all glasses. In lithium phosphoaluminoborate glasses, we studied the pressure dependence of glasses' hardness (see Figure 4-8b). We can find that the hardness of lithium phosphoaluminoborate glasses increases upon hot compression. The packing density increases upon hot compression, which leads to an increase in the number of atomic bond constraints per unit volume. This is the main reason for the pressure-induced increase in the hardness of this series of glasses.

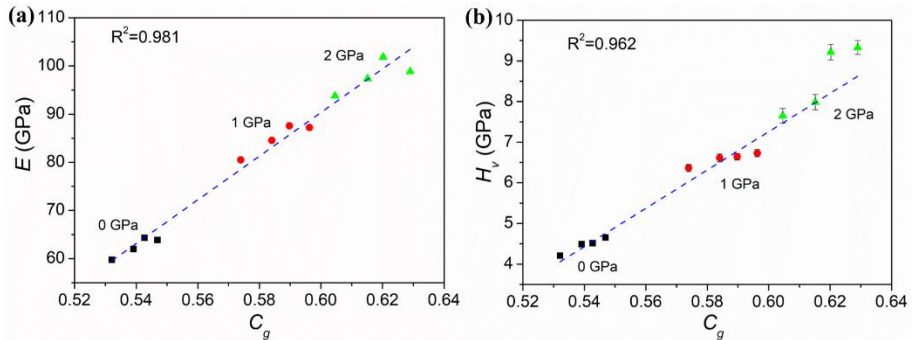


Figure 4-8. (a) The relation between Young's modulus and atomic packing density. (b) The relation between Vickers hardness and atomic packing density. Figure adapted from Paper III.

4.4.3. CRACK INITIATION RESISTANCE

Crack resistance is one of the important indicators to study the ability of glass crack initiation. In this thesis, we calculated the crack resistance of glasses by using the methods in section 2.2. we study the effect of hot compression on the crack resistance of caesium aluminoborate glass and lithium phosphoaluminoborate glasses. Take lithium phosphoaluminoborate glasses as an example, We can find from figure 4-9a

that the crack initiation resistance decreases rapidly with the increase in the extent of the pre-densification, which is found to be due to the decrease in the capability of densification in the compressed glasses. The high extent of permanent densification after hot-compression (13.3-14.8% when compressed under 2 GPa pressure in Figure 4-9b) indicates that the as-prepared glass has a great capability to accommodate the applied mechanical energy during the indentation process. This would lead to a lower level of the residual stress for driving the crack initiation in glasses, and thus result in the high CR for this series of glasses before the compression. Furthermore, the effect of the densification on the cracking behaviour is also related to its capability to undergo structural transformations under applied pressure or stress.

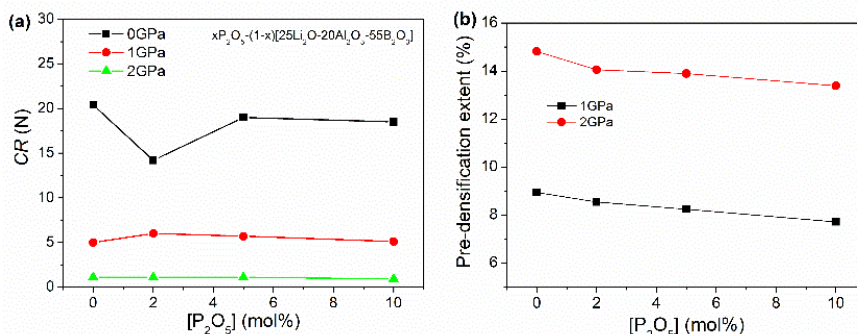


Figure 4-9. (a) Compositional and pressure dependence of crack initiation resistance in lithium phosphoaluminoborate glasses. (b) The extent of pre-densification in all lithium phosphoaluminoborate glasses. Figure adapted from Paper III.

4.5. RELATIONS OF ATOMIC SELF-ADAPTIVITY AND CRACKING BEHAVIOUR

From section 4.2, we know that the pressure-induced densification (in compression) can result in some changes in the glassy network structure, including the short- and medium-range structure. Furthermore, we find some similar structural changes in the indentation deformation process. This provides the possibility to understand the structural origin of deformation behavior and even cracking behavior in the glass during the indentation process.

For modified silica-based glasses, the structural rearrangements of amorphous silica during the indentation include the decrease in the Si-O-Si tetrahedral angle, and an increase in the abundance of three- and four-membered rings, as well as increasing the Q^2 abundance at the expense of Q^3 . We have also observed a similar phenomenon (structural rearrangements) in phosphorus glass (in Paper III). Since increasing the coordination number of Si and P atoms requires significant activation energy. In silica-based glasses and phosphorus glass, structural rearrangement is the main way to dissipate energy induced by the pressure/stress. While for the aluminoborate

glasses, there is a decrease in distances between borate rings, an increase in the B-O-B or Al-O-Al bonds angle, and changes in the abundance of different borate rings upon the indentation deformation. Furthermore, we also found (see Figure 4-3) that indentation deformation can induce the conversion of B^{III} units to B^{IV} units and Al^{IV} units to Al^V/Al^{VI}, i.e., increasing the coordination numbers of the network formers upon the pressure/stress, which is a new effective way to dissipate energy induced by the pressure/stress. From the analysis in section 4.3, we can see that the increase in the coordination numbers of the network former has a significant effect on the extent of densification in the aluminoborate glass, i.e., $\Delta V_{m(\text{Al+B})}/\Delta V_m$ can be more than 50% at 2 GPa in some cases. In addition, we know the NMR spectroscopy technology can provide some quantitative information about the short-range network structure of glass. Therefore, Januchta et al.(31) quantitatively analyze the relationship between structural changes and deformation/cracking behavior by using the atomic self-adaptivity of aluminoborate glass. The self-adaptivity of a given atomic network as:

$$\text{Atomic self-adaptivity} = \frac{\Delta n \Delta \rho}{P \rho_0} \quad (4-2)$$

where Δn is the change in coordination number as determined by NMR, $\Delta \rho$ is the change in density, ρ_0 is the initial density, and P is the applied pressure. As such, the atomic self-adaptivity is related to the densification and structural pressure sensitivity, which may better predict the cracking behaviour in glasses, such as crack initiation resistance.

To further understand the effect of the structural changes on the cracking behaviour, we study the relation between crack initiation resistance (CR) and atomic self-adaptivity in oxide glasses from our previous work. We find that the CR has a positive correlation the atomic self-adaptivity (see Figure 4-10), but still strongly depends on the composition. Silicate glass usually undergoes a decrease in the Si-O-Si angle inter-tetrahedrons and/or a change in ring size distribution under pressure/stress. This is because increasing the coordination number of Si atoms requires significant activation energy, which results in a low atomic self-adaptivity in silicate glasses, thus leading to lower CR . In contrast, the conversion of B^{III} units to B^{IV} units requires lower energy, i.e., boron-contain glasses tend to exhibit high CR .

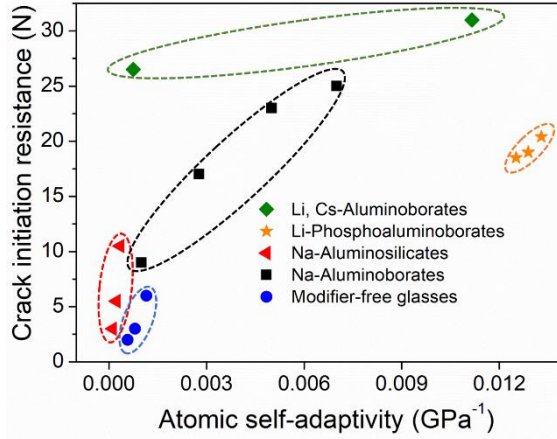


Figure 4-10. The relation between crack initiation resistance (CR) and Atomic self-adaptivity in oxide glasses. All data from ref. (26)(31)(60)(32)(33) and Paper III, IV.

We have found that in addition to the composition, atomic self-adaptivity is another important factor that affects the crack initiation ability of glasses. From equation 4-2, we can find that the atomic self-adaptivity mainly depends on the extent of densification and the pressure sensitivity of the glass structure. To further understand the relations in the atomic self-adaptivity with structural pressure sensitivity and densification, we study the correlation between atomic self-adaptivity and $\Delta V_{m(Al+B)}/\Delta V_m$ (related to the densification) and atomic packing density (related to the openness of the structure). From Figure 4-11a, we know that $\Delta V_{m(Al+B)}/\Delta V_m$ has a positive effect on the atomic self-adaptivity, indicating that the structural pressure sensitivity is beneficial to the atomic self-adaptivity. Besides, we can find that the increase in the coordination number of the network formers is generally accompanied by the densification process.

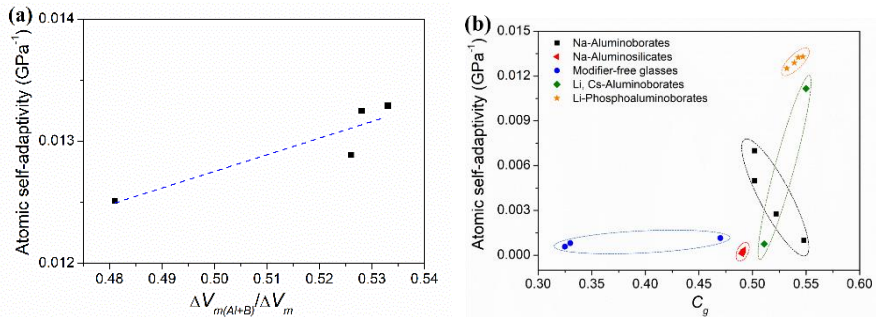


Figure 4-11. (a) Correlation between $\Delta V_{m(Al+B)}/\Delta V_m$ and atomic self-adaptivity upon hot compression at 2 GPa for the Lithium Phosphoaluminoborate Glasses. The dashed line is a guide for the eye. (b) Correlation between atomic self-adaptivity and atomic packing density. All data from ref.(26)(31)(60)(32)(33) and PaperIII, IV.

In Figure 4-11b, we can find that atomic self-adaptivity generally increase with increasing the atomic packing density, but still strongly depends on the composition. The glasses with low atomic packing density will have an open network structure, and thus have a large extent of densification during the indentation, which can dissipate more energy induced by the pressure/stress. This will result in less energy that is used to increase the coordination number of the network formers, which therefore decrease the atomic self-adaptivity.

4.6. SUMMARY

In this chapter, we have observed the pressure-induced structural changes after hot compression at T_g in aluminoborate glasses. We found that the densification of the glass is accompanied by the compression of the modifier environment, the change of the coordination numbers of the network former and the change of the intermediate structure (such as a ring). Furthermore, we find some similar structural changes in the indentation deformation process. Hot compression at T_g increases the density and hardness, but decreases the crack resistance. The indentation deformation mechanism (especially densification) controls the degree of stress dissipation and thus the tendency of crack initiation. The pressure sensitivity of the glass structure (pressure-induced structural rearrangement and coordination number changes) has a significant impact on its crack initiation ability. Our study shows that in addition to the composition, the atomic self-adaptivity related to the coordination number changes is another important factor that affects the crack initiation ability of glasses. Finally, we found that the atomic self-adaptivity strongly depends on the openness extent of structure and the coordination change contribution to the overall volume densification, as well as the glass composition.

CHAPTER 5. STRUCTURE AND MECHANICAL PROPERTIES OF HYDRATED ALUMINOBORATE GLASSES

Glasses typically fail due to the presence of surface cracks and defects, which in turn arise from corrosion, impacts and scratch events during production and daily use. These defects amplify the local tensile stress, which can result in decreasing the applied strength (durability), even the catastrophic failure (safety concerns). From Griffith-Irwin's fracture criterion(92), we know flaws with a critical size can only grow under loads that exceed the static fatigue limit. However, water penetration into the glass can affect the stable micro-defects smaller than the critical size, thereby affect crack initiation and sub-critical crack growth phenomena(93). In general, water penetration can decrease the applied strength of glasses, but the hydration surface treatment still has been found to have a certain enhancement effect on the crack initiation and crack growth in some glasses(23)(24)(94). Therefore, it is of great significance to tailor the mechanical properties of glasses by understanding the details of the glass-water interaction and the influence of the water penetration rate on the mechanical properties.

5.1. HUMID AGING POST-TREATMENT

In this thesis, aluminoborate glasses ($25M_2O-25Al_2O_3-50B_2O_3$, $M = \{Li, K, Cs\}$) and some other reference glasses were subjected to hydrate the surfaces through the controlled humid aging experiments in a climate chamber (WKL 100/40, Weiss). All these samples were optically double-side polished in ethanol, and then were immediately put into the climate chamber. The aging experiment was performed at different temperatures and RHs (relative humidity) for up to 7 days (see detailed treatment conditions in Table 5-1). Furthermore, to investigate the hydration in a high-humidity environment, experiments were also performed at 120 °C with 100% RH for 30 min in an autoclave. Due to the lower chemical durability, we also investigated the hydration for Cs-aluminoborate glasses in 99.9% ethanol for up to 14 days. The detailed experimental results are shown in Papers IV and V.

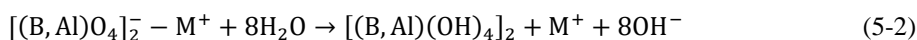
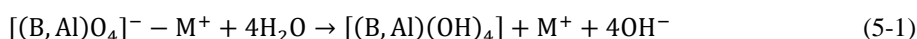
Table 5-1. The appearance (surface quality) of all studied glasses after the humid aging process under different conditions. Table adapted from Paper V.

Treatment condition	LiAIB glass	KAIB glass	CsAIB glass
23 °C, 40 % RH	Good	Good	Good
23 °C, 40 % RH			Good
23 °C, 50 % RH	-	-	Good
23 °C, 60 % RH	Good	Good	Cracks after 6 hour
23 °C, 80 % RH	Good	Good	Broken after 3 hour
30 °C, 80 % RH	Good	Good	-
35 °C, 80 % RH	Good	Cracks after 1 day	-
40 °C, 80 % RH	Good	Cracks after 1 day	-
50 °C, 80 % RH	Good	Cracks after 12 hour	-
80 °C, 80 % RH	Good	Broken after 1 day	-
120 °C, 100 % RH	Broken after 30 min	Broken after 30 min	Broken after 30 min
Submerged in ethanol	-	-	Good after 14 days

* Surface quality: Broken < Cracks < Good

5.2. CHEMICAL DURABILITY

The diffusion rate and content of water in glass strongly depend on its chemical durability (i.e. dissolution behavior in water), the content of defects (microcracks and porosity), and so on. Therefore, we pre-measured the chemical durability of bulk aluminoborate glass in a neutral (pH = 7) aqueous solution. The detailed information regarding these measurements is shown in Paper V. The dissolution mechanism of aluminoborate glass depends on the ion exchange (Equations 5-1 and 5-2) and hydrolysis (Equation 5-3) in aqueous solution and the reaction of hydrolysis (Equation 5-4) in a humid atmosphere. In a neutral (pH = 7) aqueous solution, there are usually H₂O molecules, H₃O⁺ (H⁺) and OH⁻ ions. Therefore, protonation and hydrolysis are strongly related to possible reactions:



where M represents a modifier atom.

The dissolution behavior for glasses in an aqueous solution depends on various factors, such as the atomic packing density, the rigidity of the network, the field strength of the modifier, the content of the network formation and the speciation of the network formation. Therefore, we studied the dependence of the dissolution rate of the glass in the aqueous solution on the modifier field strength and atomic packing density (C_g). Due to the different radius sizes of the modifier cations, their ability of

charge balance is different. That is, the same charge is distributed over a larger area for larger cations. Therefore, the modifier field strength (FS) can be quantitatively determined as:

$$FS = \frac{z_{alkali}}{(r_{alkali} + r_{oxygen})} \quad (5-5)$$

where z and r are the charge and the ionic radius, respectively.

In Paper V, we find that the dissolution rate decreases with the increase of the modifier field strength in the aluminoborate glasses. Modifier cations with high field strength will form stronger bonds with oxygen and have higher dissociation energy(95)(96) (under the same Al/B ratio condition), resulting in a lower dissolution rate. In addition, our work indicates that the Cs-O bond with lower dissociation energy may be more prone to nucleophilic attack by H₂O molecules during the hydration process. On the other hand, we find that the dissolution rate decreases with increasing atomic packing density. This is because that these open network structures (lower C_g) facilitate the entry of water molecules into the glass, and result in the nucleophilic attacks from H₂O molecules. These results indicate that the hydration behavior of oxide glasses can be affected by the openness of the network structure and the bonding strength of the modifier.

5.3. CONTENT AND FORM OF WATER IN GLASS

In general, there are three main mechanisms for water entry into glasses: i) hydration (molecular water penetration into the glass network), ii) hydrolysis (reaction with the glass network), iii) leaching (ion-exchange reaction with modifier cations). The water typically exists in glasses in the form of either molecules or hydroxyl groups(97)(98)(99). To determine the content and form of water in studied glasses, according to the method of Sheth et al(99), we use the ATR-IR spectroscopy to investigate the entry of water molecules into the glass surfaces during the humid aging experiments. Taking aluminoborate glasses (25M₂O-25Al₂O₃-50B₂O₃, M = {Li, K, Cs}, in Paper V) as an example, we find from figure 5-1 that for the K,Cs-aluminoborate glasses, the water mainly present in the form of the OH stretching band (ν_{OH} , ~3400 cm⁻¹), with a small amount of molecular H₂O bending band (δ_{H_2O} , ~1620 cm⁻¹). Due to the high chemical durability, we can only find the water in the form of the OH stretching band in the Li-aluminoborate glasses. To quantify the changes in the content of hydroxyl groups with the aging time in three glasses, we build the relation between the relatively intensity of OH stretching band (ν_{OH}) and humid aging time (shown in Figure 5-1d). The relatively intensity of OH stretching band (ν_{OH}) of the Li,K-aluminoborate glasses increases after humid aging under high RHs. While the humid aging process only has a minor effect on the water content in the Li,K-aluminoborate glasses under low RHs (40% and 60% RH) in Paper V. For the Cs-aluminoborate glasses, the relatively intensity of OH stretching band increases significantly after humid aging under high RHs under low RHs (40% and 50% RH),

indicating that the humid aging process has a significant influence on the surface of Cs-aluminoborate glasses.

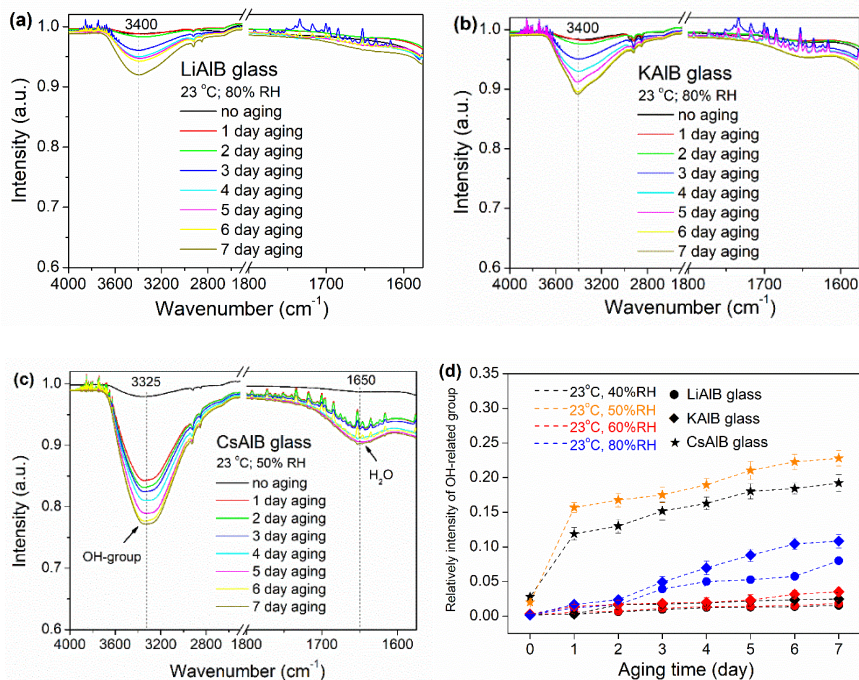


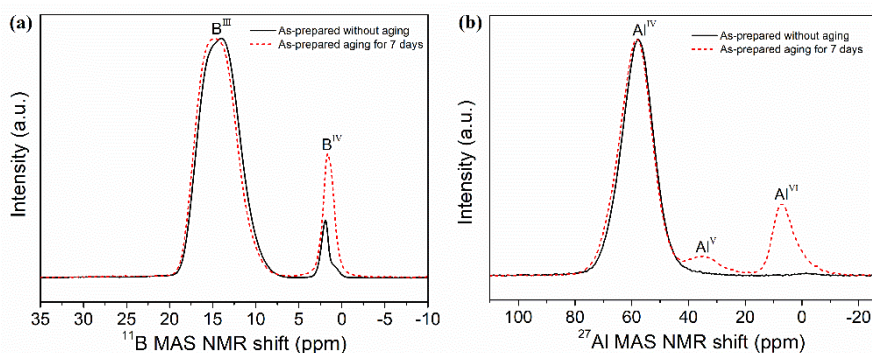
Figure 5-1. (a) ATR-IR spectra of lithium aluminoborate glass (LiAlB glasses) with different aging time at 23 °C, 80%RH. (b) ATR-IR spectra of potassium aluminoborate glass (KAIB glasses) with different aging time at 23 °C, 80%RH. (c) ATR-IR spectra of caesium aluminoborate glass (CsAlB glasses) with different aging time at 23 °C, 50%RH. (d) Relatively intensity of OH stretching band (around 3400 cm⁻¹) as a function of humid aging time of the studied bulk glasses at different RHs. Figure adapted from Paper V.

5.4. WATER EFFECT ON THE STRUCTURE OF ALUMINOBORATE GLASS

From the analysis in Section 5.3, we can see that the humid aging process has a significant effect on the surface of Cs-aluminoborate glasses, that is, a lot of water in the atmosphere enters this series of glass during the humid aging process. This water will inevitably induce some changes in the short- and medium- range structure of Cs-aluminoborate glasses. Therefore, in the thesis, we focused on the effect of water on the structure of Cs-aluminoborate glasses by using both micro-Raman and solid state NMR spectroscopy. From the NMR spectra results (see Figure 5-2), We can clearly find that the coordination numbers of Al and B together increase after the humid aging process, including the formation of six-fold Al. This result indicates that the local chemical environment of the network-former atoms in Cs-aluminoborate glasses is

sensitive to hydrolysis. Assuming that the incorporated water acts as a traditional network modifier or charge compensator, it is unexpected that water simultaneously increases the fractions of B^{IV} (requires charge compensation) and Al^{IV}/Al^{VI} (does not require charge compensation). Also, the alkali modifier has an enthalpic preference for interaction with Al^{IV} over B^{IV} in aluminoborate glasses, but this is not observed upon aging if considering water as a modifier. Therefore, it is possible that water molecules preferentially interact with boron relative to aluminum (to form B^{IV}), while some of the Cs charge-compensators for Al^{IV} are removed by aging, effectively increasing the coordination number of aluminum. Finally, we note from deconvolution of the ^{11}B MAS NMR spectra (Paper IV) that the fraction of $B^{III}_{nonring}$ increases along with the conversion of B^{III} to B^{IV} , indicating that the water molecules hydrolyze the original ring structures of the borate network as the aging time increasing. At the same time, this will result in a more open and loose glassy network structure, as well as a larger free volume, which is very beneficial for obtaining ultra-high crack resistance for glasses.

Finally, considering the effect of water on modifier cation (Cs^+ , in Figure 5-1c), we can find that the main peak about the ^{133}Cs became sharper and moved downwards (from 79 ppm to 71 ppm) after the humid aging process, indicating that humid aging caused the increase in Cs-O bond distance. This also shows that water molecules interact with Cs modifiers. Furthermore, from deconvolution of the ^{133}Cs MAS NMR spectra (in Paper IV), we know that the hydrated Cs^+ groups attached to the glass network are formed upon humid aging. These Cs-OH groups could be more free to move around and thus have higher mobility in the surface of the CsAlB glass. Such higher surface mobility is associated with higher network flexibility.



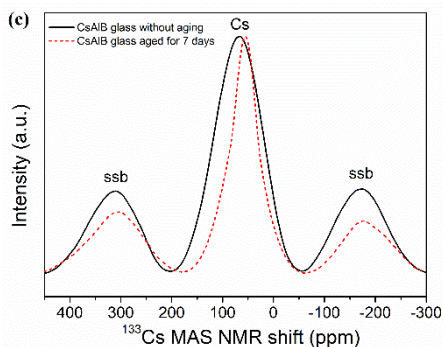


Figure 5-2. NMR spectra results for the as-prepared Cs-aluminoborate glasses with aging for 0 or 7 days at 23°C and 45% RH. Figure adapted from Paper IV.

5.5. HYDRATION LAYER DEPTH

From the water content analysis in Sections 5.3 and 5.4, we found that most water penetrates the Cs-aluminoborate glasses upon humid aging, and induced some structural changes. Therefore, the study regarding the part where water molecules penetrate the glass surface (hydration layer) is very important for understanding the deformation and cracking behavior in Cs-aluminoborate glass. We therefore focus on investigating the time dependence of the depth of the hydration layer on Cs-aluminoborate glasses by using micro-Raman spectroscopy. As observed in Figure 5-3a, the band region I (related to B-O-B, Al-O-Al, and B-O-Al stretching vibrations) hardly changes upon aging, while the intensity of band region II (associated with hydroxyl groups) increases significantly upon aging. Therefore, we calculate the area ratio of band regions I and II to capture the change in water content of Cs-aluminoborate glasses with increasing depth (Figure 5-3b). Based on this calculation methodology, we calculated the hydration layer depth in the Cs-aluminoborate glasses as a function of humid aging time under different RH (Figure 5-3c). We observe a positive correlation between hydration layer depth and both the duration of aging as well as RHs. This agrees with the variation in water content for this glass (in section 5.3). Especially, we note that a large fraction of the hydration occurs during the very early stages of aging (i.e., 13-14 μm hydration layer after humid aging for 1 day). After 7 days aging at 40% and 50% RH, the main hydration layer depth is 26.4 μm and 29.2 μm , respectively, showing that the high-RH atmosphere increases the hydration rate.

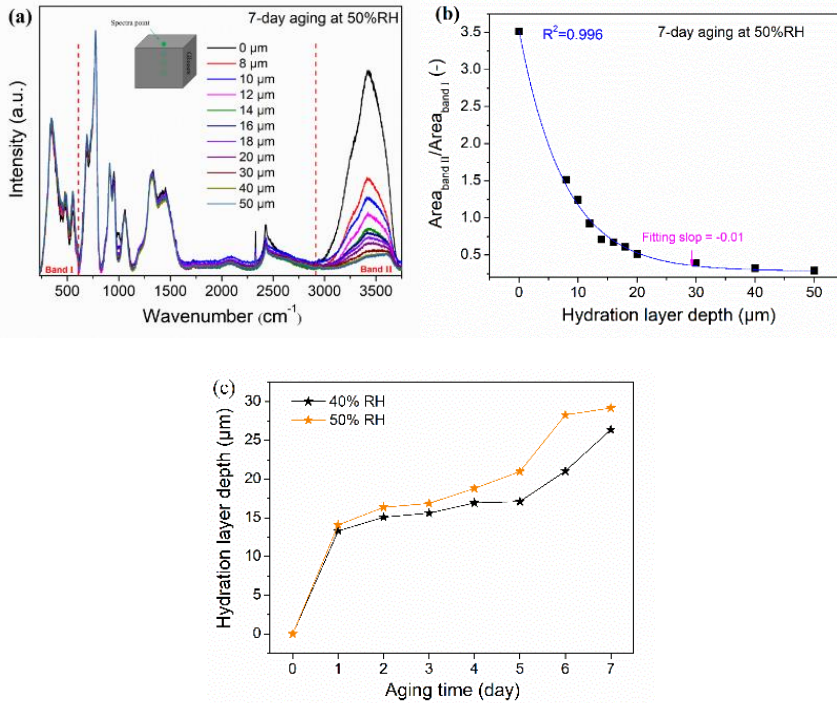


Figure 5-3. (a) Micro-Raman spectra of CsAlB glass after aging for 7 days at 50%RH. The spectra were recorded at increasing depth from the top surface toward the inside of the glass. (b) The area ratio of band I and II (from Figure 5-3 a) as a function of depth for Cs-aluminoborate glass. The experimental data is fit to an exponential function (solid line) and the hydration layer is defined as the depth for which the slope of the curve is less than $-0.01 \mu\text{m}^{-1}$. (d) Hydration layer depth as obtained from micro-Raman spectra as a function of humid aging time for the CsAlB glasses under 40% and 50% RH. Figure adapted from Paper V.

5.6. HYDRATION EFFECT ON DEFORMATION/CRACKING BEHAVIOR

From Section 5.5, we have found that a micron-size hydration layer is formed on the surface of the Cs-aluminoborate glasses after the humid aging process. The hydration layer inevitably has a great influence on the densification of the indentation deformation and cracking behavior(100)(101). Therefore, we next focus on studying the effect of hydration on deformation/cracking behavior and related properties of Cs-aluminoborate glasses.

5.6.1. INDENT SIZE LENGTH RECOVERY

Kacper et al.(23) have found the Cs-aluminoborate glass exhibits an unusual change in shape and size of the indent after humid aging in the atmosphere. This discovery

provides a new idea for preparing oxide glass with high self-healing ability. Therefore, in this thesis, we use the methods (in section 2.1) to calculate the recovery of the indentation side length (L_{AR}) upon humid aging, and study the relationship between aging time and side length recovery. From Figure 2-6, we can find that the indents show significant shrinkage after humid aging, the edge area of the indents recovered to above the original glass surface. In addition, we find that the indent before humid aging does not show a perfect square shape, indicating that the indent starts to recover during the unloading process. The qualitative observation of the indent self-recovery in the glasses is confirmed by the aging time dependence of L_{AR} . We also note from Figure 5-4a the limited indent size recovery in the other reference oxide glasses after humid aging.

Next, we evaluate the effect of aging conditions on the indent recovery of aluminoborate glasses, as shown in Figure 5-4b. we can find that the K-aluminoborate glass exhibits side length recovery above 7% and 15% after 7-days aging at 60% and 80% RH, respectively. While the Cs-aluminoborate glass exhibits recovery of around 25% and 40% after 7-days aging at 40% and 50% RH, respectively. These results show that the high-RH atmosphere increases the hydration rate. In addition, we ascribe this to the K-aluminoborate glasses' dense, rigid structure and high chemical durability, which allows for less water penetration and thus less indent volume recovery. Finally, we note that a large extent of the indent recovery occurs during the very early stages of aging, which is in good agreement with the water content analysis in Section 5.3.

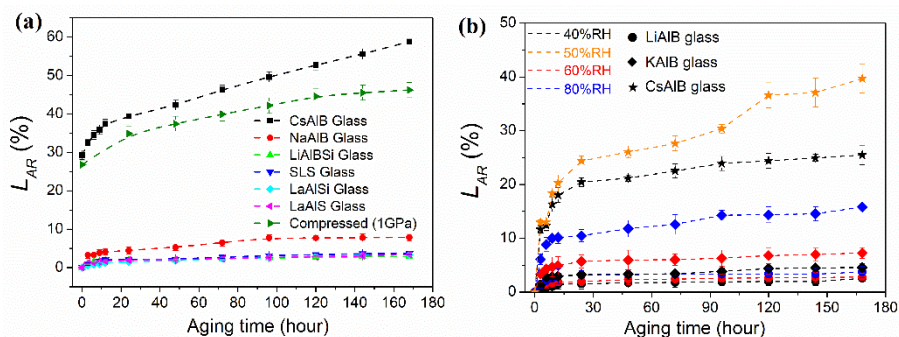


Figure 5-4. (a) Side length recovery (L_{AR}) of indents produced at 4.9 N as a function of aging time at 23 °C and 45 %RH for all the investigated glasses. (b) Side length recovery (L_{AR}) of Vickers indents produced at 9.8 N as a function of humid aging time for the investigated glasses under various RHs. Figure adapted from Paper IV and V.

5.6.2. ELASTIC RECOVERY

From the qualitative observation of the indent, we have found that the indents on the surface of the Cs-aluminoborate glass start to recover during the unloading process. Furthermore, we can find from the indent size recovery analysis that a large fraction

of the indent size recovery (“self-healing”) occurs during the very early stages of the aging (i.e., first data point after unloading). This result supports that elastic recovery has a relatively high contribution to the indentation deformation in the Cs-aluminoborate glass. Therefore, it is interesting to study the effect of water penetration rate on the elastic recovery of these glasses. Here, we use the bow-in parameter (L_D/L_S ratio), where L_D is the indent diagonal length and L_S is opposite side length(102)) of Vickers indents to describe the contribution of elastic deformation to indentation-induced deformation(103). We can find from Figure 5-5a that elastic recovery has a good negative correlation with elastic-plasticity (E/H). In addition, since only relatively few water molecules enter into the glass surfaces of Li,K-aluminoborate glasses, there is only a minor change in their L_D/L_S ratio upon humid aging (see Figure 5-5b). On the other hand, the bow-in parameter for the Cs-aluminoborate glass increases with increasing aging time and atmospheric humidity, which is in agreement with the larger extent of water entry in this glass. This indicates that the atmospheric water entry helps to promote elastic recovery during unloading.

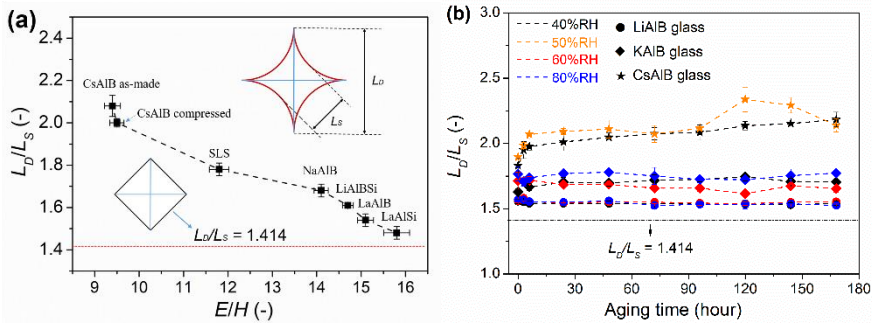


Figure 5-5. (a) Dependence of the bow-in parameter (L_D/L_S ratio) of Vickers indents produced at 4.9 N on the elastoplastic ratio (E/H). (b) Dependence of the bow-in parameter (L_D/L_S ratio) of Vickers indents produced at 9.8 N on the humid aging time for different aluminoborate glasses and RHs. Figure adapted from Paper IV and V.

5.6.3. CRACK INITIATION RESISTANCE

From Sections 5.6.1 and 5.6.2, We have found that the micron-size hydration layer has already affected the deformation behavior during the indentation process. Therefore, this hydration layer inevitably affects the crack-related properties of oxide glass. In fact, some recent studies have shown that pre-hydration on the glass surface can improve the crack resistance and strength of certain compositions(98)(104). In our work (Paper IV), We found that after low RH hydration treatment (7 days at 23 °C, 45% RH), the CR of Cs-aluminoborate glass increased from approximately 30 N to >100 N (see Figure 5-6a). For the other reference glasses, the surface aging at 45% RH has an almost negligible effect on the CR. Furthermore, in Paper V, we also studied the effect of different hydration conditions on the crack resistance of aluminoborate glass(see Figure 5-6b). The humid aging process has only a minor

effect on the CR of Li,K-aluminoborate glasses. While CR of the Cs-aluminoborate glasses increases significantly upon aging at both 40% and 50% RHs. When the aging time reaches 5 days, CR of the Cs-aluminoborate glass reaches an apparent maximum value for 50% RH. That is probably because that the hydrated surface after long-term aging becomes sufficiently depolymerized to decrease CR due to the weaker network bonding and the higher humidity can lead to a higher rate of atmospheric water permeation into the glasses surface. This suggests that the lower rate of atmospheric water permeation is beneficial to achieve a hydration layer with good performance on the glasses surface, thereby improving the crack initiation resistance of the Cs-aluminoborate glass. To further investigate the effect of the hydration layer on obtaining ultra-high crack resistance, we studied the effect of post-aging heat treatment on CR of the hydrated Cs-aluminoborate glass (Figure 5-6c). CR of the aged glass is found to decrease approximately to its initial value (before aging) after heat treatment. This confirms that the existence of the hydration layer is beneficial to improve the crack initiation resistance.

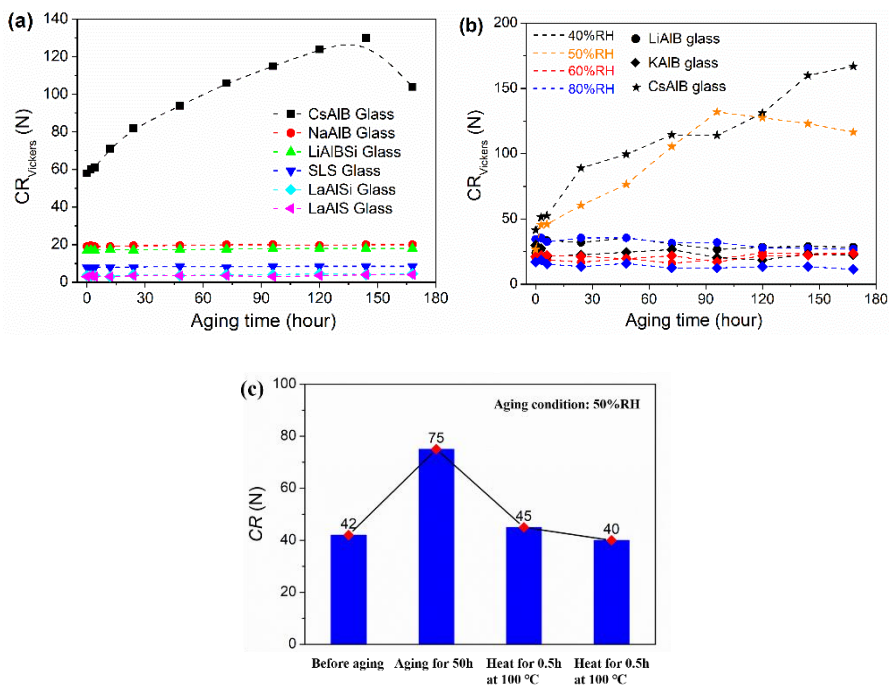


Figure 5-6. (a) Dependence of crack resistance (CR) on the humid aging time at 23 °C and 45 %RH. (b) Dependence of crack resistance (CR) on the humid aging time for different aluminoborate glasses and RHs. (c) Crack resistance (CR) of the CsAIB glasses after different treatments. Figure adapted from Paper IV and V.

Finally, according to the optical images of Vickers indents for the Cs-aluminoborate glass (see Figure 5-7), we can find that the formation of the micron-size hydration layer is indeed beneficial to improving the surface performance of the Cs-aluminoborate glass.

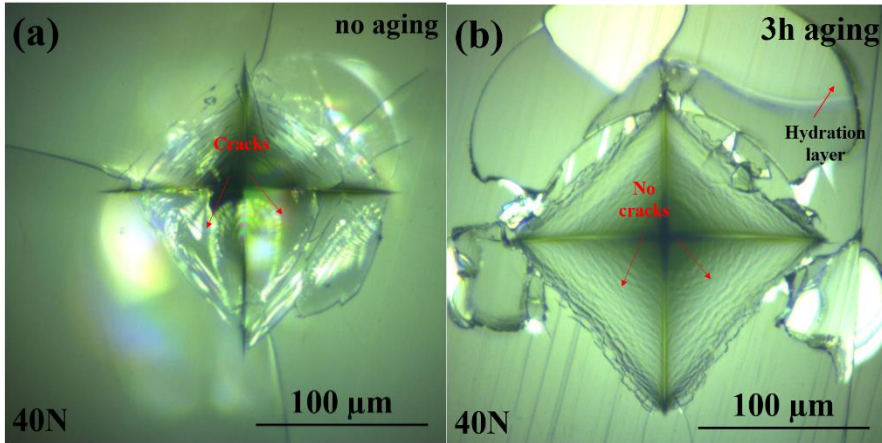


Figure 5-7. Optical images of Vickers indents produced at different loads on the surface of the CsAlB glass before and after humid aging at 60% RH: (a) Indentation at 40 N without aging. (b) Indentation at 40 N after 3 hours aging. Figure adapted from Paper V.

5.7. SUMMARY

In this chapter, we have shown that humid aging affects the indentation response of alkali aluminoborate glasses as strongly depending on the composition and chemical durability, network structures. We have shown that ultra-high resistance to sharp contact cracking can be achieved in a caesium aluminoborate glass by simply storing the glass under typical atmospheric humidity conditions. This is due to the formation of the surface hydration layer. Raman analysis has shown that the hydration layer depth after 7 days aging at 40% RH and 50% RH is 26.4 μm and 29.2 μm , respectively. This micro-size hydration layer has a network with higher freedom and Cs-OH groups with higher mobility, better protecting the glass from damage during indentation. Taken as a whole, our work provides guidelines for how to control the humid aging rate as a function of relative humidity and temperature to form a hydration layer and thus achieve ultrahigh crack resistance in such glasses.

CHAPTER 6. CONCLUSIONS AND PERSPECTIVES

In this chapter, we will briefly summarize the main findings and their potential significance, as well as discuss perspectives and suggestions for future work.

6.1. CONCLUSION

Nearly all elements of the periodic table are available for incorporation into oxide glasses, creating infinite possibilities for glass structures. Therefore, the compositional design of oxide glass compositions with improved crack resistance will be a focus of our research. In this study, we designed the composition of oxide glass by using two methods, i.e. i) introducing network formers (SiO_2 or P_2O_5) into aluminoborate glass, ii) adjusting the ratio of network modifiers (B_2O_3 or P_2O_5). This work shows that the performance of glass strongly depends on its composition and network structure, as well as the NBOs content. These findings indicate that the expected glass network structure can be obtained through the precise composition design, and then achieve glasses with the tailored properties.

Our group work suggests that the driving force for indentation cracking depends not only on the extent of densification, but also on the structural mechanisms facilitating the densification(31). Therefore, understanding the densification mechanism of glass under high pressure is very important for designing a new type of damage-resistant glass(74). In this thesis, we have studied the pressure-induced structural and properties changes after hot compression at T_g in aluminoborate glasses, as well as the pressure-induced structural changes upon indentation deformation. We find that The indentation deformation mechanism (especially densification) controls the degree of stress dissipation and thus the tendency of crack initiation. Furthermore, the pressure sensitivity of the glass structure (pressure-induced structural rearrangement and coordination number changes) has a significant impact on its crack initiation ability. That is, the atomic self-adaptivity related to the coordination number changes and densification is another important factor that affects the crack initiation ability of glasses. This atomic self-adaptivity strongly depends on the openness extent of structure and the coordination change contribution to the overall volume densification, as well as the glass composition. This work indicate that we obtain oxide galsses with ultra-high crack resistance by controlling the glassy network structural self-adaptability trough the composition design or post-treatment.

Finally, the effect of water on the strength of glass is generally considered to be negative. However, this work shows that by allowing the glass to interact with water in the atmosphere, it is possible to achieve crack-related properties, in particular to

improve the ability of crack initiation. By studying the influence of hydration conditions on the structure and performance of different oxide glasses, we find that humid aging affects the indentation response of alkali aluminoborate glasses strongly depending on the composition and chemical durability, network structures. Furthermore, the formation of the micro-size surface hydration layer with a high freedom network and mobility is one of the important factors for obtaining glasses with ultra-high crack resistance. This work provides guidelines for how to control the humid aging rate to form a hydration layer and thus achieve ultrahigh crack resistance in such glasses.

6.2. PERSPECTIVE

In this thesis, we have learned about the structural origin and related properties of glass deformation behavior and cracking behavior through composition design, pre-densification and pre-surface hydration treatment. However, the following research topics still need further investigation.

The deformation process under sharp-contact loading includes densification and structural changes (rearrangement of short- and medium-range structures.), which can dissipate the energy from the applied load. In this thesis, we studied the structural origins of deformation behavior and cracking behavior in glass. The atomic self-adaptivity has quantified the structural rearrangement of short-range structures (changes in coordination numbers of network formers) upon the deformation process. Our work fully proves that the atomic self-adaptivity strongly depends on the openness extent of structure and the coordination change contribution to the overall volume densification, as well as the glass composition. While, we still need more studies regarding the influencing factors of rearrangement of medium-range structures to further understand or quantify it, not only about the changes in coordination numbers (atomic self-adaptivity). Therefore, the cracking behavior of glass can be predicted comprehensively and accurately.

Through precise composition design, we have successfully obtained some glass combinations with high crack resistance(9)(10)(11)(31)(103). Crack initiation is just the beginning of research on fracture-related properties. Another important topic is about crack growth, i.e. fracture toughness. Recently, the understanding of structural origins and behavior of cracks growth in oxide glasses is still very limited. This requires more component design experiments and analysis. Inspired by the research experience of this thesis (introducing SiO_2 or P_2O_5 into aluminoborate glass), we will try to improve the fracture toughness of oxide glass by introducing second phase particles or pretreated second phase particles into oxide glass, such as nanoparticles, whiskers and short fibres. With more research on improving the fracture toughness of oxide glasses, the growth behavior and structural origin of cracks can be better understood, which will help to develop oxide glass combinations with ultra-high fracture toughness.

BIOGRAPHY

1. Yao A, Wang D, Huang W, Fu Q, Rahaman MN, Day DE. In Vitro Bioactive Characteristics of Borate-Based Glasses with Controllable Degradation Behavior. *J Am Ceram Soc.* 2007;90(1):303-6.
2. Donald IW, Metcalfe BL, Bradley DJ, Hill MJC, McGrath JL, Bye AD. The preparation and properties of some lithium borate based glasses. *J Mater Sci.* 1994;29(24):6379-96.
3. Ezz-Eldin F. Leaching and mechanical properties of cabal glasses developed as matrices for immobilization high-level wastes. *Nucl Instruments Methods Phys Res Sect B Beam Interact with Mater Atoms.* 2001;183(3-4):285-300.
4. Brambilla G, Payne DN. The Ultimate Strength of Glass Silica Nanowires. *Nano Lett.* 2009;9(2):831-5.
5. Frankberg EJ, Kalikka J, García Ferré F, Joly-Pottuz L, Salminen T, Hintikka J, et al. Highly ductile amorphous oxide at room temperature and high strain rate. *Science.* 2019;366(6467):864-9.
6. Wondraczek L, Mauro JC, Eckert J, Kühn U, Horbach J, Deubener J, et al. Towards Ultrastrong Glasses. *Adv Mater.* 2011;23(39):4578-86.
7. RITTER JE, SHERBURNE CL. Dynamic and Static Fatigue of Silicate Glasses. *J Am Ceram Soc.* 1971;54(12):601-5.
8. Kurkjian CR, Gupta PK, Brow RK. The Strength of Silicate Glasses: What Do We Know, What Do We Need to Know? *Int J Appl Glas Sci.* 2010 Mar;1(1):27-37.
9. Sehgal J, Ito S. A New Low-Brittleness Glass in the Soda-Lime-Silica Glass Family. *J Am Ceram Soc.* 1998;81(9):2485-8.
10. Rosales-Sosa GA, Masuno A, Higo Y, Inoue H. Crack-resistant Al_2O_3 - SiO_2 glasses. *Sci Rep.* 2016;6(1):23620.
11. Mabrouk A, De Sousa Meneses D, Pellerin N, Véron E, Genevois C, Ory S, et al. Effects of boron on structure of lanthanum and sodium aluminoborosilicate glasses studied by X-ray diffraction, transmission electron microscopy and infrared spectrometry. *J Non Cryst Solids.* 2019;503-504:69-77.
12. Rosales-Sosa GA, Masuno A, Higo Y, Inoue H, Yanaba Y, Mizoguchi T, et

- al. High Elastic Moduli of a $54\text{Al}_2\text{O}_3\text{-}46\text{Ta}_2\text{O}_5$ Glass Fabricated via Containerless Processing. *Sci Rep.* 2015;5(1):15233.
13. Mercier M, Di Muro A, Giordano D, Métrich N, Lesne P, Pichavant M, et al. Influence of glass polymerisation and oxidation on micro-Raman water analysis in alumino-silicate glasses. *Geochim Cosmochim Acta.* 2009;73(1):197-217.
 14. Sglavo VM, Prezzi A, Zandonella T. Engineered Stress-Profile Silicate Glass: High Strength Material Insensitive to Surface Defects and Fatigue. *Adv Eng Mater.* 2004;6(5):344-9.
 15. Gupta PK, Mauro JC. Composition dependence of glass transition temperature and fragility. I. A topological model incorporating temperature-dependent constraints. *J Chem Phys.* 2009;130(9):094503.
 16. Brow RK, Tallant DR. Structural design of sealing glasses. *J Non Cryst Solids.* 1997;222:396-406.
 17. Jones JR, Clare AG. Bioactive borate glasses. *Bio-glasses an Introd.* 2012;75-95.
 18. Kim JG, Son B, Mukherjee S, Schuppert N, Bates A, Kwon O, et al. A review of lithium and non-lithium based solid state batteries. *J Power Sources.* 2015;282:299-322.
 19. Konijnendijk WL, Stevels JM. The structure of borate glasses studied by Raman scattering. *J Non Cryst Solids.* 1975;18(3):307-31.
 20. Meera BN, Ramakrishna J. Raman spectral studies of borate glasses. *J Non Cryst Solids.* 1993;159:1-21.
 21. Wright AC. My Borate Life: An Enigmatic Journey. *Int J Appl Glas Sci.* 2015;6(1):45-63.
 22. Sen S, Xu Z, Stebbins J. Temperature dependent structural changes in borate, borosilicate and boroaluminate liquids: high-resolution ^{11}B , ^{29}Si and ^{27}Al NMR studies. *J Non Cryst Solids.* 1998;226:29-40.
 23. Januchta K, Stepniewska M, Jensen LR, Zhang Y, Somers MAJ, Bauchy M, et al. Breaking the Limit of Micro-Ductility in Oxide Glasses. *Adv Sci.* 2019;6(18):1901281.
 24. Liu P, Youngman RE, Jensen LR, Bockowski M, Smedskjaer MM. Achieving

- ultrahigh crack resistance in glass through humid aging. *Phys Rev Mater.* 2020;4(6):063606.
25. Wu J, Gross TM, Huang L, Jaccani SP, Youngman RE, Rzoska SJ, et al. Composition and pressure effects on the structure, elastic properties and hardness of aluminoborosilicate glass. *J Non Cryst Solids.* 2020;530:119797.
 26. Kapoor S, Guo X, Youngman RE, Hogue CL, Mauro JC, Rzoska SJ, et al. Network Glasses Under Pressure: Permanent Densification in Modifier-Free $\text{Al}_2\text{O}_3\text{-B}_2\text{O}_3\text{-P}_2\text{O}_5\text{-SiO}_2$ Systems. *Phys Rev Appl.* 2017;7(5):054011.
 27. Lee SK, Eng PJ, Mao H, Meng Y, Newville M, Hu MY, et al. Probing of bonding changes in B_2O_3 glasses at high pressure with inelastic X-ray scattering. *Nat Mater.* 2005;4(11):851-4.
 28. BOULOS EN, KREIDL NJ. Structure and Properties of Silver Borate Glasses. *J Am Ceram Soc.* 1971;54(8):368-75.
 29. SHELBY JE. Thermal Expansion of Alkali Borate Glasses. *J Am Ceram Soc.* 1983;66(3):225-7.
 30. Mauro JC, Gupta PK, Loucks RJ. Composition dependence of glass transition temperature and fragility. II. A topological model of alkali borate liquids. *J Chem Phys.* 2009;130(23):234503.
 31. Januchta K, Youngman RE, Goel A, Bauchy M, Logunov SL, Rzoska SJ, et al. Discovery of Ultra-Crack-Resistant Oxide Glasses with Adaptive Networks. *Chem Mater.* 2017;29(14):5865-76.
 32. Svenson MN, Bechgaard TK, Fuglsang SD, Pedersen RH, Tjell AØ, Østergaard MB, et al. Composition-Structure-Property Relations of Compressed Borosilicate Glasses. *Phys Rev Appl.* 2014;2(2):024006.
 33. Bechgaard TK, Goel A, Youngman RE, Mauro JC, Rzoska SJ, Bockowski M, et al. Structure and mechanical properties of compressed sodium aluminosilicate glasses: Role of non-bridging oxygens. *J Non Cryst Solids.* 2016;441:49-57.
 34. Wang M, Smedskjaer MM, Mauro JC, Sant G, Bauchy M. Topological Origin of the Network Dilation Anomaly in Ion-Exchanged Glasses. *Phys Rev Appl.* 2017;8(5):054040.
 35. Yu Y, Wang M, Smedskjaer MM, Mauro JC, Sant G, Bauchy M. Thermometer Effect: Origin of the Mixed Alkali Effect in Glass Relaxation.

- Phys Rev Lett. 2017;119(9):095501.
36. Section SP, Railways B, Centre T, Physics S. Surface energy and the contact of elastic solids. Proc R Soc London A Math Phys Sci. 1971;324(1558):301-13.
 37. Peter KW. Densification and flow phenomena of glass in indentation experiments. J Non Cryst Solids. 1970;5(2):103-15.
 38. Yoshida S, Sanglebœuf J-C, Rouxel T. Quantitative evaluation of indentation-induced densification in glass. J Mater Res. 2005;20(12):3404-12.
 39. Rouxel T, Ji H, Guin JP, Augereau F, Rufflé B. Indentation deformation mechanism in glass: Densification versus shear flow. J Appl Phys. 2010;107(9):094903.
 40. ERNSBERGER FM. Role of Densification in Deformation of Glasses Under Point Loading. J Am Ceram Soc. 1968;51(10):545-7.
 41. J. T. Hagan. Shear deformation under pyramidal indentations in soda-lime glass. J Mater Sci. 1980;15.
 42. Chakraborty R, Dey A, Mukhopadhyay AK. Loading Rate Effect on Nanohardness of Soda-Lime-Silica Glass. Metall Mater Trans A. 2010;41(5):1301-12.
 43. Kilymis DA, Delaye J-M. Deformation mechanisms during nanoindentation of sodium borosilicate glasses of nuclear interest. J Chem Phys. 2014;141(1):014504.
 44. Rouxel T, Sanglebœuf J-C, Moysan C, Truffin B. Indentation topometry in glasses by atomic force microscopy. J Non Cryst Solids. 2004;344:26-36.
 45. Evans AG, Wilshaw TR. Quasi-static solid particle damage in brittle solids-I. Observations analysis and implications. Acta Metal. 1976;24(10):939-56.
 46. Hagan JT, Swain M V. The origin of median and lateral cracks around plastic indents in brittle materials. J Phys D Appl Phys. 1978;11(15):2091-102.
 47. Arora A, Marshall DB, Lawn BR, Swain MV. Indentation deformation/fracture of normal and anomalous glasses. J Non Cryst Solids. 1979;31(3):415-28.
 48. Hagan JT. Cone cracks around Vickers indentations in fused silica glass. J

- Mater Sci. 1979;14(2):462-6.
49. Lee JH, Gao YF, Johanns KE, Pharr GM. Cohesive interface simulations of indentation cracking as a fracture toughness measurement method for brittle materials. *Acta Mater.* 2012;60(15):5448-67.
 50. Yoffe EH. Elastic stress fields caused by indenting brittle materials. *Philos Mag A.* 1982;46(4):617-28.
 51. Rouxel T. Driving force for indentation cracking in glass: composition, pressure and temperature dependence. *Philos Trans R Soc A Math Phys Eng Sci.* 2015;373(2038):20140140.
 52. Wada M, Furukawa H, Fujita K. Crack resistance of glass on Vickers indentation. In *Proc. Int. Congr. Glass 10th 1974 (Vol. 11, pp. 39-46).*
 53. Zachariasen WH. The atomic arrangement in glass. *Journal of the American Chemical Society.* 1932 Oct;54(10):3841-51.
 54. Huang PY, Kurasch S, Srivastava A, Skakalova V, Kotakoski J, Krashennnikov A V., et al. Direct Imaging of a Two-Dimensional Silica Glass on Graphene. *Nano Lett.* 2012;12(2):1081-6.
 55. Lichtenstein L, Büchner C, Yang B, Shaikhutdinov S, Heyde M, Sierka M, et al. The Atomic Structure of a Metal-Supported Vitreous Thin Silica Film. *Angew Chemie Int Ed.* 2012;51(2):404-7.
 56. Farnan I, Grandinetti PJ, Baltisberger JH, Stebbins JF, Werner U, Eastman MA, et al. Quantification of the disorder in network-modified silicate glasses. *Nature.* 1992;358(6381):31-5.
 57. Greaves GN. EXAFS and the structure of glass. *J Non Cryst Solids.* 1985;71:203-17.
 58. Krogh-Moe J. The structure of vitreous and liquid boron oxide. *J Non Cryst Solids.* 1969;1(4):269-84.
 59. Zhong J, Bray PJ. Change in boron coordination in alkali borate glasses, and mixed alkali effects, as elucidated by NMR. *J Non Cryst Solids.* 1989;111(1):67-76.
 60. Januchta K, Youngman RE, Goel A, Bauchy M, Rzoska SJ, Bockowski M, et al. Structural origin of high crack resistance in sodium aluminoborate glasses. *J Non Cryst Solids.* 2017;460:54-65.

61. Li H, Su Y, Li L, Strachan DM. Raman spectroscopic study of gadolinium(III) in sodium-aluminoborosilicate glasses. *J Non Cryst Solids*. 2001;292:167-76.
62. Konijnendijk WL, Stevels JM. The structure of borosilicate glasses studied by Raman scattering. *J Non Cryst Solids*. 1976;20(2):193-224.
63. Kamitsos EI, Chrysikos GD. Borate glass structure by Raman and infrared spectroscopies. *J Mol Struct*. 1991;247(C):1-16.
64. Vignarooban K, Boolchand P, Micoulaut M, Malki M, Bresser WJ. Rigidity transitions in glasses driven by changes in network dimensionality and structural groupings. *Europhysics Lett*. 2014;108(5):56001.
65. McMillan P, Piriou B. Raman spectroscopy of calcium aluminate glasses and crystals. *J Non Cryst Solids*. 1983;55(2):221-42.
66. Licheron M, Montouillout V, Millot F, Neuville DR. Raman and ^{27}Al NMR structure investigations of aluminate glasses: $(1-x)\text{Al}_2\text{O}_3-x\text{MO}$, with $\text{M}=\text{Ca}$, Sr , Ba and $0.5 < x < 0.75$. *J Non Cryst Solids*. 2011;357(15):2796-801.
67. Ollier N, Charpentier T, Boizot B, Wallez G, Ghaleb D. A Raman and MAS NMR study of mixed alkali Na-K and Na-Li aluminoborosilicate glasses. *J Non Cryst Solids*. 2004;341:26-34.
68. Yano T, Kunimine N, Shibata S, Yamane M. Structural investigation of sodium borate glasses and melts by Raman spectroscopy.: I. Quantitative evaluation of structural units. *J Non Cryst Solids*. 2003;321(3):137-46.
69. Anedda A, Carbonaro CM, Clemente F, Corpino R, Ricci PC. Raman Investigation of Surface OH-Species in Porous Silica. *J Phys Chem B*. 2003;107(49):13661-4.
70. Guerette M, Ackerson MR, Thomas J, Yuan F, Bruce Watson E, Walker D, et al. Structure and Properties of Silica Glass Densified in Cold Compression and Hot Compression. *Sci Rep*. 2015;5(1):15343.
71. Mozzi RL, Warren BE. The structure of vitreous silica. *J Appl Crystallogr*. 1969;2(4):164-72.
72. Smedskjaer MM, Mauro JC, Yue Y. Prediction of Glass Hardness Using Temperature-Dependent Constraint Theory. *Phys Rev Lett*. 2010;105(11):115503.
73. Wilkinson CJ, Zheng Q, Huang L, Mauro JC. Topological constraint model

- for the elasticity of glass-forming systems. *J Non-Crystalline Solids X*. 2019;2:100019.
74. Mauro JC, Tandia A, Vargheese KD, Mauro YZ, Smedskjaer MM. Accelerating the Design of Functional Glasses through Modeling. *Chem Mater*. 2016;28(12):4267-77.
 75. Kapoor S, Wondraczek L, Smedskjaer MM. Pressure-Induced Densification of Oxide Glasses at the Glass Transition. *Front Mater*. 2017;4:1-20.
 76. Uhlmann DR. Densification of alkali silicate glasses at high pressure. *J Non Cryst Solids*. 1973;13(1):89-99.
 77. Kanzaki M. Melting of Silica up to 7 GPa. *J Am Ceram Soc*. 1990;73(12):3706-7.
 78. Salmon PS, Zeidler A. Networks under pressure: the development of in situ high-pressure neutron diffraction for glassy and liquid materials. *J Phys Condens Matter*. 2015;27(13):133201.
 79. Smedskjaer MM, Youngman RE, Striepe S, Potuzak M, Bauer U, Deubener J, et al. Irreversibility of Pressure Induced Boron Speciation Change in Glass. *Sci Rep*. 2015;4(1):3770.
 80. Striepe S, Smedskjaer MM, Deubener J, Bauer U, Behrens H, Potuzak M, et al. Elastic and micromechanical properties of isostatically compressed soda-lime-borate glasses. *J Non Cryst Solids*. 2013;364(1):44-52.
 81. Smedskjaer MM, Rzoska SJ, Bockowski M, Mauro JC. Mixed alkaline earth effect in the compressibility of aluminosilicate glasses. *J Chem Phys*. 2014;140(5):054511.
 82. Lee SK, Cody GD, Fei Y, Mysen BO. Nature of polymerization and properties of silicate melts and glasses at high pressure. *Geochim Cosmochim Acta*. 2004;68(20):4189-200.
 83. Wilding M, Guthrie M, Kohara S, Bull CL, Akola J, Tucker MG. Corrigendum: The structure of MgO-SiO₂ glasses at elevated pressure. *J Phys Condens Matter*. 2012;24(33):339501.
 84. Svenson MN, Thirion LM, Youngman RE, Mauro JC, Rzoska SJ, Bockowski M, et al. Pressure-Induced Changes in Interdiffusivity and Compressive Stress in Chemically Strengthened Glass. *ACS Appl Mater Interfaces*. 2014;6(13):10436-44.

85. Svenson MN, Thirion LM, Youngman RE, Mauro JC, Bauchy M, Rzoska SJ, et al. Effects of Thermal and Pressure Histories on the Chemical Strengthening of Sodium Aluminosilicate Glass. *Front Mater.* 2016;3:1-11.
86. Gurr GE, Montgomery PW, Knutson CD, Gorres BT. The crystal structure of trigonal diboron trioxide. *Acta Crystallogr Sect B Struct Crystallogr Cryst Chem.* 1970;26(7):906-15.
87. Le Saoût G, Simon P, Fayon F, Blin A, Vaills Y. Raman and infrared study of $(\text{PbO})_x(\text{P}_2\text{O}_5)_{(1-x)}$ glasses. *J Raman Spectrosc.* 2002;33(9):740-6.
88. Lee SK, Mun KY, Kim Y-H, Lhee J, Okuchi T, Lin J-F. Degree of Permanent Densification in Oxide Glasses upon Extreme Compression up to 24 GPa at Room Temperature. *J Phys Chem Lett.* 2020;11(8):2917-24.
89. Sellappan P, Rouxel T, Celarie F, Becker E, Houizot P, Conradt R. Composition dependence of indentation deformation and indentation cracking in glass. *Acta Mater.* 2013;61(16):5949-65.
90. Rouxel T. Elastic Properties and Short-to Medium-Range Order in Glasses. *J Am Ceram Soc.* 2007;90(10):3019-39.
91. Rouxel T, Yoshida S. The fracture toughness of inorganic glasses. *J Am Ceram Soc.* 2017;100(10):4374-96.
92. Griffiths AA. VI. The phenomena of rupture and flow in solids. *Philos Trans R Soc London Ser A, Contain Pap a Math or Phys Character.* 1921;221:163-98.
93. Seaman JH, Blanchet TA, Tomozawa M. Origin of the Static Fatigue Limit in Oxide Glasses. Rouxel T, editor. *J Am Ceram Soc.* 2016;99(11):3600-9.
94. Wiederhorn SM, Fett T, Rizzi G, Fünfschilling S, Hoffmann MJ, Guin J-P. Effect of Water Penetration on the Strength and Toughness of Silica Glass. *J Am Ceram Soc.* 2011;94:s196-203.
95. Sun K-H. FUNDAMENTAL CONDITION OF GLASS FORMATION. *J Am Ceram Soc.* 1947;30(9):277-81.
96. Makishima A, Mackenzie JD. Direct calculation of Young's modulus of glass. *J Non Cryst Solids.* 1973;12(1):35-45.
97. Wang B, Krishnan NMA, Yu Y, Wang M, Le Pape Y, Sant G, et al. Irradiation-induced topological transition in SiO_2 : Structural signature of

- networks' rigidity. *J Non Cryst Solids*. 2017;463:25-30.
98. Luo J, Huynh H, Pantano CG, Kim SH. Hydrothermal reactions of soda lime silica glass-Revealing subsurface damage and alteration of mechanical properties and chemical structure of glass surfaces. *J Non Cryst Solids*. 2016;452:93-101.
 99. Sheth N, Luo J, Banerjee J, Pantano CG, Kim SH. Characterization of surface structures of dealkalized soda lime silica glass using X-ray photoelectron, specular reflection infrared, attenuated total reflection infrared and sum frequency generation spectroscopies. *J Non Cryst Solids*. 2017;474:24-31.
 100. Sheth N, Hahn SH, Ngo D, Howzen A, Bermejo R, van Duin ACT, et al. Influence of acid leaching surface treatment on indentation cracking of soda lime silicate glass. *J Non Cryst Solids*. 2020;543:120144.
 101. Sheth N, Greenley C, Bermejo R, Mauro JC, Pantano CG, Kim SH. Effects of acid leaching treatment of soda-lime silicate glass on crack initiation and fracture. *J Am Ceram Soc*. 2021:jace.17840.
 102. Yoshida S, Kato M, Yokota A, Sasaki S, Yamada A, Matsuoka J, et al. Direct observation of indentation deformation and cracking of silicate glasses. *J Mater Res*. 2015;30(15):2291-9.
 103. Januchta K, Bauchy M, Youngman RE, Rzoska SJ, Bockowski M, Smedskjaer MM. Modifier field strength effects on densification behavior and mechanical properties of alkali aluminoborate glasses. *Phys Rev Mater*. 2017 Nov 28;1(6):063603.
 104. Lezzi PJ, Xiao QR, Tomozawa M, Blanchet TA, Kurkjian CR. Strength increase of silica glass fibers by surface stress relaxation: A new mechanical strengthening method. *J Non Cryst Solids*. 2013;379:95-106.

LIST OF PUBLICATIONS

PUBLICATIONS IN PEER-REVIEW JOURNALS

Contributed as first author or main co-author:

P.F. Liu, K. Januchta, L.R. Jensen, M. Bauchy, M.M. Smedskjaer, “Competitive Effects of Free Volume, Rigidity, and Self-Adaptivity on Indentation Response of Silicoaluminoborate Glasses”. *Journal of American Ceramic Society*. 103 (2020) 944-954

K. Januchta, **P.F. Liu**, S.R. Hansen, T. To, M.M. Smedskjaer, “Indentation cracking and deformation mechanism of sodium aluminoborosilicate glasses”. *Journal of American Ceramic Society*. 103 (2020) 1656-1665

P.F. Liu, A.L.S. Søndergaard, R.E. Youngman, S.J. Rzoska, M. Bockowski, L.R. Jensen, M.M. Smedskjaer, “Structural densification of lithium phosphoaluminoborate glasses”. *Journal of American Ceramic Society*. 104 (2021) 1345-1359

P.F. Liu, R.E. Youngman, L.R. Jensen, M. Bockowski, M.M. Smedskjaer, “Achieving Ultrahigh Crack Resistance in Glass through Humid Aging”. *Physical Review Materials*. 4 (2020) 63606

X.T Ren, **P.F. Liu**, S.J. Rzoska, B. Lucznik, M. Bockowski, M.M. Smedskjaer, “Indentation response of calcium aluminoborosilicate glasses subjected to humid aging and hot compression”. *Materials*. 14 (2021) 3450

P.F. Liu, L.R. Jensen, C.W. Gao, M.M. Smedskjaer, “Indentation deformation and cracking behavior of hydrated aluminoborate glasses”. Manuscript submitted to *Journal of American Ceramic Society*

P.F. Liu, R.E. Youngman, L.R. Jensen, M.M. Smedskjaer, “Structural Transition in Lithium Borophosphate Glasses Explains the Variation in their Mechanical Properties”.

ORAL AND POSTER PRESENTATIONS AT CONFERENCES

P.F. Liu, M.M. Smedskjaer, “Composition-Structure-Mechanical Property Relations in Lithium Aluminoborate Glasses”. Oral presentation: *Engineering Mechanics Institute Conference and Probabilistic Mechanics & Reliability Conference (EMI-PMC 2021)*, May 28, online 2021.

Paper I

Competitive effects of free volume, rigidity, and self-adaptivity on indentation response of silicoaluminoborate glasses

Pengfei Liu¹  | Kacper Januchta¹  | Lars R. Jensen² | Mathieu Bauchy³  | Morten M. Smedskjaer¹ 

¹Department of Chemistry and Bioscience, Aalborg University, Aalborg, Denmark

²Department of Materials and Production, Aalborg University, Aalborg, Denmark

³Department of Civil and Environmental Engineering, University of California, Los Angeles, USA

Correspondence

Morten M. Smedskjaer, Department of Chemistry and Bioscience, Aalborg University, Aalborg, Denmark.
Email: mos@bio.aau.dk

Funding information

China Scholarship Council, Grant/Award Number: 201806370210; National Science Foundation, Grant/Award Numbers: 1562066, 1762292 and 1826420

Abstract

Lithium aluminoborate glasses have recently been found to feature high resistance to crack initiation during indentation, but suffer from relatively low hardness and chemical durability. To further understand the mechanical properties of this glass family and their correlation with the network structure, we here study the effect of adding SiO₂ to a 25Li₂O–20Al₂O₃–55B₂O₃ glass on the structure and mechanical properties. Addition of silica increases the average network rigidity, but meanwhile its open tetrahedral structure decreases the atomic packing density. Consequently, we only observe a minor increase in hardness and glass transition temperature, and a decrease in Poisson's ratio. The addition of SiO₂, and thus removal of Al₂O₃ and/or B₂O₃, also makes the network less structurally adaptive to applied stress, since Al and B easily increase their coordination number under pressure, while this is not the case for Si under modest pressures. As such, although the silica-containing networks have more free volume, they cannot densify more during indentation, which in turn leads to an overall decrease in crack resistance upon SiO₂ addition. Our work shows that, although pure silica glass has very high glass transition temperature and relatively high hardness, its addition in oxide glasses does not necessarily lead to significant increase in these properties due to the complex structural interactions in mixed network former glasses and the competitive effects of free volume and network rigidity.

KEYWORDS

cracks/cracking, glass, hardness, indentation

1 | INTRODUCTION

Oxide glasses play a critical role for innovation in a range of industries due to their combination of properties such as transparency, high hardness, relatively lightweight, and chemical durability.¹ However, these materials are brittle

since they lack a stable shearing mechanism. The practical strength of glass is also low due to the presence of surface flaws and defects, which act to amplify local tensile stresses, resulting in catastrophic failures.^{2,3} This obviously limits many industrial applications within energy, medicine, consumer electronics, etc. There is thus a need to develop new glasses with higher inherent damage or crack resistance in order to minimize the number of cracks and their propensity to propagate from flaws, for example, created during handling. To achieve this aim, various extrinsic posttreatment

methods have been used in oxide glasses, such as chemical strengthening that result in the formation of a compressive stress layer at the surface, thereby limiting any propagating cracks.⁴ However, postprocessing is expensive and consistently accompanied by undesirable side effects.^{5,6} Therefore, there is an increasing interest in enhancing the inherent mechanical properties of oxide glass by a rational design of the chemical composition.⁷

Recent progress has been made in the area of composition design by focusing on controlling the network topology (eg, through mixed network formers or modifiers) and the resulting deformation mechanism. This has led to the discovery of various glass families with high inherent damage resistance, including mixed modifier aluminosilicate,⁸ binary aluminosilicate,⁹ calcium boroaluminosilicate,¹⁰ tantalum aluminate,¹¹ and alkali aluminoborate compositions.^{12,13} In these previous works, the damage resistance has been evaluated using indentation, since sharp contact is the primary failure mode of glasses for many applications. Indentation thus mimics real-life damage incidents under controlled conditions, requiring relatively small sample area and with short experiment time.^{14,15} However, we note that it is important to distinguish between resistance to crack initiation and crack growth, as high crack initiation resistance (which is measured by indentation) does not necessarily entail large fracture toughness.¹⁶ By studying different glass compositions, Peter showed that the deformation mechanism of oxide glasses to indentation in general includes both densification and shear flow.¹⁷ Kato et al have shown that glass compositions prone to undergo densification during indentation can lower the residual stress acting as the driving force for cracking, since densification does not lead to an expansion of the plastic zone.¹⁸ This can in turn be achieved by producing glasses with high levels of free volume within their atomic network,⁸ designing self-adaptive networks where structural rearrangements promote densification,¹² or controlling rigidity fluctuations on the nanoscale.¹⁹ However, more understanding is needed to properly link glass chemistry and network structure with the indentation deformation mechanism and cracking resistance.

In this work, we build on the recent progress made in achieving high crack resistance in alkali aluminoborate glasses.^{13,20,21} Specifically, we discovered a melt-quenchable lithium aluminoborate glass with very high resistance to indentation cracking, that is, Vickers indentation loads close to 2 kgf (~20 N) are needed to induce radial cracking.¹² Structural analyses revealed that the coordination numbers of both boron and aluminum in this glass increase dramatically upon densification, for example, the average Al coordination number increases from 4.29 to 4.85 upon hot compression at 2 GPa. These structural changes and volume densification manifest themselves in record-high (compared to previously studied oxide glasses) pressure-induced changes in material properties, such as Vickers hardness and Young's modulus.

On the basis of the pressure dependence of density and the short-range order of boron and aluminum, we have introduced a new parameter (atomic self-adaptivity) for understanding high crack resistance in oxide glasses. High self-adaptivity corresponds to large pressure-driven changes in density and coordination numbers of the network formers.¹² Future applications of the lithium aluminoborate glass are, however, limited by its relatively low hardness²¹ and chemical durability.²²

To further understand the mechanical properties of this glass family and their correlation with the network structure, we study the effect of adding SiO₂ (up to 20 mol%) to a 25Li₂O–20Al₂O₃–55B₂O₃ glass on the structure and mechanical properties. SiO₂ addition is interesting to explore, since pure silica glass features relatively high values of glass transition temperature, hardness, and chemical durability.^{23,24} We refer to the present glasses as silicoaluminoborates, since B₂O₃ remains the major network-forming oxide, unlike typical aluminoborosilicate glasses with SiO₂ content above, for example, 50 mol%.^{25–27} In previous related work, Morin et al have found that the glass transition temperature (T_g) of modified SiO₂–Al₂O₃–B₂O₃ glasses with relatively small SiO₂ content is mostly controlled by modifier cation-oxygen bond strength, and not to Al and B coordination.²⁸ Besides, Khanna et al have shown that increase in silica concentration suppresses the concentration of five- and six-fold Al in bismuth aluminoborate glasses.²⁹ In this study, we synthesize two glass series, in which we keep the Li/Al ratio constant. This is done to keep the structural role of Al approximately constant, since it has a strong enthalpic preference for being charge stabilized by alkali cations (eg, Li⁺) in tetrahedral configuration.¹² In the first series, SiO₂ is added while the remaining components are scaled down proportionally: $x\text{SiO}_2-(1-x)[25\text{Li}_2\text{O}-20\text{Al}_2\text{O}_3-55\text{B}_2\text{O}_3]$. In the second series, SiO₂ is substituted for B₂O₃: $y\text{SiO}_2-25\text{Li}_2\text{O}-20\text{Al}_2\text{O}_3-(55-y)\text{B}_2\text{O}_3$. For both series, we investigate the effect of the SiO₂ doping on glass transition temperature, density, structure (as probed by Raman spectroscopy), hardness, elastic moduli, indentation deformation mechanism, and crack resistance.

2 | EXPERIMENTAL PROCEDURE

2.1 | Glass preparation

We prepared two series of lithium silicoaluminoborate glasses using the traditional melt-quenching technique. That is, $x\text{SiO}_2-(1-x)[25\text{Li}_2\text{O}-20\text{Al}_2\text{O}_3-55\text{B}_2\text{O}_3]$ (named *x*-series) with $x = \{2,5,10,20\}$ and $y\text{SiO}_2-25\text{Li}_2\text{O}-20\text{Al}_2\text{O}_3-(55-y)\text{B}_2\text{O}_3$ (named *y*-series) with $y = \{2,5,10,20\}$ (in mol%). We also synthesized the base lithium aluminoborate glass with $x = y = 0$. The nominal chemical compositions of the glasses are shown in Table S1. The utilized raw materials were Li₂CO₃ (≥98.5%, Merck KGaA), Al₂O₃ (99.5%,

Sigma-Aldrich), H_3BO_3 ($\geq 99.5\%$, Honeywell International), and SiO_2 ($\geq 99.5\%$, 0.2–0.8 mm, Merck KGaA). First, according to the target composition, all raw materials were weighed and thoroughly mixed. The mixed batch materials were then stepwise added to a Pt-Rh crucible in a furnace at 800°C to remove H_2O and CO_2 . Subsequently, the batch was melted at 1400°C for 2 hours in air, where after the melt was poured onto a steel plate for quenching. The obtained glasses were quickly transferred to a preheated annealing furnace at an estimated glass transition temperature (T_g) value based on the previous studies.¹² X-ray diffraction (XRD) patterns of the specimens were acquired (Empyrean XRD, PANalytical) from 0° to 70° at 40 kV with a scanning speed of $8^\circ/\text{min}$. As shown in Figure S1, none of the samples show any signs of crystallization.

We determined T_g of the glasses from differential scanning calorimetry measurements (STA 449 F3 Jupiter, Netzsch) at 10 K/min on specimens with a known thermal history (ie, with a preceding cooling rate of 10 K/min). T_g values and other property data are summarized in Table S2. These samples were analyzed using Pt crucible in argon (gas flow 60 mL/min). The recorded heat flow curves are shown in Figure S2. The intercept between the tangent to the inflection point of the endothermic peak and the extrapolated heat flow of the glass was interpreted as the onset of the glass transition. Following determination of T_g , the glasses were reannealed for 0.5 hour at their measured T_g value and cooled down to room temperature at a cooling rate of approximately 3 K/min. After re-annealing, all the glasses were cut into desired dimensions for density, modulus, Raman, and indentation experiments, and then optically polished in ethanol using diamond grinding disks.

2.2 | Density

Density (ρ) of the glass specimens was determined using Archimedes' principle of buoyancy. The weight of each specimen (at least 1.5 g) was measured in air and ethanol 10 times. Based on the ratio between molar mass and density, we calculate the molar volume (V_m). To also quantify differences in free volume among the different glasses, we calculate the atomic packing density (C_g) based on these data. This was done by assuming sixfold coordination for Li, twofold coordination for O, fourfold coordination for Si, 83% threefold and 17% fourfold coordination for B, and 74% fourfold, 23% fivefold and 3% sixfold coordination for Al.¹² The boron and aluminum speciation is based on previous structural work on the lithium aluminoborate glass with $x = y = 0$,¹² but we note that the C_g values are relatively insensitive to those speciation fractions. C_g is defined as the ratio between the theoretical molar volume occupied by the ions and the effective molar volume of the glass:

$$C_g = \frac{\sum f_i V_i}{\sum f_i M_i} \rho \quad (1)$$

Here, $V_i = \frac{4}{3}\pi N (xr_A^3 + yr_B^3)$ represents the molar volume of an oxide A_xB_y with the molar fraction f_i and the molar mass M_i , N denotes the Avogadro number, and r_A and r_B are the ionic radii of the cations and anions, respectively, which are taken from Shannon.³⁰

2.3 | Elastic moduli

The elastic properties of the glasses were measured by ultrasonic echography using an ultrasonic thickness gauge (38DL Plus, Olympus) equipped with 20 MHz delay line transducers for the determination of the longitudinal V_1 and transversal wave velocities V_2 . The longitudinal modulus C_{11} , shear modulus G , bulk modulus B , and Young's modulus E as well as the Poisson ratio ν were calculated using the following relations, which are applicable for isotropic materials:

$$C_{11} = \rho V_1^2, \quad (2)$$

$$G = \rho V_2^2, \quad (3)$$

$$B = C_{11} - \frac{4}{3}G, \quad (4)$$

$$\nu = \frac{3B - 2G}{6B + 2G}, \quad (5)$$

$$E = 2G(1 + \nu). \quad (6)$$

2.4 | Raman spectroscopy

Raman spectra were collected using a micro-Raman spectrometer (inVia, Renishaw). The sample surface was excited by a 532 nm green HeNe laser for an acquisition time of 10 s. The range of the spectrum was from 250 to 1750 cm^{-1} and the resolution was better than 2 cm^{-1} . Spectra from five different locations on the glass were accumulated for each specimen to ensure homogeneity. All spectra were uniformly treated in Origin software for background correction and area normalization.

2.5 | Vickers micro-indentation

We determined the Vickers hardness (H_V) using a Nanovea CB500 hardness tester. On each specimen, 20 indents with a maximum load of 9.8 N (1 kgf) were generated. The loading duration and dwell time were set to 15 and 10 seconds, respectively. The residual imprints were subsequently analyzed with an optical microscope and H_V was calculated as,

$$H_V = 1.8544 \frac{P}{\left(\frac{d_1 + d_2}{2}\right)^2}, \quad (7)$$

where P is the contact load, and d_1 and d_2 are the length of the projected indent diagonals.

Vickers indentation was also used to evaluate the crack resistance (CR), that is, the resistance of the glass towards corner crack initiation upon indentation. For this purpose, the glass specimens were indented with stepwise increasing loads (from 2 to 42 N), and the numbers of corner cracks emanating from the residual imprints were counted. Following the method of Wada,³¹ the probability of crack initiation (PCI) was derived as the ratio between the number of corners, where a corner crack was formed and the total number of corners on all indents. The crack resistance is defined as the load at which an average of two cracks (PCI = 50%) occurred. On every specimen, at least 30 indents were made with loading durations of 15 seconds and dwell times of 10 seconds. The measurements were conducted at laboratory conditions (room temperature, relative humidity ~45% RH). The cracks were counted 2 hours after unloading.

In order to evaluate the indentation deformation mechanism of the glasses, we determined the recovery of the indent side length. This approach consists of recording topographic images of the indent site before and after a thermal treatment at $0.9 T_g$ for 2 hours,²³ which is used to measure how much the side length of indent cavity shrinks upon annealing. On every specimen, we analyzed at least 10 indents with a load of 4 N, loading duration of 15 seconds, and dwell time of 10 seconds. The indentation side length, $L_{s,i}$, was determined from the optical microscope. After annealing, the indentation side length, now $L_{s,f}$, was determined again. Similarly to the recovery of indentation volume following Yoshida's method,²³ the contribution of densification to the overall indentation deformation is estimated from the temperature-induced side length recovery (L_{SR}),

$$L_{SR} = \frac{L_{s,i} - L_{s,f}}{L_{s,i}} \quad (8)$$

3 | RESULTS AND DISCUSSION

3.1 | Raman spectroscopy

Structural changes due to silica addition in the lithium aluminoborate glasses are investigated by Raman spectroscopy (Figure 1). The spectrum exhibits many features characteristic of alkali borate glasses, but additional bands from other structural units are also observed. We divide the spectrum into five main bands enumerated *I* through *V*, with the expected assignments outlined in the following. All expected band assignments are summarized in Table S3.

Band region I (~ 280 to 625 cm^{-1}) is expected to contain contributions originating from B–O–B, Al–O–Al, and B–O–Al stretching.²⁶ Besides, vibrations due to superstructural

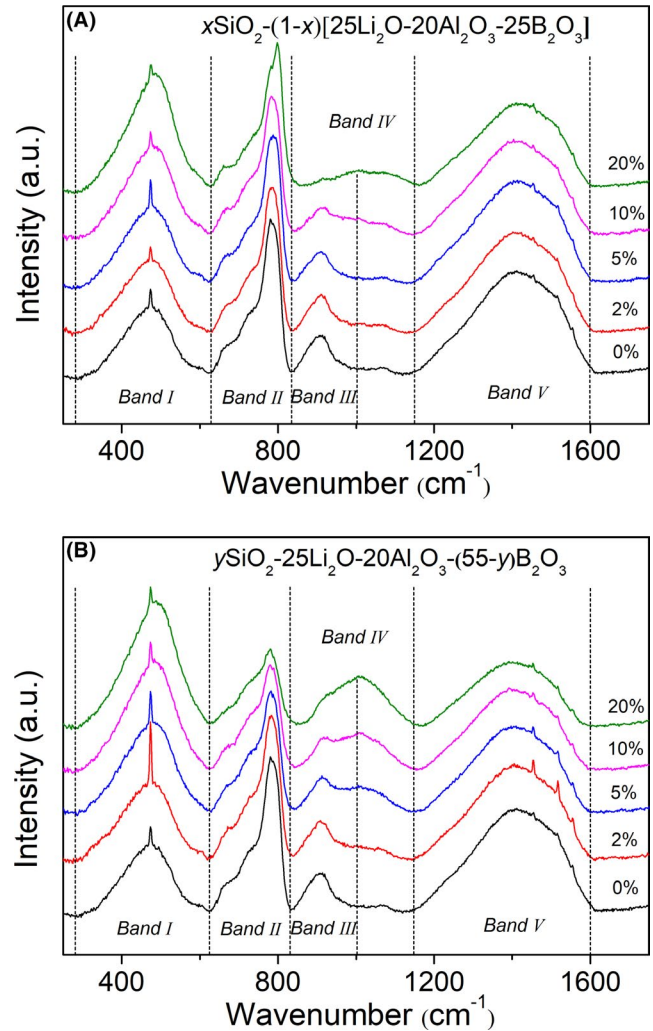


FIGURE 1 Micro-Raman spectra of the two series of lithium silicoaluminoborate glasses with different content of SiO_2 . The spectra are divided into five different band regions. (A) *x*-series. (B) *y*-series [Color figure can be viewed at wileyonlinelibrary.com]

units such as pentaborates may occur in this region. Furthermore, Si–O–Si network units may also occur in this region.²⁶ We find that the relative intensity of this band region increases with the content of SiO_2 for both series of glasses. Finally, we also note a small sharp peak in band region I, indicating a minor degree of crystallization although not detectable by XRD. Band region II (~ 625 to 815 cm^{-1}) is characteristic for B_2O_3 -rich glasses,²⁶ since peaks in this frequency range are typically assigned to borate superstructures such as chain and ring metaborates,^{32,33} di-triborates,³⁴ and penta-, tetra-, or triborates,^{32–35} as well as boroxol rings.^{32,36} In addition, B–O–Al stretching and aluminate network may occur in this region. For the *x*-series glasses where SiO_2 is added and other oxides are scaled down proportionally, there is no significant compositional change in this band region. However, it decreases in intensity with the content of SiO_2 increasing for the *y*-series glasses with Si-for-B substitution,

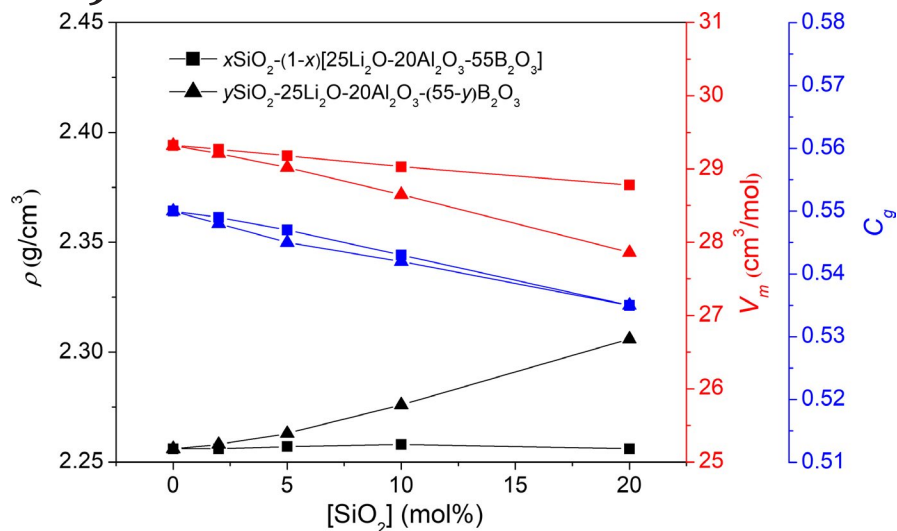


FIGURE 2 Composition dependence of density (ρ), molar volume (V_m) and atomic packing density (C_g) for the two series of lithium silicoaluminoborate glasses. The errors in ρ , V_m , and C_g do not exceed 0.002 g/cm^3 , $0.02 \text{ cm}^3/\text{mol}$, and 0.001 , respectively [Color figure can be viewed at wileyonlinelibrary.com]

since the addition of SiO_2 , and thus removal of B_2O_3 , must decrease the probability of forming medium-range order borate superstructures.

Band region III (~ 815 to 1000 cm^{-1}) is expected to result from vibrations of AlO_4 units ($\sim 900 \text{ cm}^{-1}$),^{37,38} Al-B network ($\sim 980 \text{ cm}^{-1}$),²⁷ and borate superstructures ($\sim 930 \text{ cm}^{-1}$).^{26,33} For both series of glasses, this band region decreases in intensity with the content of SiO_2 . Band region IV (~ 900 to 1150 cm^{-1}) is expected to contain contributions originating from the Q^n species (SiO_4 units with n bridging oxygens)²⁶ with bands at 1000 and 1150 cm^{-1} attributed to the stretching Si–O vibration in Q^2 and Q^3 species,²⁷ respectively. Furthermore, intermediate bands at 900 – 940 cm^{-1} are indication of Si–O–Al network.³⁹ For the x -series glasses where SiO_2 is added and other oxides are scaled down proportionally, this peak increases slightly in intensity with the content of SiO_2 . However, it increases significantly in intensity with the content of SiO_2 increasing for the y -series glasses with Si-for-B substitution, since the addition of SiO_2 , and thus removal of B_2O_3 , must decrease the fraction of the Al–O–B network, leading to more Si–O–Al bonds.

Finally, band region V (~ 1150 to 1600 cm^{-1}) is expected to be dominated by signal contributions from vibrations of superstructural units such as pyroborate units, chain and ring metaborate units.⁴⁰ For the x -series glasses where SiO_2 is added and other oxides are scaled down proportionally, there is no significant compositional change in this band region. However, it decreases in intensity with the content of SiO_2 increasing for the y -series glasses with Si-for-B substitution, since the addition of SiO_2 , and thus removal of B_2O_3 , must decrease the fraction of borate superstructures.

3.2 | Atomic packing and network rigidity

Figure 2 shows the composition dependence of density (ρ), molar volume (V_m), and atomic packing density (C_g) for the

two series of lithium silicoaluminoborate glasses. Addition of SiO_2 has only a minor effect on density when the other components are scaled down proportionally, whereas for the y -series of glasses, the density increases monotonically with the content of SiO_2 . However, since the molar mass is also changing with composition, we calculate the molar volume to evaluate changes in overall network packing. For both series, V_m decreases with the content of SiO_2 , showing that the glass network takes up less volume per mol of glass after silica addition. However, since there are also changes in the size of the atoms, we finally calculated the atomic packing density to understand differences in free volume. C_g also decreases with the content of SiO_2 for both series. This result shows that the network becomes gradually more open with silica addition, almost independent of how silica is added, since the two curves almost overlap in Figure 2. This is consistent with the open microstructure of pure silica glass.

To quantify the changes in network connectivity upon silica introduction into the glasses, we use topological constraint theory^{41–45} to enumerate the number of bond constraints per atom (n_c). Chemical bonds and bond angles constrain atoms in network glasses, with the strengths of the constraints depending on the local topology and the chemical nature of elements. Building on knowledge of the atomic coordination numbers (CN) of the network formers, we can compute the total number of linear bond stretching ($n_{c,\text{linear}} = \text{CN}/2$) and angular bond bending ($n_{c,\text{angular}} = 2\text{CN} - 3$) constraints for each network-forming atom, in addition to any constraints on the network modifiers.⁴⁶

For the present glasses, we estimate the number of constraints based on the topological model for sodium borosilicate glasses⁴⁶ and the previous structural work on the lithium aluminoborate glass with $x = y = 0$.¹² For this composition, it has been shown that the boron speciation is a mix of 83% B^{III} and 17% B^{IV} , while the aluminum speciation is a mix of 74% Al^{IV} , 23% Al^{V} , and 3% Al^{VI} . The structural changes

FIGURE 3 Composition dependence of n_c (number of constraints per atom) and n' (number of constraints per volume) for the two series of lithium silicoaluminoborate glasses [Color figure can be viewed at wileyonlinelibrary.com]

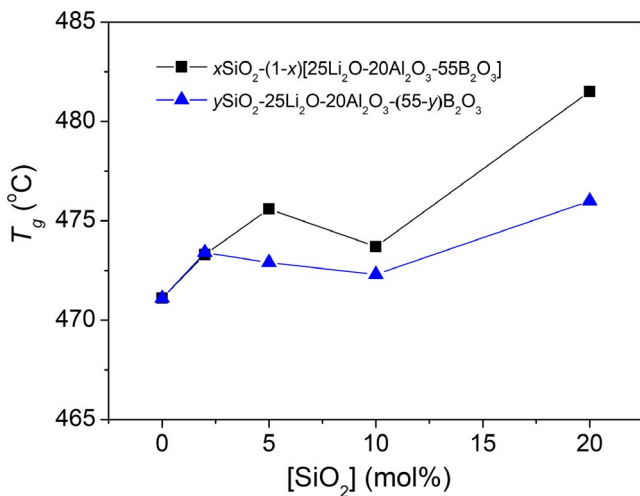
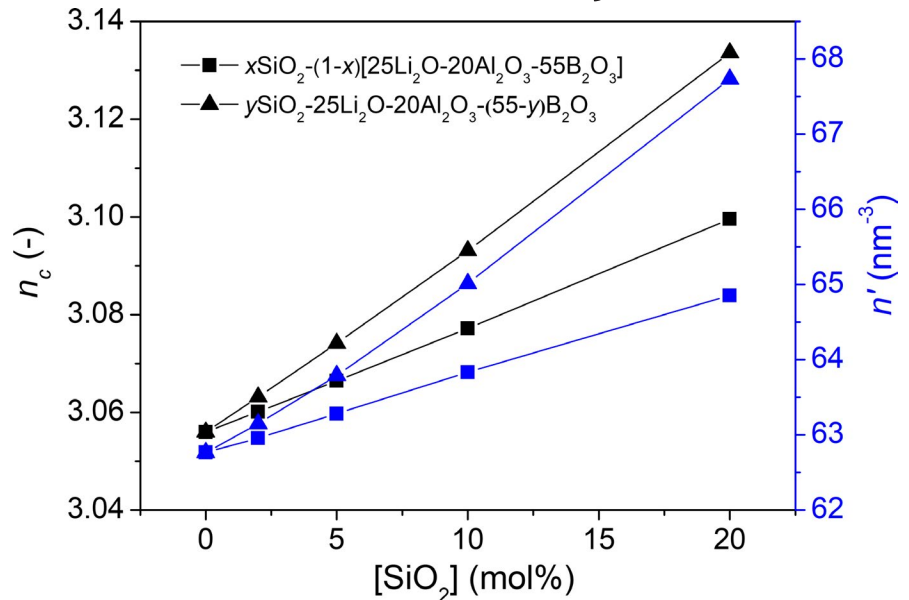


FIGURE 4 Composition dependence of the glass transition temperature (T_g) for the two series of lithium silicoaluminoborate glasses. The error in T_g does not exceed 2°C [Color figure can be viewed at wileyonlinelibrary.com]

in such silicoaluminoborate glasses are mostly dominated by the modifier-to-alumina ratio,⁴⁷ and since this ratio is kept constant in all the present glasses, we assume the boron and aluminum speciation to be constant in the following estimation of the number of constraint (since no structural data are available for the present glasses). We note that this assumption is not fully accurate, especially for the y -series glasses with Si-for-B substitution, but any variations are not expected to qualitatively influence the compositional trends in network rigidity. With these assumptions, we find that n_c increases with SiO_2 content in both series of glasses (Figure 3). The changes in network rigidity are generally small, but we find a larger increase in n_c for the y -series glasses with Si-for-B substitution.

In recent work, properties such as hardness⁴⁸ and elastic moduli^{49,50} have been found to scale better with constraint density (n'), that is, the number of constraints per volume. We compute n' based on n_c and the measured molar volume. n' also increases with increasing silica content, but the larger increase for the second glass series is even more pronounced for n' compared to that for n_c (Figure 3). We note that this increase in network rigidity upon silica addition is expected to improve the chemical durability of the aluminoborate glasses,²² but it has not been measured in the present study.

3.3 | Glass transition temperature

Figure 4 shows the compositional evolution of the glass transition temperature (T_g). We find that T_g is slightly positively correlated with the addition of SiO_2 . As discussed above, the addition of SiO_2 results in a more rigid glass network, that is, more atomic constraints per atom (higher connectivity), which has been shown in earlier work to be positively correlated with higher glass transition temperature.⁵¹ In agreement with the relatively small changes in n_c with composition (Figure 3), the changes in T_g are small (up to ~10 K) compared to the large change in composition (20 mol%). Furthermore, we note that there is a larger apparent increase in T_g for the x -series of glasses where SiO_2 is introduced by scaling down the other components proportionally, despite its smaller estimated increase in n_c compared to the y -series of glasses. This is likely because the average bond energy increases more in the former, since weak Li–O bonds are replaced by stronger Si–O bonds.

3.4 | Elasticity and hardness

Figure 5 shows the elastic moduli (E , G , B) and Poisson's ratio (ν) of the glasses with different extent of SiO_2 doping.

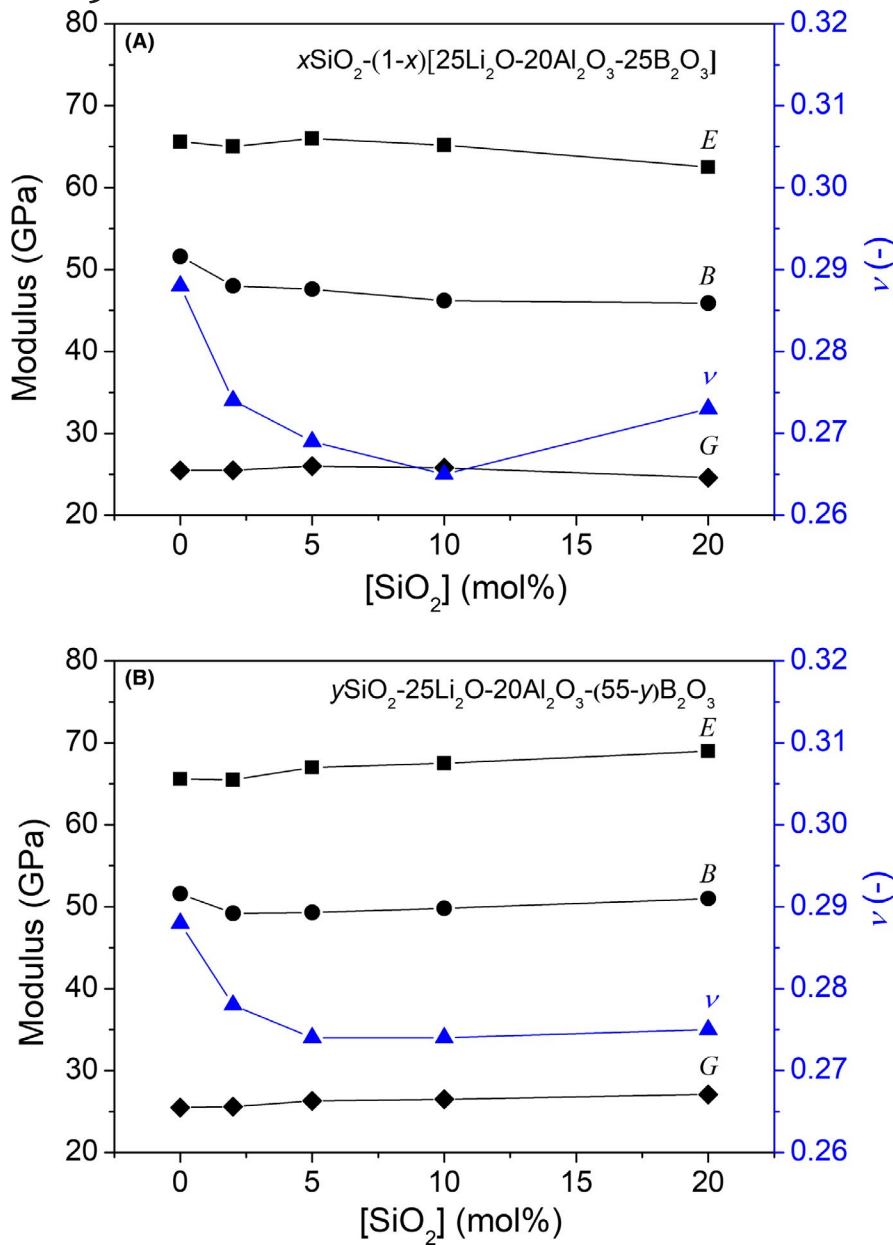


FIGURE 5 Composition dependence of elastic moduli (Young's (E), shear (G), bulk (B)) and Poisson's ratio (ν) for the two series of lithium silicoaluminoborate glasses. The errors in E , G , B , and ν do not exceed 2, 1, 1 GPa, and 0.005, respectively. (A) x -series. (B) y -series [Color figure can be viewed at wileyonlinelibrary.com]

As seen for glass transition temperature, the addition of SiO_2 has only a relatively small effect on the elastic moduli for the two series glasses. For the x -series glasses (Figure 5A), there is either no change or a small decrease in elastic moduli with SiO_2 content. On the other hand, the y -series glasses exhibit a small increase in elastic moduli (Figure 5B). Elastic moduli generally increase with the bond strength and the number of bonds per volume.⁵² Recent topological models have found E to be positively correlated with n' ,^{49,50} which qualitatively agrees with the larger increase in n' for the y -series glasses with Si-for-B substitution (Figure 3). However, it cannot explain why there is a minor decrease in E with silica content for the x -series glasses (Figure 5A). According to the model in Ref. [50], this could only be possible if some linear bond stretching constraints are transformed into angular bond

bending constraints, since the typical free energy for the former is larger than for the latter type of constraints. Additional structural characterization or atomistic simulations would be needed to confirm this.

The addition of SiO_2 also affects the Poisson's ratio for both series of glasses, although all glasses are within the relatively narrow range of 0.26 to 0.29. For the initial silica addition (2–10 mol%), Poisson's ratio for both series shows a negative correlation with the addition of SiO_2 . This makes sense in terms of the compositional trend in C_g (Figure 2), since more open networks are generally found to feature more volume compared to shape change upon deformation and thus have lower Poisson's ratio.⁵² However, when the silica addition increases to 20 mol%, the Poisson's ratio increases, especially for the x -series glasses. For this series, when the addition of

silica reaches 20 mol%, Al_2O_3 and Li_2O are strongly diluted. Therefore, the probability of finding Li^+ ions in proximity to aluminum species could be decreasing. It is thus possible that more lithium ions than the simple excess (ie, $[\text{Li}_2\text{O}]-[\text{Al}_2\text{O}_3]$) act as modifiers instead of charge-compensating aluminum tetrahedra. Such structure changes should increase the extent of NBO formation, which makes the network more prone to shear, resulting in an increase in ν .¹⁴

Figure 6 shows the composition dependence of Vickers hardness, which has been determined using the micro-indentation method. The addition of SiO_2 has a positive effect on the Vickers hardness for both series of glasses. As for elastic moduli, the results can be understood in terms of the changes in constraint density with composition, which has been proposed to scale with hardness.⁴⁸ That is, hardness increases with silica content due to the concomitant increase in n' , which also explains the larger observed increase in hardness for the y -series glasses with Si-for-B substitution (Figure 6). The hardness model of Zheng et al.⁴⁸ is given as,

$$H_V = (dH_V/dn') \cdot n' \quad (9)$$

where dH_V/dn' is a scaling factor. By setting $dH_V/dn' = 0.071 \text{ GPa nm}^3$, which is within the range of values reported previously,⁴⁸ we obtain hardness values of 4.5, 4.6, and 4.8 GPa for the glasses with $x = y = 0$, $x = 20$, and $y = 20$, respectively. These model predictions (see dashed lines in Figure 6) are in good agreement with the experimental data in Figure 6.

3.5 | Indentation deformation

Next, we consider the extent of densification during indentation to understand the cracking behavior of the glasses. Figure

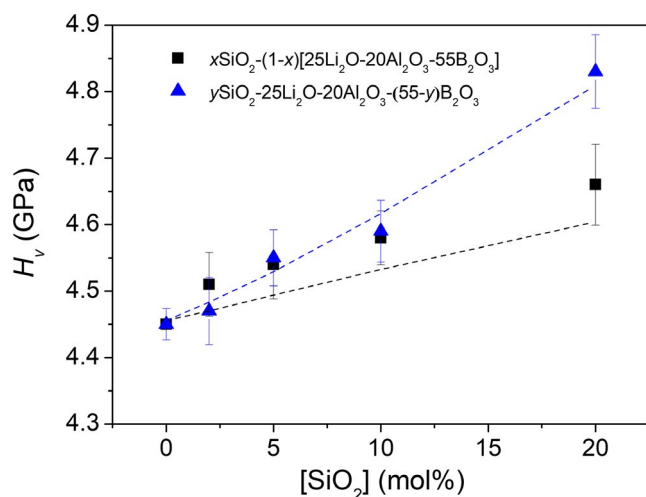


FIGURE 6 Composition dependence of indentation hardness for the two series of lithium silicoaluminoborate glasses. The dashed lines represent the model predictions using Equation (9) with $dH_V/dn' = 0.071 \text{ GPa nm}^3$ [Color figure can be viewed at wileyonlinelibrary.com]

7 shows optical micrographs of indents produced at 4 N on the surface of the glass $20\text{SiO}_2-35\text{B}_2\text{O}_3-25\text{Li}_2\text{O}-20\text{Al}_2\text{O}_3$ ($y = 20$) before and after annealing at $0.9T_g$ for 2 hour. A significant deformation recovery zone is observed in the glass after annealing the indent. As shown in Figure S3, there is an apparent recovery zone for both series of glasses after re-annealing at $0.9T_g$ for 2 hour. However, the addition of SiO_2 does not cause noticeable differences in the extent of the deformation recovery zone.

The extent of indentation-induced densification is typically quantified from the ratio between the densification and the total indentation volumes, referred to as the volume recovery ratio (V_R).²³ Here, we use a similar metric, which we have found to scale well with V_R (unpublished data), namely the recovery of the indentation side length upon annealing (L_{SR}). Figure 8 shows the composition dependence of L_{SR} . It is clear that the addition of SiO_2 has a negligible effect on the side recovery of the indents in the glasses, which we interpret as a competition of two effects. On the one hand, B and Al atoms are removed due to the addition of SiO_2 , leading to less densification, since Si (unlike B and Al) does not readily change its coordination number as a result of the stresses created during indentation. On the other hand, C_g of the two series of glasses decreases with the increasing content of SiO_2 . More open glass networks could lead to more densification. Therefore, it is possible that these two opposite effects cancel each other, resulting in constant densification contribution to indentation upon silica addition.

3.6 | Indentation cracking

In the Vickers indentation test, crack initiation occurs under a sufficiently high load, and is attributed to the mismatch between the plastic deformation volume and the surrounding elastically deformed material.^{53,54} Crack resistance (CR) is derived from the load leading to formation of two corner cracks per indent, which are the dominant crack type in the investigated glasses. Figure S4 shows images of the radial cracks generated in the two glass series. Figure 9 shows the composition dependence of CR of the two series of glasses. Different experiment conditions (such as relative humidity, loading rate, and surface quality) and slight composition variations can have a pronounced impact on the value of CR. Therefore, compared with the previous work,¹² the $55\text{B}_2\text{O}_3-25\text{Li}_2\text{O}-20\text{Al}_2\text{O}_3$ ($x = y = 0$) glass in this study has a lower CR value than that previously reported. Furthermore, the addition of SiO_2 has a significant effect on the CR for both series, that is, CR decreases with the silica content. Building on our recent work¹² showing that the coordination number changes during indentation (termed self-adaptivity) are more important for CR than packing density, the observed decrease in CR is due to the removal of Al_2O_3 and/or B_2O_3 with the addition of SiO_2 . This compositional changes

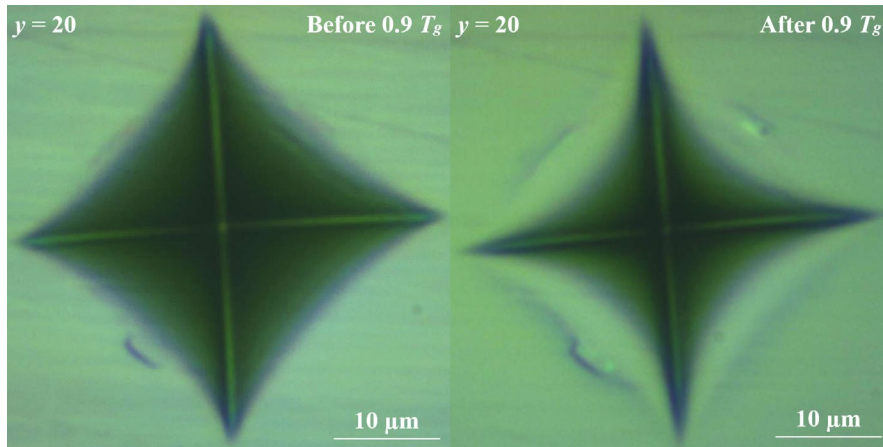


FIGURE 7 Optical micrographs of indents produced at 4 N on the surface of the glass ($20\text{SiO}_2\text{-}35\text{B}_2\text{O}_3\text{-}25\text{Li}_2\text{O-}20\text{Al}_2\text{O}_3$) before and after re-annealing at $0.9T_g$ for 2 h [Color figure can be viewed at wileyonlinelibrary.com]

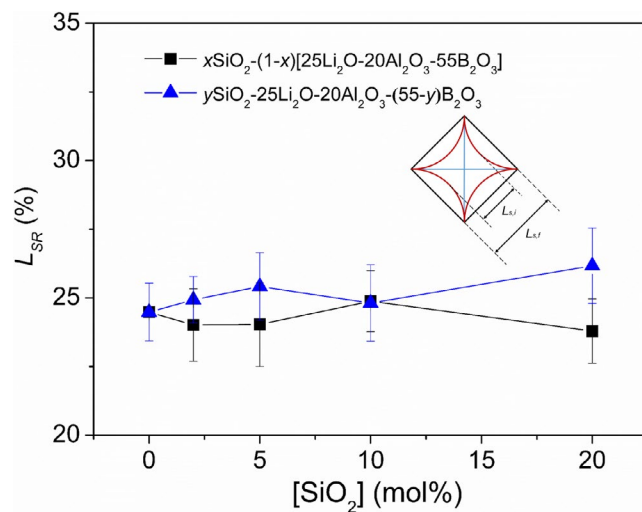


FIGURE 8 Composition dependence of indentation side recovery (L_{SR}) for the two series of lithium silicoaluminoborate glasses [Color figure can be viewed at wileyonlinelibrary.com]

makes the network less structurally adaptive to applied stress, although the silica-containing networks have more free volume. However, they cannot densify more during densification (Figure 8), and this leads to an overall decrease in crack resistance upon SiO_2 addition. Finally, we note that besides the overall decrease in CR with silica addition, there is a local minimum in CR for both the glasses with $x = 2$ and $y = 2$. The structural origin of this apparent minimum is unknown.

4 | CONCLUSIONS

We have studied the structure and mechanical properties of two series $\text{SiO}_2\text{-B}_2\text{O}_3\text{-Li}_2\text{O-Al}_2\text{O}_3$ glasses with varying addition of SiO_2 . By using micro-Raman spectroscopy, we have found that the addition of SiO_2 partially disturbs the borate network, thus increases the average network rigidity but decreasing the atomic packing density, that is, that the network

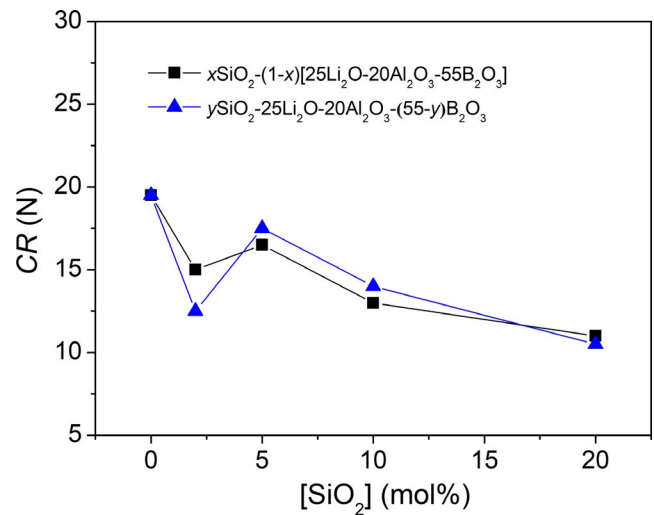


FIGURE 9 Composition dependence of the crack resistance (CR) for the two series of lithium silicoaluminoborate glasses. The estimated error in CR is 20% of its value [Color figure can be viewed at wileyonlinelibrary.com]

becomes gradually more open and rigid with silica addition. By using a previous constraint hardness model, we are able to quantitatively account for the composition dependence of hardness based on the competing effects of free volume and network rigidity. The removal of B and Al atoms due to the addition of SiO_2 should lead to less structural densification (ie, involving changes in coordination numbers), whereas the more open glass networks should lead to more densification (ie, at constant coordination numbers). As a result, there is no apparent effect of silica addition on the side recovery of the indents, that is, on the indentation deformation mechanism. In agreement with our recent work showing that the coordination number changes during indentation (termed self-adaptivity) are more important for crack resistance than packing density, we find that the addition of SiO_2 leads to an overall decrease in crack resistance. In other words, the addition of SiO_2 does not necessarily lead to a pronounced increase in

physical properties, although pure SiO₂ has high glass transition temperature, hardness, and crack resistance. As shown and discussed in this work, it is due to the complex structural interactions in mixed network former glasses and the competitive effects of free volume and network rigidity.

ACKNOWLEDGMENTS

This work was supported by the China Scholarship Council (CSC No. 201806370210). MB acknowledges funding from the National Science Foundation under Grants No. 1562066, 1762292, and 1826420.

ORCID

Pengfei Liu  <https://orcid.org/0000-0003-2885-4721>

Kacper Januchta  <https://orcid.org/0000-0002-5204-0755>

Mathieu Bauchy  <https://orcid.org/0000-0003-4600-0631>

Morten M. Smedskjaer  <https://orcid.org/0000-0003-0476-2021>

REFERENCES

- Mostofa MG, Park CI, Park SS. AFM probe based nano mechanical scribing of soda-lime glass. *J Manuf Process*. 2013;15(4):625–34.
- Griffith AA. The phenomena of rupture and flow in solids. *Philos Trans R Soc*. 1921;221(582–593):163–98.
- Cormack AN, Segre U, Menziani MC, Malavasi G, Pedone A. Molecular dynamics studies of stress-strain behavior of silica glass under a tensile load. *Chem Mater*. 2008;20(13):4356–66.
- Kistler SS. Stresses in glass produced by nonuniform exchange of monovalent ions. *J Am Ceram Soc*. 1962;45(2):59–68.
- Wondraczek L, Mauro JC, Eckert J, Kühn U, Horbach J, Deubener J, et al. Towards ultrastrong glasses. *Adv Mater*. 2011;23(39):4578–86.
- Shi Y, Luo J, Yuan F, Huang L. Intrinsic ductility of glassy solids. *J Appl Phys*. 2014;115(4):043528.
- Mauro JC, Tandia A, Vargheese KD, Mauro YZ, Smedskjaer MM. Accelerating the design of functional glasses through modeling. *Chem Mater*. 2016;28(12):4267–77.
- Sehgal J, Ito S. A new low-brittleness glass in the soda-lime-silica glass family. *J Am Ceram Soc*. 2010;81(9):2485–8.
- Rosales-Sosa GA, Masuno A, Higo Y, Inoue H. Crack-resistant Al₂O₃-SiO₂ glasses. *Sci Rep*. 2016;6(3):1–7.
- Mabrouk A, De Sousa Meneses D, Pellerin N, Véron E, Genevois C, Ory S, et al. Effects of boron on structure of lanthanum and sodium aluminoborosilicate glasses studied by X-ray diffraction, transmission electron microscopy and infrared spectrometry. *J Non Cryst Solids*. 2019;503–504(9):69–77.
- Rosales-Sosa GA, Masuno A, Higo Y, Inoue H, Yanaba Y, Mizoguchi T, et al. High elastic moduli of a 54Al₂O₃-46Ta₂O₅ glass fabricated via containerless processing. *Sci Rep*. 2015;5(1):1–8.
- Januchta K, Youngman RE, Goel A, Bauchy M, Logunov SL, Rzoska SJ, et al. Discovery of ultra-crack-resistant oxide glasses with adaptive networks. *Chem Mater*. 2017;29(14):5865–76.
- Youngman RE, Januchta K, Smedskjaer MM, Bauchy M, Rzoska SJ, Bockowski M. Modifier field strength effects on densification behavior and mechanical properties of alkali aluminoborate glasses. *Phys Rev Mater*. 2017;1(6):1–12.
- Januchta K, Smedskjaer MM. Indentation deformation in oxide glasses: quantification, structural changes, and relation to cracking. *J Non-Crystalline Solids X*. 2019;1(9):100007.
- Yoshida S. Indentation deformation and cracking in oxide glass -toward understanding of crack nucleation. *J Non-Crystalline Solids X*. 2019;1(11):100009.
- Rouxel T, Yoshida S. The fracture toughness of inorganic glasses. *J Am Ceram Soc*. 2017;100(10):4374–96.
- Peter KW. Densification and flow phenomena of glass in indentation experiments. *J Non Cryst Solids*. 1970;5(2):103–15.
- Kato Y, Yamazaki H, Yoshida S, Matsuoka J. Effect of densification on crack initiation under Vickers indentation test. *J Non Cryst Solids*. 2010;356(35–36):1768–73.
- Benzine O, Bruns S, Pan Z, Durst K, Wondraczek L. Local deformation of glasses is mediated by rigidity fluctuation on nanometer scale. *Adv Sci*. 2018;5(10):1800916.
- Januchta K, Youngman RE, Goel A, Bauchy M, Rzoska SJ, Bockowski M, et al. Structural origin of high crack resistance in sodium aluminoborate glasses. *J Non Cryst Solids*. 2017;460:54–65.
- Frederiksen KF, Januchta K, Mascaraque N, Youngman RE, Bauchy M, Rzoska SJ, et al. Structural compromise between high hardness and crack resistance in aluminoborate glasses. *J Phys Chem B*. 2018;122(23):6287–95.
- Mascaraque N, Januchta K, Frederiksen KF, Youngman RE, Bauchy M, Smedskjaer MM. Structural dependence of chemical durability in modified aluminoborate glasses. *J Am Ceram Soc*. 2019;102(3):1157–68.
- Yoshida S, Sanglebœuf JC, Rouxel T. Quantitative evaluation of indentation-induced densification in glass. *J Mater Res*. 2005;20(12):3404–12.
- Arora A, Marshall DB, Lawn BR, Swain MV. Indentation deformation/fracture of normal and anomalous glasses. *J Non Cryst Solids*. 1979;31(3):415–28.
- Du LS, Stebbins JF. Network connectivity in aluminoborosilicate glasses: a high-resolution 11B, 27Al and 17O NMR study. *J Non Cryst Solids*. 2005;351(43–45):3508–20.
- Li H, Su Y, Li L, Strachan DM. Raman spectroscopic study of gadolinium(III) in sodium-aluminoborosilicate glasses. *J Non Cryst Solids*. 2001;292(1–3):167–76.
- Ollier N, Charpentier T, Boizot B, Wallez G, Ghaleb D. A Raman and MAS NMR study of mixed alkali Na-K and Na-Li aluminoborosilicate glasses. *J Non Cryst Solids*. 2004;341(1–3):26–34.
- Morin EI, Wu J, Stebbins JF. Modifier cation (Ba, Ca, La, Y) field strength effects on aluminum and boron coordination in aluminoborosilicate glasses: the roles of fictive temperature and boron content. *Appl Phys A Mater Sci Process*. 2014;116(2):479–90.
- Khanna A, Saini A, Chen B, González F, Pesquera C. Structural study of bismuth borosilicate, aluminoborate and aluminoborosilicate glasses by 11B and 27Al MAS NMR spectroscopy and thermal analysis. *J Non Cryst Solids*. 2013;373–374:34–41.
- Shannon RD. Revised effective ionic radii and systematic studies of interatomic distances in halides and chalcogenides. *Acta Crystallogr A*. 1976;32(5):751–67.
- Wada M, Furukawa H, Fujita K. Crack resistance of glass on Vickers indentation. *Proc Int Congr Glass*. 1974;11:39–46.

32. Konijnendijk WL, Stevels JM. The structure of borosilicate glasses studied by Raman scattering. *J Non Cryst Solids*. 1976;20(2):193–224.
33. Kamitsos EI, Chryssikos GD. Borate glass structure by Raman and infrared spectroscopies. *J Mol Struct*. 1991;47(C):1–16.
34. Meera BN, Ramakrishna J. Raman spectral studies of borate glasses. *J Non Cryst Solids*. 1993;159(1–2):1–21.
35. Vignarooban K, Boolchand P, Micoulaut M, Malki M, Bresser WJ. Rigidity transitions in glasses driven by changes in network dimensionality and structural groupings. *Europhys Lett*. 2014;108(5):56001.
36. Solids J, Co NP. The structure of liquid and vitreous boron oxide. *J Non Cryst Solids*. 1969;1(1):269–84.
37. McMillan P, Piriou B. Raman spectroscopy of calcium aluminate glasses and crystals. *J Non Cryst Solids*. 1983;55(2):221–42.
38. Licheron M, Montouillout V, Millot F, Neuville DR. Raman and ^{27}Al NMR structure investigations of aluminate glasses: $(1-x)\text{Al}_2\text{O}_3\text{-}x\text{MO}$, with $\text{M} = \text{Ca}, \text{Sr}, \text{Ba}$ and $0.5 < x < 0.75$). *J Non Cryst Solids*. 2011; 357(15):2796–801.
39. Neuville DR, Cormier L, Massiot D. Al coordination and speciation in calcium aluminosilicate glasses: effects of composition determined by ^{27}Al MQ-MAS NMR and Raman spectroscopy. *Chem Geol*. 2006;229(1–3):173–85.
40. Yano T, Kunimine N, Shibata S, Yamane M. Structural investigation of sodium borate glasses and melts by Raman spectroscopy. I. Quantitative evaluation of structural units. *J Non Cryst Solids*. 2003;321(3):137–46.
41. Gupta PK, Mauro JC. Composition dependence of glass transition temperature and fragility. I. A topological model incorporating temperature-dependent constraints. *J Chem Phys*. 2009;130(9):094503.
42. Smedskjaer MM, Mauro JC, Sen S, Yue Y. Quantitative design of glassy materials using temperature-dependent constraint theory. *Chem Mater*. 2010;22(18):5358–65.
43. Bauchy M, Micoulaut M. Atomic scale foundation of temperature-dependent bonding constraints in network glasses and liquids. *J Non Cryst Solids*. 2011;357(14):2530–7.
44. Rodrigues BP, Wondraczek L. Medium-range topological constraints in binary phosphate glasses. *J Chem Phys*. 2013;138(24):244507.
45. Bauchy M, Micoulaut M. Transport anomalies and adaptive pressure-dependent topological constraints in tetrahedral liquids: evidence for a reversibility window analogue. *Phys Rev Lett*. 2013;110(9):1–5.
46. Smedskjaer MM. Topological model for boroaluminosilicate glass hardness. *Front Mater*. 2014;1(1):1–6.
47. Zheng QJ, Youngman RE, Hogue CL, Mauro JC, Potuzak M, Smedskjaer MM, et al. Structure of boroaluminosilicate glasses: Impact of $[\text{Al}_2\text{O}_3]/[\text{SiO}_2]$ ratio on the structural role of sodium. *Phys Rev B—Condens Matter Mater Phys*. 2012;86(5):1–12.
48. Zheng Q, Yue Y, Mauro JC. Density of topological constraints as a metric for predicting glass hardness. *Appl Phys Lett*. 2017;111(1):011907.
49. Wilkinson CJ, Zheng Q, Huang L, Mauro JC. Topological constraint model for the elasticity of glass-forming systems. *J Non-Crystalline Solids X*. 2019;2(11):100019.
50. Yang K, Yang B, Xu X, Hoover C, Smedskjaer MM, Bauchy M. Prediction of the Young's modulus of silicate glasses by topological constraint theory. *J Non Cryst Solids*. 2019;514(3):15–9.
51. Mauro JC, Gupta PK, Loucks RJ. Composition dependence of glass transition temperature and fragility. II. A topological model of alkali borate liquids. *J Chem Phys*. 2009;130(23):234503.
52. Rouxel T. Elastic properties and short-to medium-range order in glasses. *J Am Ceram Soc*. 2007;90(10):3019–39.
53. Limbach R, Winterstein-Beckmann A, Dellith J, Möncke D, Wondraczek L. Plasticity, crack initiation and defect resistance in alkali-borosilicate glasses: from normal to anomalous behavior. *J Non Cryst Solids*. 2015;417–418:15–27.
54. Cook RF, Pharr GM. Direct observation and analysis of indentation cracking in glasses and ceramics. *J Am Ceram Soc*. 1990;73(4):787–817.

SUPPORTING INFORMATION

Additional supporting information may be found online in the Supporting Information section at the end of the article.

How to cite this article: Liu P, Januchta K, Jensen LR, Bauchy M, Smedskjaer MM. Competitive effects of free volume, rigidity, and self-adaptivity on indentation response of silicoaluminoborate glasses. *J Am Ceram Soc*. 2020;103:944–954. <https://doi.org/10.1111/jace.16790>

SUPPORTING INFORMATION

Competitive Effects of Free Volume, Rigidity, and Self-Adaptivity on Indentation Response of Silicoaluminoborate Glasses

Pengfei Liu¹, Kacper Januchta¹, Lars R. Jensen², Mathieu Bauchy³, Morten M. Smedskjaer^{1,*}

¹*Department of Chemistry and Bioscience, Aalborg University, Aalborg, Denmark*

²*Department of Materials and Production, Aalborg University, Aalborg, Denmark*

³*Department of Civil and Environmental Engineering, University of California, Los Angeles, USA*

**Corresponding author. e-mail: mos@bio.aau.dk*

Table S1. Nominal chemical compositions of all the lithium silicoaluminoborate glasses (in mol%).

Glass	SiO₂	B₂O₃	Al₂O₃	Li₂O
$x = y = 0$	0	55	20	25
$x\text{SiO}_2-(1-x)[25\text{Li}_2\text{O}-20\text{Al}_2\text{O}_3-55\text{B}_2\text{O}_3]$				
$x = 2$	2	53.9	19.6	24.5
$x = 5$	5	52.25	19	23.75
$x = 10$	10	49.5	18	22.5
$x = 20$	20	44	16	20
$y\text{SiO}_2-25\text{Li}_2\text{O}-20\text{Al}_2\text{O}_3-(55-y)\text{B}_2\text{O}_3$				
$y = 2$	2	53	20	25
$y = 5$	5	50	20	25
$y = 10$	10	45	20	25
$y = 20$	20	35	20	25

Table S2. Overview of the properties of the prepared glasses, including glass transition temperature (T_g), density (ρ), molar volume (V_m), atomic packing density (C_g), Young's modulus (E), shear modulus (G), bulk modulus (B), Poisson's ratio (ν), Vickers hardness (H_v), and crack resistance (CR).

Glass	T_g [°C]	ρ [g/cm ³]	V_m [cm ³ /mol]	C_g [-]	E [GPa]	G [GPa]	B [GPa]	ν [-]	$H_v^{(*)}$ [GPa]	$CR^{(**)}$ [N]
$x = y = 0$	471	2.256	29.32	0.550	66	26	52	0.280	4.45	19.5
$x\text{SiO}_2-(1-x)[25\text{Li}_2\text{O}-20\text{Al}_2\text{O}_3-55\text{B}_2\text{O}_3]$										
$x = 2$	473	2.256	29.27	0.549	65	26	48	0.274	4.51	15
$x = 5$	476	2.257	29.18	0.547	66	26	48	0.269	4.54	16.5
$x = 10$	474	2.258	29.03	0.543	65	26	46	0.265	4.58	13
$x = 20$	482	2.256	28.78	0.535	63	25	46	0.273	4.66	11
$y\text{SiO}_2-25\text{Li}_2\text{O}-20\text{Al}_2\text{O}_3-(55-y)\text{B}_2\text{O}_3$										
$y = 2$	473	2.258	29.21	0.548	66	26	49	0.278	4.47	12.5
$y = 5$	473	2.263	29.02	0.545	67	26	49	0.274	4.55	17.5
$y = 10$	472	2.276	28.65	0.542	68	27	50	0.274	4.59	14
$y = 20$	476	2.306	27.86	0.535	69	27	51	0.275	4.83	10.5
Error estimate	2	0.002	0.02	0.001	2	1	1	0.005	≤ 0.15	20%

(*) H_v measured at ambient conditions at load of 9.8 N (1 kgf).

(**) CR measured at ambient conditions (temperature 24 ± 1 °C, relative humidity ~25%).

Table S3. Raman band deconvolution assignment with references.

Structural unit	Wavenumber [cm ⁻¹]	Ref
B-O-B stretch & BO ₄ unit	450-570 & 900-1000	1
Al-O-B stretch & aluminate network	480-500 & 700-720	1
Ring metabotare	630 & 1300-1600	1,2,3
Chain metaborate	730 & 1300-1600	1,2
Si-O-Al network	900-940	4
Di-triborate	755	5
Tri-, Tetra- or Pengtaborate	770 & 930	2,3,5,6
Boroxol ring	808	2,7
Pyroborate	820 & 1200-1300	1,2,3
AlO ₄ unit	790 & 900	8,9
Orthoborate	890-940	1
Diborate	1100	3
BO ₃ unit	1260, 1350, 1470, & 1530	10
BO ₂ O- unit	1490 & 1550	10
Al-B network	980	11
Q ⁰ unit	850	1,12
Q ¹ unit	700 & 900	1
Q ² unit	592-612 & 950-1000	1,12
Q ³ unit	524-530 & 1050-1100	1,12
Q ⁴ unit	430-440, 1150 & 1200	1
Q ¹ units mixed bending and stretching with Q ⁴	670	1
Q ² units mixed bending and stretching with Q ⁴	640	1
Q ³ units mixed bending and stretching with Q ⁴	600	1

Note: $Q^0 = SiO_4^{4-}$, $Q^1 = Si_2O_7^{6-}$, $Q^2 = SiO_3^{2-}$, $Q^3 = Si_2O_5^{2-}$ and $Q^4 = SiO_2$

Figure S1. X-ray diffraction spectra of the as-prepared lithium silicoaluminoborate glasses. No sharp peaks are observed in the spectra, confirming the non-crystalline nature of the samples.

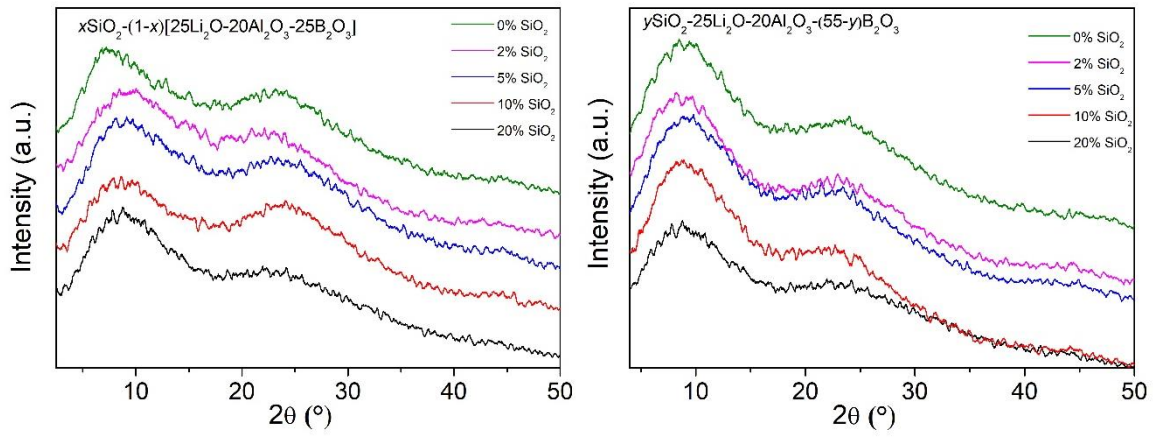


Figure S2. Differential scanning calorimetry heating scans of the as-prepared lithium silicoaluminoborate glasses.

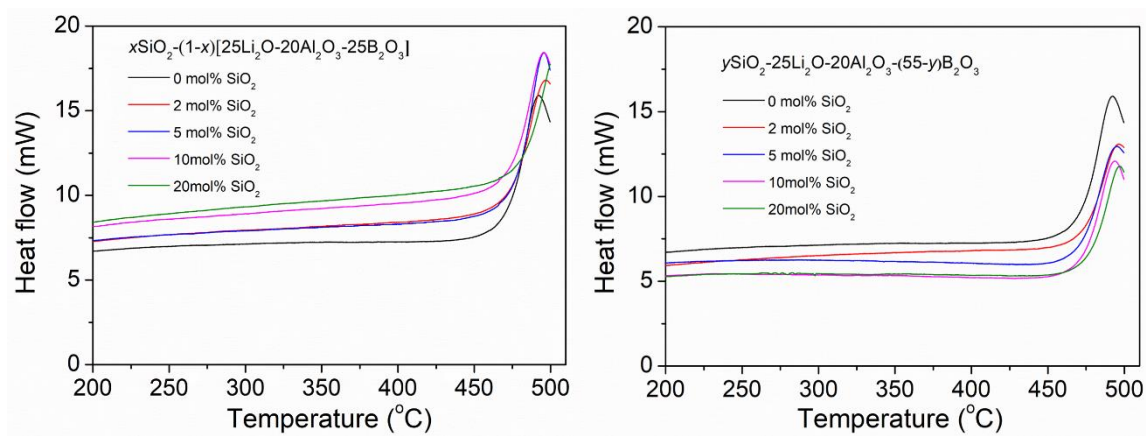


Figure S3. Optical micrographs of indents produced at 4 N on the surface of the as-prepared lithium silicoaluminoborate glasses after re-annealing at $0.9T_g$.

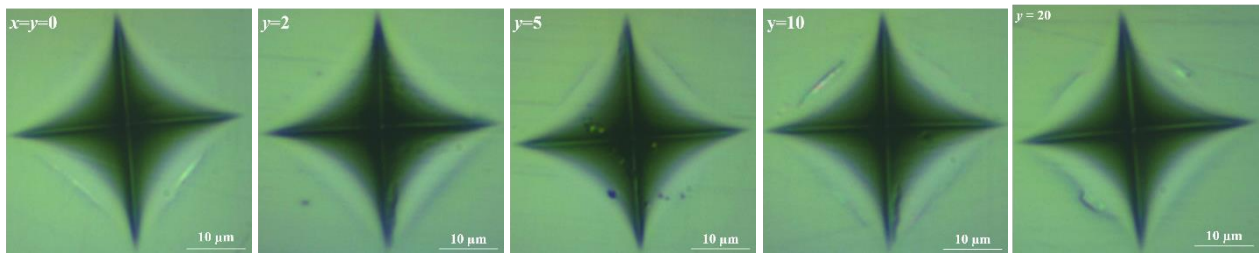
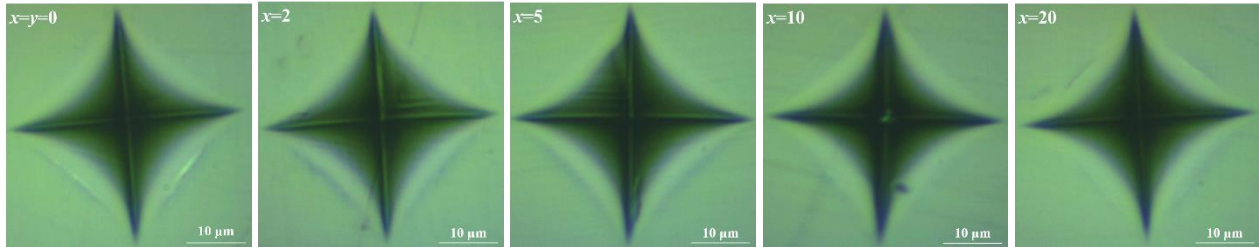
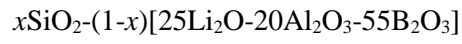


Figure S4. Optical images of indents produced at 19.6 N (2 kgf) on the surface of the as-prepared glasses.

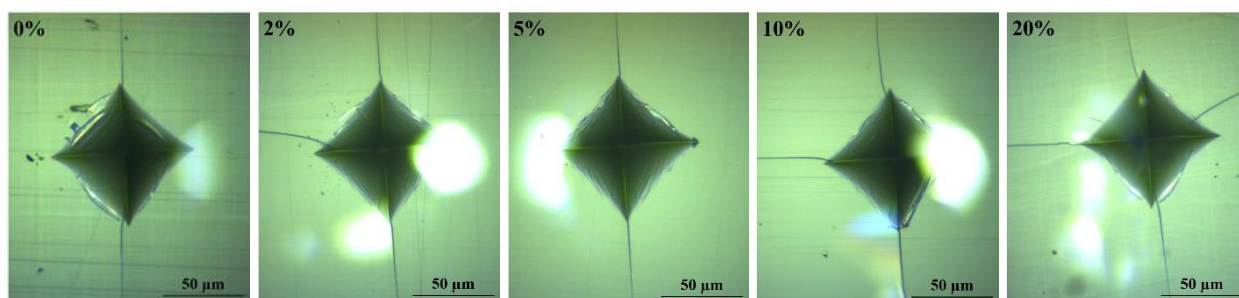
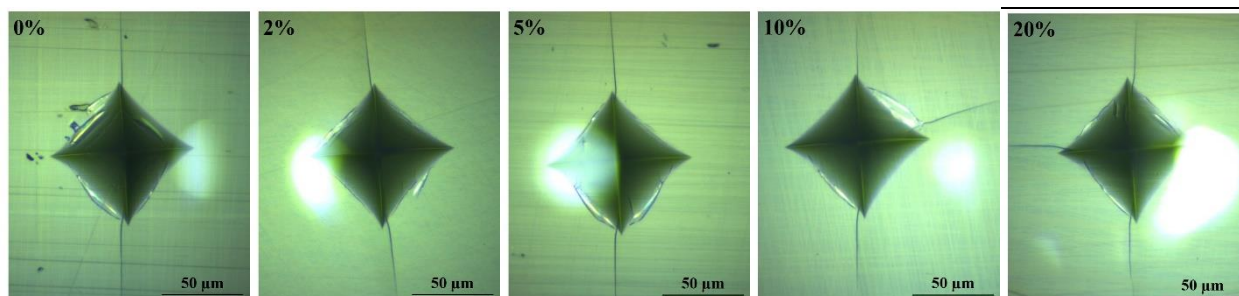
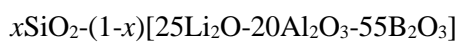
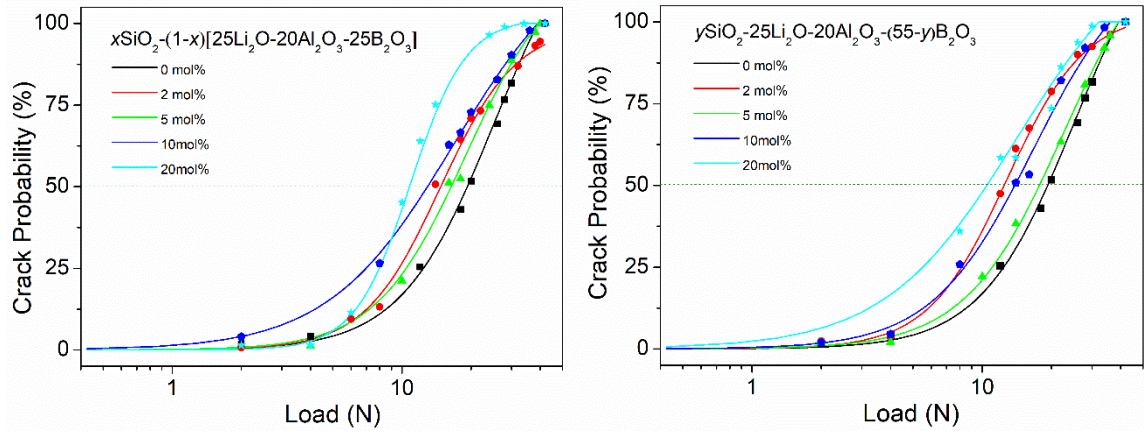


Figure S5. Crack probability as a function of applied indentation load for the as-prepared lithium silicoaluminoborate glasses. The experimental data was fit to a sigmoidal function of the form $y = A_2 + (A_1 - A_2)/[1 + (x/x_0)^p]$ (solid lines), and the crack resistance (dashed line) was derived from the load at which an average of two radial cracks (probability of 50%) formed at the corners of the Vickers imprints.




Supporting References

- (1) Li, H.; Su, Y.; Li, L.; Strachan, D. M. Raman Spectroscopic Study of Gadolinium(III) in Sodium-Aluminoborosilicate Glasses. *J. Non. Cryst. Solids* **2001**, 292 (1–3), 167–176.
[https://doi.org/10.1016/S0022-3093\(01\)00878-X](https://doi.org/10.1016/S0022-3093(01)00878-X).
- (2) Konijnendijk, W. L.; Stevels, J. M. The Structure of Borosilicate Glasses Studied by Raman Scattering. *J. Non. Cryst. Solids* **1976**, 20 (2), 193–224. [https://doi.org/10.1016/0022-3093\(76\)90132-0](https://doi.org/10.1016/0022-3093(76)90132-0).
- (3) Kamitsos, E. I.; Chryssikos, G. D. Borate Glass Structure by Raman and Infrared Spectroscopies. *J. Mol. Struct.* **1991**, 247 (C), 1–16. [https://doi.org/10.1016/0022-2860\(91\)87058-P](https://doi.org/10.1016/0022-2860(91)87058-P).
- (4) Neuvillle, D. R.; Cormier, L.; Massiot, D. Al Coordination and Speciation in Calcium Aluminosilicate Glasses: Effects of Composition Determined by ^{27}Al MQ-MAS NMR and Raman Spectroscopy. *Chem. Geol.* **2006**, 229 (1–3), 173–185. <https://doi.org/10.1016/j.chemgeo.2006.01.019>.
- (5) Meera, B. N.; Ramakrishna, J. Raman Spectral Studies of Borate Glasses. *J. Non. Cryst. Solids* **1993**, 159 (1–2), 1–21. [https://doi.org/10.1016/0022-3093\(93\)91277-A](https://doi.org/10.1016/0022-3093(93)91277-A).
- (6) Vignarooban, K.; Boolchand, P.; Micoulaut, M.; Malki, M.; Bresser, W. J. Rigidity Transitions in Glasses Driven by Changes in Network Dimensionality and Structural Groupings. *Epl* **2014**, 108 (5).
<https://doi.org/10.1209/0295-5075/108/56001>.
- (7) Solids, J. O. F. N.; Co, N. P. The Structure of Liquid and Vitreous Boron Oxide. *J. Non. Cryst. Solids* **1969**, 1 (January), 269–284.
- (8) McMillan, P.; Piriou, B. Raman Spectroscopy of Calcium Aluminate Glasses and Crystals. *J. Non. Cryst. Solids* **1983**, 55 (2), 221–242. [https://doi.org/10.1016/0022-3093\(83\)90672-5](https://doi.org/10.1016/0022-3093(83)90672-5).
- (9) Licheron, M.; Montouillout, V.; Millot, F.; Neuvillle, D. R. Raman and ^{27}Al NMR Structure Investigations of Aluminate Glasses: $(1 - X)\text{Al}_2\text{O}_3 - x\text{MO}$, with $\text{M} = \text{Ca}, \text{Sr}, \text{Ba}$ and $0.5 < x < 0.75$). *J. Non. Cryst. Solids* **2011**, 357 (15), 2796–2801. <https://doi.org/10.1016/j.jnoncrysol.2011.03.001>.
- (10) Yano, T.; Kunimine, N.; Shibata, S.; Yamane, M. Structural Investigation of Sodium Borate Glasses and Melts by Raman Spectroscopy. I. Quantitative Evaluation of Structural Units. *J. Non. Cryst. Solids* **2003**, 321 (3), 137–146. [https://doi.org/10.1016/S0022-3093\(03\)00158-3](https://doi.org/10.1016/S0022-3093(03)00158-3).

- (11) Brow, R. K.; Tallant, D. R.; Turner, G. L. Polyhedral Arrangements in Lanthanum Aluminoborate Glasses. *J. Am. Ceram. Soc.* **2010**, *80* (5), 1239–1244. <https://doi.org/10.1111/j.1151-2916.1997.tb02970.x>.
- (12) Ollier, N.; Charpentier, T.; Boizot, B.; Wallez, G.; Ghaleb, D. A Raman and MAS NMR Study of Mixed Alkali Na-K and Na-Li Aluminoborosilicate Glasses. *J. Non. Cryst. Solids* **2004**, *341* (1–3), 26–34. <https://doi.org/10.1016/j.jnoncrysol.2004.05.010>.

Paper II

Indentation cracking and deformation mechanism of sodium aluminoborosilicate glasses

Kacper Januchta  | Pengfei Liu  | Søren R. Hansen | Theany To | Morten M. Smedskjaer 

Department of Chemistry and Bioscience,
Aalborg University, Aalborg, Denmark

Correspondence

Morten M. Smedskjaer, Department
of Chemistry and Bioscience, Aalborg
University, Aalborg, Denmark.
Email: mos@bio.aau.dk

Funding information

Villum Fonden, Grant/Award Number:
13253

Abstract

Developing less brittle oxide glasses is a grand challenge in the field of glass science and technology, as it would pave the way toward new glass applications and limit the overall raw material usage and energy consumption. However, in order to achieve this goal, more insight into the correlation between the chemical composition and material properties is required. In this work, we focus on the mechanical properties of quaternary sodium aluminoborosilicate glasses, wherein systematic changes in glass chemistry yield different resistances to indentation crack initiation. We discuss the origin of the composition dependence of indentation cracking based on an evaluation of the deformation mechanism taking place during the indentation event. To this end, we use a simple metric, the extent of indent side length recovery upon annealing, to quantify the extent of reversible volume deformation. Finally, we also compare the compositional trend in crack initiation resistance to that in crack growth resistance (fracture toughness), showing no simple correlation among the two.

KEYWORDS

cracks/cracking, fracture mechanics/toughness, glass, indentation

1 | INTRODUCTION

In daily life, glasses, commonly used for windows, bottles, or electronic displays, are arguably most well known for their transparency and brittle fracture behavior. These products are all based on silicate-based compositions, since these have historically offered the best compromise between raw material and manufacturing costs, and material properties such as transparency, chemical durability, and mechanical performance. With the growing demand for improved glass products as well as new specialized niche applications, the chemical composition of the utilized glass needs to be optimized based on the application. Therefore, it is essential to understand how the addition of various oxides in different proportions to silicate glasses will affect the properties of interest. In this regard, addressing the high

brittleness and low fracture toughness of silicate glasses is essential.^{1–5}

This tendency for brittle fracture experienced by oxide glasses is essentially a result of two phenomena. First, the inevitable formation of surface cracks throughout the lifetime of a glass product. These occur when the glass interacts with foreign bodies, for example, a stone hitting the windshield of a moving car. Such contact, especially with a sharp object, results in a complex deformation mechanism, potentially leading to formation of micro-cracks,^{6,7} the extent of which depends on factors such as the exerted force and sharpness of the object.⁴ Second, when glass bodies or products encompassing glasses are subjected to macroscopic deformation, for example bending, tensile stresses may be induced across the glass surface. These stresses intensify around defects such as micro-cracks, causing them to grow.⁸ At a sufficiently high

magnitude of stress, spontaneous crack growth will occur, resulting in a catastrophic fracture.

As a result of this drawback, it is of both scientific and engineering interest to develop new glass compositions, which are (a) less-prone to form micro-cracks upon sharp contact loading, and (b) more resistant to growth of pre-existing cracks under tension. In other words, a glass composition with both high crack resistance (CR)—a metric originally suggested by Wada *et al.*⁹—and high fracture toughness (K_{Ic}). In a recent work,¹⁰ we investigated the composition dependence of the latter in a series of sodium aluminoborosilicate model glasses. Specifically, 20 glasses in the system $25Na_2O-xAl_2O_3-yB_2O_3-(75-x-y)SiO_2$ with $x = 0$ to 30 mol% and $y = 0$ to 75 mol%. We demonstrated how knowledge of the chemical composition and network topology can be used to predict the major trends in hardness, elastic moduli, and fracture toughness. In the present work, we study the same series of glasses to understand how glass composition controls CR , that is, the propensity to form cracks during instrumented sharp contact loading.

Furthermore, we also study the characteristics of the indentation deformation, as it is known to be strongly linked to the crack initiation resistance.^{11–14} As such, the distribution of the deformation volume into different types of plastic displacement (densification and shear flow) has been proposed to control the magnitude of stress stored in the glass upon unloading,¹¹ but also the cracking pattern.¹³ In 2005, an approach to quantitatively characterize the deformation mechanism was proposed.¹⁵ However, it requires indent volume measurements, which can be time consuming if analyzed by, for example, atomic force microscopy (AFM). As a result, the amount of such data continues to be too limited to develop a quantitative model that would predict CR based on the chemical composition.⁴ In this study, we investigate a more straightforward technique relying on the same principles as the original methodology¹⁵ to investigate the indentation deformation mechanism.

2 | EXPERIMENTAL PROCEDURE

2.1 | Sample preparation

We consider 20 glasses in the system $25Na_2O-xAl_2O_3-yB_2O_3-(75-x-y)SiO_2$ with $x = 0$ to 30 mol% and $y = 0$ to 75 mol%. The glasses' nominal compositions, and their measured properties, are given in Table 1. Using the melt-quenching technique, all glasses were synthesized from powdered precursor chemicals in a conventional electric furnace using PtRh crucibles. The melting and annealing temperatures were chosen according to the chemical composition. The details of this synthesis procedure have been reported elsewhere.¹⁰ Specimens of each annealed glass were cut into appropriate dimensions ($20 \times 20 \times 5 \text{ mm}^3$), and then ground

and polished using SiC adhesive discs in ethanol to avoid surface hydration.

2.2 | Indentation deformation mechanism

The indentation deformation mechanism was studied by subjecting the glasses to a series of Vickers indentations (4 N peak load, 15 seconds hold time) utilizing an instrumented indentation apparatus (CB500, Nanovea). The images of all indents were recorded by means of the built-in microscope. The specimen was then inserted into a preheated annealing furnace (at a temperature equal to 90% of its glass transition temperature T_g in K), and kept there for 2 hours, according to the methodology suggested by Yoshida *et al.*¹⁵ The specimen was retracted from the hot furnace, cooled in air, and transferred to the indenter stage. The same indents were localized and images recorded. The dimensions of the indents before and after annealing were evaluated to compute the annealing-induced recovery of the diagonal length (L_{DR}) and the side length (L_{SR}), as illustrated in Figure 1.

In addition to the 20 sodium aluminoborosilicate glasses, L_{SR} and L_{DR} were also evaluated for a variety of other oxide glasses, including sodium aluminoborates,¹⁶ lithium aluminoborates,¹⁷ potassium, magnesium, and lanthanum aluminoborates,^{18–20} mixed alkali magnesium aluminoborosilicates,²¹ lanthanum aluminogermanate,²⁰ a modifier-free boroaluminophosphosilicate,²² soda lime silica,¹⁵ and amorphous silica.¹⁵ This was done to investigate the correlation between L_{SR} or L_{DR} and the volume recovery ratio (V_R), which is the relative change of the indent cavity volume induced by sub- T_g annealing, corresponding to the volume fraction of the densification-displaced material. Only glasses available in our laboratory with known V_R values were included in this study.

2.3 | Indentation cracking

Each specimen of the 20 sodium aluminoborosilicate glasses was placed on the stage of the instrumented indenter and subjected to several series of at least 20 identical indentation cycles with a Vickers diamond tip, that is, with the same loading and unloading rates, hold time (15 seconds), and peak load. Each series of indentation cycles had a different peak load, with loading and unloading rates scaled accordingly to the increase in peak load, and a fixed hold time. The lower and upper limits of the applied peak load were determined individually for each glass composition, depending on its propensity for crack initiation. The extent of cracking was evaluated by means of a built-in microscope, and quantified by counting the number of corner cracks (ie, radial or half-penny cracks emanating from the four corners of a Vickers indent impression) relative to the amount of corners. The

TABLE 1 Nominal compositions (all containing 25 mol% Na₂O), length side recovery ratio (L_{SR}), diagonal recovery ratio (L_{DR}), Vickers indentation crack resistance (CR), and bulk modulus (B)

[Al ₂ O ₃] (mol%)	[B ₂ O ₃] (mol%)	[SiO ₂] (mol%)	L_{SR} (%)	L_{DR} (%)	CR (N)	B (GPa)
0	0	75	18	6	3.0	36
0	12.5	62.5	6	3	0.4	44
0	25	50	14	5	0.05	44
0	37.5	37.5	9	2	1.3	49
0	50	25	29	9	0.05	47
0	62.5	12.5	38	7	0.2	42
0	75	0	37	4	1.8	39
12.5	0	62.5	30	12	0.4	41
12.5	12.5	50	20	6	0.3	43
12.5	25	37.5	30	8	1.7	42
12.5	37.5	25	33	4	1.8	39
12.5	50	12.5	33	3	2.3	37
12.5	62.5	0	36	3	5.8	34
25	0	50	32	4	1.1	41
25	12.5	37.5	26	5	0.4	41
25	25	25	30	6	4.5	37
25	37.5	12.5	33	8	10	36
25	50	0	26	2	12	35
30	45	0	31	3	0.8	41
30	32.5	12.5	33	2	4.5	37

Note: The errors in L_{SR} , L_{DR} , and B do not exceed 7%, 5%, and 1 GPa, respectively. The estimated error for CR is 20% of its value.

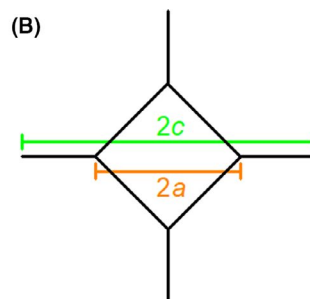
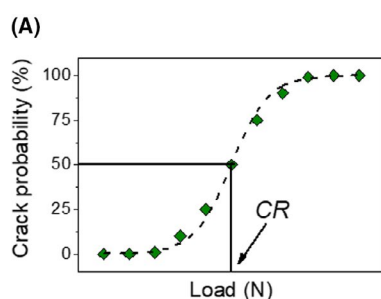
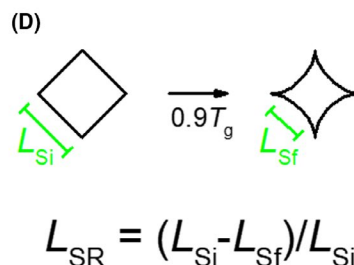
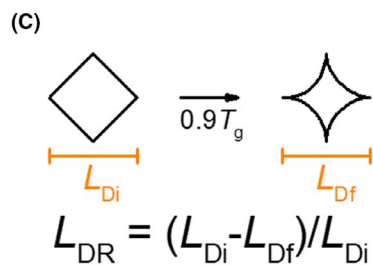


FIGURE 1 Graphical representation of the quantification of (A) crack resistance (CR), (B) half-penny crack length ($2c$) and indent diagonal ($2a$), (C) indent diagonal recovery ratio (L_{DR}), and (D) indent side length recovery ratio (L_{SR}) [Color figure can be viewed at wileyonlinelibrary.com]



load corresponding to 50% crack probability (ie, 2 out of 4 possible cracks on average) was defined as CR (see Figure 1), as suggested by Wada *et al.*⁹ The indentation was performed under ambient conditions (room temperature, ~40% relative

humidity). Cracks were recorded at least 12 hours after unloading to enable development of cracks (aging in the same atmosphere).²³ The same specimens were also subjected to an analogous experiment, where the Vickers diamond tip was

replaced by a sharper cube-corner diamond tip. The extent of cracking was evaluated using optical microscopy as well, but quantification of the resistance to cracking was complicated as most glasses already exhibited indentation corner cracking at the lowest reliable load applicable by the utilized indenter (50 mN). CR determined using the cube-corner indenter tip was also defined as the load corresponding to 50% crack probability (ie, 1.5 out of 3 possible corner cracks emanating from the triangular impression).

The cracking pattern following Vickers indentation was studied from top view, as described above. Additionally, the cracking pattern was also examined from a horizontal point of view, that is, through a cross-section, by placing a line of identical Vickers indents exhibiting corner cracking throughout the width of the specimen. The peak load was determined based on the CR of the glass. The Vickers indents were separated by a distance of $6c$, where c is the distance between the tips of two opposing corner cracks (see Figure 1). The indented specimen was then supported on two ceramic plates with a gap between them, while the line of indents was facing downward and was aligned with the gap. A steel block was then placed on top of the specimen, and gently pressed to initiate crack growth. One half of the broken specimen was then evaluated under an optical microscope.

3 | RESULTS

3.1 | Indent recovery

The shrinkage of the Vickers indents induced by a thermal treatment was quantified by determining L_{SR} (Figure 2A) and L_{DR} (Figure 2B). The former metric exhibits systematic compositional trends, with the binary sodium borate displaying the highest extent of shrinkage (ie, the highest extent of reversible deformation). The minimum in L_{SR} in the ternary diagram is situated around the Si-rich sodium borosilicate glasses. However, the other metric, L_{DR} , appears to have a substantially different compositional dependence compared to L_{SR} . Furthermore, we note that the diagonals of the indents tend to shrink much less than the side of the indents, in agreement with previous findings.^{16,24} This is also apparent from the observation that L_{SR} ranges from 6% to almost 40%, while L_{DR} only ranges from 2% to 12%. Considering that the experimental error for L_{DR} can be as high as $\pm 4\%$, we do not recommend using the diagonal shrinkage as a metric for reversible volume deformation upon indentation. On the other hand, the experimental error for L_{SR} values is $\pm 4\%$ on average ($\pm 7\%$ in the worst case), which is a much smaller relative error, thus enabling L_{SR} to be used as a metric for determining compositional trends in densification contribution to indentation deformation, as

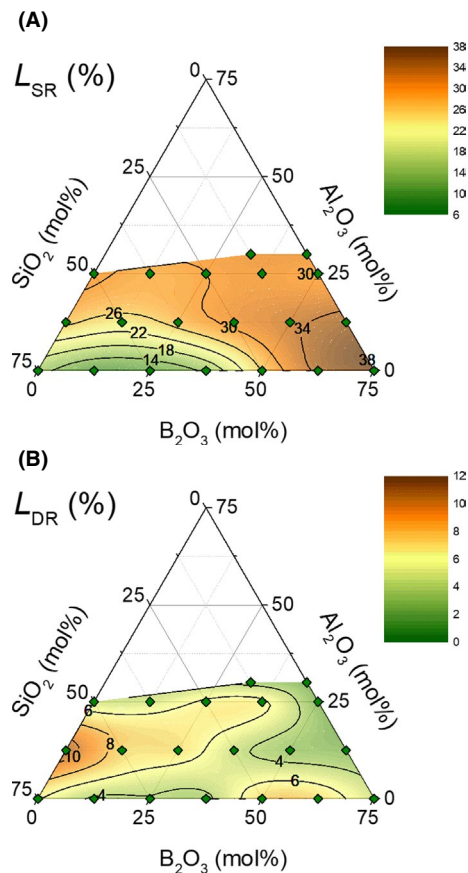


FIGURE 2 Dependence of (A) side length recovery ratio (L_{SR}) and (B) diagonal recovery ratio (L_{DR}) on composition in the sodium aluminoborosilicate glasses. The data has been acquired at 4 N load for all glasses. The contour map represents a pseudoternary slice through the quaternary composition diagram with $[Na_2O] = 25$ mol%. The isocontours are drawn as a guide for the eye, and are based on linear interpolation between the experimental data points marked by green diamonds. The estimated average errors are 2% and 4% for L_{DR} and L_{SR} , respectively [Color figure can be viewed at wileyonlinelibrary.com]

apparent from Figure 2A. We note that the compositional trend along the SiO_2 -free edge of the ternary diagram (decreasing L_{SR} with increasing Al_2O_3 content) is inconsistent with the V_R data recorded for a series of sodium aluminoborate glasses, that is, a local maximum around the meta-luminous composition.¹⁶ A possible explanation for this discrepancy is the difference in the applied load, as V_R has recently been shown to be load-dependent.^{25,26} That is, the trend may change with increasing load (0.25 N in previous work,¹⁶ 4 N in this work), or alternatively, it is due to the difference in the deformation mechanism evaluation method (AFM vs. optical).

In addition to the 20 sodium aluminoborosilicate glasses, we have also evaluated L_{SR} and L_{DR} for a series of other oxide glasses with known V_R values from previous studies.^{15–22} In general, the L_{SR} values are within a range of 21 to 36%, while L_{DR} values are within a range of 2 to 14%. The results along

Glass composition	L_{SR} (%)	L_{DR} (%)	V_R (%)	Ref.
Sodium aluminoborates	36	5	76	16
	33	5	73	
	31	5	80	
	32	3	80	
	29	3	83	
	27	3	75	
Lithium aluminoborates	32	13	68	17
	33	7	74	
	32	14	68	
	19	2	58	
Potassium aluminoborate	34	9	83	18
Magnesium aluminoborate	21	2	50	19
Lanthanum aluminoborate	19	2	39	20
Lanthanum aluminogermanate	14	2	22	20
Alkali-magnesium aluminoborosilicates	34	6	78	21
	35	7	86	
	34	6	83	
	35	6	76	
	34	9	79	
Boroaluminophosphosilicate	31	13	75	22
Soda lime silica	25	8	52	15
Amorphous silica	36	13	84	15

Note: The errors in L_{SR} , L_{DR} , and V_R do not exceed 7%, 4%, and 8%, respectively.

with the investigated glass compositions and their V_R values are given in Table 2.

3.2 | Indentation cracking

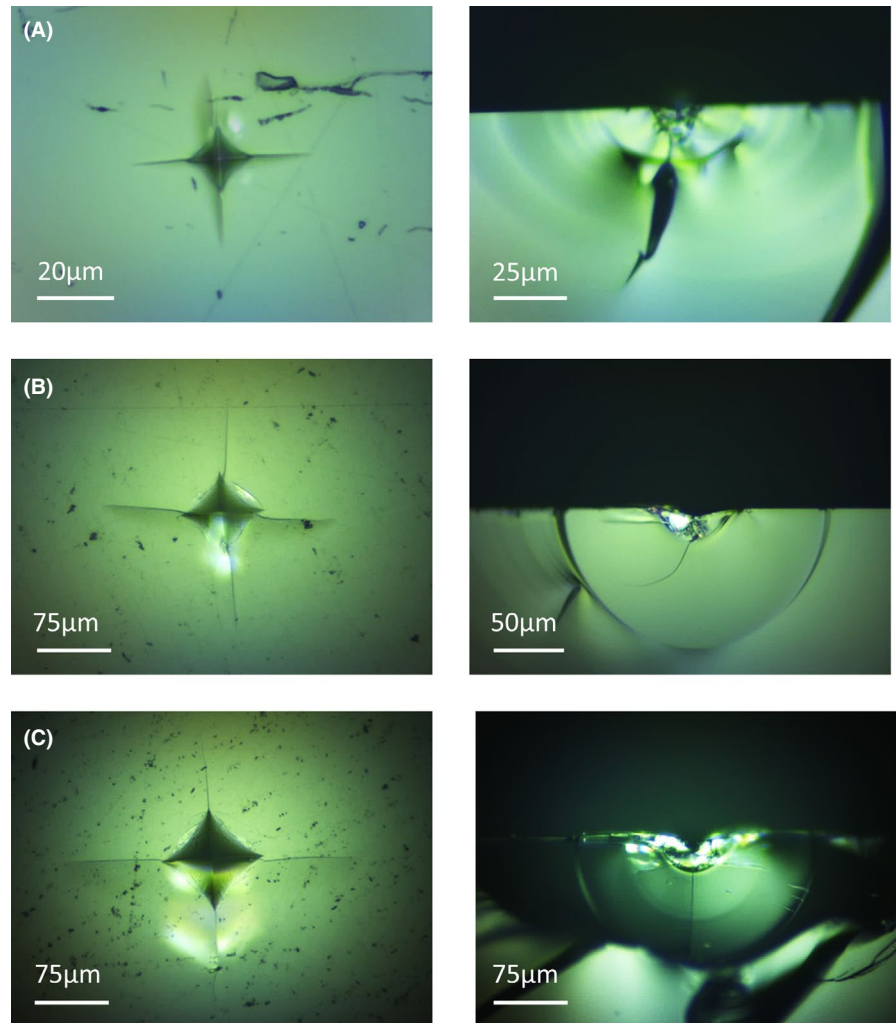
All investigated glasses develop corner cracks upon Vickers indentation, if a sufficiently high peak load is applied (Figure 3, left panel). Moreover, all the glasses exhibit median cracks, which is evident from the cross-section views of the indent sites (Figure 3, right panel). This suggests that the corner cracks observed in the top view are half-penny cracks originating from the median crack during the unloading process. Such mechanism is consistent with normal glasses.^{6,27} We also note that none of the glasses exhibit purely radial (or Palmqvist) cracks, which is somewhat surprising considering the high Poisson's ratio of many of the investigated glasses.¹⁰ Glasses with high Poisson's ratio are expected to have a relatively large driving force for radial crack initiation based on theoretical calculations of the indentation-induced stress field.^{13,28} Furthermore, in previous work we have observed the existence of radial cracks in a sodium aluminoborate glass with similar composition to the ones investigated herein.¹⁸ This difference could arise

TABLE 2 Glass composition, length side recovery ratio (L_{SR}), diagonal recovery ratio (L_{DR}), volume recovery ratio (V_R), and paper reference

from the use of different indentation apparatuses (eg, different loading scheme), difference in the extent of wear on the Vickers tip, or difference in the surface quality upon polishing.

The resistance to indentation cracking varies significantly across the investigated glasses. The lowest and highest values of CR are determined to be 0.1 and 12.5 N, respectively, corresponding to a two orders of magnitude difference. All CR data have been compiled into a ternary diagram (where Na_2O content is fixed), reflecting the compositional trends (Figure 4). More crack-resistant glasses are mainly found in the aluminoborate-rich region, where three-coordinated boron dominates the network structure.¹⁶ Another local maximum in CR is found for the binary sodium silicate glass, which is rich in non-bridging oxygens (NBOs). Lower CR values are found for borosilicate and aluminosilicate glasses, which tend to have highly cross-linked rigid networks. In general, we note some discrepancies between the absolute CR values determined in this study and those in previous work on similar glasses.^{16,29} For instance, the SiO_2 -free aluminoborate glasses,¹⁶ and the B_2O_3 -free aluminosilicate glasses²⁹ have been reported to have higher CR values compared to this work. There are several possible explanations for this: (a) the synthesized glass specimens

FIGURE 3 Representative images of top-view (left panel) and cross-section view (right panel) of Vickers indents produced in three different glass compositions: (A) $25\text{Na}_2\text{O}-25\text{B}_2\text{O}_3-50\text{SiO}_2$, (B) $25\text{Na}_2\text{O}-12.5\text{Al}_2\text{O}_3-37.5\text{B}_2\text{O}_3-25\text{SiO}_2$, and (C) $25\text{Na}_2\text{O}-30\text{Al}_2\text{O}_3-45\text{B}_2\text{O}_3$. The indents were produced at loads of 1, 10, and 20 N, respectively [Color figure can be viewed at wileyonlinelibrary.com]



originate from different laboratories and even slight composition differences can influence *CR* significantly;⁴ (b) indentation cracking was evaluated on two different apparatuses with differences in loading rate that is also known to affect *CR*;³⁰ (c) crack formation was evaluated either immediately or after a ~12 hours sit-in time, respectively, which has also been shown to affect *CR* significantly;²³ and (d) the relative humidity, which is known to influence crack initiation, was different during the experiments.²³ This thus corroborates previous findings that *CR* of different oxide glasses should be compared under identical testing conditions, complicating the development of a composition-dependent *CR* model based on literature data.⁴

The resistance to cube-corner indentation cracking proved challenging to evaluate since the majority of the glasses exhibit extensive cracking even at very low loads (<50 mN). This is consistent with literature results, reporting that the resistance to indentation cracking strongly depends on the sharpness of the indenter tip,^{24,31} with smaller compositional differences as the indenter tip gets sharper.³² An example of a crack probability vs. load curve for a crack-resistant glass, namely the metaluminous sodium aluminoborate

($25\text{Na}_2\text{O}-25\text{Al}_2\text{O}_3-50\text{B}_2\text{O}_3$), is included in Figure 5, showing the large difference in crack resistance between cube corner and Vickers indentation. *CR* evaluated using the Vickers geometry tip is ~12.5 N, while the resistance to cube corner indentation cracking is merely ~150 mN. Other glasses crack even more easily when subjected to cube corner indentation. As such, it is clear that high *CR* for a Vickers tip does not necessarily translate into high *CR* for a sharper tip (eg, cube corner). Unfortunately, due to a poor reliability of the present indenter at loads below 50 mN, the resistance to indentation cracking cannot be accurately quantified throughout the entire series of glasses.

4 | DISCUSSION

4.1 | Side length shrinkage as a measure of indentation deformation mechanism

In various studies,^{11,13-15,33} the indentation deformation mechanism has been studied following the methodology suggested by Yoshida *et al.*,¹⁵ which consists of indentation,

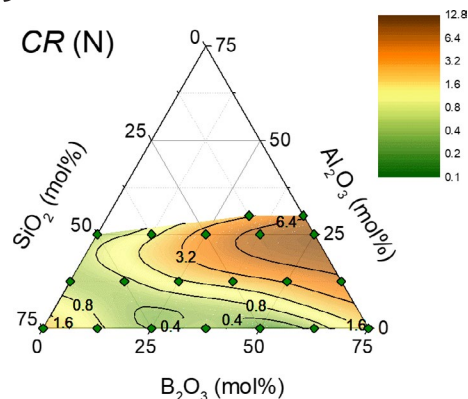


FIGURE 4 Dependence of crack resistance (CR) on composition in the sodium aluminoborosilicate glasses. The contour map represents a pseudoternary slice through the quaternary composition diagram with $[Na_2O] = 25$ mol%. The isocontours are drawn as a guide for the eye, and are based on linear interpolation between the experimental data points marked by green diamonds. The estimated error is 20% of the CR value [Color figure can be viewed at wileyonlinelibrary.com]

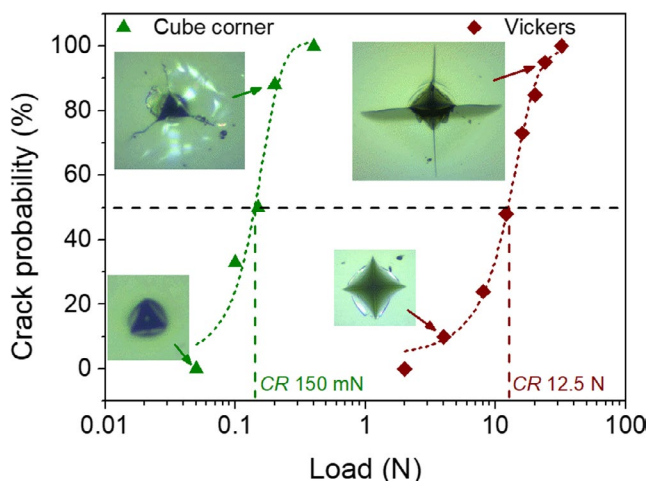


FIGURE 5 Crack probability as a function of applied load for the $25Na_2O-25Al_2O_3-50B_2O_3$ glass using both Vickers and cube-corner indenter geometry. The green and red dashed lines are intended as guides for the eye. The horizontal black dashed line represents 50% crack probability, used to define crack resistance (CR) for both cube corner and Vickers indenter geometries. The indent images are not to scale [Color figure can be viewed at wileyonlinelibrary.com]

evaluation of the indent cavity volume (typically determined using AFM), sub- T_g annealing, and finally re-evaluation of the indent cavity volume. In this work, we have used a very similar methodology, where we have substituted the tedious and time-consuming AFM-evaluation with a quick and straightforward evaluation of the top view of an indent using an optical microscope. As a result of this difference, we have found that relatively large indents (here 4 N load compared to 0.25 N in the original procedure¹⁵) are needed to obtain a sufficient resolution of the optical image. Because

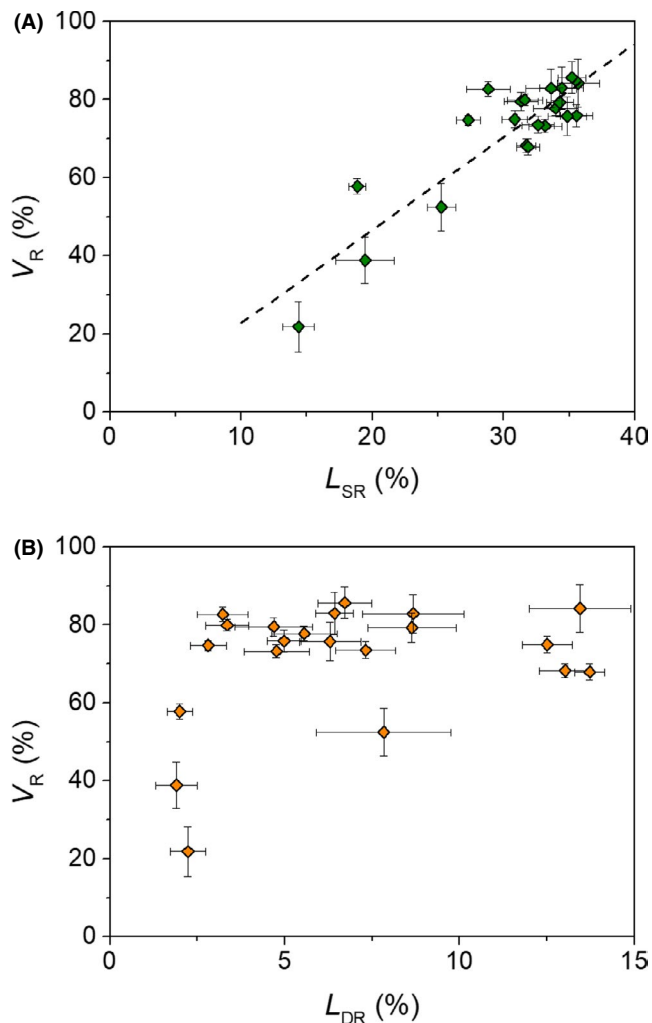


FIGURE 6 Volume recovery ratio (V_R) as a function of (A) side length recovery ratio (L_{SR}) and (B) diagonal recovery ratio (L_{DR}). The V_R data are collected from previous studies^{15,16,18-22}. In (A), the dashed line is a guide for the eye [Color figure can be viewed at wileyonlinelibrary.com]

of this higher peak load, indentation cracking will be present in many oxide glasses at 4 N, which might interfere with the recovery mechanism. In addition, the difference in load may also affect the volumetric ratio of densified over total displaced material.²⁵

To further evaluate the possibility to use L_{SR} as a surrogate for V_R computed from AFM measurements, we have determined L_{SR} and L_{DR} for a series of oxide glasses with known V_R values reported in previous work.¹⁵⁻²² Figure 6A shows an apparent positive correlation between L_{SR} and V_R for the relatively wide range of glass chemistries and V_R values from 20% to 90%, although we note that the majority of the data is for V_R in the range of 70 to 90%. On the other hand, there appears to be no correlation between V_R and L_{DR} (Figure 6B), as anticipated based on the higher relative error associated with the limited diagonal shrinkage in Vickers indents. In conclusion, L_{SR} seems to be a satisfactory surrogate for V_R ,

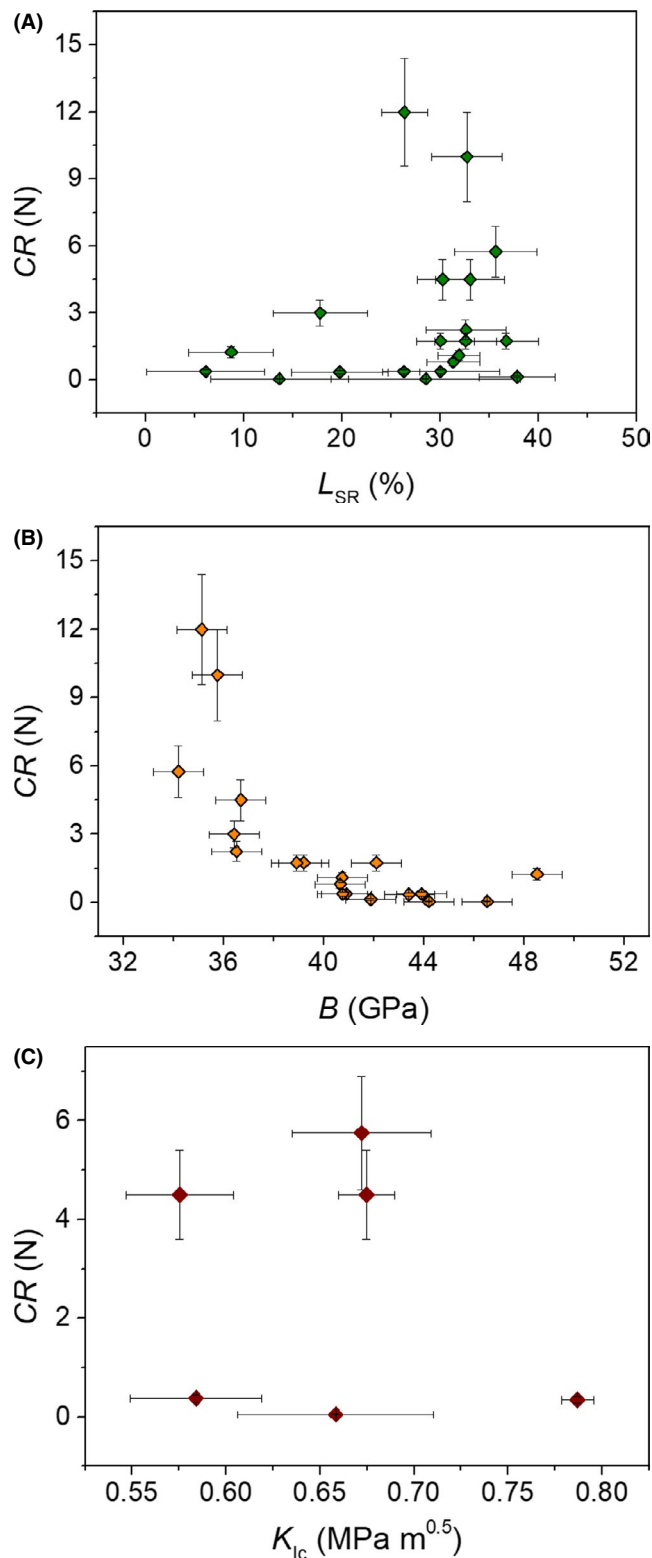


FIGURE 7 Crack resistance (CR) as a function of (A) side length recovery (L_{SR}), (B) bulk modulus (B), and (C) fracture toughness (K_{Ic}) for the investigated sodium aluminoborosilicate glasses [Color figure can be viewed at wileyonlinelibrary.com]

enabling the use of L_{SR} data for the sodium aluminoborosilicate glasses to shed light on the origin of the compositional variation in CR .

4.2 | Origin of variation in crack resistance

The deformation under sharp contact loading in oxide glasses consists of several contributions: (a) elastic, (b) plastic densification, and (c) shear flow.^{4,15,34} The relative contribution of these mechanisms, particularly the two latter, has been linked with the propensity for cracking,^{4,11,13} since densification is not resulting in expansion of the plastic zone surrounding the indent site,¹¹ which in turn allows for a larger recovery of the elastically deformed material around the plastic zone. However, as discussed in Section 3.2, the magnitude of CR for different glass compositions can be difficult to compare due to differences in testing conditions etc Hence, it is desirable to assess a large amount of glasses within a single study, as done herein. Based on the positive correlation between V_R and L_{SR} (Figure 6A), we use L_{SR} as a measure of the extent of densification upon indentation. However, for the 20 oxide glasses investigated in this study, there appears to be no or possibly only a very weak correlation between CR and L_{SR} (Figure 7A), although we note that there appears to be no data points in the upper left corner of the diagram. In other words, in order to achieve a high CR , a glass needs to exhibit a certain critical value of L_{SR} . When L_{SR} is relatively high (>20%), the variation in CR values increases, suggesting that other factors may also influence the resistance to indentation cracking. For example, recent work has shown that the density of shear bands in calcium aluminoborosilicate glasses with similar extent of densification affects the value of CR .³⁵

Next, we consider another property, which could be linked to the resistance to indentation cracking, namely the bulk modulus (B). The above explanation focuses on energy dissipation through densification, a type of plastic deformation. The bulk modulus, however, is an elastic property, but it should be kept in mind that indentation consists of both plastic and elastic deformations. The material in close vicinity to the point of contact is undergoing permanent changes during indentation, as the threshold for plastic yielding is exceeded at a certain critical stress value. The combination of compressive and shear stresses present during sharp contact loading allows the glassy network to reorganize, becoming locked in the reorganized structure.³⁶ This results in a hemispherical area of densified material surrounding the indentation cavity, called a plastic zone, which can be seen in the cross-sections of the indent sites (Figure 3). The part of the material outside the plastic zone has undergone elastic deformation during loading, meaning that the material is in a compressed state as long as the load is maintained. Upon unloading, the material should recover to its original state, but because of the locked structure in the plastic zone, the expansion of the elastically compressed material is inhibited, resulting in residual stresses throughout the entire elastic field.^{2,28} The highest magnitude of residual stress is expected to be just on the border to the plastic zone, where median cracking often initiates, and results in the development of a half-penny crack

system.⁶ The extent of elastic deformation is linked to B and could therefore be considered when evaluating the origin of variations in CR . As such, glasses with low B , being more flexible, will tend to have a more far-reaching elastic field, resulting in a lower magnitude of residual stresses in close vicinity to the plastic zone. On the other hand, more rigid glasses, that is, with high B , will tend to concentrate those residual stresses within a closer range from the plastic zone. This should lead to a negative correlation between B and CR , which is indeed observed for the 20 glasses studied herein (Figure 7B). We chose to study the correlation with B rather than Young's modulus (E) or shear modulus (G), because B describes the material's resistance to elastic isostatic compression being the most accurate description of what the material experiences during indentation. We note that a similar correlation could be achieved with E or G , as all three moduli scale well with each other within this system.¹⁰

4.3 | Links to fracture toughness

As described in the Introduction, both CR and K_{IC} are important material properties for evaluating the mechanical performance of brittle glasses. Discussions regarding the similarity of the two properties and a positive scaling between them can be found in the literature,^{11,37} although the positive correlations are usually limited to narrow compositional ranges. However, it is important to distinguish between CR and K_{IC} , although they are both related to cracking. The fundamental difference is that CR relates to the *initiation of cracks* upon an external impulse, while K_{IC} is linked to *crack growth* of pre-existing scratches, micro-cracks, or other defects. This is an important point, since not only is the definition and involved physical phenomena different, but they may also scale differently with glass composition and structure. Indeed, the CR data from this study and the K_{IC} data from our previous work using the single-edge pre-cracked beam technique¹⁰ show no apparent correlation (Figure 7C).

In fact, the lack of correlation between CR and K_{IC} is not surprising. As discussed in the previous section, CR appears to be inversely correlated with B , given that more flexible glasses will tend to distribute the residual stresses throughout a larger elastic field compared to the more rigid glasses. On the other hand, K_{IC} is expected to be positively correlated with the elastic modulus, which is essentially a measure of the energy stored in the chemical bonds of the material³⁸—bonds which a crack front needs to break in order to propagate through the material.³⁹ The lack of a universal one-to-one correlation between K_{IC} and B (not shown) is a result of other factors, for example, the type and number of bonds that need to be broken to facilitate crack growth. As discussed in our previous work,¹⁰ glasses with flexible structures such as the ones rich in trigonal boron may have the possibility to accelerate crack growth if certain structural domains may be circumvented by the propagating crack front, resulting in a low

K_{IC} value. The flexibility of the glassy network can on the other hand be beneficial for avoiding initiation of cracking during impact.¹⁷ As such, CR and K_{IC} are different properties, they exhibit no correlation within the investigated glass system, and they are expected to have opposite dependence on B . Unfortunately this complicates the design of new damage-resistant and damage-tolerant glasses, since there may be a trade-off between improving CR by including a certain structural feature into the glassy network, which could have a negative effect on K_{IC} .

5 | CONCLUSIONS

We have investigated 20 different sodium aluminoborosilicate glasses at fixed soda content. Vickers and cube corner indentation were used to study the cracking and deformation characteristics of the glasses. All glasses exhibit half-penny corner cracking when indented with a Vickers geometry tip, with large variations in the loads needed to initiate cracking. Cube corner indentation results in severe cracking even at the lowest applied load (50 mN) for the majority of the glasses. The metaluminous sodium aluminoborate glass with mostly trigonal boron exhibits the highest resistance to indentation cracking. This is ascribed to its relatively high extent of densification, quantified through the thermally induced shrinkage of the indent size, and to its low bulk modulus. The rigid sodium borosilicate glasses, which are rich in tetrahedral boron, display the lowest crack resistance as well as the lowest proneness to densify during indentation. In general, there is a weak positive correlation between the extent of densification and Vickers crack resistance, and a strong negative correlation between crack resistance and bulk modulus. However, crack initiation resistance and fracture toughness do not correlate within the studied glass family, in agreement with the fact that they refer to different physical phenomena.


ACKNOWLEDGMENT

This work was supported by VILLUM FONDEN under research grant no. 13253.

ORCID

Kacper Januchta  <https://orcid.org/0000-0002-5204-0755>

Pengfei Liu  <https://orcid.org/0000-0003-2885-4721>

Morten M. Smedskjaer  <https://orcid.org/0000-0003-0476-2021>

[org/0000-0003-0476-2021](https://orcid.org/0000-0003-0476-2021)

REFERENCES




1. Wondraczek L, Mauro JC, Eckert J, Kühn U, Horbach J, Deubener J, et al. Towards ultrastrong glasses. *Adv Mater*. 2011;23(39):4578–86.
2. Rouxel T. Driving force for indentation cracking in glass: composition, pressure and temperature dependence. *Philos Trans A Math Phys Eng Sci*. 2015;373(2038). <https://doi.org/10.1098/rsta.2014.0140>

3. Varshneya AK. Stronger glass products: lessons learned and yet to be learned. *Int J Appl Glas Sci.* 2018;9(2):140–55.
4. Januchta K, Smedskjaer MM. Indentation deformation in oxide glasses: quantification, structural changes, and relation to cracking. *J Non-Crystalline Solids X.* 2019;1:100007.
5. Yoshida S. Indentation deformation and cracking in oxide glass – toward understanding of crack nucleation. *J Non-Crystalline Solids X.* 2019;1:100009.
6. Arora A, Marshall DB, Lawn BR, Swain MV. Indentation deformation/fracture of normal and anomalous glasses. *J Non Cryst Solids.* 1979;31(3):415–28.
7. Lawn BR, Swain MV. Microfracture beneath point indentations in brittle solids. *J Mater Sci.* 1975;10(1):113–22.
8. Griffith AA. The phenomena of rupture and flow in solids. *Philos Trans R Soc London Ser A.* 1921;221:163–98.
9. Wada M, Furukawa H, Fujita K. Crack resistance of glass on vickers indentation. In: Kunigi M, Tashiro M, Saga N, editors. *Proceedings of the 10th International Congress on Glass.* Kyoto: Ceramic Society of Japan, 1974;39.
10. Januchta K, To T, Bødker MS, Rouxel T, Smedskjaer MM. Elasticity, hardness, and fracture toughness of sodium aluminoborosilicate glasses. *J Am Ceram Soc.* 2019;102(8):4520–37.
11. Kato Y, Yamazaki H, Yoshida S, Matsuoka J. Effect of densification on crack initiation under vickers indentation test. *J Non Cryst Solids.* 2010;356:1768–73.
12. Hermansen C, Matsuoka J, Yoshida S, Yamazaki H, Kato Y, Yue YZ. Densification and plastic deformation under microindentation in silicate glasses and the relation to hardness and crack resistance. *J Non Cryst Solids.* 2013;364:40–3.
13. Sellappan P, Rouxel T, Celarie F, Becker E, Houizot P, Conradt R. Composition dependence of indentation deformation and indentation cracking in glass. *Acta Mater.* 2013;61(16):5949–65.
14. Limbach R, Winterstein-Beckmann A, Dellith J, Möncke D, Wondraczek L. Plasticity, crack initiation and defect resistance in alkali-borosilicate glasses: from normal to anomalous behavior. *J Non Cryst Solids.* 2015;417–418:15–27.
15. Yoshida S, Sangleboeuf J-C, Rouxel T. Quantitative evaluation of indentation-induced densification in glass. *J Mater Res.* 2005;20(12):3404–12.
16. Januchta K, Youngman RE, Goel A, Bauchy M, Rzoska SJ, Bockowski M, et al. Structural origin of high crack resistance in sodium aluminoborate glasses. *J Non Cryst Solids.* 2017;460:54–65.
17. Januchta K, Youngman RE, Goel A, Bauchy M, Logunov SL, Rzoska SJ, et al. Discovery of ultra-crack-resistant oxide glasses with adaptive networks. *Chem Mater.* 2017;29(14):5865–76.
18. Januchta K, Bauchy M, Youngman RE, Rzoska SJ, Bockowski M, Smedskjaer MM. Modifier field strength effects on densification behavior and mechanical properties of alkali aluminoborate glasses. *Phys Rev Mater.* 2017;1(6):63603.
19. Frederiksen KF, Januchta K, Mascaraque N, Youngman RE, Bauchy M, Rzoska SJ, et al. Structural compromise between high hardness and crack resistance in aluminoborate glasses. *J Phys Chem B.* 2018;122:6287–95.
20. Januchta K, Sun R, Huang L, Bockowski M, Rzoska SJ, Jensen LR, et al. Deformation and cracking behavior of La_2O_3 -doped oxide glasses with high poisson's ratio. *J Non Cryst Solids.* 2018;494:86–93.
21. Aakermann KG, Januchta K, Pedersen JAL, Svenson MN, Rzoska SJ, Bockowski M, et al. Indentation deformation mechanism of isotropically compressed mixed alkali aluminosilicate glasses. *J Non Cryst Solids.* 2015;426:175–83.
22. Kapoor S, Januchta K, Youngman RE, Guo X, Mauro JC, Bauchy M, et al. Combining high hardness and crack resistance in mixed network glasses through high-temperature densification. *Phys Rev Mater.* 2018;2(6):63603.
23. Bechgaard TK, Mauro JC, Smedskjaer MM. Time and humidity dependence of indentation cracking in aluminosilicate glasses. *J Non Cryst Solids.* 2018;491:64–70.
24. Yoshida S, Wada K, Fujimura T, Yamada A, Kato M, Matsuoka J, et al. Evaluation of sinking-in and cracking behavior of soda-lime glass under varying angle of trigonal pyramid indenter. *Front Mater.* 2016;3:54.
25. Kazembeyki M, Bauchy M, Hoover CG. New insights into the indentation size effect in silicate glasses. *J Non Cryst Solids.* 2019;521:119494.
26. Kato Y, Yamazaki H, Itakura S, Yoshida S, Matsuoka J. Load dependence of densification in glass during vickers indentation test. *J Ceram Soc Japan.* 2011;119(1386):110–5.
27. Hagan JT. Shear deformation under pyramidal indentations in soda-lime glass. *J Mater Sci.* 1980;15(6):1417–24.
28. Yoffé EH. Elastic stress fields caused by indenting brittle materials. *Philos Mag A.* 1982;46(4):617–28.
29. Bechgaard TK, Goel A, Youngman RE, Mauro JC, Rzoska SJ, Bockowski M, et al. Structure and mechanical properties of compressed sodium aluminosilicate glasses: role of non-bridging oxygens. *J Non Cryst Solids.* 2016;441:49–57.
30. Gross TM, Price JJ. Vickers indentation cracking of ion-exchanged glasses: quasi-static vs. dynamic contact. *Front Mater.* 2017;4:4.
31. Gross TM. Deformation and cracking behavior of glasses indented with diamond tips of various sharpness. *J Non Cryst Solids.* 2012;358(24):3445–52.
32. Gross TM, Youngman R. Low modulus, damage resistant glass for ultra-thin applications. In: *Flexible glass: enabling thin, lightweight, and flexible electronics.* Garner SM, editor. Hoboken: Wiley; 2017: p. 359.
33. Barlet M, Delaye J-M, Charpentier T, Gennisson M, Bonamy D, Rouxel T, et al. Hardness and toughness of sodium borosilicate glasses via vickers's indentations. *J Non Cryst Solids.* 2015;417–418:1–15.
34. Peter KW. Densification and flow phenomena of glass in indentation experiments. *J Non Cryst Solids.* 1970;5(2):103–15.
35. Gross TM, Wu J, Baker DE, Price JJ, Yongsunthon R. Crack-resistant glass with high shear band density. *J Non Cryst Solids.* 2018;494:13–20.
36. Neely JE, Mackenzie JD. Hardness and low-temperature deformation of silica glass. *J Mater Sci.* 1968;3(6):603–9.
37. Sehgal J, Ito S. Brittleness of glass. *J Non Cryst Solids.* 1999;253(1–3):126–32.
38. Makishima A, Mackenzie JD. Direct calculation of young's modulus of glass. *J Non Cryst Solids.* 1973;12(1):35–45.
39. Rouxel T. Fracture surface energy and toughness of inorganic glasses. *Scr Mater.* 2017;137:109–13.

How to cite this article: Januchta K, Liu P, Hansen SR, To T, Smedskjaer MM. Indentation cracking and deformation mechanism of sodium aluminoborosilicate glasses. *J Am Ceram Soc.* 2020;103:1656–1665. <https://doi.org/10.1111/jace.16894>

Paper III

Structural densification of lithium phosphoaluminoborate glasses

Pengfei Liu¹  | Andreas L. S. Søndergaard¹ | Randall E. Youngman²  |
Sylwester J. Rzoska³ | Michal Bockowski³ | Lars R. Jensen⁴ | Morten M. Smedskjaer¹ 

¹Department of Chemistry and Bioscience, Aalborg University, Aalborg, Denmark

²Science and Technology Division, Corning Incorporated, Corning, NY, USA

³Institute of High-Pressure Physics, Polish Academy of Sciences, Warsaw, Poland

⁴Department of Materials and Production, Aalborg University, Aalborg, Denmark

Correspondence

Morten M. Smedskjaer, Department of Chemistry and Bioscience, Aalborg University, Aalborg, Denmark.

Email: mos@bio.aau.dk

Funding information

China Scholarship Council, Grant/Award Number: 201806370210

Abstract

Lithium aluminoborate glasses have recently been found to undergo dramatic changes in their short-range structures upon compression at moderate pressure (~1 GPa), most notably manifested in an increase in network forming cation coordination number (CN). This has important consequences for their mechanical behavior, and to further understand the structural densification mechanisms of this glass family, we here study the effect of P₂O₅ incorporation in a lithium aluminoborate glass (with fixed Li/Al/B ratio) on the pressure-induced changes in structure, density, and hardness. We find that P₂O₅ addition results in a more open and soft network, with P-O-Al and P-O-B bonding, a slightly smaller fraction of tetrahedral-to-trigonal boron, and an unchanged aluminum speciation. Upon compression, the cation-oxygen CNs of both boron and aluminum increase systemically, whereas the number of bridging oxygens around phosphorous (Q^n) decreases. The glasses with higher P₂O₅ content feature a larger decrease in Q^n (P) upon compression, which leads to more non-bridging oxygen that in turn fuel the larger increase in CN of B and Al for higher P₂O₅ content. We find that the CN changes of Al and B can account for a large fraction (around 50% at 2 GPa) of the total volume densification and that the extent of structural changes (so-called atomic self-adaptivity) scales well with the extent of volume densification and pressure-induced increase in hardness.

KEYWORDS

borates, glass, hardness, nuclear magnetic resonance, structure

1 | INTRODUCTION

Oxide glasses play a critical role for innovation in a range of industries due to their combination of favorable properties such as transparency, high hardness, relatively light weight, and chemical durability.¹ Although the ultimate strength and ductility of defect-free amorphous oxides can be high,^{2,3} bulk oxide glasses generally possess low fracture toughness (around 0.5 to 1.0 MPa m^{0.5}) because of the lack of a stable shearing deformation mechanism and limited resistance to crack growth.⁴⁻⁶ In the past few decades, scientists have made great efforts to improve the mechanical reliability and resistance to surface damage of glasses through effective surface

treatments, among which thermal tempering⁷ and chemical strengthening^{8,9} are the most widespread, with the aim to improve the strength and increase the critical stress needed for crack initiation. In addition to adding extra cost, these methods are also limited to either relatively thick glasses (thermal tempering) or mobile ion-containing glasses (chemical strengthening).

A key consideration when designing new damage-resistant glasses is their densification mechanism under high pressure.¹⁰ Moreover, compression treatments could potentially provide an additional degree of freedom to balance different properties in the composition-temperature-pressure plane. The change in glass properties under an applied pressure is related to the

extent of volume densification and corresponding structural changes at both short- and intermediate-range length scales.¹¹ Although oxide glasses are macroscopically brittle, they undergo plastic deformation under high stresses, for example, during indentation.¹² By studying different glass compositions, Peter showed that the indentation deformation mechanism of oxide glasses in general includes both shear flow and densification,¹³ with the simple notion that shear flow is the dominant process for glasses with compact structures, whereas densification becomes increasingly important in more open glasses.^{14,15} Densification causes volume shrinkage, but can be recovered upon sub- T_g (where T_g is the glass transition temperature) annealing.^{15,16} In turn, predensification of a glass affects the deformation mechanism during subsequent indentation as well as other mechanical properties. For example, Svenson et al¹⁷ found that the pressure-induced changes in elastic moduli are not governed by the specific structural changes, but rather by the overall degree of network densification. Deschamps et al¹⁸ found that the variation in the elastic moduli is also dependent on the compression path taken to reach permanent densification. Hardness is also affected by densification, since it is sensitive to the local bonding and atomic packing behavior of the constituent atoms and presence of, for example, non-bridging oxygens (NBOs).¹⁹ In general, hardness increases with density, and Kapoor et al²⁰ found that an overall network densification is responsible for this increase. Furthermore, Smedskjaer et al²¹ found that the changes in hardness also depend on the compression path taken to reach permanent densification, such as annealing versus hot compression. Despite the importance of volume densification, the structural changes, such as increasing network-former coordination numbers (CNs) (eg, for B and Al) upon densification,²² need to be considered for properties such as crack initiation resistance.^{23,24,25,19}

In this work, we build on previous studies in understanding structural densification mechanisms in alkali aluminoborate glasses.^{26,27,28} These glasses generally exhibit high crack initiation resistance upon indentation, including for a lithium aluminoborate glass²³ that shows a dramatic increase in the CNs of both boron and aluminum upon high-temperature densification. In a recent work, we studied the effect of adding SiO₂ (up to 20 mol%) to a 25Li₂O-20Al₂O₃-55B₂O₃ glass on the structure and mechanical properties.²⁹ Addition of silica increases the average network rigidity, but meanwhile its open tetrahedral structure decreases the atomic packing density and also makes the network less structurally adaptive to applied stress. This is because Al and B easily increase their CN under pressure, while this is not the case for Si under modest pressures. As such, although the silica-containing networks have more free volume, they cannot densify more during indentation, which in turn leads to an overall decrease in crack resistance upon SiO₂ addition. In a related work,³⁰ Dickinson and de Jong found an increase in the boron CN upon P₂O₅ addition in borosilicate glass. Previous studies^{31,24}

have shown that the presence of B^{IV} relative to B^{III} units decreases the extent of volume densification in borosilicate glasses due to a more open network and planar structure of the latter.

To further understand the structural densification behavior of this glass family, we here study the effect of P₂O₅ addition (up to 10 mol%) to a 25Li₂O-20Al₂O₃-55B₂O₃ glass on the pressure-induced changes in glass structure using Raman, NMR spectroscopy, density measurements, indentation hardness testing, and ultrasonic echography. We refer to these glasses as lithium phosphoaluminoborate glasses, since B₂O₃ remains the major network-forming oxide. In this glass series, we keep the Li/Al/B ratio constant. This is done to keep the structural role of Al unchanged, which is expected to be possible because it has a strong enthalpic preference for being charge-stabilized by alkali cations (eg, Li⁺) in tetrahedral configuration.²³

2 | EXPERIMENTAL PROCEDURES

2.1 | Glass preparation

Lithium phosphoaluminoborate glasses, xP₂O₅-(1-x)[25Li₂O-20Al₂O₃-55B₂O₃] with $x = \{0, 2, 5, 10\}$ (in mol%), were synthesized using the traditional melt-quenching approach. The utilized raw materials were Li₂CO₃ (≥98.5%, Merck KGaA), Al₂O₃ (99.5%, Sigma-Aldrich), H₃BO₃ (≥99.5%, Honeywell International), and NH₆PO₄ (≥99.5%, Merck KGaA). First, according to the target composition, all raw materials were weighed and thoroughly mixed. In order to prevent excessive foaming, the mixed powders were stepwise added to a 100 mL alumina crucible and heated to around 500°C in an electric furnace (Entech) to remove the excess H₂O, CO₂, and NH₃. The mixture was melted and homogenized at 1150-1250°C for 1 h in air. Then, the melt was poured onto a brass plate for quenching. Finally, the obtained glasses were immediately transferred to a preheated annealing furnace at an estimated glass transition temperature (T_g) value for 30 min, and then slowly cooled down to room temperature. The chemical compositions of the glasses were analyzed using inductively coupled plasma optical emission spectroscopy for P₂O₅, Al₂O₃, and B₂O₃, and flame emission spectroscopy for determination of Li₂O content (see Table 1). Furthermore, as shown in Figure S1, x-ray diffraction analysis indicated that none of the samples showed any signs of crystallization.

We determined T_g of the glasses using differential scanning calorimetry (STA 449 F3 Jupiter, Netzsch). The measurements were done at 10 K/min on specimens with a known thermal history (ie, with a preceding cooling rate of 10 K/min) using Pt crucible in argon (gas flow 60 mL/min). T_g values and other property data are summarized in Table S1.

TABLE 1 Analyzed chemical compositions of the lithium phosphoaluminoborate glasses (in mol%). The uncertainty is around $\pm 1\%$

Glass ID	P ₂ O ₅	B ₂ O ₃	Al ₂ O ₃	Li ₂ O
P0	0	53.6	20.7	25.7
P2	2.2	51.8	20.9	25.1
P5	4.9	50.9	20.4	23.8
P10	9.7	46.5	21.6	22.2

Following determination of T_g , the glasses were re-annealed for 30 min at their measured T_g value and cooled down to room temperature at a cooling rate of approximately 3 K/min. After re-annealing, all the glasses were cut into desired dimensions and optically polished in ethanol using SiC grinding paper ranging from grit 220 to 4000 in six steps.

2.2 | Hot compression

Following the method described in the previous study,³² all four annealed glasses were subjected to an isostatic N₂-mediated pressure treatment at both 1 and 2 GPa. The compression was carried out at the measured ambient-pressure T_g value for 30 min. The samples were subsequently quenched at an initial cooling rate of 60 K/min. The pressure chamber was then decompressed at a rate of 30 MPa/min at room temperature.

2.3 | Density

Density (ρ) of the glass specimens was determined using Archimedes principle of buoyancy. The weight of each specimen (at least 1.5 g) was measured in air and ethanol for 10 times. Based on the ratio between molar mass and density, we calculate the molar volume (V_m). To also quantify differences in free volume among the different glasses, we calculate the atomic packing density (C_g) based on these data. This was done by assuming sixfold coordination for Li and two-fold coordination for O, while the CNs for B and Al are taken from the NMR results. C_g is defined as the ratio between the theoretical molar volume occupied by the ions and the effective molar volume of the glass,

$$C_g = \rho \frac{\sum f_i V_i}{\sum f_i M_i} \quad (1)$$

here, $V_i = \frac{4}{3}\pi N (x r_A^3 + y r_B^3)$ represents the molar volume of an oxide $A_x B_y$ with the molar fraction f_i and the molar mass M_i , N denotes Avogadro's number, and r_A and r_B are the ionic radii of the cations and anions, respectively, which are taken from Shannon.³³

2.4 | Raman spectroscopy

To study the short- and intermediate-range structural changes due to composition variation and hot compression, we have acquired micro-Raman spectra of the glasses. The spectra were collected on an inVia micro-Raman spectrometer (Renishaw). All sample surfaces were excited by a 532 nm green diode laser for an acquisition time of 10 s. The range of all spectra was from 220 to 1700 cm⁻¹, with resolution better than 2 cm⁻¹. Spectra from three different locations on the glass were compared for each specimen to verify chemical homogeneity (see Figure S2). All spectra were uniformly treated in Origin software for background correction and area normalization.

2.5 | Solid-state NMR spectroscopy

¹¹B and ²⁷Al magic-angle spinning nuclear magnetic resonance (MAS NMR) experiments were conducted at 16.4 T using a commercial spectrometer (VNMRS, Agilent) and a commercial 3.2 mm MAS NMR probe (Agilent). Resonance frequencies for ¹¹B and ²⁷Al at this external magnetic field were 224.52 and 182.34 MHz, respectively. Glasses were powdered with an agate mortar and pestle, and then loaded into low-Al zirconia rotors for sample spinning at 20 and 22 kHz for ¹¹B and ²⁷Al MAS NMR. Data for both nuclei were collected with short radio-frequency pulse widths of 0.6 μ s ($\pi/12$ tip angle) and relaxation delays of 4s and 2s for ¹¹B and ²⁷Al, respectively. Signal averaging was performed using 600 to 1000 scans per experiment.

³¹P MAS NMR data were acquired using a commercial console (VNMRS, Varian) and 3.2 mm MAS NMR probe (Chemagnetics), in conjunction with an 11.7 T wide bore superconducting magnet and a resonance frequency of 202.30 MHz. Powdered glasses were contained in 3.2 mm zirconia rotors and sample spinning was computer controlled to 20 kHz. Measurement conditions included $\pi/6$ pulse widths of 1.2 μ s, recycle delays of 60s, and acquisition of nominally 1500 scans.

MAS NMR spectra for these three nuclei were processed without any additional apodization, plotted using the normal shielding convention, and with shift referencing to aqueous boric acid (19.6 ppm), aqueous aluminum nitrate (0.0 ppm), and 85% H₃PO₄ solution (0.0 ppm). ¹¹B and ²⁷Al MAS NMR data were fit with DMFit utilizing second-order quadrupolar lineshapes for ¹¹B trigonal peaks, a combination of Gaussian and Lorentzian lineshapes for ¹¹B tetrahedral resonances, and the CzSimple model for ²⁷Al³⁴. In the case of ¹¹B MAS NMR data, the overlapping satellite transition for the B^{IV} resonance was also fit and subtracted from the integration, yielding accurate site intensities for all B^{III} and B^{IV} peaks. ³¹P MAS NMR data were fit using DMFit and 100% Gaussian lineshapes.

2.6 | Vickers hardness and elastic moduli

We determined the Vickers hardness (H_V) of all glasses using a Nanovea CB500 hardness tester. On each specimen, 20 indents were generated. The loading duration and dwell time were set to 6 s and 10 s, respectively. The residual imprints were subsequently analyzed with an optical microscope and H_V was calculated as,

$$H_V = 1.8544 \frac{P}{\left(\frac{d_1+d_2}{2}\right)^2}, \quad (2)$$

where P is the contact load of 4.9 N, and d_1 and d_2 are the length of the projected indent diagonals.

Furthermore, the elastic properties of the glasses were measured by ultrasonic echography using an ultrasonic thickness gauge (38DL Plus, Olympus) equipped with 20 MHz delay line transducers for the determination of the longitudinal V_1 and transversal wave velocities V_2 . The longitudinal modulus C_{11} , shear modulus G , bulk modulus B , and Young's modulus E , as well as the Poisson ratio ν , were calculated using the following relations, which are applicable for isotropic materials:

$$C_{11} = \rho V_1^2, \quad (3)$$

$$G = \rho V_2^2, \quad (4)$$

$$B = C_{11} - \frac{4}{3}G, \quad (5)$$

$$\nu = \frac{3B - 2G}{6B + 2G}, \quad (6)$$

$$E = 2G(1 + \nu). \quad (7)$$

3 | RESULTS AND DISCUSSION

3.1 | Raman spectroscopy

Figure 1A shows the Raman spectra of both as-prepared and compressed lithium phosphoaluminoborate glasses with different content of P_2O_5 . We divide the spectra into four main band regions, with the expected assignments outlined in the following (see also Table S2).

The lowest frequency band region I, ranging from ~ 280 to 625 cm^{-1} , is expected to contain contributions originating from B-O-B, Al-O-Al, and B-O-Al stretching.³⁵ In addition, vibrations due to bending of PO_4 units may occur in this region (I_a).³⁶ We find that the relative intensity of this band region increases with the content of P_2O_5 for the four as-prepared glasses, consistent with a larger concentration of PO_4

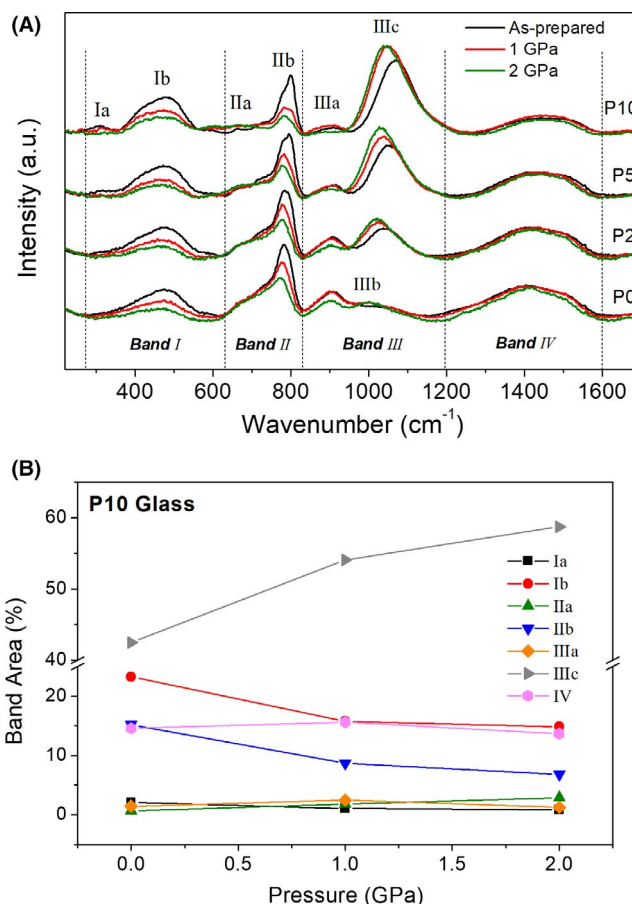


FIGURE 1 (A) Micro-Raman spectra of the as-prepared and compressed lithium phosphoaluminoborate glasses with different content of P_2O_5 (see sample IDs in Table 1). The spectra are divided into four main different band regions. (B) Pressure dependence of the relative area fractions of the main Raman bands in the P10 glass [Color figure can be viewed at wileyonlinelibrary.com]

units. Band region II (~ 625 to 815 cm^{-1}) is characteristic for B_2O_3 -rich glasses,³⁵ since peaks in this frequency range are typically assigned to borate superstructures (II_b), such as chain and ring metaborates,^{37,38} di-triborates,³⁹ and penta-, tetra-, or triborates,^{37,38,39,40} as well as boroxol rings.^{37,41} B-O-Al stretching and aluminate network vibrations may occur in the band II_a region.⁴² The band II_b region decreases in intensity with the content of P_2O_5 , since the addition of P_2O_5 , and thus removal of B_2O_3 , decreases the fraction of borate superstructures. Band region III (~ 815 to 1200 cm^{-1}) is expected to result from vibrations of AlO_4 units (III_a) ($\sim 900 \text{ cm}^{-1}$),^{43,44} Al-B network ($\sim 980 \text{ cm}^{-1}$),⁴⁵ borate superstructures (III_b) ($\sim 930 \text{ cm}^{-1}$),^{35,38} and PO_2^- , $P_2O_7^{4-}$, and PO_3^{2-} units (III_c) (~ 1039 - 1090 cm^{-1})⁴⁶. We find that the relative intensity of III_a band region decreases with the content of P_2O_5 for the four as-prepared glasses, since the addition of P_2O_5 , and thus removal of Al_2O_3 , decreases the probability of forming AlO_4 units. In addition, the relative intensity of III_c band region increases with the content of P_2O_5 for the four as-prepared glasses. The bands in region III_b lie under those of III_c ,

making it difficult to determine the impact of glass composition on their relative intensities. However, these are minor intensity bands associated with the borate superstructural units contributing to the more intense bands at II_b , so dilution of borate groups with increasing P_2O_5 is likely to decrease the intensity of bands III_b in the same manner as for II_b . Finally, a high-frequency region, band region IV ($\sim 1200\text{--}1600\text{ cm}^{-1}$), is expected to be dominated by contributions from vibrations of superstructural units such as pyroborate units, chain, and ring metaborate units.⁴⁷ This peak decreases in intensity with the content of P_2O_5 , since the addition of P_2O_5 , and thus removal of B_2O_3 , decreases the fraction of borate superstructures as noted for other regions of these Raman spectra.

Next, we consider the variations in the Raman spectra upon hot compression (Figure 1A). In the glass without P_2O_5 (P0 Glass), we find that the area fractions of bands I and II are suppressed with increasing pressure, indicating the breakage of some superstructural borate (and possibly aluminoborate) units. The suppression of bands I and II is accompanied by an increase in the area of bands III and IV upon compression. Considering the P10 glass as an example, Figure 1B shows the pressure dependence of the relative area fractions of the main Raman bands. The area fractions of bands I_b and II_b decrease significantly with increasing pressure, while that of band III_c increases. The other glasses show the same trend upon compression (see Figure S3). The band III_c may be ascribed to the formation of PO_2^- , $\text{P}_2\text{O}_7^{4-}$, and PO_3^{2-} units⁴⁶ upon addition of P_2O_5 . Hot compression of the P10 glass does not result in the formation of any new bands (Figure 1A), but following the permanent densification, the high-frequency band III_c broadens slightly and becomes more intense upon hot compression, especially in high- P_2O_5 glasses. Such increase in band width can be the result of P-O-P bond angle distortion.

3.2 | ^{27}Al MAS NMR spectroscopy

To further understand the effects of P_2O_5 addition and compression on the short-range structure of the studied lithium phosphoaluminoborate glasses, we performed ^{27}Al , ^{11}B , and ^{31}P MAS NMR spectroscopy measurements. The spectral deconvolution and determined speciation are shown in Tables S3, S4, S5, and S6 respectively, and Figure S4A.

Figure 2 shows the ^{27}Al MAS NMR spectra for the as-prepared glasses with different content of P_2O_5 . The three peaks at about 65, 37, and 9 ppm in the spectrum of the P_2O_5 -free glass can be unambiguously assigned to Al^{IV} , Al^{V} , and Al^{VI} , respectively,²⁰ as the chemical shifts are similar to those in previous studies on phosphorous-free aluminoborate and aluminosilicate glasses.^{23,48,49} The relative amount of each species is proportional to the corresponding area under its peak, and the fitted values are shown in Table S4. Figure 2 shows that the ^{27}Al peak position shifts to higher shielding

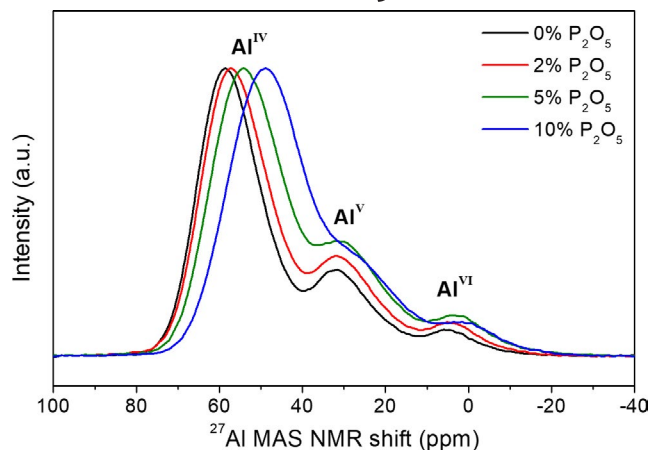


FIGURE 2 ^{27}Al MAS NMR spectra for the as-prepared lithium phosphoaluminoborate glasses with different content of P_2O_5 [Color figure can be viewed at wileyonlinelibrary.com]

(from 65 to 56 ppm) with increasing P_2O_5 content (from 0 to 10 mol%). This is likely due to the association of aluminum and phosphorus polyhedra, leading to the formation of Al-O-P linkages in the glass network. Such Al-O-P bonding has, however, only a slight effect on the CN of aluminum (see below). These results are in agreement with previous studies,^{20,50} where for P-containing glasses, the presence of P next nearest neighbor (NNN) polyhedra increase the shielding of ^{27}Al resonances. As demonstrated by the data in Figure 2 and the extracted chemical shifts in Table S4, the impact of P_2O_5 on the ^{27}Al NMR data is seen for all of the resonances, indicating that Al^{IV} , Al^{V} , and Al^{VI} groups are all affected by neighboring phosphate groups, and thus these glasses contain a substantial amount of mixing between aluminoborate and phosphate polyhedra.

Figure 3 shows the effect of densification on the ^{27}Al MAS NMR spectra for the four different glasses. Generally, we observe pronounced changes in the aluminum despite the relative modest pressure, in agreement with previous studies on lithium aluminoborate glasses.²³ The areas of the Al^{V} and Al^{VI} peaks increase upon hot compression, corresponding to the conversion of Al^{IV} to Al^{V} and Al^{VI} units, as also found in earlier studies.^{24,19,25,11} Consequently, the CN of aluminum increases with increasing pressure (Figure 4A). The high- P_2O_5 glasses have the largest pressure-induced increase in the Al CN (from 4.26 to 4.90 for P10 glass) (Figure 4B). In fact, to our knowledge, the extent of the changes in Al speciation for P10 glass is the largest ever reported for an oxide glass under similar pressure/temperature conditions.^{23,11} This indicates that the addition of P_2O_5 positively influences the pressure-induced conversion of Al^{IV} to Al^{V} and Al^{VI} , in turn suggesting a link between aluminum and phosphate units as suggested by formation of Al-O-P bonding and the possibility for higher coordinated Al to charge-stabilize phosphate NBOs. Furthermore, we note from Figure 4A that the P_2O_5 content has a negligible effect on the Al CN in the as-prepared

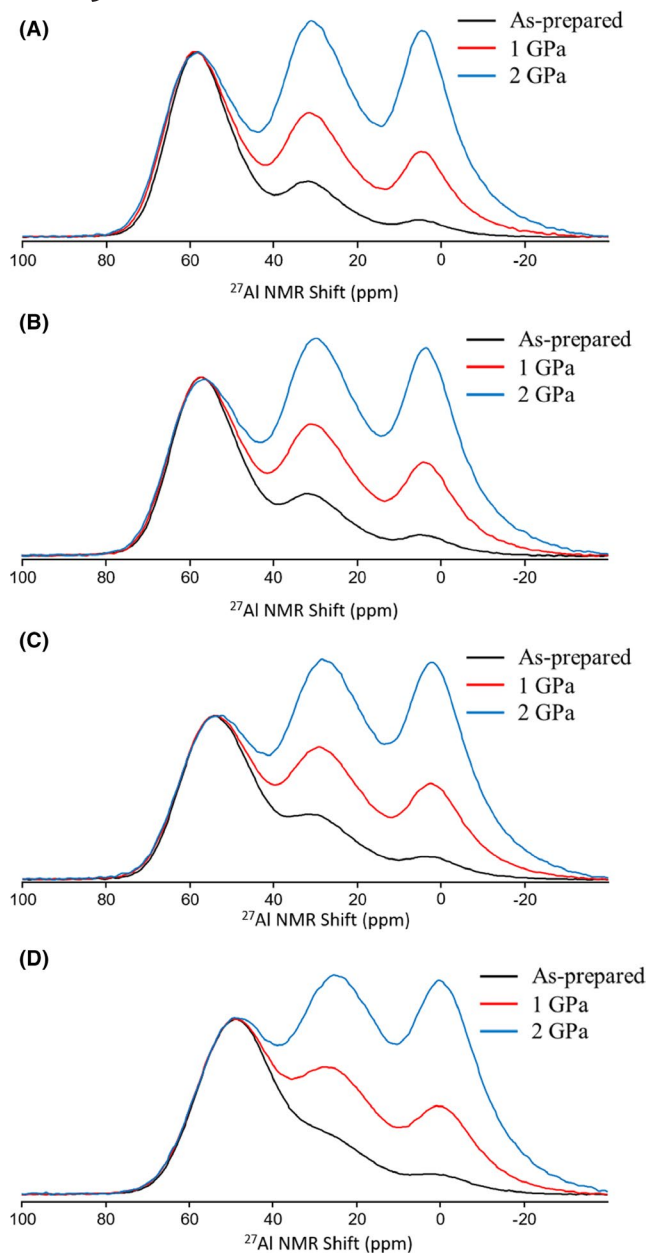


FIGURE 3 Effect of hot compression on the ^{27}Al MAS NMR spectra for (A) P0 glass, (B) P2 glass, (C) P5 glass, and (D) P10 glass [Color figure can be viewed at [wileyonlinelibrary.com](#)]

glasses. This could be because it mostly depends on the modifier-to-aluminum ratio (at least in aluminoborosilicate-type glasses), which is not changing in the studied glasses.

The other feature to note in Figure 3 is that the peak positions for the three different Al sites are unaffected by compression. As indicated by the fitting parameters in Table S4, while the intensities of the Al sites vary significantly with compression, the isotropic chemical shifts for each peak are within 1 ppm from as-made to compression at 2 GPa. This suggests that while P_2O_5 content has a strong influence on the chemical shielding of ^{27}Al resonances, as discussed above for the as-made glasses, the application of hot compression does

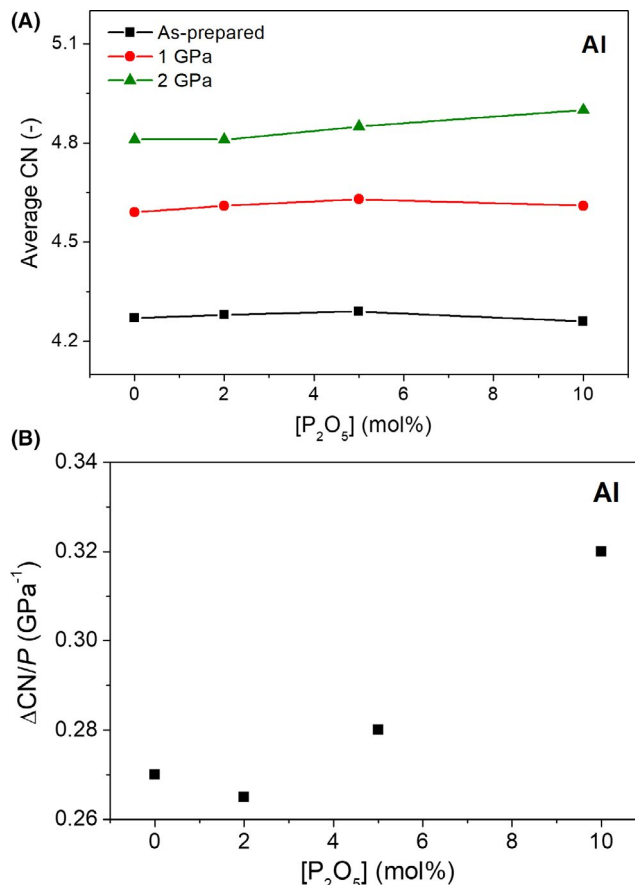


FIGURE 4 (A) Composition and pressure dependence of the average coordination number (CN) of aluminum. (B) Composition dependence of the change in aluminum coordination number with pressure ($\Delta\text{CN}/P$). The error in aluminum's CN is around ± 0.02 [Color figure can be viewed at [wileyonlinelibrary.com](#)]

not appear to change the extent of mixing between aluminum and phosphate polyhedra. That is, the higher shielding exhibited for P-containing glasses is maintained even with structural changes due to compression, consistent with preservation of P NNN even as Al^{IV} is converted to higher CN.

3.3 | ^{11}B MAS NMR spectroscopy

Figure 5 shows the ^{11}B MAS NMR spectra for the as-prepared glasses with different content of P_2O_5 . The glassy networks all consist of both B^{III} (around 5 to 20 ppm) and B^{IV} units (around -2.5 to 5 ppm). The fraction of B^{IV} decreases slightly upon the addition of P_2O_5 , indicating that the addition of P_2O_5 is beneficial for the conversion of B^{IV} to B^{III} . This could be because the introduced phosphate competes with boron for some of the Li modifiers, leading to fewer Li- B^{IV} interactions and thus a lower level of modification of the borate polyhedra. Other changes in the ^{11}B MAS NMR data are observed with increasing P_2O_5 . Arrows in Figure 5 indicate subtle alterations of the B^{III} region of the spectrum, with

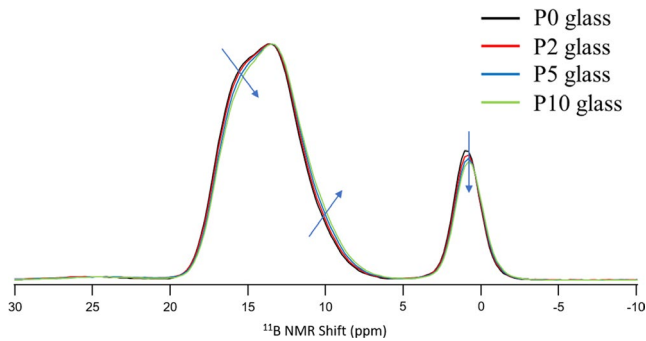


FIGURE 5 ^{11}B MAS NMR spectra for the as-prepared lithium phosphoaluminoborate glasses with different content of P_2O_5 . Arrows indicate changes in the direction of increasing P_2O_5 content [Color figure can be viewed at wileyonlinelibrary.com]

a slight decrease in intensity at the highest shift side of the signal (around 16–17 ppm), and a corresponding increase in intensity near 10 ppm. Fitting of these data (see Table S3 and Figure S4A) provides additional insight into these changes, as deconvolution of the B^{III} lineshape into two distinct B^{III} units can be achieved. As a result, it now is apparent that addition of P_2O_5 leads to a direct reduction in the population of the downfield (more positive) B^{III} resonance and an increase in the more shielded (less positive) B^{III} peak intensity. The former is assigned to B^{III} in superstructural units, consistent with some of the Raman spectroscopy features described earlier, and a well-known feature in B-rich glasses.⁵¹ The latter B^{III} signal is attributed to non-ring B^{III} , that is, those B^{III} groups not incorporated into the geometrically constrained environments of borate superstructural units. Thus, increasing P_2O_5 content at the expense of B_2O_3 leads to a reduction in the number of ring-type borate groups, which arises due to decreasing B_2O_3 content and the inability to maintain the number of such structural groupings. This is analogous to the decreasing intensity of band II_b in the Raman spectra of the as-made glasses with increasing P_2O_5 content (Figure 1).

The other change in boron environment with glass composition (no compression) is a slight increase in shielding of the B^{IV} signal (Figure 5). This is not necessarily easy to see in the stack plot, but after fitting of the ^{11}B MAS NMR data (Figure S4B), the glasses containing P_2O_5 required the addition of a second B^{IV} resonance, which was at a more negative shift relative to that in the P0 glass. This peak also increases in relative intensity with increasing P_2O_5 content, suggesting a close relation to phosphorus. In fact, the impact of P NNN groups on ^{11}B shielding is similar to that described above for ^{27}Al shielding. Interaction of phosphate groups with B^{IV} units leads to a more negative shift, up to the limit of -3.3 ppm found in crystalline BPO_4 .⁵² Studies of P-containing borosilicate glasses indicate that the new peaks formed with P_2O_5 addition are consistent with B–O–P linkages involving B^{IV} groups.⁵³ Thus, the B^{IV} groups in these glasses, while diminishing overall in intensity due to less available modifier, are

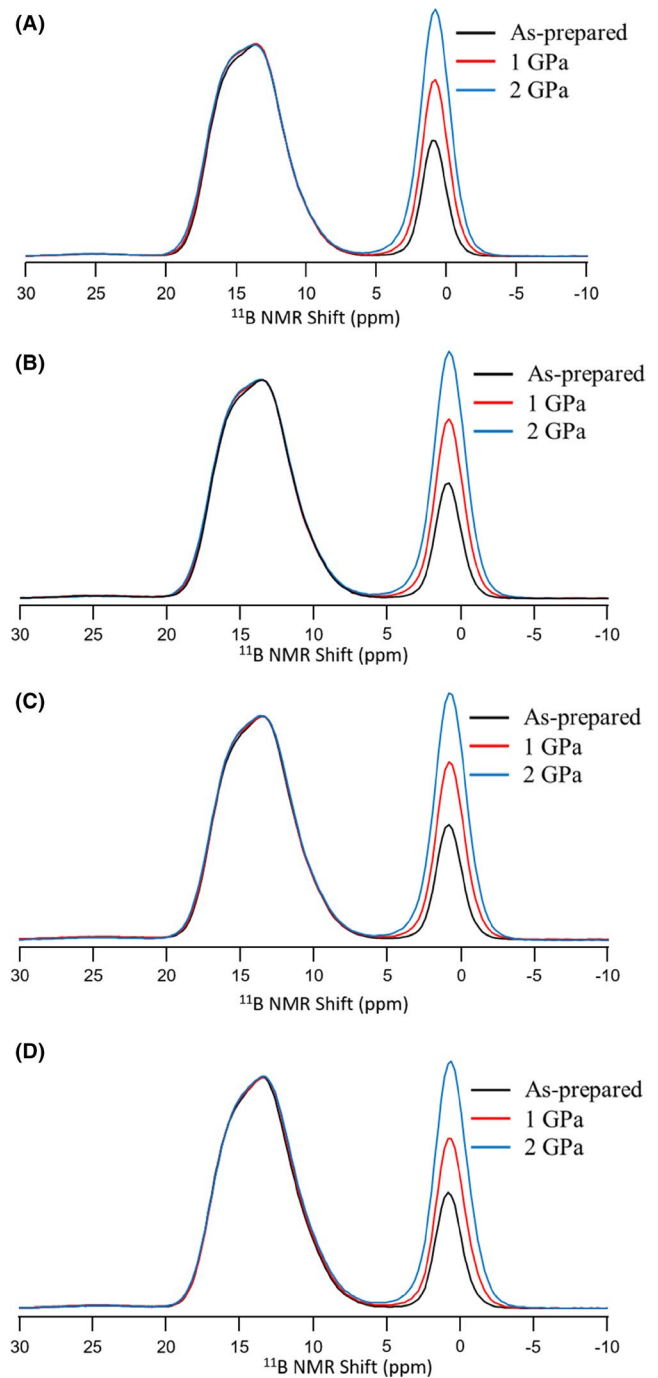


FIGURE 6 Effect of hot compression on the ^{11}B MAS NMR spectra for (A) P0 glass, (B) P2 glass, (C) P5 glass, and (D) P10 glass [Color figure can be viewed at wileyonlinelibrary.com]

also being redistributed into network structure having pronounced connectivity between B^{IV} and phosphate polyhedra.

These local boron environments are, such as those of aluminum, very sensitive to densification, with boron increasing its average CNs upon compression (see Figure 6).^{24,19} This has been reported to be related to the presence of NBO, that is, $\text{B}^{\text{III}} + \text{NBO} \rightarrow \text{B}^{\text{IV}}$.⁵⁴ Indeed, the ^{11}B MAS NMR spectra show that the average CN of boron increases upon hot compression (Figure 7A). Unlike aluminum, the addition of P_2O_5

has a negligible effect on the pressure-induced change in the B CN (see Figure 7B), with each glass composition showing similar pressure-induced changes in B^{III} and B^{IV} populations. In addition, there is a small, but noticeable change in the B^{III} peak, near the position previously identified as belonging to ring-type B^{III} units. As seen before in studies of similarly compressed borate and borosilicate glasses,^{25,55} the ring B^{III} unit is more strongly impacted by compression, with glass densification accompanied by a decrease in the amount of superstructural units. This is corroborated by the decrease in Raman band II_b intensity (Figure 1) as these glasses are compressed at 1 and 2 GPa. The intensity decrease in these bands, as well as the change in ring-type B^{III} peak intensity in these ¹¹B MAS NMR data, occurs similarly for all glasses, regardless of the amount of P₂O₅.

3.4 | ³¹P MAS NMR spectroscopy

Figure 8 shows the ³¹P MAS NMR spectra for the as-prepared glasses with different content of P₂O₅, with the average

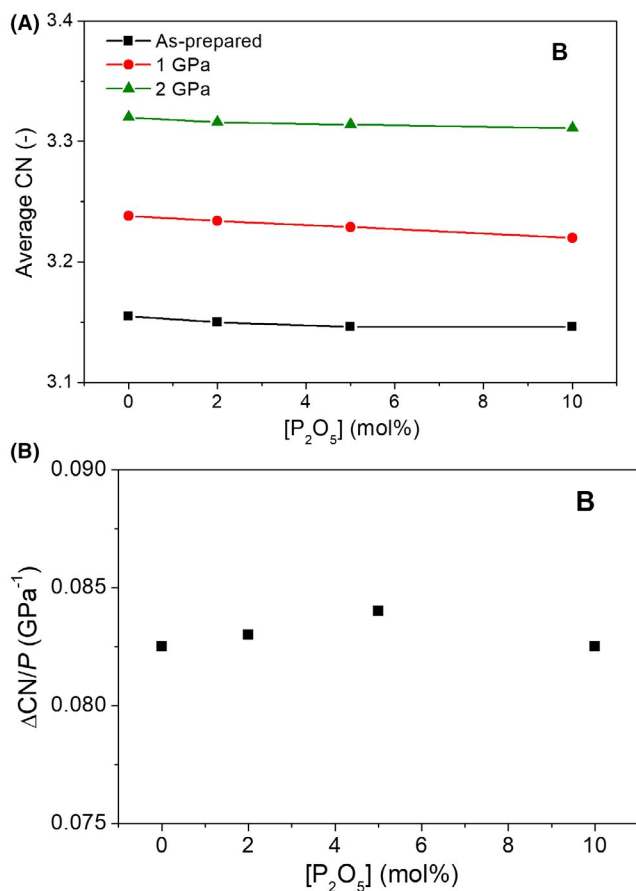


FIGURE 7 (A) Composition and pressure dependence of the average coordination number (CN) of boron. (B) Composition dependence of the change in boron coordination number with pressure ($\Delta\text{CN}/P$). The error in boron's CN is around ± 0.01 [Color figure can be viewed at wileyonlinelibrary.com]

peak position moving toward more negative shift values with increasing level of P₂O₅. The ³¹P chemical shift is highly sensitive to the immediate geometry of the phosphate tetrahedra (ie, number of bridging and NBO) and also to the connected (neighboring) polyhedra, with a lower chemical shift corresponding to higher shielding from the groups surrounding phosphorus. In the case of these lithium-modified aluminoborate glasses, there are several possible contributors to the trends exhibited in Figure 8. First, the Qⁿ speciation of the phosphate groups may be affected by the overall glass composition, where competition for the lithia modifiers between aluminum, boron, and phosphorus changes with P₂O₅ levels. As seen above for both aluminum and boron speciation, these cations are greatly impacted by the alkali, forming both Al^{IV} and B^{IV} tetrahedra in response to the presence of modifier. As P₂O₅ is added to the P0 glass, aluminum coordination is mostly unaffected, while boron shows a slight reduction in the fraction of B^{IV} groups, indicating that the added P₂O₅ does remove Li⁺ modifiers from mainly the borate portion of the network, and as a result, some of the phosphorus polyhedra will have NBO and thus the phosphate groups are not entirely Q³ units. This is evidenced by the ³¹P MAS NMR data in Figure 8, where the peak position for the P2 glass is centered around -10 ppm, well downfield from the shifts normally found for Q³ phosphate groups (around -35 to -55 ppm).⁵⁶ According to literature studies of lithium phosphate glasses, the main peak for the P2 glass around -10 ppm lies between those of Q¹ and Q² polyhedra,⁵⁷ so in neglecting the impact of neighboring polyhedra, this might reflect a mixture of Q¹ and Q² phosphate groups in the P2 glass. This simple interpretation would require 2 and 1 Li⁺ for each group, respectively, so 1.5 Li₂O for every mol of P₂O₅. For the P2 glass, this means that 3 moles of Li₂O would be necessary to form a 50:50 mixture of Q¹ and Q² phosphate groups, and given the results above for aluminum and boron speciation, this Li₂O

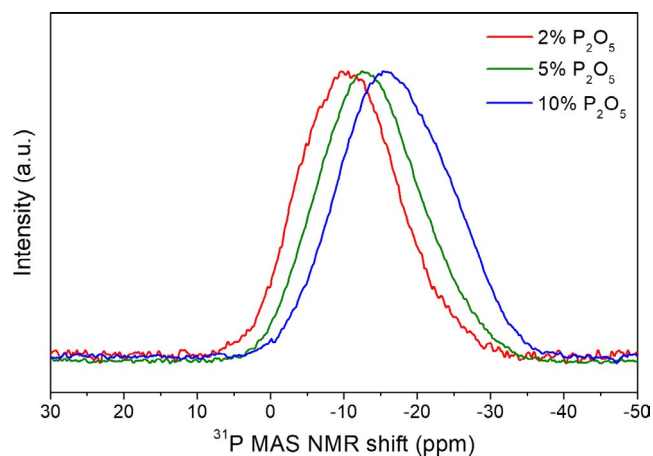


FIGURE 8 ³¹P MAS NMR spectra for the as-prepared lithium phosphoaluminoborate glasses with different content of P₂O₅ [Color figure can be viewed at wileyonlinelibrary.com]

would likely be taken from the boron groups, both seen as a reduction in N_4 (Figure 5) and also the concomitant reduction in B_2O_3 content with added P_2O_5 (Table 1). Considering both of these factors, the observation of partially depolymerized phosphate groups is expected. The exact nature of the phosphate groups in the as-made P2 glass is more complicated than this simple “binary” model, as indicated by the deconvolution of the ^{31}P MAS NMR data in the supplemental section (see Figure S4C). In this case, at least three resonances are required for fitting, with two of these corresponding directly to Q^1 and Q^2 groups like those in lithium phosphate glasses (eg, peaks at -6 and -22 ppm, respectively). A third resonance around -13 ppm is necessary, and indicates additional complexity in the phosphate speciation.

Another key contributor to ^{31}P chemical shifts in Al- (and B-) containing glasses is the impact of these other cations when bonded to the phosphate groups. There are five primary possibilities for attaching groups to phosphorus, which all are determined by the chemical shift (see Figure S4 and Table S5). First, we note that the ^{31}P peak of the P10 glass is broadened relative to those with smaller phosphorus content, which could be a result of an increasing amount of different phosphate species. We here denote these as Q^n units, where n is the number of bridging oxygens. By deconvolution, we can assign a peak at -6 ppm to Q^1 groups⁵⁷ without any Al (or B) NNNs and another peak at -22 ppm to Q^2 groups⁵⁷ without any Al (or B) NNNs, showing that there is a substantial amount of P-O-P bonding in the studied glasses. Based on the above analysis, we find that the content of B^{IV} is relatively low, leading to the fewer B-O-P bonds. This is because B/P association does not typically involve B^{III} .⁵⁸ Since the amount of P with B NNN is low (although the ^{11}B MAS NMR data suggest that it is non-zero), we assume that the various Q^n groups do not have B NNNs. Instead, we consider the impact of Al as the NNNs, as supported from the steady increase in ^{27}Al NMR shielding above. Although the content of B_2O_3 is higher than that of Al_2O_3 in the glasses, it seems that P/Al association is stronger than P/B, at least for these studied glasses. Therefore, we assign the more intense peak around -13 ppm to Q^{1-1} groups, which must be a Q^1 phosphate group with one Al NNN. Since replacing the P-O-P with P-O-Al leads to an increased shielding of around 7 ppm^{59,60} (the decrease in chemical shift from -6 to -13 ppm), the most plausible assignment is for a Q^1 with one Al NNN. A very weak peak at 8.5 ppm assigned to the Q^0 groups (ie, no connectivity with Al or B) is close to that in lithium orthophosphate (10 ppm). Finally, we assign the peak around -29.6 ppm to Q^{2-1} groups, which is a Q^2 phosphate group with one Al NNN (around 7 ppm increase in shielding). From the deconvolution, we find that the area of the Q^1 units decreases while that of the Q^2 units increases upon the addition of P_2O_5 (Table S5). This indicates that Q^1 units convert to higher Q^n units, and as a result, the ^{31}P average peak

position shifts to higher shielding (from -9.5 to -15.5 ppm) with increasing P_2O_5 content from 2 to 10 mol%.

Figure 9A-C shows the effect of densification on the ^{31}P MAS NMR spectra for the three P-containing glasses. Upon hot compression, the ^{31}P peak position slightly increases, which we ascribe to a decrease in the amount of P^3 units and simultaneous increase in P^1 units. In turn, this facilitates the change in Al coordination, as higher coordinated Al can serve as a charge compensator for some of the negative charges on these polyhedra. Figure 9D shows that the average Q^n (P) increases with the addition of P_2O_5 . The increase in the content of P_2O_5 promotes B-P association via formation of B-O-P bonds (P^2 and P^3 units), and thus increase the average Q^n (P). Surprisingly, we note that glasses with higher P_2O_5 content show larger decrease (from -0.041 to -0.087) in the average Q^n (P) upon compression (Figure 10). Due to the decrease in the average Q^n (P), there is formation of more NBOs in studied glasses upon pressure. The high-P content can promote the B-P association for the formation of B-O-P units, and thus leading to more pressure-induced depolymerization of B-O-P units (P^2 and P^3 units) for the conversion of B^{III} to B^{IV} ($B^{III} + NBO \rightarrow B^{IV}$ ⁵⁴).

3.5 | Volume densification and self-adaptivity

Figure 11A shows the compositional and pressure dependence of density (ρ) before and after hot compression at 1 GPa and 2 GPa. The addition of P_2O_5 has only a slight effect on the density, while the density of each studied glass increases dramatically upon hot compression, which is in agreement with previous work.^{23,11,17} Furthermore, since there are also changes in the size of the atoms upon addition of P_2O_5 , we calculate the atomic packing density (C_g) to further understand the differences in free volume. Figure 11B shows the compositional and pressure dependence of atomic packing density (C_g). We can find that C_g decreases with the content of P_2O_5 for all studied glasses, showing that the network becomes gradually more open with P_2O_5 addition. In order to better understand the difference in the extent of pressure-induced densification for all lithium phosphoaluminoborate glasses, we calculate the irreversible plastic compressibility, that is, the extent of volume densification following decompression.²⁰ As shown in Figure 11C, the plastic compressibility decreases with increasing P_2O_5 content. To further understand the relation between volume densification and the short-range order structural changes, we calculated the correlation between plastic compressibility and atomic self-adaptivity (inset Figure 11D). Self-adaptivity is defined as $(\langle \Delta n \rangle \Delta \rho) / (\rho_0 P)$, where $\langle \Delta n \rangle$ is the change in CN as determined by NMR, $\Delta \rho$ is the change in density, ρ_0 is the initial density, and P is the applied pressure. As such, the ability to

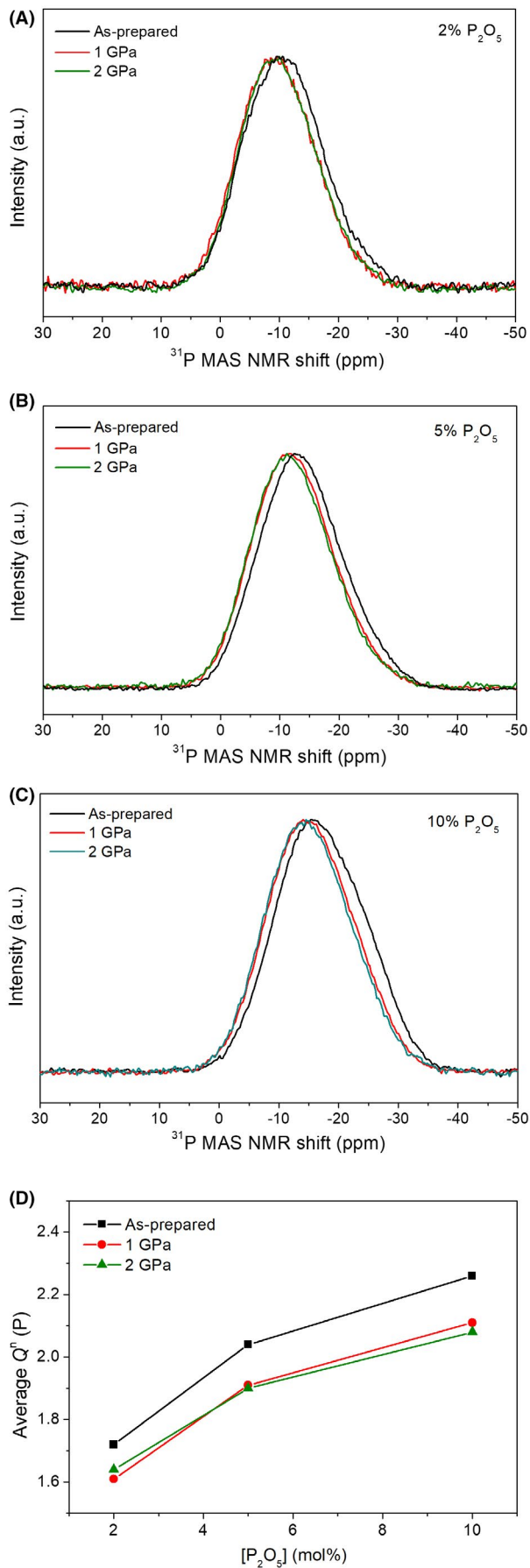


FIGURE 9 Effect of pressure on the ^{31}P MAS NMR spectra for (A) P2 glass, (B) P5 glass, and (C) P10 glass. (D) Composition and pressure dependence of the average Q^n (P) [Color figure can be viewed at wileyonlinelibrary.com]

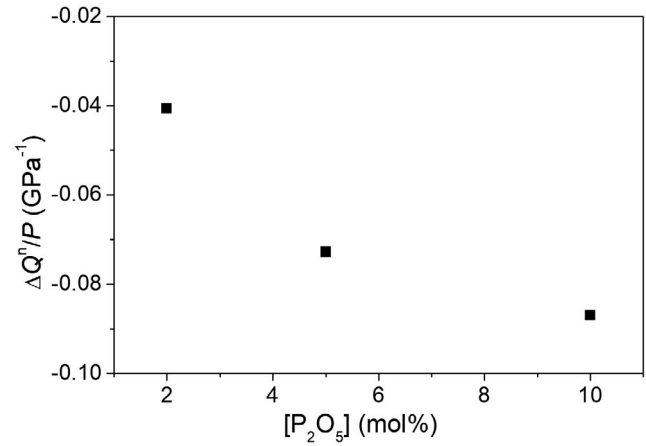


FIGURE 10 Composition dependence of the change in phosphorous speciation with pressure ($\Delta Q^n/P$)

self-adapt results from the balance between the energy cost associated with each densification mechanism (inversely correlated to the extent of pressure-induced change in CN $\langle \Delta n \rangle / P$), and its efficiency in increasing the packing density (proportional to the accompanying change in density $\Delta \rho / \rho_0$). We find a positive correlation between atomic self-adaptivity and the pressure-induced volume densification. Previous studies^{31,24} have shown that B^{IV} units decrease the extent of densification in borosilicate glasses, whereas B^{III} units enhance the densification of the glasses due to a more open network and planar structure.

Despite the positive correlation in Figure 11D, the change in the CN of boron and aluminum does not constitute the full volume densification. Additional contributions include decrease in the inter-tetrahedral bond angles and the average ring size, and increase in the distribution of network-former oxygen-bond lengths.⁶¹ To quantify the contribution of the boron and aluminum CN changes to the overall pressure-induced volume densification ($\Delta V_{m(\text{Al+B})} / \Delta V_m$), we follow the approach of Wu et al.⁶² This involves calculating the pressure-induced molar volume change only due to boron and aluminum coordination changes ($\Delta V_{m(\text{Al+B})}$) and the measured pressure-induced molar volume change (ΔV_m). $\Delta V_{m(\text{Al+B})}$ is calculated as,

$$V_{m(\text{Al+B})} = \left[X_{\text{Al}_2\text{O}_3} \sum x_i V_{(\text{I|Al})} \right] + \left[X_{\text{B}_2\text{O}_3} \sum x_i V_{(\text{I|B})} \right] \quad (8)$$

where $X_{\text{Al}_2\text{O}_3}$ and $X_{\text{B}_2\text{O}_3}$ are molar fractions of Al_2O_3 and B_2O_3 in the glass, x_i is the fraction of Al or B in each coordination state, which is obtained from NMR data (Tables S3 and S4),

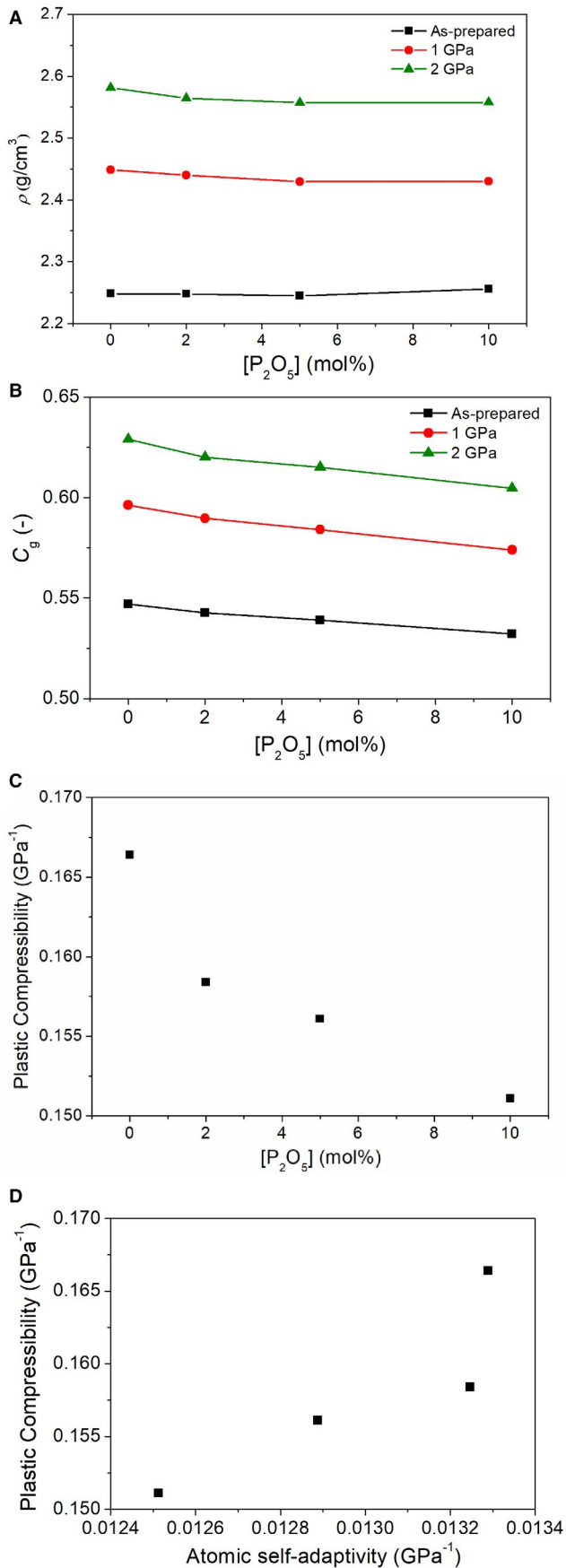


FIGURE 11 Compositional and pressure dependence of (A) density (ρ) and (B) atomic packing density (C_g). (C) Composition dependence of plastic compressibility. (D) Correlation between plastic compressibility and atomic self-adaptivity [Color figure can be viewed at wileyonlinelibrary.com]

TABLE 2 Estimation of volume changes based on the boron and aluminum coordination changes between as-prepared and compressed glasses ($\Delta V_{m(\text{Al+B})}$) by Equation (8) and the measured molar volume changes between as-made and compressed glasses (ΔV_m)

Glass	P0 Glass	P2 Glass	P5 Glass	P10 Glass
ΔV_m at 1 GPa (cm ³ /mol)	2.40	2.38	2.38	2.38
ΔV_m at 2 GPa (cm ³ /mol)	3.79	3.73	3.82	3.91
$\Delta V_{m(\text{Al+B})}$ at 1 GPa (cm ³ /mol)	1.05	1.04	1.03	0.88
$\Delta V_{m(\text{Al+B})}$ at 2 GPa (cm ³ /mol)	2.02	1.97	2.01	1.88
$\Delta V_{m(\text{Al+B})}/\Delta V_m$ at 1 GPa	43.8%	43.7%	43.3%	37.0%
$\Delta V_{m(\text{Al+B})}/\Delta V_m$ at 2 GPa	53.3%	52.8%	52.6%	48.1%

and $V_{(i|\text{Al})}$ and $V_{(i|\text{B})}$ are partial molar volumes of Al₂O₃ and B₂O₃ in each coordination state i . The simplest assumption is that the partial molar volume of each oxide component in a glass is the same as the molar volume of its pure oxide phase. Hence, the molar volume of B₂O₃ with three coordinated boron $V_{m([3]\text{B})}$ can be approximated as that for pure B₂O₃ glass (38.4 cm³/mol) and the molar volume of B₂O₃ with four coordinated boron $V_{m([4]\text{B})}$ is taken as half of $V_{m([3]\text{B})}$ (19.2 cm³/mol). $^{62}V_{m([6]\text{Al})}$ can be taken as that for α -alumina (31.59 cm³/mol) and $V_{m([4]\text{Al})}$ as 37.42 cm³/mol. $V_{m([5]\text{Al})}$ is set to 34.505 cm³/mol as the average of its four- and six-coordinated counterparts.⁶² As shown in Table 2, we can find that there is a smaller change from 1 to 2 GPa than from ambient to 1 GPa for both the molar volume (V_m) and $V_{m(\text{Al+B})}$ upon hot compression. The contribution of the boron and aluminum CN changes to the overall pressure-induced densification can be expressed by the ratio $\Delta V_{m(\text{Al+B})}/\Delta V_m$, with contributions above 50% at 2 GPa (Table 2). This is a large proportion of the pressure-induced volume densification compared to that found for calcium aluminoborosilicate glasses (9%–36% at 2 GPa).⁶² This is likely because the present glasses have more pronounced CN changes of Al and B upon compression, which in turn is due to the high concentration of B₂O₃ and Al₂O₃ and lithium as modifier. That is, reassociation of charge-balancing modifier cations from Al^{IV} to B^{IV} sites is required upon compression, which is promoted by the mobility of small lithium cations.²³ As shown in Table 2, we also find that the $V_{m(\text{Al+B})}$ contribution to the overall change in measured V_m becomes smaller with increasing content of P₂O₅, matching the compositional trend in self-adaptivity (Figure S5). This is expected since phosphorous does

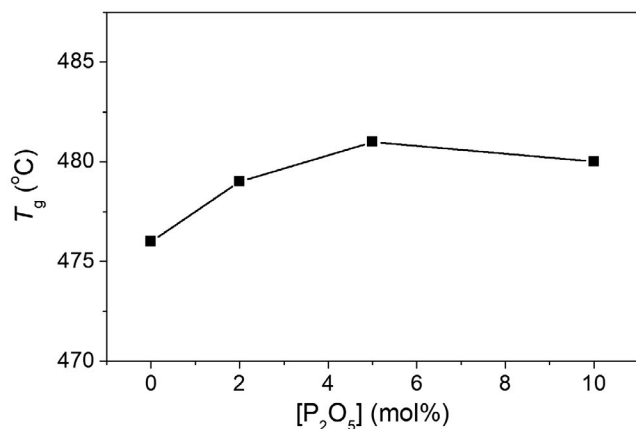


FIGURE 12 Composition dependence of the glass transition temperature (T_g) for as-prepared lithium phosphoaluminoborate glasses with different content of P_2O_5 . The error in T_g does not exceed 2°C

not contribute to the CN changes, but only to changes in Q -speciation with limited differences in partial molar volume.²⁰

3.6 | Glass properties: T_g , elastic moduli, and hardness

Figure 12 shows the compositional evolution of the glass transition temperature (T_g). We can find that the addition of P_2O_5 leads to a slight increase in the T_g of the lithium phosphoaluminoborate glasses. This indicates that the addition of P_2O_5 results in a more rigid glass network, that is, more atomic constraints per atom, which has been shown in earlier work to be positively correlated with higher glass transition temperature.²⁰

Next, we measured the elastic moduli and Poisson's ratio (ν) for the as-prepared and hot compressed glasses (Figure 13A and Figure S6). As seen for glass transition temperature, the addition of P_2O_5 has only a relatively small effect on the elastic moduli for all studied glasses. There is a slight decrease in elastic moduli with the P_2O_5 content. Elastic moduli generally increase with the bond strength and the number of bonds per volume.⁶³ Recent topological models have found E to be positively correlated with the volumetric constraint density.^{64,65} That is, the number of constraints per volume decreases significantly with addition of P_2O_5 , which is mainly as a result of the decrease of C_g with P_2O_5 (Figure 11B). This is because the number of constraints per atom only increases slightly when considering the relatively small variation in T_g (Figure 12).

The role of packing density on elastic moduli is also seen from the pressure-induced increase in all elastic moduli, as consistent with previous findings.^{17,11} Indeed, packing density scales positively with E across pressures and compositions (Figure 13B). We note that the elastic moduli also exhibit record high changes (eg, 59% increase in E for P2 glass upon

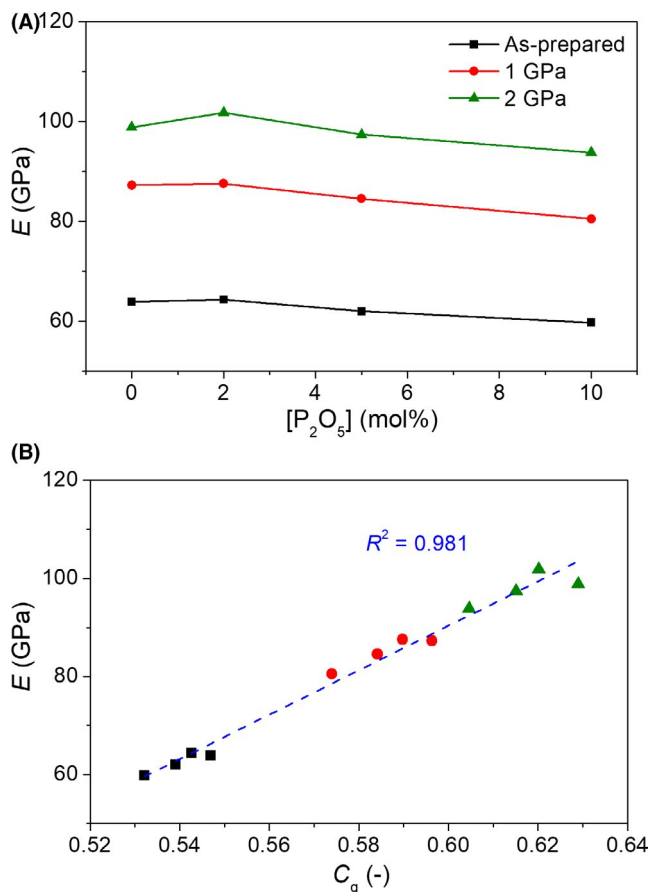


FIGURE 13 (A) Compositional and pressure dependences of the elastic moduli (Young's (E)) in the lithium phosphoaluminoborate glasses. (B) The relation between Young's modulus and atomic packing density [Color figure can be viewed at wileyonlinelibrary.com]

compression at 2 GPa) as a result of compression (Table S1), which is in agreement with the high extent of permanent volume densification exhibited by the studied glass composition in comparison to other oxide glasses.^{11,17} Although the elastic moduli are thus easily changed by compression, Vickers hardness is even more sensitive to the pressure treatment (see below), resulting in a decrease in the elastoplastic ratio E/H with increasing pressure (Figure S6D).

Figure 14A shows the compositional and pressure dependence of Vickers hardness (H_V), with the addition of P_2O_5 having a negative effect on H_V . Furthermore, we find that H_V increases upon hot compression, which is in agreement with the previous works.^{23,11,17} The packing density increases and hence the number of atomic bond constraints per unit volume also increases upon hot compression, resulting in the increase of the Vickers hardness (Figure 14B). Furthermore, the extent of the increase in Vickers hardness upon 2 GPa compression is more pronounced in glasses with higher plastic compressibility (Figure 11C) and lower network former CN changes (Figure S7). However, the H_V versus C_g trend is not perfect (Figure 14B), suggesting that the pressure-induced increase in packing density is not the

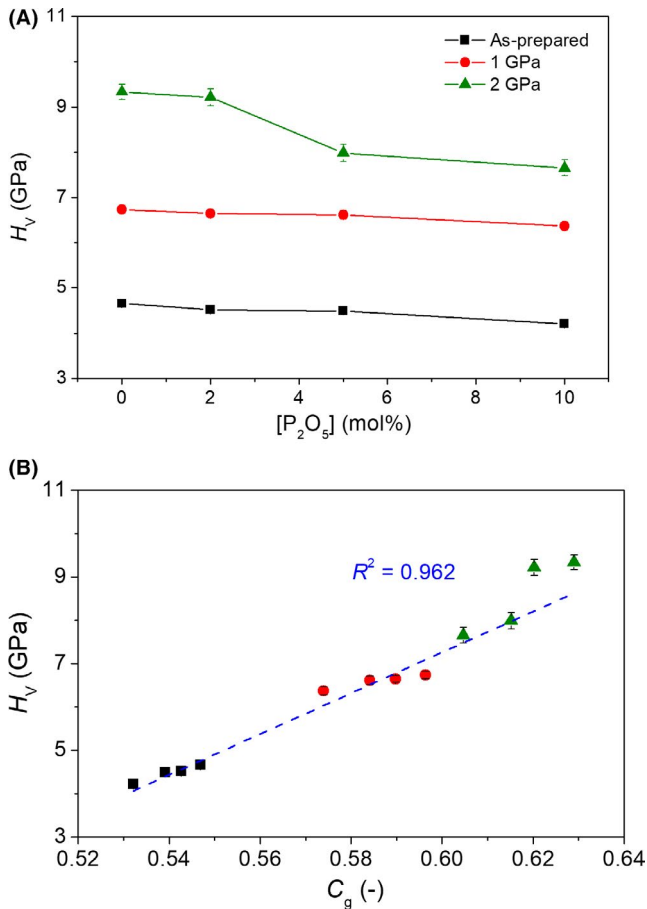


FIGURE 14 (A) Compositional and pressure dependence of Vickers hardness (H_V) in the lithium phosphoaluminoborate glasses. (B) The relation between Vickers hardness and atomic packing density [Color figure can be viewed at wileyonlinelibrary.com]

only reason for the increase in hardness. Indeed, the CNs of the network-forming boron and aluminum cations increase upon compression (Figure S7), resulting in more bond constraints per atom, and thus also contributes to the increase of Vickers hardness.

4 | CONCLUSIONS

In this study, we have investigated the influence of composition and hot compression on the structure and mechanical properties of lithium phosphoaluminoborate glasses. The addition of P_2O_5 partially disturbs the aluminoborate network through the formation of mainly P-O-Al and some P-O-B units, thus decreasing the atomic packing density. The P_2O_5 addition also results in a minor decrease in the CN of boron, but no change in that of aluminum. The introduced phosphate thus competes with boron for some of the Li modifiers, leading to fewer Li-B^{IV} interactions. The average Q^n (P) increases with the addition of P_2O_5 , as more P_2O_5 promotes formation of B-O-P bonds (P^2 and P^3 units), and thus increases the average Q^n (P). The cation-oxygen CNs of both


boron and aluminum increase upon hot compression, while the average Q^n (P) decreases. The high- P_2O_5 glasses have the largest pressure-induced increase in the Al CN (from 4.26 to 4.90 for P10 glass) and largest decrease in the average Q^n (P), resulting in the formation of more NBOs in the compressed glasses, indicating that the higher coordinated Al units are needed to charge-stabilize phosphate NBOs. The B and Al CN changes are found to contribute significantly (around 50% at 2 GPa) to the overall volume densification, which is significantly higher than that found in silicate glasses. The increases in bond constraint density (due to volume densification) and network rigidity (due to higher average CN) is responsible for the pressure-induced increase in hardness and elastic moduli.

ACKNOWLEDGMENTS

This work was supported by the China Scholarship Council (CSC No. 201806370210).

ORCID

Pengfei Liu  <https://orcid.org/0000-0003-2885-4721>

Randall E. Youngman  <https://orcid.org/0000-0002-6647-9865>

Morten M. Smedskjaer  <https://orcid.org/0000-0003-0476-2021>

REFERENCES

- Mostofa MG, Park CI, Park SS. AFM probe based nano mechanical scribing of soda-lime glass. *J Manuf Process*. 2013;15(4):625–34.
- Brambilla G, Payne DN. The ultimate strength of glass silica nanowires. *Nano Lett*. 2009;9(2):831–5.
- Frankberg EJ, Kalikka J, García Ferré F, Joly-Pottuz L, Salminen T, Hintikka J, et al. Highly ductile amorphous oxide at room temperature and high strain rate. *Science*. 2019;366(6467):864–9.
- Wondraczek L, Mauro JC, Eckert J, Kühn U, Horbach J, Deubener J, et al. Towards ultrastrong glasses. *Adv Mater*. 2011;23(39):4578–86.
- Ritter JE, Sherburne CL. Dynamic and static fatigue of silicate glasses. *J. Am Ceram Soc*. 1971;54(12):601–5.
- Kurkjian CR, Gupta PK, Brow RK. The strength of silicate glasses: What do we know, what do we need to know? *Int J Appl Glas Sci*. 2010;1(1):27–37.
- Gardon R. CHAPTER 5 - Thermal Tempering of Glass. *Glass Sci Technol*. 1980;5:145–216.
- Sglavo VM, Prezzi A, Zandonella T. Engineered stress-profile silicate glass: high strength material insensitive to surface defects and fatigue. *Adv Eng Mater*. 2004;6(5):344–9.
- Varshneya AK. Chemical Strengthening of Glass: Lessons Learned and Yet To Be Learned. *Int J Appl Glass Sci*. 2010;1(2):094503.131–142.
- Mauro JC, Tandia A, Vargheese KD, Mauro YZ, Smedskjaer MM. Accelerating the design of functional glasses through modeling. *Chem Mater*. 2016;28(12):4267–77.
- Kapoor S, Wondraczek L, Smedskjaer MM. Pressure-Induced densification of oxide glasses at the glass transition. *Front Mater*. 2017;4:1–20.

12. Januchta K, Stepniewska M, Jensen LR, Zhang Y, Somers MAJ, Bauchy M, et al. Breaking the limit of micro-ductility in oxide glasses. *Adv Sci*. 2019;6(18):1901281.
13. Peter KW. Densification and flow phenomena of glass in indentation experiments. *J Non Cryst Solids*. 1970;5(2):103–15.
14. Rouxel T, Ji H, Guin JP, Augereau F, Rufflé B. Indentation deformation mechanism in glass: densification versus shear flow. *J Appl Phys*. 2010;107(9):094903.
15. Yoshida S, Sanglebœuf JC, Rouxel T. Quantitative evaluation of indentation-induced densification in glass. *J Mater Res*. 2005;20(12):3404–12.
16. Yoshida S, Sawasato H, Sugawara T, Miura Y, Matsuoka J. Effects of indenter geometry on indentation-induced densification of soda-lime glass. *J Mater Res*. 2010;25(11):2203–11.
17. Svenson MN, Guerette M, Huang L, Lönnroth N, Mauro JC, Rzoska SJ, et al. Universal behavior of changes in elastic moduli of hot compressed oxide glasses. *Chem Phys Lett*. 2016;651:88–91.
18. Deschamps T, Margueritat J, Martinet C, Mermet A, Champagnon B. Elastic moduli of permanently densified silica glasses. *Sci Rep*. 2015;4(1):7193.
19. Bechgaard TK, Goel A, Youngman RE, Mauro JC, Rzoska SJ, Bockowski M, et al. Structure and mechanical properties of compressed sodium aluminosilicate glasses: Role of non-bridging oxygens. *J Non Cryst Solids*. 2016;441:49–57.
20. Kapoor S, Guo X, Youngman RE, Hogue CL, Mauro JC, Rzoska SJ, et al. Network glasses under pressure: Permanent densification in modifier-free $\text{Al}_2\text{O}_3\text{-B}_2\text{O}_3\text{-P}_2\text{O}_5\text{-SiO}_2$ Systems. *Phys Rev Appl*. 2017;7(5):054011.
21. Smedskjaer MM, Bauchy M, Mauro JC, Rzoska SJ, Bockowski M. Unique effects of thermal and pressure histories on glass hardness: structural and topological origin. *J Chem Phys*. 2015;143(16):164505.
22. Lee SK, Mun KY, Kim Y, Lhee J, Okuchi T, Lin J. Degree of permanent densification in oxide glasses upon extreme compression up to 24 gpa at room temperature. *J Phys Chem Lett*. 2020;11(8):2917–24.
23. Januchta K, Youngman RE, Goel A, Bauchy M, Logunov SL, Rzoska SJ, et al. Discovery of ultra-crack-resistant oxide glasses with adaptive networks. *Chem Mater*. 2017;29(14):5865–76.
24. Svenson MN, Bechgaard TK, Fuglsang SD, Pedersen RH, Tjell AØ, Østergaard MB, et al. Composition-Structure-Property relations of compressed borosilicate glasses. *Phys Rev Appl*. 2014;2(2):024006.
25. Østergaard MB, Youngman RE, Svenson MN, Rzoska SJ, Bockowski M, Jensen LR, et al. Temperature-Dependent densification of sodium borosilicate glass. *RSC Adv*. 2015;5(96):78845–51.
26. Januchta K, Bauchy M, Youngman RE, Rzoska SJ, Bockowski M, Smedskjaer MM. Modifier field strength effects on densification behavior and mechanical properties of alkali aluminoborate glasses. *Phys Rev Mater*. 2017;1(6):063603.
27. Januchta K, Youngman RE, Goel A, Bauchy M, Rzoska SJ, Bockowski M, et al. Structural origin of high crack resistance in sodium aluminoborate glasses. *J Non Cryst Solids*. 2017;460:54–65.
28. Frederiksen KF, Januchta K, Mascaraque N, Youngman RE, Bauchy M, Rzoska SJ, et al. Structural compromise between high hardness and crack resistance in aluminoborate glasses. *J Phys Chem B*. 2018;122(23):6287–95.
29. Liu P, Januchta K, Jensen LR, Bauchy M, Smedskjaer MM. Competitive effects of free volume, rigidity, and self-adaptivity on indentation response of silicoaluminoborate glasses. *J Am Ceram Soc*. 2020;103(2):944–54.
30. Dickinson JE, de Jong BHWS, Schramm CM. Hydrogen-Containing glass and Gas-Ceramic microfoams: Raman, XPS, and MAS-NMR Results on the structure of precursor $\text{SiO}_2\text{-B}_2\text{O}_3\text{-P}_2\text{O}_5$ Glasses. *J Non Cryst Solids*. 1988;102(1–3):196–204.
31. Kato Y, Yamazaki H, Kubo Y, Yoshida S, Matsuoka J, Akai T. Effect of B_2O_3 Content on crack initiation under vickers indentation test. *J Ceram Soc Japan*. 2010;118(1381):792–8.
32. Smedskjaer MM, Rzoska SJ, Bockowski M, Mauro JC. Mixed alkaline earth effect in the compressibility of aluminosilicate glasses. *J Chem Phys*. 2014;140(5):054511.
33. Shannon RD. Revised effective ionic radii and systematic studies of interatomic distances in halides and chalcogenides. *Acta Crystallogr Sect A*. 1976;32(5):751–67.
34. Massiot D, Fayon F, Capron M, King I, Le Calvé S, Alonso B, et al. Modelling One- and Two-Dimensional Solid-State NMR Spectra. *Magn Reson Chem*. 2002;40(1):70–6.
35. Li H, Su Y, Li L, Strachan DM. Raman Spectroscopic Study of Gadolinium(III) in Sodium-Aluminoborosilicate Glasses. *J Non Cryst Solids*. 2001;292(1–3):167–76.
36. Lai YM, Liang XF, Yang SY, Wang JX, Zhang BT. Raman spectra study of iron phosphate glasses with sodium sulfate. *J Mol Struct*. 2012;1013:134–7.
37. Konijnendijk WL, Stevels JM. The structure of borosilicate glasses studied by Raman Scattering. *J Non Cryst Solids*. 1976;20(2):193–224.
38. Kamitsos EI, Chryssikos GD. Borate glass structure by Raman and infrared spectroscopies. *J Mol Struct*. 1991;247(C):1–16.
39. Meera BN, Ramakrishna J. Raman spectral studies of borate glasses. *J Non Cryst Solids*. 1993;159(1–2):1–21.
40. Vignarooban K, Boolchand P, Micoulaut M, Malki M, Bresser WJ. Rigidity Transitions in glasses driven by changes in network dimensionality and structural groupings. *Europhysics Lett*. 2014;108(5):56001.
41. Krogh-Moe J. The Structure of vitreous and liquid boron oxide. *J Non Cryst Solids*. 1969;1(4):269–84.
42. Hudgens JJ, Brow RK, Tallant DR, Martin SW. Raman spectroscopy study of the structure of lithium and sodium ultraphosphate glasses. *J Non Cryst Solids*. 1998;223(1–2):21–31.
43. McMillan P, Piriou B. Raman spectroscopy of calcium aluminate glasses and crystals. *J Non Cryst Solids*. 1983;55(2):221–42.
44. Licheron M, Montouillout V, Millot F, Neuville DR. Raman and ^{27}Al NMR Structure Investigations of Aluminate Glasses: $(1-x)\text{Al}_2\text{O}_3\text{-xMO}$, with $\text{M}=\text{Ca, Sr, Ba}$ and $0.5 < x < 0.75$. *J Non Cryst Solids*. 2011;357(15):2796–801.
45. Ollier N, Charpentier T, Boizot B, Wallez G, Ghaleb D. A Raman and MASNMR Study of Mixed Alkali Na-K and Na-Li Aluminoborosilicate Glasses. *J Non Cryst Solids*. 2004;341(1–3):26–34.
46. Le Saoût G, Simon P, Fayon F, Blin A, Vaills Y. Raman and infrared study of $(\text{PbO})_x(\text{P}_2\text{O}_5)_{(1-x)}$ Glasses. *J Raman Spectrosc*. 2002;33(9):740–6.
47. Yano T, Kunimine N, Shibata S, Yamane M. Structural investigation of sodium borate glasses and melts by Raman Spectroscopy. *J Non Cryst Solids*. 2003;321(3):137–46.
48. Weber R, Sen S, Youngman RE, Hart RT, Benmore CJ. Structure of High Alumina Content $\text{Al}_2\text{O}_3\text{-SiO}_2$ Composition Glasses. *J Phys Chem B*. 2008;112(51):16726–33.
49. Du LS, Stebbins JF. Site connectivities in sodium aluminoborate glasses: multinuclear and multiple quantum NMR Results. *Solid State Nucl Magn Reson*. 2005;27(1–2):37–49.

50. Aitken BG, Youngman RE, Deshpande RR, Eckert H. Structure-Property relations in mixed-network glasses: Multinuclear solid state NMR investigations of the system $x\text{Al}_2\text{O}_3:(30-x)\text{P}_2\text{O}_5:70\text{SiO}_2$. *J Phys Chem C*. 2009;113(8):3322–31.
51. Youngman RE, Zwanziger JW. Network modification in potassium borate glasses: Structural studies with NMR and Raman Spectroscopies. *J Phys Chem*. 1996;100(41):16720–8.
52. Turner GL, Smith KA, Kirkpatrick RJ, Oldfield E. Boron-11 Nuclear magnetic resonance spectroscopic study of borate and borosilicate minerals and a borosilicate glass. *J Magn Reson*. 1986;67(3):544–50.
53. Michaelis VK, Kachhadia P, Kroeker S. Clustering in Borate-Rich alkali borophosphate glasses: A ^{11}B and ^{31}P MAS NMR study. *Phys Chem Glas Eur J Glas Sci Technol Part B*. 2013;54(1):20–6.
54. Bista S, Morin EI, Stebbins JF. Response of complex networks to compression: Ca, La, and Y Aluminoborosilicate glasses formed from liquids at 1 to 3 GPa Pressures. *J Chem Phys*. 2016;144(4):044502.
55. Svenson MN, Youngman RE, Yue Y, Rzoska SJ, Bockowski M, Jensen LR, et al. Volume and structural relaxation in compressed sodium borate glass. *Phys Chem Chem Phys*. 2016;18(43):29879–91.
56. Brow RK. Review: The structure of simple phosphate glasses. *J Non Cryst Solids*. 2000;263–264:1–28.
57. van Wüllen L, Eckert H, Schwering G. Structure-Property Correlations in Lithium Phosphate Glasses: New Insights from $^{31}\text{P} \leftrightarrow ^7\text{Li}$ Double-Resonance NMR. *Chem Mater*. 2000;12(7):1840–6.
58. Uesbeck T, Eckert H, Youngman R, Aitken B. The structure of borophosphosilicate pure network former glasses studied by multinuclear NMR Spectroscopy. *J Phys Chem C*. 2017;121(3):1838–50.
59. Cody GD, Mysen B, Sághi-Szabó G, Tossell JA. Silicate-Phosphate Interactions in Silicate Glasses and Melts: I. A Multinuclear (^{27}Al , ^{29}Si , ^{31}P) MAS NMR and Ab Initio Chemical Shielding (^{31}P) Study of Phosphorous Speciation in Silicate Glasses. *Geochim Cosmochim Acta*. 2001; 65(14):2395–411.
60. Brow RK, Kirkpatrick RJ, Turner GL. Local Structure of $\text{XAl}_2\text{O}_3(1-x)\text{NaPO}_3$ Glasses: An NMR and XPS Study. *J Am Ceram Soc*. 1990;73(8):2293–300.
61. Wu J, Deubener J, Stebbins JF, Grygarova L, Behrens H, Wondraczek L, et al. Structural response of a highly viscous aluminoborosilicate melt to isotropic and anisotropic compressions. *J Chem Phys*. 2009;131(10):104504.
62. Wu J, Gross TM, Huang L, Jaccani SP, Youngman RE, Rzoska SJ, et al. composition and pressure effects on the structure, elastic properties and hardness of aluminoborosilicate glass. *J Non Cryst Solids*. 2020;530:119797.
63. Rouxel T. Elastic properties and Short-to Medium-Range order in glasses. *J Am Ceram Soc*. 2007;90(10):3019–39.
64. Wilkinson CJ, Zheng Q, Huang L, Mauro JC. Topological constraint model for the elasticity of Glass-Forming systems. *J Non-Crystalline Solids X*. 2019;2:100019.
65. Yang K, Yang B, Xu X, Hoover C, Smedskjaer MM, Bauchy M. Prediction of the young's modulus of silicate glasses by topological constraint theory. *J Non Cryst Solids*. 2019;514:15–9.

SUPPORTING INFORMATION

Additional supporting information may be found online in the Supporting Information section.

How to cite this article: Liu P, Søndergaard ALS, Youngman RE, et al. Structural densification of lithium phosphoaluminoborate glasses. *J Am Ceram Soc*. 2021;104:1345–1359. <https://doi.org/10.1111/jace.17559>

SUPPORTING INFORMATION

Structural Densification of Lithium Phosphoaluminoborate Glasses

Pengfei Liu¹, Andreas L. S. Søndergaard¹, Randall E. Youngman², Sylwester J. Rzoska³, Michal Bockowski³, Lars R. Jensen⁴, Morten M. Smedskjaer^{1,*}

¹*Department of Chemistry and Bioscience, Aalborg University, Aalborg, Denmark*

²*Science and Technology Division, Corning Incorporated, Corning, USA*

³*Institute of High-Pressure Physics, Polish Academy of Sciences, Warsaw, Poland*

⁴*Department of Materials and Production, Aalborg University, Aalborg, Denmark*

* Corresponding author. e-mail: mos@bio.aau.dk

Table S1. Overview of the properties of the as-prepared and hot compressed (at 1 and 2 GPa) glasses, including glass transition temperature (T_g), density (ρ), molar volume (V_m), atomic packing density (C_g), Young's modulus (E), shear modulus (G), bulk modulus (B), Poisson's ratio (ν), and Vickers hardness (H_v).

Glass	T_g [°C]	ρ [g/cm ³]	V_m [cm ³ /mol]	C_g [-]	E [GPa]	G [GPa]	B [GPa]	ν [-]	$H_v^{(*)}$ [GPa]
As-prepared									
P0	476	2.248	29.37	0.547	64	25	46	0.270	4.65
P2	479	2.248	30.21	0.543	64	25	47	0.270	4.51
P5	481	2.245	31.28	0.539	62	24	45	0.269	4.49
P10	480	2.256	33.15	0.532	60	24	42	0.260	4.21
Compressed at 1 GPa									
P0	-	2.449	26.97	0.596	87	35	61	0.263	6.73
P2	-	2.440	27.83	0.590	88	35	61	0.263	6.64
P5	-	2.430	28.90	0.584	85	34	59	0.260	6.61
P10	-	2.430	30.77	0.574	81	32	54	0.253	6.37
Compressed at 2 GPa									
P0	-	2.581	25.58	0.629	99	40	60	0.227	9.33
P2	-	2.564	26.48	0.620	102	41	63	0.232	9.21
P5	-	2.557	27.46	0.615	97	39	62	0.237	7.98
P10	-	2.558	29.24	0.605	94	39	55	0.214	7.65
Error estimate	≤2	≤0.002	≤0.02	0.001	≤1	≤1	≤1	≤0.005	≤0.2

(*) H_v measured at ambient conditions at load of 4.9 N.

(**) CR measured at ambient conditions (temperature 22 °C, relative humidity ~45 %).

Table S2. Raman band deconvolution assignment with references.

Structural unit	Wavenumber [cm⁻¹]	Ref
Bending of PO₄ unit	303-337	1
B-O-B stretch & BO₄ unit	450-570 & 900-1000	2
Al-O-B stretch & aluminate network	480-500 & 700-720	2
P₂O₇⁴⁻ unit	525-583	1
Ring metaborate	630 & 1300-1600	2,3,4
P-O-P bridging	685	5
Chain metaborate	730 & 1300-1600	2,3
Di-triborate	755	6
Tri-, Tetra- or Pentaborate	770 & 930	3,4,6,7
Boroxol ring	808	3,8
Pyroborate	820 & 1200-1300	2,3,4
AlO₄ unit	790 & 900	9,10
Orthoborate	890-940	2
PO₂⁻, P₂O₇⁴⁻, PO₃²⁻	1039-1090	11
Diborate	1100, 465-500	4,12
BO₃ unit	1260, 1350, 1470, & 1530	13
BO₂O- unit	1490 & 1550	13
Al-B network	980	14

Table S3. Parameters used in deconvolution of ^{11}B MAS NMR spectra and the resulting boron speciation (with errors smaller than $\pm 1\%$). We have used two B^{III} sites, attributed to ring (r) and non-ring (nr) BO_3 polyhedra, and one or two B^{IV} sites (labeled a and b), as described in the main text. The 'Q mas $\frac{1}{2}$ ' function in DMFit was used to simulate the 2nd-order quadrupolar lineshape of B^{III} resonances, yielding estimates for isotropic chemical shift (δ_{CS}), quadrupolar coupling constant (C_Q) and peak area (Int). B^{IV} peaks were fitted with a 'Gaus/Lor' function in DMFit, providing δ_{CS} and peak area. We note that the B^{IV} peaks were fitted to determine total N_4 values rather than the relative fraction of the different types of B^{IV} .

Pressure	$\text{B}^{\text{III}}(\text{r})$			$\text{B}^{\text{III}}(\text{nr})$			$\text{B}^{\text{IV}}(\text{a})$		$\text{B}^{\text{IV}}(\text{b})$	
	Int (%)	δ_{CS} (ppm)	C_Q (MHz)	Int (%)	δ_{CS} (ppm)	C_Q (MHz)	Int (%)	δ_{CS} (ppm)	Int (%)	δ_{CS} (ppm)
P0										
As-prepared	62.0	18.0	2.66	22.5	16.1	2.62	15.5	0.9	---	---
1 GPa	61.7	18.0	2.65	14.5	15.7	2.57	23.8	0.8	---	---
2 GPa	50.9	18.1	2.67	17.1	16.4	2.62	28.9	0.8	3.1	-0.6
P2										
As-prepared	62.2	17.9	2.60	22.8	15.6	2.48	7.7	1.0	7.3	0.4
1 GPa	59.9	17.9	2.63	16.7	15.6	2.53	14.3	1.0	9.1	0.2
2 GPa	53.1	18.0	2.64	15.3	15.7	2.53	27.1	0.8	4.5	-0.4
P5										
As-prepared	60.1	17.8	2.60	25.3	15.6	2.51	7.3	1.0	7.3	0.4
1 GPa	51.6	18.0	2.66	25.5	16.3	2.63	12.1	0.9	10.8	0.2
2 GPa	24.8	18.1	2.72	43.8	17.3	2.66	25.0	0.8	6.4	-0.4
P10										
As-prepared	28.9	18.1	2.68	56.5	16.9	2.64	8.5	0.9	6.1	0.3
1 GPa	26.7	18.0	2.69	51.3	17.0	2.66	9.8	0.9	12.2	0.1
2 GPa	25.8	18.0	2.69	43.1	17.1	2.68	22.6	0.8	8.5	-0.4

Table S4. Al polyhedra and associated NMR parameters for glasses obtained by deconvolution of ^{27}Al MAS NMR spectra. The errors of the uncertainties in intensity (Int), isotropic chemical shift (δ_{CS}), and quadrupolar coupling constant (C_Q) do not exceed $\pm 1\%$, ± 1 ppm and ± 0.1 MHz, respectively.

Pressure	Al^{IV}			Al^{V}			Al^{VI}		
	Int (%)	δ_{CS} (ppm)	C_Q (MHz)	Int (%)	δ_{CS} (ppm)	C_Q (MHz)	Int (%)	δ_{CS} (ppm)	C_Q (MHz)
P0									
As-prepared	77	65	6.4	19	37	7.1	4	9	6.0
1 GPa	55	66	7.3	31	38	7.9	14	9	6.1
2 GPa	40	67	8.3	39	38	8.6	21	9	6.1
P2									
As-prepared	76	64	6.7	20	36	7.3	4	8	5.7
1 GPa	53	65	7.5	33	37	8.2	14	8	6.2
2 GPa	40	66	8.6	39	37	8.9	21	8	6.3
P5									
As-prepared	76	61	7.0	19	35	7.8	5	6	5.6
1 GPa	52	62	7.7	33	36	8.5	15	7	6.2
2 GPa	37	63	8.6	41	36	9.0	22	7	6.4
P10									
As-prepared	78	56	6.2	18	32	7.7	4	4	5.1
1 GPa	52	56	6.4	35	33	8.5	13	4	6.0
2 GPa	32	55	6.0	46	33	8.6	22	5	6.5

Table S5. Phosphorus speciation derived from ^{31}P MAS NMR measurements. The estimated errors in shift, full width at half maximum (FWHM), and area are ± 1 ppm, ± 1 ppm, and $\pm 3\%$, respectively.

	2P			5P			10P		
	Shift (ppm)	FWHM (ppm)	Area (%)	Shift (ppm)	FWHM (ppm)	Area (%)	Shift (ppm)	FWHM (ppm)	Area (%)
Q^0	8.5	9	1	-	-	-	-	-	-
Q^1	-6.1	11	41	-6.1	10.1	19	-6.1	10.1	8
Q^{1-1}	-13.2	11	47	-13.2	11.3	57	-13.6	10.8	43
Q^2	-22	12	11	-21.7	12.7	24	-21.8	13.2	46
Q^{2-1}	-	-	-	-	-	-	-29.6	13	3

Figure S1. X-ray diffraction (XRD) spectra for the as-prepared lithium phosphoaluminoborate glasses with different content of P_2O_5 . No sharp peaks are observed in the spectra, confirming the non-crystalline nature of the glasses at least within the XRD detection limit.

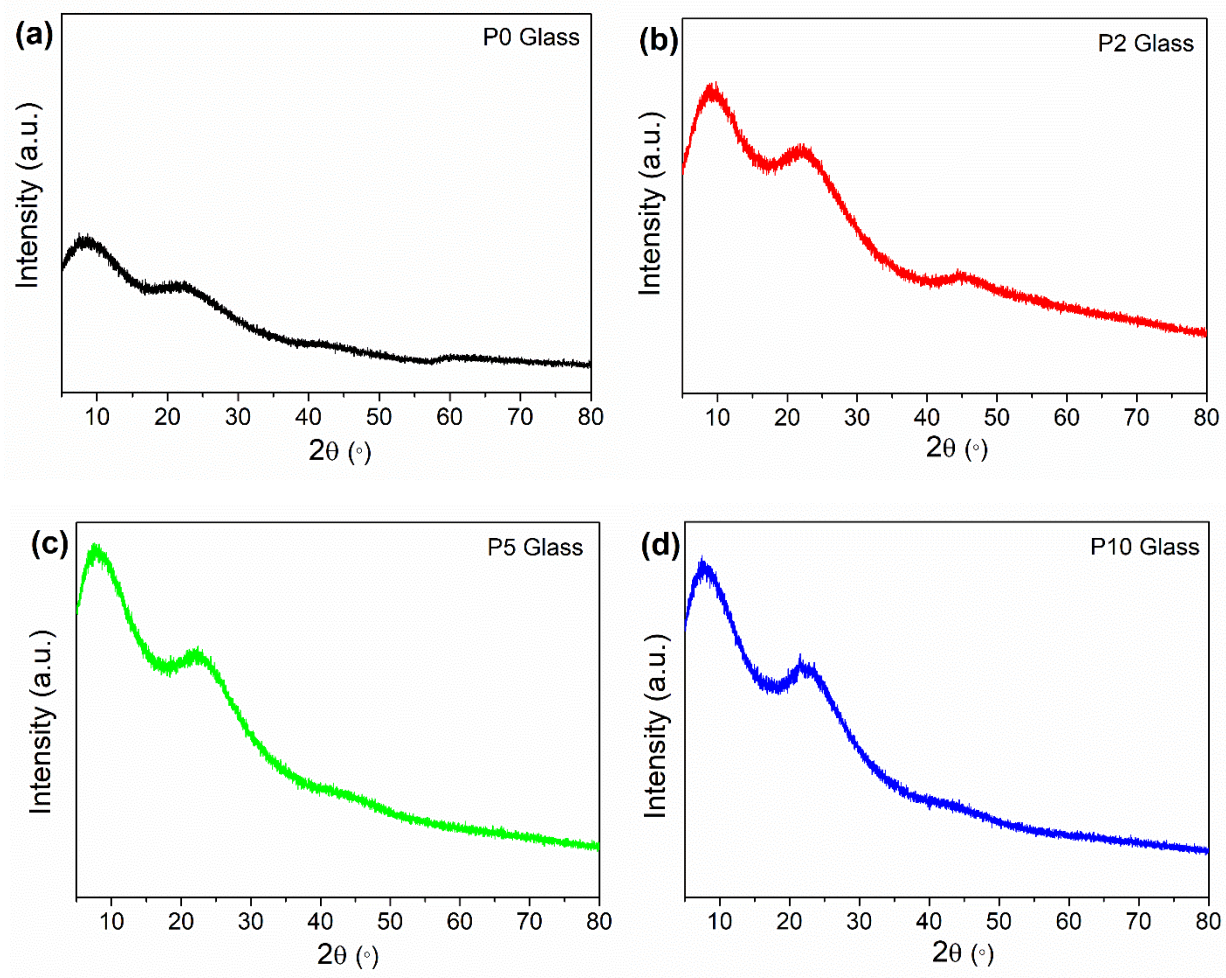


Figure S2. Micro-Raman spectra on the surface of the as-prepared lithium phosphoaluminoborate glasses at three different locations. No significant differences across the sample surface are observed, suggesting that the glasses are compositionally homogeneous.

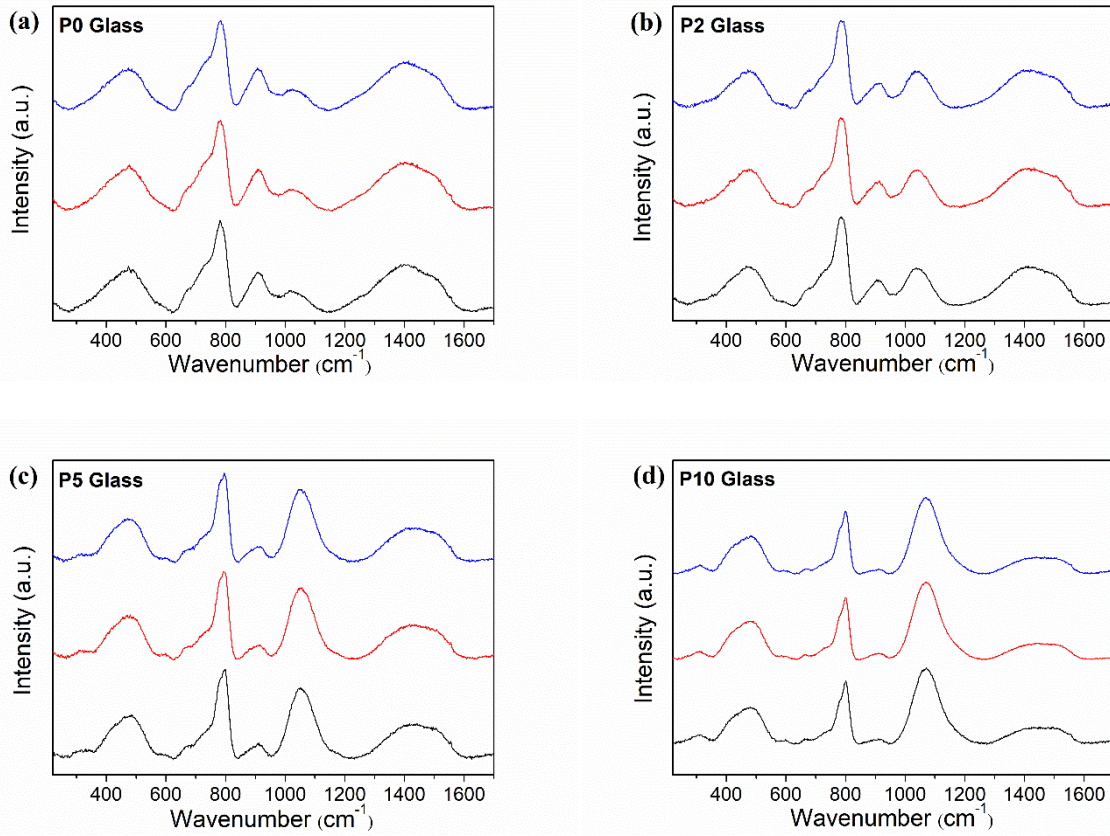


Figure S3. Pressure dependence of the relative area fractions of the main Raman bands for the four lithium phosphoaluminoborate glasses.

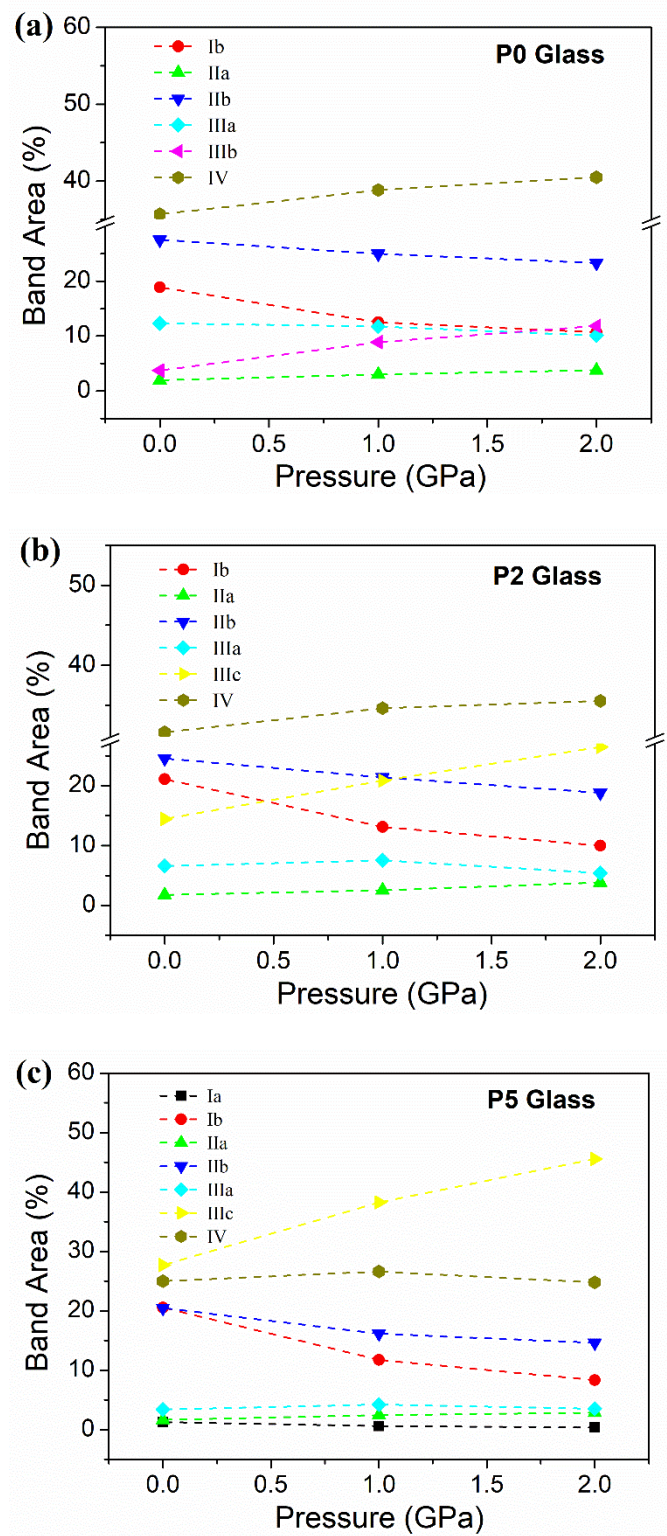


Figure S4. Examples of deconvolutions of solid state NMR spectra for the present glasses: (a) Deconvolution of ^{27}Al MAS NMR spectrum of P0 glass compressed at 1 GPa; (b) Deconvolution of ^{11}B MAS NMR spectra for the as-prepared glasses, where the filled, black curve denotes an underlying satellite transition resonance (see main text); (c) Deconvolution of ^{31}P MAS NMR spectra for the as-prepared P-containing glasses.

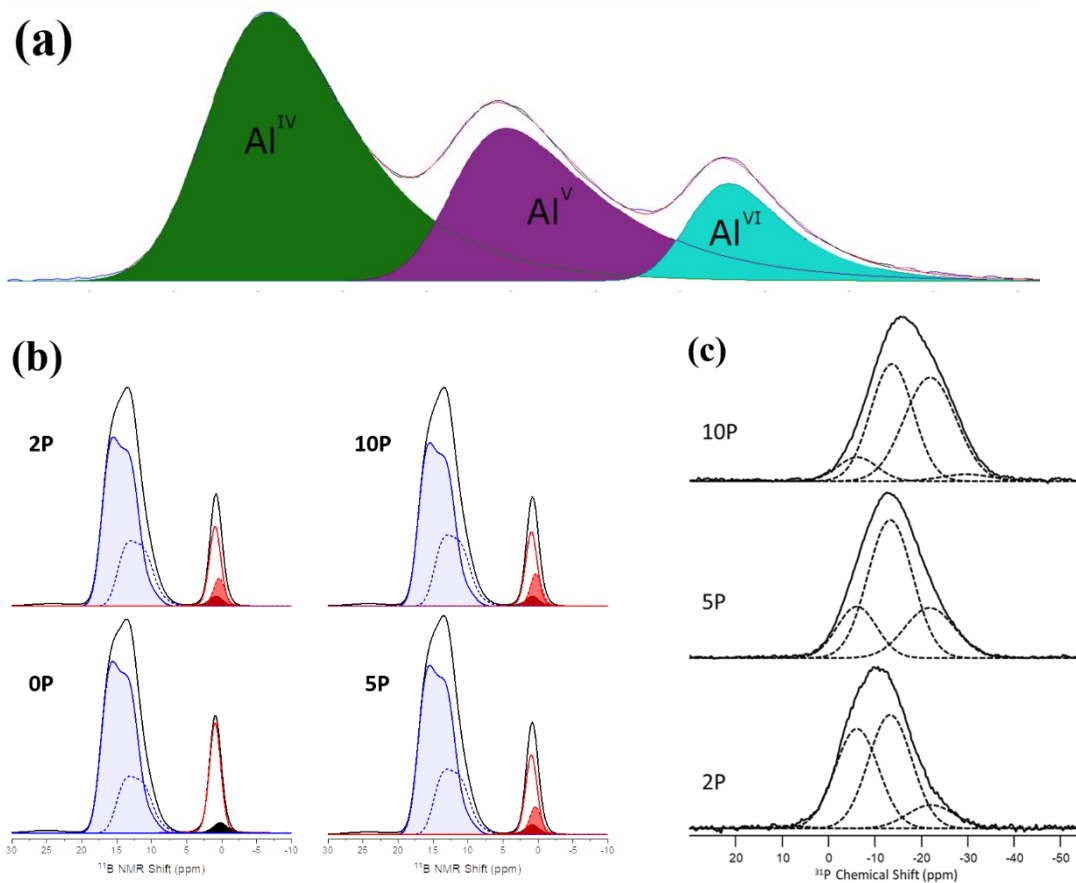


Figure S5. Correlation between $\Delta V_{m(\text{Al+B})}/\Delta V_m$ (the boron and aluminum coordination change contribution to the overall volume densification) and atomic self-adaptivity ($\langle \Delta n \rangle \Delta \rho / (\rho_0 P)$) upon hot compression at 2 GPa for the four present glasses. The dashed line is a guide for the eye.

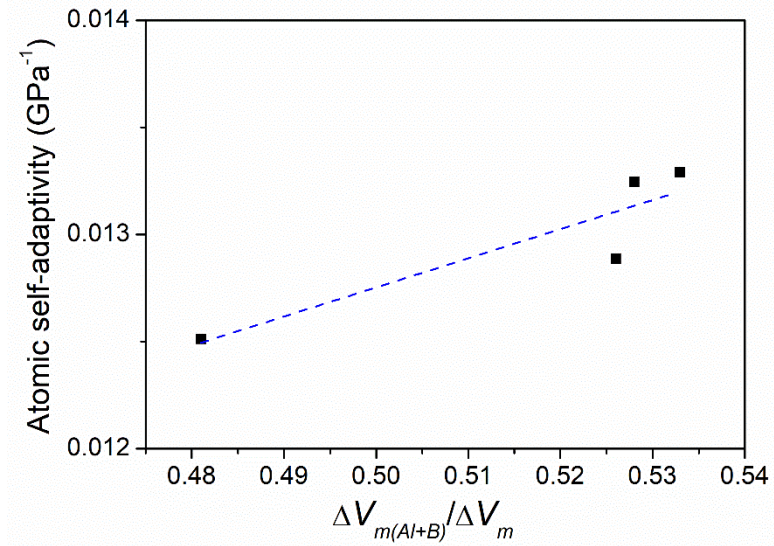


Figure S6. Composition and pressure dependence of (a) shear modulus G , (b) bulk modulus B , (c) Poisson's ratio ν , and (d) elastoplastic ratio E/H_V for the lithium phosphoaluminoborate glasses.

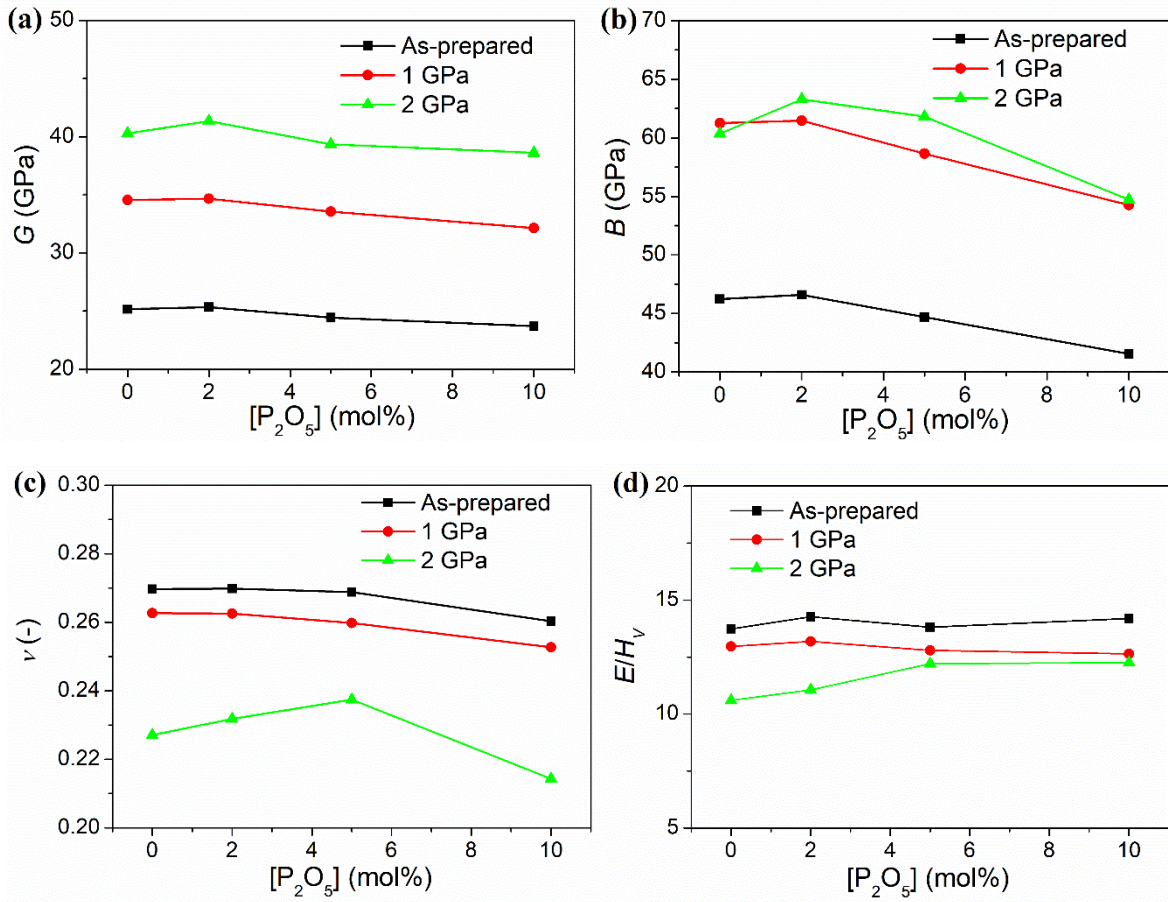
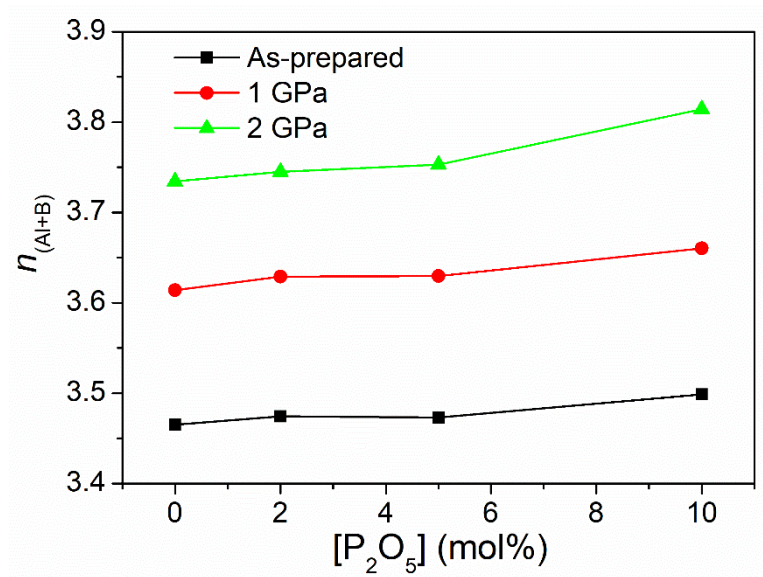


Figure S7. Compositional and pressure dependence of network former (boron and aluminum) coordination numbers.



Supporting References

- (1) Lai, Y. M.; Liang, X. F.; Yang, S. Y.; Wang, J. X.; Zhang, B. T. Raman Spectra Study of Iron Phosphate Glasses with Sodium Sulfate. *J. Mol. Struct.* **2012**, *1013*, 134–137.
- (2) Li, H.; Su, Y.; Li, L.; Strachan, D. M. Raman Spectroscopic Study of Gadolinium(III) in Sodium-Aluminoborosilicate Glasses. *J. Non. Cryst. Solids* **2001**, *292* (1–3), 167–176.
- (3) Konijnendijk, W. L.; Stevels, J. M. The Structure of Borosilicate Glasses Studied by Raman Scattering. *J. Non. Cryst. Solids* **1976**, *20* (2), 193–224.
- (4) Kamitsos, E. I.; Chryssikos, G. D. Borate Glass Structure by Raman and Infrared Spectroscopies. *J. Mol. Struct.* **1991**, *247* (C), 1–16.
- (5) Hudgens, J. J.; Brow, R. K.; Tallant, D. R.; Martin, S. W. Raman Spectroscopy Study of the Structure of Lithium and Sodium Ultraphosphate Glasses. *J. Non. Cryst. Solids* **1998**, *223* (1–2), 21–31.
- (6) Meera, B. N.; Ramakrishna, J. Raman Spectral Studies of Borate Glasses. *J. Non. Cryst. Solids* **1993**, *159* (1–2), 1–21.
- (7) Vignarooban, K.; Boolchand, P.; Micoulaut, M.; Malki, M.; Bresser, W. J. Rigidity Transitions in Glasses Driven by Changes in Network Dimensionality and Structural Groupings. *EPL (Europhysics Lett.)* **2014**, *108* (5), 56001.
- (8) Krogh-Moe, J. The Structure of Vitreous and Liquid Boron Oxide. *J. Non. Cryst. Solids* **1969**, *1* (4), 269–284.
- (9) McMillan, P.; Piriou, B. Raman Spectroscopy of Calcium Aluminate Glasses and Crystals. *J. Non. Cryst. Solids* **1983**, *55* (2), 221–242.
- (10) Licheron, M.; Montouillout, V.; Millot, F.; Neuville, D. R. Raman and ^{27}Al NMR Structure Investigations of Aluminate Glasses: $(1-x)\text{Al}_2\text{O}_3-x\text{MO}$, with $\text{M}=\text{Ca}, \text{Sr}, \text{Ba}$ and $0.5 < x < 0.75$). *J. Non. Cryst. Solids* **2011**, *357* (15), 2796–2801..
- (11) Le Saoût, G.; Simon, P.; Fayon, F.; Blin, A.; Vaills, Y. Raman and Infrared Study of $(\text{PbO})_x (\text{P}_2\text{O}_5)_{(1-x)}$ Glasses. *J. Raman Spectrosc.* **2002**, *33* (9), 740–746.
- (12) Yadav, A. K.; Singh, P. A Review of the Structures of Oxide Glasses by Raman Spectroscopy. *RSC Adv.* **2015**, *5* (83), 67583–67609.
- (13) Yano, T.; Kunimine, N.; Shibata, S.; Yamane, M. Structural Investigation of Sodium Borate Glasses and Melts by Raman Spectroscopy. *J. Non. Cryst. Solids* **2003**, *321* (3), 137–146.
- (14) Brow, R. K.; Tallant, D. R.; Turner, G. L. Polyhedral Arrangements in Lanthanum Aluminoborate Glasses. *J. Am. Ceram. Soc.* **2005**, *80* (5), 1239–1244.

Paper IV

Achieving ultrahigh crack resistance in glass through humid aging

Pengfei Liu,¹ Randall E. Youngman², Lars R. Jensen³, Michal Bockowski,⁴ and Morten M. Smedskjaer^{1,*}

¹*Department of Chemistry and Bioscience, Aalborg University, 9220 Aalborg, Denmark*

²*Science and Technology Division, Corning Incorporated, Corning, New York 14831, USA*

³*Department of Materials and Production, Aalborg University, 9220 Aalborg, Denmark*

⁴*Institute of High-Pressure Physics, Polish Academy of Sciences, 01-142 Warsaw, Poland*



(Received 26 February 2020; revised manuscript received 14 May 2020; accepted 22 May 2020; published 19 June 2020)

Oxide glasses continue to be among the most important materials for a sustainable society owing to their unique advantages, e.g., transparency, formability, low cost, and tailorable properties and functionalities. However, their high brittleness has severely been hindering the use of oxide glasses for many engineering and functional applications. Previous approaches to overcome this limitation by improving the fracture toughness have largely failed, but herein we report the use of a simple post-treatment, namely surface aging in a humid atmosphere, to improve not the resistance to crack growth, but rather the resistance to crack initiation. The effect of such aging on the mechanical performance is found to be highly composition dependent, and in stark contrast to most previous work, we thus find that water incorporation is not always a foe, but can also be a friend for glass mechanics. Specifically, we demonstrate crack-free ultrasharp cube corner indents in an aged caesium aluminoborate glass at loads above 25 N, while other aged oxide glasses studied in this work easily crack at loads below 1 N. The aging effect is found to be due to a combination of stress and hydrolysis assisted structural changes in the flexible aluminoborate glass network.

DOI: [10.1103/PhysRevMaterials.4.063606](https://doi.org/10.1103/PhysRevMaterials.4.063606)

I. INTRODUCTION

Oxide glasses continue to be among the most important engineering and functional manmade materials due to their useful properties, such as good transparency, relatively high hardness, and good chemical durability. Although the ultimate strength and ductility of defect-free amorphous oxides can be high [1,2], all known bulk oxide glasses are inherently brittle because of the lack of a stable shearing deformation mechanism and limited resistance to crack growth (low fracture toughness) [3–5]. To overcome this limitation, various postprocessing methods are used in industry, most notably thermal tempering [6] and chemical strengthening [7,8], with the aim to increase the critical stress needed for crack initiation and to retard the rate of crack growth by counteracting the stresses acting on the crack tip. In addition to adding extra cost, these methods are also limited to either relatively thick glasses (thermal tempering) or mobile ion-containing glasses (chemical strengthening). Alternatively, recent work has shown some promise in toughening oxide glasses by incorporating crystalline or glassy nanoparticles in the glass, but these treatments either require high pressure (and thus limits the sample size) or lead to a loss of transparency [9,10].

Another attractive strategy to overcome the limitations of brittleness is to enhance the damage or crack resistance through rational composition design [11–13]. Crack resistance (CR) here refers to the glass' ability to withstand stress without initiation of cracks upon sharp contact loading [14],

specifically the load resulting in 50% probability of corner crack formation during indentation [14]. Such sharp contact deformation is a typical failure mode in the field for, e.g., cover glasses, and particularly radial cracks, propagating perpendicular to the glass surface, are believed to be important, as they can become the strength-limiting factor for many applications [15]. Recent examples of such tailored crack-resistant glasses include mixed modifier aluminosilicate [16], binary aluminosilicate [13], calcium boroaluminosilicate [17], tantalum aluminate [18], and alkali aluminoborate compositions [12,19]. On the other hand, post-treatment that increases the glass density (e.g., by low-temperature annealing or hot compression) typically leads to a decrease in CR [20]. Besides composition and post-treatment, it is known that other factors such as loading/unloading rate, surface quality, indenter tip geometry, time after unloading, and atmospheric conditions (temperature and humidity) also influence the crack resistance of glasses [21–23]. Particularly, the relative humidity (RH) plays a major role for the indentation response of glasses [23,24].

Understanding the details of glass-water interactions is thus crucial for tailoring the mechanical performance of oxide glasses. Besides water entry from a humid environment via diffusion or hydrolysis and condensation, water may already be present in the as-melted glass, e.g., as an impurity in the raw materials. Water typically exists in glasses in the form of either molecules or hydroxyl groups, depending on the glass composition and water content [25,26]. Wiederhorn [27] first studied the influence of atmospheric humidity on the cracking behavior of soda-lime-silicate glasses, and attributed the fatigue phenomenon to subcritical crack growth enhanced by

*Corresponding author: mos@bio.aau.dk

TABLE I. Overview of glass transition temperature (T_g), density (ρ), Young's (E) modulus, Poisson's ratio (ν), and Vickers hardness (H_v) for the present glasses prior to any aging.

Glass ID	Composition (mol %)	T_g (°C)	E (GPa)	ν	ρ (g/cm ³)	H_v (GPa)	Reference
CsAIB	25Cs ₂ O-25Al ₂ O ₃ -50B ₂ O ₃	402	24.5	0.322	3.006	2.6	this work
NaAIB	25Na ₂ O-20Al ₂ O ₃ -55B ₂ O ₃	451	46.5	0.291	2.240	3.3	[37]
LiAIBSi	55SiO ₂ -25Li ₂ O-20Al ₂ O ₃ -50B ₂ O ₃	473	67.0	0.274	2.263	4.6	[38]
SLS	13Na ₂ O-6MgO-10CaO-71SiO ₂	562	72.0	0.230	2.512	6.1	[39]
LaAIBSi	25La ₂ O ₃ -15Al ₂ O ₃ -60SiO ₂	862	113.7	0.305	4.336	7.2	[40]
LaAIB	25La ₂ O ₃ -15Al ₂ O ₃ -60B ₂ O ₃	658	107.4	0.298	3.998	7.1	[40]

stress corrosion, in which the silicon-oxygen bond is assumed to undergo a hydrolysis reaction. Later work has shown that water entry during indentation leads to softening [28], molecular water surrounding the crack tip can lower the fracture toughness [29,30], and stress corrosion under high humidity increases the crack initiation probability [31]. On the other hand, water penetration has also been shown to inhibit crack growth in silica glass by shielding the crack tip due to network swelling [32,33] and result in fast stress relaxation [34].

Indeed, a few recent studies have shown that prehydration of a glass surface can increase the crack resistance for certain compositions. Namely, hydrothermal treatment (150 °C at 100% RH for 3 days) of soda-lime-silica (window) glass increases CR from around 0.5 to 3 N [35], while a lower temperature aging (22 °C at 85% RH for 30 days) increases CR from 50 to 100 N of some phosphoaluminosilicate glasses, but not for others [36]. Our recent study on a caesium aluminoborate glass shows an increase in CR from around 30 to >100 N upon low-RH treatment (23 °C at 45% RH for 7 days) [24], i.e., surface aging in a humid atmosphere. There is thus a strong composition dependence of the hydration-induced increase in CR and we infer that favorable intrinsic mechanical properties (prior to aging) likely need to be combined with a tailored propensity to undergo surface hydration to achieve the ultrahigh CR values. If the glass hydrates too rapidly, a white surface layer will form. For future applications, it would thus be beneficial if the surface could be prehydrated at high-RH conditions, but not undergo further pronounced hydration when taken back to ambient conditions.

In this work, we aim to understand these phenomena further by performing controlled low-temperature aging experiments of a metaluminous caesium aluminoborate glass. Compared to our recent work [24], we here perform much more detailed structural and mechanical characterization on samples with varying degree of aging. We also compare the aging behavior of the caesium aluminoborate glass with that of various oxide reference glasses (see Table I), which have been chosen to exhibit a wide range of network rigidity, as evidenced by the large span in glass transition temperature (from ~400 to 860 °C) and hardness (from ~2.6 to 7.2 GPa). Since aluminoborate glasses are known to be self-adaptive by easily changing the coordination numbers of Al and B under stress [12], we also perform aging experiments on a permanently densified caesium aluminoborate glass, which shows limited densification during subsequent indentation. We thus compare aging effects in both as-made and compressed glasses in order

to decipher the role of coordination number changes on crack resistance. These changes are possible in the as-made glasses, but to a much smaller extent in the compressed glasses. Using a combination of mechanical characterization, solid-state nuclear magnetic resonance (NMR) spectroscopy of ¹¹B, ²⁷Al, and ¹³³Cs, and micro-Raman spectroscopy analyses of aged and densified glasses, we then show how a combination of stress and hydrolysis assisted structural changes in the flexible aluminoborate glass network is responsible for its ultrahigh crack resistance. These findings have important implications for utilizing humid aging as a simple post-treatment method to improve the fracture resistance of oxide glasses.

II. EXPERIMENT

A. Glass synthesis

We have prepared a bulk glass with nominal composition (in mol %) of 25Cs₂O-25Al₂O₃-50B₂O₃ using the traditional melt-quenching technique. The composition is similar to that in our recent study [24], but here designed to have a lower fraction of tetrahedral boron (due to [Cs₂O] = [Al₂O₃]), which has been found to give a high CR value in sodium aluminoborate glasses [37]. The utilized raw materials were Al₂O₃ (99.5%, Sigma-Aldrich), H₃BO₃ (≥99.5%, Honeywell International), and Cs₂CO₃ (99.5%, Sigma-Aldrich). First, the raw materials were weighed and thoroughly mixed. To prevent excessive foaming, the mixture was stepwise added to a Pt-Rh crucible and heated to around 800 °C in an electric furnace to remove the excess H₂O and CO₂. Subsequently, in order to homogenize the melt, the mixture was melted at 1070 °C for 2 h in air. Finally, it was poured onto a steel plate for quenching. The obtained glasses were immediately transferred to a preheated annealing furnace at 405 °C (estimated glass transition temperature) for 30 min, and then slowly cooled to room temperature. The composition of the glass was analyzed by inductively coupled plasma optical emission spectroscopy for Al₂O₃ and B₂O₃, and flame emission spectroscopy for the Cs₂O content, and found to be 24.5Cs₂O-24.1Al₂O₃-51.4B₂O₃.

For comparison with the caesium aluminoborate glass (named CsAIB hereafter; see Table I), we also prepared five reference glasses based on our previous studies. All glasses' nominal chemical compositions and their measured properties are shown in Table I. These reference glasses include sodium aluminoborate glass (25.5Na₂O-20.4Al₂O₃-54.1B₂O₃) [37],

lithium silicoaluminoborate glass (5SiO₂-25Li₂O-20Al₂O₃-50B₂O₃) [38], a soda-lime-silica float glass (13Na₂O-6MgO-10CaO-71SiO₂) [39], lanthanum aluminosilicate glass (25La₂O₃-15Al₂O₃-60SiO₂) [40], and lanthanum aluminoborate glass (25La₂O₃-15Al₂O₃-60B₂O₃) [40]. These glasses were also produced by melt quenching, with the details given in the corresponding references [37,40].

Following determination of the glass transition temperature (T_g ; see Sec. II C), all the glasses were re-annealed for 30 min at their measured T_g and cooled down to room temperature at a cooling rate of approximately 3 K/min. After reannealing, samples were cut for the needed dimensions for density, modulus, x-ray diffraction, ultraviolet-visible (UV-VIS) spectroscopy, Raman spectroscopy, and indentation experiments (see Sec. II C). Subsequently these samples were optically polished in ethanol by using abrasive SiC disks (up to grit 4000). Finally, all the samples were kept in a desiccator to avoid hydration of the surface, or in a climate chamber to induce aging experiments (see Sec. II B).

B. Post-treatment: densification and aging

Following the treatment protocol described in previous work [41], the 24.5Cs₂O-24.1Al₂O₃-51.4B₂O₃ glass samples were subjected to isostatic N₂-mediated pressure treatment at 1 GPa. The compression was carried out at its measured T_g (402 °C) for 0.5 h, and subsequent quenching with an initial cooling rate of 60 K/min. The pressure chamber was then decompressed at a 30-MPa/min rate. This gives rise to permanent volume densification, associated with both structural and property changes [41].

The present CsAIB glass (annealed and compressed version), as well as all the reference glasses were also subjected to controlled humid aging experiments in a climate chamber (WKL 100/40, Weiss) to hydrate their surfaces. Following our recent work [24], the aging experiment was done at 23 °C with 45% RH for varying duration up to 7 days. All the glass samples were immediately put into the climate chamber after being optically double-side polished in ethanol.

C. Basic property characterization

To confirm the amorphous nature, x-ray diffraction (XRD) patterns of the CsAIB glass were acquired (Empyrean XRD, PANalytical) from 0° to 70° at 40 kV with a scanning speed of 8°/min. The noncrystalline nature of the reference glasses has previously been confirmed [37,38,40]. Moreover, the chemical homogeneity of the CsAIB glass was investigated by acquiring micro-Raman spectra ranging from 250 to 1700 cm⁻¹ (InVia, Renishaw) at five different surface locations that were separated by at least 1 mm. The measurements were done using a 532-nm laser with 10-s excitation time. The acquired spectra were subjected to baseline subtraction and normalization with respect to their area.

To confirm the incorporation of water in the CsAIB glass upon aging, we performed Fourier transform infrared (FTIR) spectroscopy measurements on a ground and polished sample with uniform thickness of 1.0 mm. The FTIR spectra were acquired using a Spectrum One spectrometer (PerkinElmer

STA 6000) on a Ge crystal under ambient conditions with subsequent background subtraction. The absorption spectra (averaged over 64 scans) were collected in the wave-number region from 400 to 4000 cm⁻¹. The estimation of the water content in the oxide glasses is based on the Beer-Lambert law, which relates the concentration (by weight) of water in the glass ($c_{\text{H}_2\text{O}}$) to the absorbance of the FTIR beam through the glass (A), the samples thickness (Δx), and the molar absorption coefficient ($\epsilon_{\text{H}_2\text{O}}$) related to the overall concentration of water in the glass [42]. The molar absorption coefficient of OH groups (ϵ_{OH}) is approximately equal to one-half of $\epsilon_{\text{H}_2\text{O}}$. We do not know the actual values of ϵ_{OH} for the studied glasses, but previous studies [43] have shown that variations of ϵ_{OH} are of the same order of magnitude for various oxide glasses. Following the approach of Wu *et al.* [42], we calculate

$$c_{\text{H}_2\text{O}}\epsilon_{\text{OH}} = \frac{AM_{\text{H}_2\text{O}}}{2\Delta x\rho}, \quad (1)$$

where $M_{\text{H}_2\text{O}}$ is the molar mass of H₂O (18.02 g/mol) and ρ is the density of the glass (g/cm³). That is, with this approach we are not relying on the absolute value of ϵ_{OH} to estimate variations in OH content among the samples.

T_g of the CsAIB glass was determined by differential scanning calorimetry measurements (STA 449 F3 Jupiter, Netzsch) at 10 K/min on specimens with a known thermal history (i.e., with a preceding cooling rate of 10 K/min). These samples were analyzed using Pt crucibles in argon (gas flow 60 mL/min). The intercept between the tangent to the inflection point of the endothermic peak and the extrapolated heat flow of the glass was interpreted as the onset of the glass transition (T_g). T_g values of the reference glasses were taken from the previous studies [37–40].

The density (ρ) of all glass samples was determined by Archimedes' principle of buoyancy. The weight of each specimen (at least 2 g) was measured in air and ethanol ten times. Based on the ratio between molar mass and density, we also calculated the molar volume (V_m). The elastic properties of the glasses were measured by ultrasonic echography using an ultrasonic thickness gauge (38DL Plus, Olympus) equipped with 20-MHz delay line transducers for the determination of the longitudinal V_1 and transversal wave velocities V_2 . The detailed calculation method was shown in the previous study [38].

To evaluate whether the humid surface aging affects the visual appearance of the glass, we determined the optical transparency of the as-made and aged CsAIB glass on a 1.5-mm-thick sample. This sample was optically double-side polished in ethanol by using SiC disks (up to grit 4000) and then immediately transferred into the climate chamber for aging up to 7 days. Subsequently, the sample was analyzed in a UV-VIS spectrometer (Cary 50 Bio, Varian) every day, recording the transmission at wavelengths between 255 and 800 nm. We measured five different areas (at least 2 mm apart) of this sample to ensure the homogeneity. All UV-VIS transmittance spectra were normalized to 1 mm thickness.

D. Structural characterization

To study the structural changes induced by humid aging, we performed ¹¹B, ²⁷Al, and ¹³³Cs magic angle spinning

(MAS) NMR experiments for four different CsAlB glass samples: as-made/no aging, compressed/no aging, as-made/7 days aging, and compressed/7 days aging. Since the NMR measurements have to be done on powdered samples and the humid aging is expected to mostly affect the surface structure, the glasses were powdered with an agate mortar and pestle prior to aging (but not prior to hot compression, which is known to homogeneously densify the bulk structure [44]). Aging of glasses for NMR spectroscopy was done by placing powdered glasses in a humidity controlled chamber (45% RH) at 23 °C for 7 days. After aging, the powdered glasses were sealed in glass vials to prevent further changes. ^{11}B , ^{27}Al , and ^{133}Cs MAS NMR experiments were conducted at 16.4 T using a commercial spectrometer (VNMRs, Agilent) and a 3.2-mm MAS NMR probe (Varian/Chemagnetics). The powdered samples were packed into 3.2-mm zirconia rotors, with sample spinning of 20 kHz for ^{11}B and 22 kHz for ^{27}Al and ^{133}Cs . ^{11}B and ^{27}Al MAS NMR data were collected at resonance frequencies of 224.5 and 182.3 MHz, respectively, utilizing radio-frequency pulses of 0.6 μs ($\pi/12$ tip angles), with 4-s recycle delay and signal averaging of 1000 acquisitions for ^{11}B MAS NMR, and a pulse delay of 2 s and collection of typically 600 scans for ^{27}Al MAS NMR. Additional ^{11}B and ^{27}Al MAS NMR data were acquired with ^1H decoupling to account for possible interactions in hydrated glasses, but these data were not different from the nondecoupled MAS NMR data, and therefore were not used further. ^{133}Cs MAS NMR data, at a resonance frequency of 91.8 MHz, were collected using short rf pulses (0.6 μs), recycle delays of 60 s, and accumulation of 400 scans for each experiment. MAS NMR spectra for ^{11}B and ^{27}Al were processed without any additional apodization, while those for ^{133}Cs benefitted from application of 100 Hz line broadening. MAS NMR data were plotted using the normal shielding convention and with shift referencing to aqueous boric acid (19.6 ppm) or aqueous aluminum nitrate (0 ppm). The latter shift referencing was also used for ^{133}Cs following the International Union of Pure and Applied Chemistry recommendation of using the ratio of frequencies for ^{27}Al and ^{133}Cs . ^{11}B MAS NMR data were fit with DMFit utilizing second-order quadrupolar line shapes for trigonal (B^{III}) resonances, and a combination of Gaussian and Lorentzian functions for the B^{IV} resonances. The overlapping satellite transition for the B^{IV} resonance was also fit and subtracted from the integration, yielding accurate site intensities for all B^{III} and B^{IV} peaks. The CzSimple model in DMFit was used to fit ^{27}Al MAS NMR data [45]. ^{133}Cs MAS NMR data were fit also with DMFit, using combinations of Gaussian and Lorentzian line shapes to reproduce the experimental data.

In addition to solid-state NMR spectroscopy analysis, we also acquired micro-Raman spectra of as-made and compressed CsAlB glasses with different aging condition, since this technique allows us to directly probe the medium-range structure as well as the structure of the surface regions deformed by indentation (see Sec. II E). Raman spectra were collected on an inVia micro-Raman spectrometer (Renishaw) with a 532-nm laser and an acquisition time of 10 s. The range of all spectra was from 250 to 4000 cm^{-1} , with resolution better than 2 cm^{-1} . The micro-Raman spectra were acquired around Vickers indents produced at 19.6 and 4.9 N, with

increasing distances from the center to the edge of the Vickers indent. Two spectra were accumulated in each position to minimize the signal-to-noise ratio. All spectra were uniformly treated for background correction and area normalization.

E. Microindentation

We determined the Vickers hardness (H_V) and crack resistance (CR) of as-prepared, compressed, and aged glasses by using a CB500 microindenter (Nanovea). On each sample, ten Vickers indents with a load of 9.8 N (1 kgf) were generated to determine H_V . The loading duration and dwell time were set to 6 and 10 s, respectively. The residual imprints were subsequently analyzed with an optical microscope and H_V was calculated as

$$H_V = 1.8544 \frac{P}{\left(\frac{d_1+d_2}{2}\right)^2}, \quad (2)$$

where P is the contact load, and d_1 and d_2 are the lengths of the projected indent diagonals. We note that d_1 and d_2 were measured immediately after unloading (20–30 s), but as described in Sec. III B below, the indents of the CsAlB glass recover quickly. As such, the reported hardness of this glass may be higher than its “real value” due to humidity-induced recovery.

To evaluate CR, all glass samples were indented at different loads using both Vickers and cube corner diamond tip geometries. According to the method of Wada *et al.* [14], the probability of crack initiation (PCI) at each load was derived as the ratio between the number of corners with a corner crack and the total number of corners (4 for Vickers and 3 for cube corner). The crack resistance is defined as the load at which an average of 2 cracks for Vickers and 1.5 cracks for cube corner (PCI = 50%) occurred. On every specimen, at least ten indents were made by using the Vickers indenter tip (loading rate of 7.5 N/s and dwell time of 5 s) and cube-corner indenter tip (loading duration of 6 s and dwell time of 10 s). The measurements were conducted under laboratory conditions (room temperature, relative humidity of 50–55%).

In order to evaluate the effect of aging time on the indentation deformation mechanism of the CsAlB glasses and the other reference glasses, we determined the recovery of the indent side length over time. To do so, all samples were first optically polished in ethanol using SiC disks (up to grit 4000) and immediately afterwards indented ten times by a Vickers tip at a load of 4.9 N with loading duration of 6 s and dwell time of 10 s. Then images of the indents were recorded by means of the built-in microscope. After indentation and imaging, these samples were immediately transferred into the climate chamber (temperature: 23 °C, relative humidity: 45%) for aging, and then the existing indents were imaged once every day. The initial (20–30 s after unloading) indentation side length, $L_{s,i}$, was determined and then determined again after aging, $L_{s,a}$. Similarly to the recovery of indentation volume following the method of Yoshida *et al.* [46] to estimate densification contribution to overall indentation deformation [47], we calculate the aging-induced side length recovery (L_{AR}),

$$L_{AR} = \frac{L_{s,i} - L_{s,a}}{L_{s,i}}. \quad (3)$$

TABLE II. Effect of hot compression on density (ρ), molar volume (V_m), atomic packing density (C_g), elastic moduli [Young's (E), shear (G), and bulk (B) moduli], Poisson's ratio (ν), Vickers hardness (H_v), and Vickers crack resistance (CR) of the caesium aluminoborate glass without aging.

Glass	ρ (g/cm ³)	V_m (cm ³ /mol)	C_g	E (GPa)	G (GPa)	B (GPa)	ν	H_v (GPa)	CR (N)
As prepared	3.006	43.58	0.511	24.5	9.3	22.9	0.322	2.6	58
Compressed	3.129	41.79	0.532	30.5	11.7	26.0	0.304	3.2	8
Error estimate	0.001	0.01	0.001	0.5	0.5	0.5	0.005	0.1	20%

III. RESULTS AND DISCUSSION

A. Glass formation and basic characterization prior to aging

Based on the x-ray-diffraction analysis (Fig. S1 in the Supplemental Material [48]), we find that there is no long-range-ordered structure in the as-prepared CsAIB glass. It also exhibits a typical glass transition in the heat capacity vs temperature curve with $T_g = 402$ °C (Fig. S2 in the Supplemental Material [48]). As seen from the micro-Raman spectra in Fig. S3 in the Supplemental Material [48], there are no significant differences among these across the sample surface, suggesting that the glass is compositionally homogeneous. Furthermore, the glass is found to be transparent in the wavelength range of visible light, with only minor changes in optical transmittance due to the surface aging at 45% RH (Fig. S4 in the Supplemental Material [48]). Table I shows the overview of T_g , density (ρ), Young's modulus (E), Poisson's ratio (ν), and Vickers hardness (H_v) for the as-prepared CsAIB glass and the other reference glasses. The CsAIB glass features a low glass transition temperature ($T_g = 402$ °C), low hardness ($H_v = 2.6$ GPa) and low Young's modulus ($E = 24.5$ GPa), but relatively high density ($\rho = 3.006$ g/cm³) and high Poisson's ratio ($\nu = 0.322$) compared to the reference glasses. We note that the fracture toughness (K_{Ic}) of a compositionally similar caesium aluminoborate glass has recently been found to be 0.42 MPa m^{0.5} [49].

To evaluate the water content in the as-melted CsAIB glass prior to aging, we consider the FTIR spectroscopy analysis (Fig. S5 in the Supplemental Material [48]). Almost all water in borate glasses is accommodated in the form of hydroxyl groups at relatively small concentrations of water [50], with the IR bands related to the stretching of B-OH groups present at wavelengths between 3600 – 3750 cm⁻¹ and 3200 – 3500 cm⁻¹ [50,12] depending on the glass composition. Based on Eq. (1), we calculate the value of $c_{H_2O}\epsilon_{OH}$ in the CsAIB glass to be ~ 0.49 (Fig. S6 in the Supplemental Material [48]) before aging, which is relatively low compared to that found in some soda lime borosilicate glasses [51]. As such, although the alkali aluminoborate glasses are known to feature low chemical durability compared to other oxide glasses [52], the water content of the as-made, polished glass is not unusually high and it may thus increase upon aging in humid atmosphere, i.e., the surface is not already fully hydrated prior to aging.

The effect of hot compression (prior to any aging) on ρ , molar volume (V_m), atomic packing density (C_g), E , shear modulus (G), bulk modulus (B), ν , H_v , and crack resistance (CR) of the CsAIB glass is summarized in Table II. To quantify changes in the free volume, we calculate the atomic

packing density in addition to molar volume based on the ionic radii from Shannon [53] and the assumption of spherical atoms. C_g of as-prepared and densified CsAIB glasses is estimated to be 0.511 and 0.532, respectively, by assuming eightfold coordination for Cs, twofold coordination for O, and coordination numbers for B and Al based on the NMR results (see Table S1 in the Supplemental Material [48]). Upon volume densification (i.e., V_m decreases and C_g increases), the hardness of the glass increases, in agreement with previous work [44,54,55] on other oxide glasses. In addition to the structural changes upon densification (see Sec. III D), the denser structure gives rise to more atomic constraints per unit volume, which is known to increase hardness [44]. There is also a significant increase in all three elastic moduli upon hot compression, but a decrease in Poisson's ratio (Fig. S7 in the Supplemental Material [48]), as discussed in detail elsewhere for various oxide glasses [56].

B. Indent size recovery

Upon humid aging, we find that the water content of the CsAIB glass increases systematically with aging time (Fig. S6 in the Supplemental Material [48]), showing that atmospheric water permeates into the glass. It is also confirmed by the thermogravimetric analysis (Fig. S8 in the Supplemental Material [48]). This has important consequences for its mechanical behavior.

First, to understand the deformation mechanism of both the as-made and densified CsAIB glass relative to that of the other reference glasses, we consider the change in size of the Vickers indent as a function of aging time. Figure 1(a) shows representative optical images of 4.9-N indents on the surface of the as-made and densified CsAIB glass before and after aging for 7 days at 45% RH. The indents in both the as-made and densified glasses exhibit significant shrinkage upon aging, as also found in our recent study of an as-made peralkaline caesium aluminoborate glass [24]. In fact, even the images recorded immediately (20–30 s) after indentation unloading do not show the perfect square shape, indicating recovery already during the unloading process. However, the predensified CsAIB glass shows less indent size recovery upon aging, possibly because its dense structure allows for less water penetration to induce the indent volume recovery [44].

Figure S9 in the Supplemental Material [48] shows the time evolution of the indent size and shape of the as-made glass upon aging. With increasing aging time, the size of the indent becomes monotonically smaller, and the edge of the indent appears to have recovered above the original glass

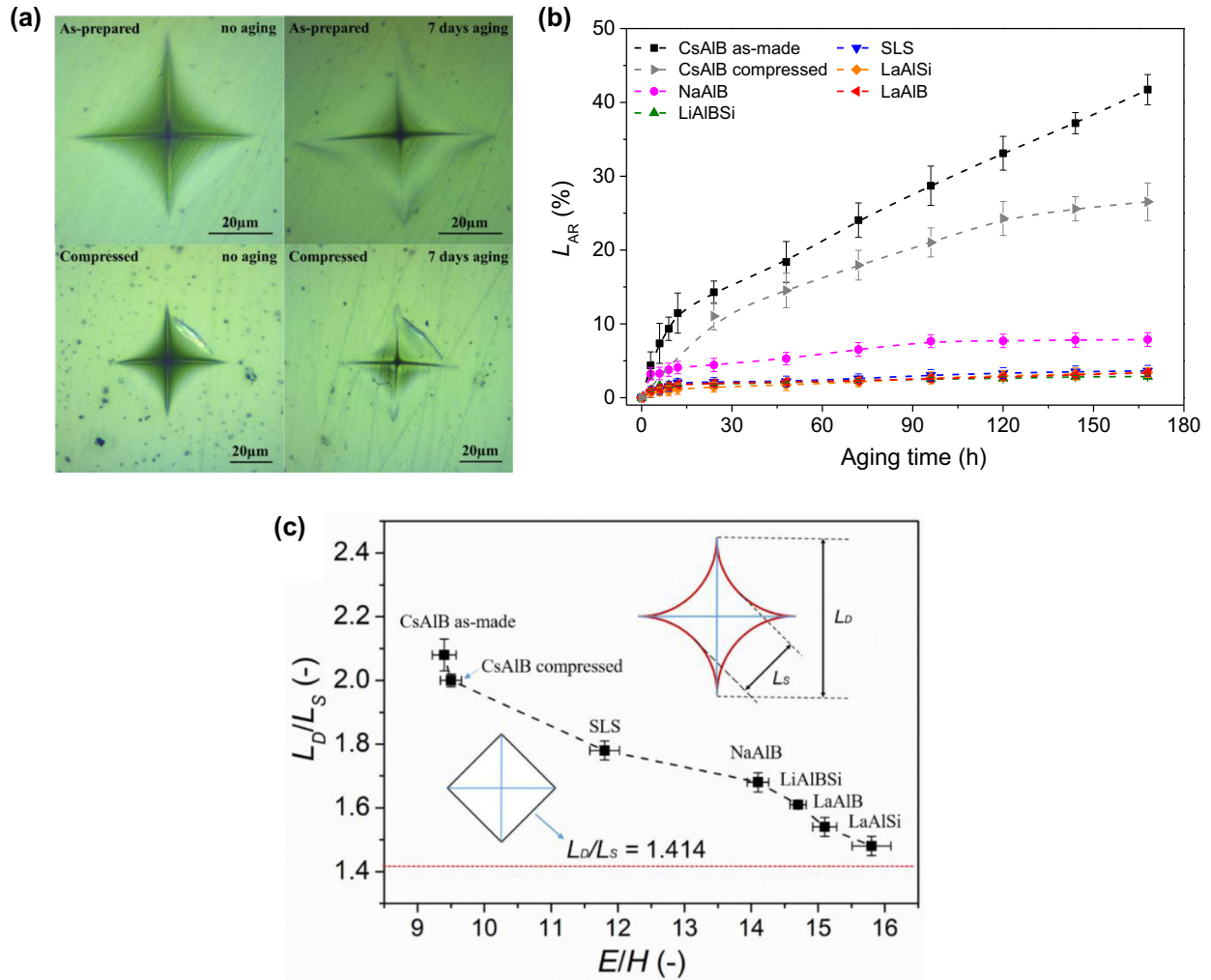


FIG. 1. (a) Optical images of Vickers indents produced at 4.9 N on the surface of the as-prepared glass and the compressed glass at 1 GPa before and after aging for 7 days. (b) Side length recovery (L_{AR}) of indents produced at 4.9 N as a function of aging time for all the investigated glasses. (c) Dependence of the bow-in parameter (L_D/L_S ratio) of Vickers indents produced at 4.9 N on the elastoplastic ratio (E/H) for all the investigated glasses before aging. The red dashed line represents the theoretical minimum L_D/L_S value (i.e., the case with no bow-in).

surface. As a consequence of the continuous recovery of the indent size and shape in a humid atmosphere, we cannot apply the traditional method by Yoshida *et al.* [46] for quantification of the densification contribution to the indentation volume based on annealing and volume recovery experiments. To quantify the rate of indentation recovery in the CsAIB glass and compare it with that of the reference glasses, we measure the aging time dependence of the recovery of the indentation side length (L_{AR}). The results are shown in Fig. 1(b). The qualitative observation of the indent self-recovery in the as-made and densified CsAIB glasses are confirmed by the aging time dependence of L_{AR} . We also note the limited indent size recovery in the other reference oxide glasses. Only the NaAIB glass shows recovery above 5%, pointing to the unusual indent recovery behavior of the CsAIB glass. For this composition, we note that a large fraction of the recovery occurs during the very early stages of the aging (i.e., first data point after unloading), but the shrinkage gradually continues even after 7 days of aging.

Next, we consider the interplay of the glasses' elastic vs aging-induced recovery of the indent shape by evaluating the

bow-in parameter (L_D/L_S ratio), which exhibits systematic composition dependence. Figure 1(c) shows the dependence of L_D/L_S of indents produced at 4.9 N on the elastoplastic ratio (E/H) for all the investigated glasses before aging. By measuring the indent diagonal length (L_D) and the opposite side length (L_S), the elastic response of the material surrounding the indentation-induced cavity can be quantified by calculating the L_D/L_S ratio [57]. This bow-in parameter exhibits a negative linear scaling with the elastoplastic ratio E/H , in agreement with previous work [19]. The CsAIB glass has a very high bow-in parameter, close to that (2.2) of polydimethylsiloxane [57], which is likely due to a combination of elastic recovery and aging during unloading.

Finally, we study the aging time dependence of the Vickers hardness of the CsAIB glass (Figs. S10 and S11 in the Supplemental Material [48]). Vickers hardness first increases slightly with the aging time in the early stage of the aging, in which atmospheric water permeates into the glass at a high rate (Fig. S6 in the Supplemental Material [48]). This results in larger indent recovery during unloading, and thus smaller residual imprint and a higher apparent Vickers hardness. With

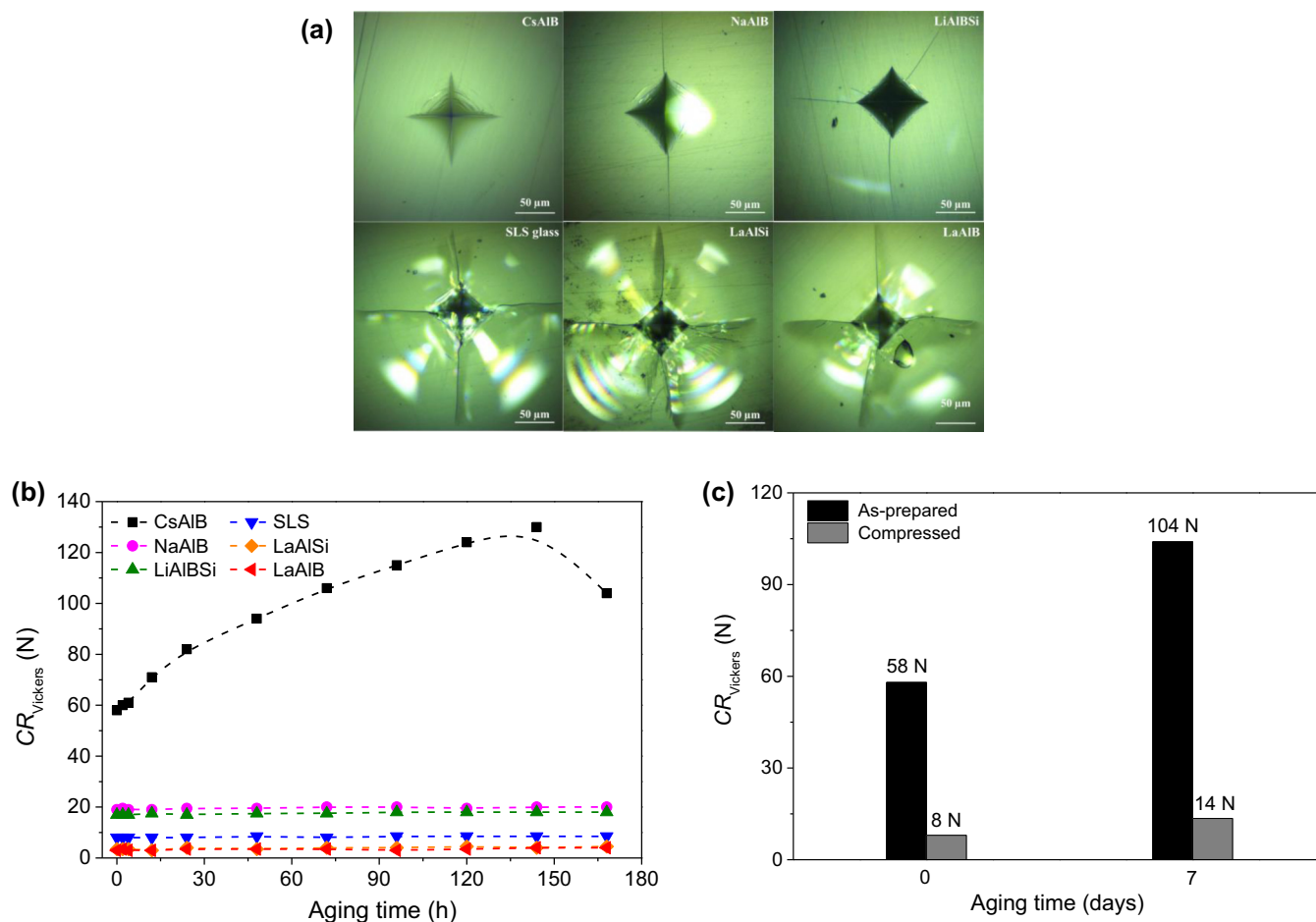


FIG. 2. (a) Optical images of Vickers indents produced at 19.6 N on the surface of all the investigated glasses prior to aging. (b) Crack resistance for Vickers indentation (CR_{Vickers}) as a function of aging time for all the investigated glasses. (c) CR_{Vickers} of the as-prepared and compressed CsAIB glasses with aging for 0 or 7 days. The estimated error in crack resistance is around $\pm 20\%$.

increased aging time, the rate of atmospheric water permeation decreases, resulting in the smaller relative recovery during unloading. The depolymerizing effect of water on the glass network likely causes the slight decrease in Vickers hardness for the longer aging time.

C. Indentation cracking resistance

In our previous studies [12,24,37], aluminoborate glasses have been found to generally feature high resistance to crack initiation. Especially the previously studied peralkaline caesium aluminoborate glass features high CR > 100 N, depending on the aging conditions [24]. Here, we systematically investigate the effect of surface hydration on the crack initiation behavior of various oxide glasses by studying the indentation behavior of both freshly polished (in ethanol) surfaces and those that have undergone aging at 45% RH for up to 7 days. Figure 2(a) shows optical images of Vickers indents produced at 19.6 N on the various oxide glasses prior to aging. We note that this applied load is insufficient to induce corner cracking in the as-made CsAIB glass, while corner cracks are visible in the other reference oxide glasses, highlighting the high CR of the CsAIB glass even before aging.

Figure 2(b) shows the effect of aging duration on the CR for Vickers indentation of all the as-made glasses,

while examples of PCI vs load curves used to determine CR are given in Fig. S12 in the Supplemental Material [48]. We find that CR of the CsAIB glasses increases from around 58 N prior to aging to around 130 N after 6 days of aging. The preaging CR value is higher than that of the previously studied peralkaline caesium aluminoborate glass, while the 1-week aged CR value is smaller than that of the peralkaline caesium aluminoborate glass [24]. This could be because the peralkaline composition ($[Cs_2O] > [Al_2O_3]$) has more tetrahedral boron ($\sim 8\%$ B^{IV} of 55 mol % B_2O_3) [19] than the present metaluminous glass ($\sim 5\%$ B^{IV} of 51 mol % B_2O_3), giving rise to a more rigid and less self-adaptive network prior to aging [37]. For the other reference glasses, the surface aging at 45% RH has an almost negligible effect on the CR. For the as-made CsAIB glass, when the aging time reaches 6 days, CR reaches an apparent maximum value. During aging, the network should expand, driven by a structural relaxation towards lower potential energy state (from intact dense network to a looser hydrolyzed network), corresponding to relaxation of the indent cavities. We note that the indent cavities continue to recover and expand beyond 6 days (see Fig. S9 in the Supplemental Material [48]), indicating that the atmospheric water is continuously entering the glass surface [58]. As such, it is possible that the hydrated surface after long-term aging

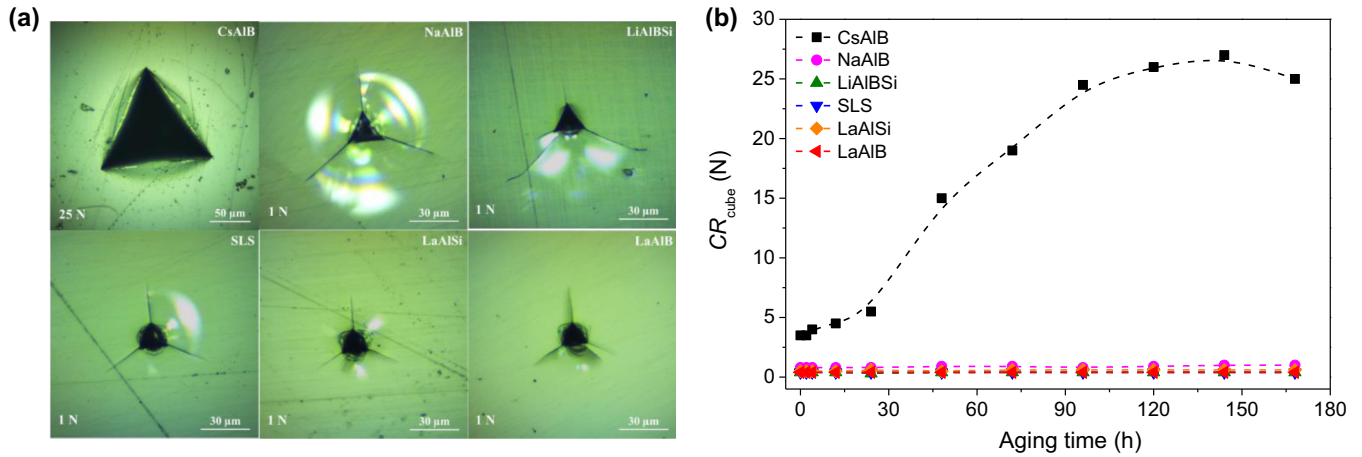


FIG. 3. (a) Optical images of cube corner indents produced at 25 N for as-made CsAIB and 1 N for the reference glasses after humid aging for 7 days. (b) Crack resistance for cube corner indentation (CR_{cube}) as a function of aging time for the as-made CsAIB and reference oxide glasses.

becomes sufficiently depolymerized to decrease CR due to the weaker network bonding.

Figure 2(c) shows the comparison of CR for the as-made and densified CsAIB glasses. Both before and after aging (7 days), the crack resistance is significantly lower in the densified glasses, which has previously been ascribed in other oxide glasses to the reduced ability of the densified glass to further densify during indentation [12]. In addition, the densified glass shows a smaller aging-induced increase in CR. Finally, we note that while the edge of the indent in the as-prepared glasses has recovered above the glass surface after aging [Fig. 1(a)], there is a smaller extent of indent size recovery in the compressed glass [Fig. 1(b)]. The reduced free volume in the compressed glass likely decreases the water intake, and thus limits the positive effect of humid aging on CR. This will be further investigated in Sec. III D.

Next, we consider the glasses' resistance to crack initiation under a sharper diamond tip, namely a cube corner indenter (three-sided pyramid with mutually perpendicular faces). This tip allows for less densification, higher residual stress, and easier crack initiation compared to the 136° four-sided pyramid Vickers diamond indenter [15]. Figure 3(a) shows the optical images of cube corner indents produced at 25 N for the as-made CsAIB glass and 1 N for the reference glasses after aging for 7 days. All the reference glasses already crack at all three corners at 1 N, while the CsAIB is able to survive indentation at more than ten times higher loading without cracking. The quantified cube corner crack resistance as a function of aging time is shown in Fig. 3(b), showing the same overall trend as that for Vickers crack resistance in Fig. 2(b). Namely, the CsAIB is highly affected by surface aging at 45% RH, while this is not the case for the selected reference glasses. All the glasses feature lower CR for cube corner than Vickers, with the aged CsAIB glasses having an ultrahigh crack resistance for cube corner (27 N) compared to that of the reference glasses (in the range of 0.4–1 N).

Finally, we consider the loading rate dependence of Vickers crack initiation probability for the freshly polished CsAIB glass and that aged for 7 days at 45% RH (Fig. 4). Normally,

there is a higher crack initiation probability for longer indentation time [23]. Note that due to the large difference in CR before and after aging, the maximum load is not the same, but set to 30 and 90 N, respectively. We observe an anomalous increase in crack initiation probability with loading rate for the freshly polished CsAIB, but a normal decrease in crack initiation probability with loading rate for the aged sample. The highly stressed glass network is more vulnerable to the attack of water from the environment [24], and therefore, for the freshly polished glass, the relatively low loading rates allow sufficient time for the attack of water from the environment during the loading process. As discussed above, such water entry decreases the crack initiation probability for this glass (Figs. 2 and 3). On the other hand, the surface of the 7-days preaged glass has already been hydrated to a large extent, i.e., the extra time at lower loading rate does not lead to higher crack resistance. Instead the glass exhibits a normal loading rate dependence with less time for surface damage at higher loading rates.

D. Stress and Hydrolysis Induced Structural Changes in CsAIB

In order to understand the structural changes responsible for the ultrahigh crack resistance of the aged CsAIB glass and the significant effect of predensification on the aging behavior, we analyze the structure of densified and aged CsAIB samples using both micro-Raman and solid-state NMR spectroscopy. Figure 5 shows the micro-Raman spectra of the indented as-made and densified glasses with or without aging. These spectra were recorded at increasing distances (about $4 \mu\text{m}$) from the center to the edge of a Vickers indent produced at 4.9 N. We divide the spectra into seven main band regions, with the expected assignments outlined in detail in Fig. S13 and Table S2 in the Supplemental Material [48].

Overall, we find that the surface becomes hydrated by exposure to ambient humid air, which manifests itself through the increase in intensity of the band region around $2850\text{--}3800 \text{ cm}^{-1}$, typically assigned to hydroxyl groups [59]. For the as-prepared glass, this band region increases

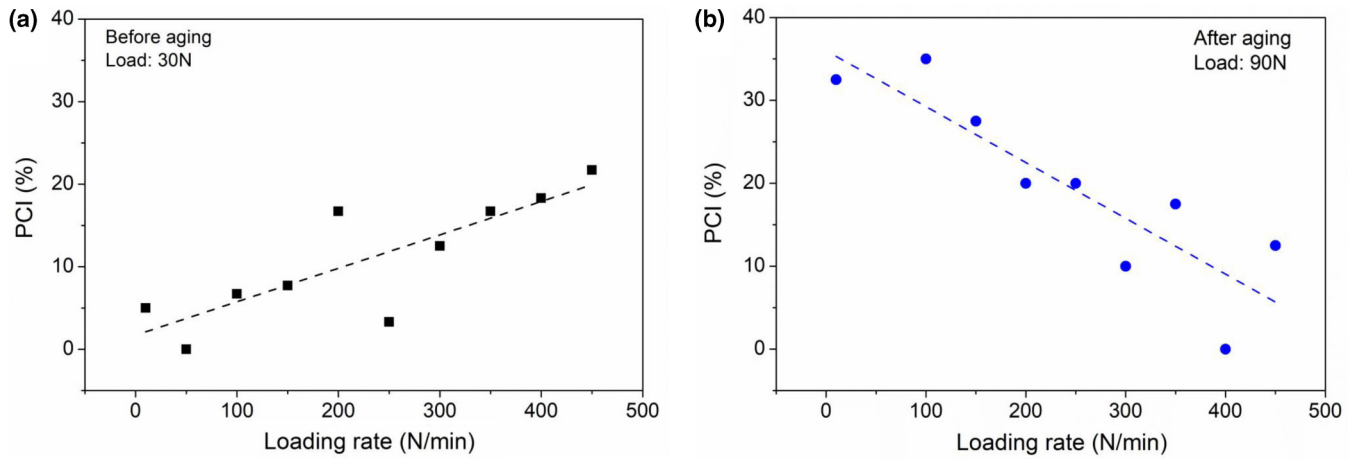


FIG. 4. Loading rate dependence of the Vickers crack initiation probability (PCI) for the CsAIB glass (a) before and (b) after aging for 7 days. The dashed lines are guides for the eyes.

observably in intensity after aging for 7 days, confirming the expectation that more atmospheric water permeates into the glasses with increasing aging time and thus supporting the indentation recovery behavior with aging time [Fig. 1(b)]. On the other hand, the region from ~ 625 to 815 cm^{-1} is suppressed after aging, indicating that the borate superstructural units (diborates) are broken because of the hydrolyzation, i.e., the borate ring units are depolymerized into smaller ones. For the compressed glass with less free volume, the aging has a minor effect on the surface structure as detected by Raman spectroscopy (see Fig. S14 in Supplemental Material [48]), indicating less pronounced water permeation. This result may lead to the lower indentation side length recovery [Fig. 1(b)]

and smaller CR [Fig. 2(c)] compared to the as-prepared CsAIB glass.

Considering next the indent position dependency of the structural changes in the glasses, we have calculated the relative area of the band region from ~ 2850 to 3800 cm^{-1} at different positions. As shown in Fig. S15 in the Supplemental Material [48], the aging-induced increase in the hydroxyl-related band becomes less pronounced from position 1 to 5 [i.e., from high to low stress; see Fig. 5(a)], indicating that the material under the center of the indent is hydrated more quickly compared to the edge of the indent. This suggests that the highly stressed glass network is more vulnerable to the attack of water from the environment, in agreement

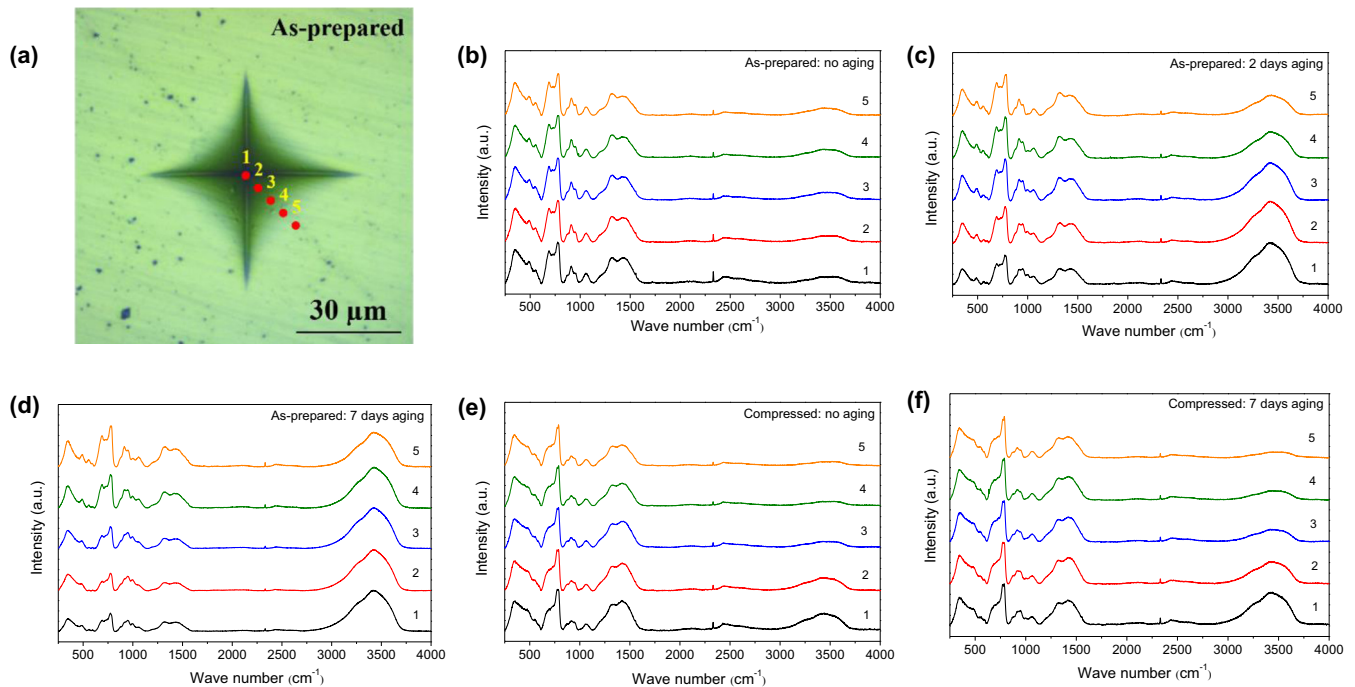


FIG. 5. Micro-Raman spectra of as-prepared CsAIB glass with aging for (b) 0, (c) 2, or (d) 7 days and compressed CsAIB glass with aging for (e) 0 or (f) 7 days. As shown in (a), the spectra were recorded at increasing distances (about $4\ \mu\text{m}$) from the center to the edge of a Vickers indent produced at 4.9 N.

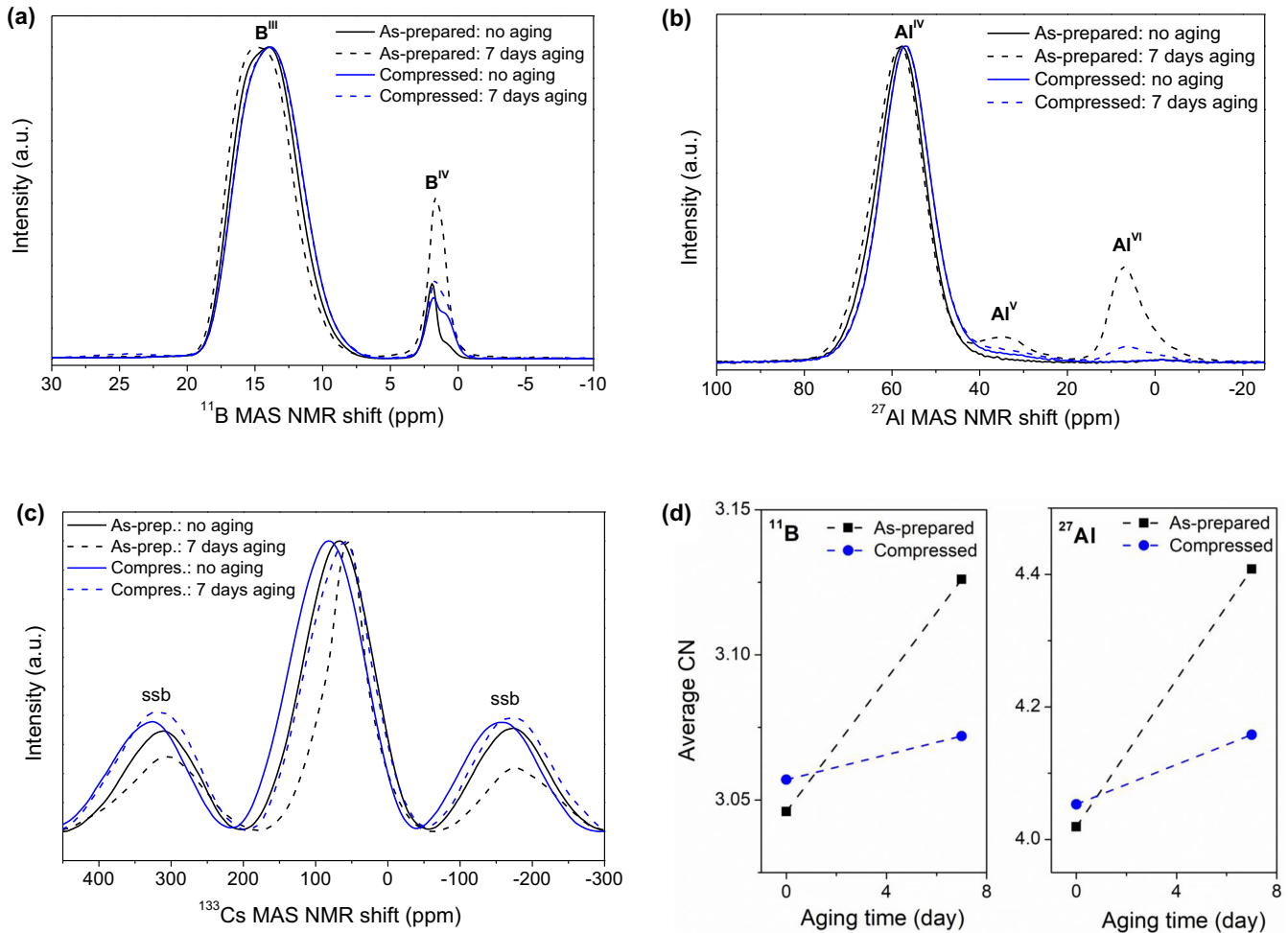


FIG. 6. (a) ^{11}B MAS NMR spectra for the as-prepared and compressed CsAIB glass with aging for 0 or 7 days. (b) ^{27}Al MAS NMR spectra for the as-prepared and compressed CsAIB glass with aging for 0 or 7 days. (c) ^{133}Cs MAS NMR spectra for the as-prepared and compressed CsAIB glass with aging for 0 or 7 days. Spinning sidebands (ssb) are indicated. (d) Effect of aging on the average coordination number (CN) of boron and aluminum in as-made and compressed glasses.

with previous studies on crack tips in oxide glasses, which are believed to propagate faster through the material once water can hydrolyze the strained network bonds [27,60]. Moreover, the extent of hydration increases with increasing indentation load, as seen by comparing the Raman spectra in Fig. 5(b) with those in Fig. S16 in the Supplemental Material [48]. This result supports that the highly stressed glass network is more vulnerable to the attack of water from the environment.

To further understand the effect of aging and pressure on the short-range structure of the studied CsAIB glasses, we performed ^{11}B , ^{27}Al , and ^{133}Cs MAS NMR spectroscopy measurements on powdered samples (Fig. 6). The determined speciation and spectral deconvolution are shown in Table S1 and Figs. S17 and S18, respectively, in the Supplemental Material [48]. Consistent with the preference for alkali modifier cations to charge-balance AlO_4^- relative to BO_4^- units in aluminoborate glasses [61–63], the network of the as-made glass consists mainly of B^{III} and Al^{IV} , with only minor fractions of higher coordinated boron and aluminum. Prior to any aging, this local chemical environment of the network-former atoms is sensitive to densification, as boron

and aluminum can increase their coordination numbers with pressure [64,65]. Indeed, the ^{11}B and ^{27}Al MAS NMR spectra show that the average coordination numbers of B and Al increase upon compression [Fig. 6(d)], although the changes are much smaller than those observed in sodium and lithium aluminoborate glasses under the same pressure conditions [12]. Moreover, for the lithium aluminoborate glasses, the increase in coordination numbers of boron and aluminum is accompanied by a slight increase in ^6Li MAS NMR shift. In the present CsAIB glass, the ^{133}Cs MAS NMR shift also increases from 79 to 87 ppm upon 1 GPa hot compression [Fig. 6(c)]. This may be because the partial negative charge on the oxygen atom around boron increases with the pressure-induced conversion of B^{III} to B^{IV} , which is expected to increase their charge-compensation demand. Hence, the interactions between oxygen and caesium ions in the network become strengthened under the applied pressure, leading to a shrinkage of the average distance between oxygen and modifying cations. Moreover, since both aluminum and boron enter a higher coordination state with different need for charge compensation when the glass is compressed, some caesium cations are reassigned from charge-compensating Al^{IV} in the

as-made glass to charge-compensating B^{IV} in the compressed glass. Finally, we note that the majority of the trigonal boron signal in the as-made CsAlB glass can be assigned to ring sites (B_{ring}^{III}) [66,67], with the minor trigonal boron signal being assigned to nonring sites ($B_{nonring}^{III}$), as seen Table S1 in the Supplemental Material [48]. Support for the resolution and assignment of two types of B^{III} environments has been obtained from ^{11}B triple quantum MAS NMR analysis on the as-made glass (Fig. S19 in the Supplemental Material [48]), and the findings are consistent with numerous other studies of B-rich glasses. Upon compression, we find that the fraction of $B_{nonring}^{III}$ increases, accompanied by the conversion of B^{III} to B^{IV} , consistent with other borate and borosilicate glasses studied under similar densification treatments [12].

Next, we study the effect of aging on the structure of the as-made and densified CsAlB glasses. Generally the coordination numbers of Al and B increase upon aging, including the formation of sixfold Al [Figs. 6(a) and 6(b)], indicating that the local chemical environment of the network-former atoms is sensitive to hydrolysis. In the as-prepared glass, aging is found to have a more significant effect on the change of coordination numbers of Al and B compared to compression [Fig. 6(d)]. Assuming that the incorporated water acts as a traditional network modifier or charge compensator, it is unexpected that water simultaneously increases the fractions of B^{IV} (requires charge compensation) and Al^V/Al^{VI} (does not require charge compensation). As discussed above, alkali modifiers have an enthalpic preference for interaction with Al^{IV} over B^{IV} in aluminoborate glasses, but this is not observed upon aging if considering water as a modifier. Moreover, the ^{133}Cs MAS NMR spectra show water interaction with Cs modifiers and it is thus possible that water preferentially interacts with boron relative to aluminum (to form B^{IV}), while some of the Cs charge-compensators for Al^{IV} are removed by aging, effectively increasing the coordination number of aluminum. For the compressed glass, there is a minor change in the coordination numbers of Al and B upon aging compared to the as-prepared glass, in agreement with the Raman spectroscopy analysis, showing that less water molecules interact with the surface of the compressed glass upon aging. Finally, we note that the fraction of $B_{nonring}^{III}$ increases along with the conversion of B^{III} to B^{IV} , indicating that the water molecules hydrolyze the original ring structures of the borate network as the aging time increasing. This result is also in good agreement with the Raman spectroscopy analysis, showing that the borate superstructures are broken up upon aging.

Considering again the ^{133}Cs MAS NMR spectra in Fig. 6(c), we find that the main peak becomes sharper upon aging and shifts downwards (from 79 to 71 ppm), indicating that aging leads to an increase in the Cs-O bond distance. As seen in Fig. S20 and Table S3 in the Supplemental Material [48], the ^{133}Cs MAS NMR signal in the as-prepared and compressed glasses after aging can be deconvoluted into at least two distinct Cs^+ environments (sites I and II). Site I is the same as that in the as-made glass before aging, while the new

site II is expected to be associated with hydrated Cs^+ groups attached to the glass network resulting from aging [68]. The latter interpretation is supported by several studies related to the impact of hydration on the ^{133}Cs NMR line shape [69,70], the effect of dehydration in titanosilicate minerals on the ^{133}Cs NMR spectra [71], the relation between Cs^+ mobility and motional narrowing of the ^{133}Cs resonance [72], and the role of hydration/dehydration on the ^{133}Cs quadrupolar coupling constant [73].

These Cs-OH groups could be more free to move around and thus have higher mobility in the surface of the glass, and would be consistent with both the relatively narrow and much more Lorentzian line shape for the Cs II site. In terms of the mechanical performance, such higher surface mobility is associated with higher network flexibility, as evidenced by the slightly lower hardness upon long-term aging (Fig. S10 in the Supplemental Material [48]). This effect is likely a contributing factor to the superior crack resistance of the aged CsAlB glass, as it could enable the indented glass to release the residual stress by structural rearrangements.

IV. CONCLUSIONS

We have shown that ultrahigh resistance to sharp contact cracking can be achieved in a caesium aluminoborate glass by simply storing the glass under typical atmospheric humidity (RH \sim 45%) conditions. The same pronounced effect of humid aging on crack resistance is not found for a range of other tested oxide glasses. As the most significant finding, we have observed crack-free cube corner indents above 25 N in the aged caesium aluminoborate glass, which is the highest ever recorded crack resistance for cube corner indentation to our knowledge, even including commercial ion exchanged cover glasses. The caesium aluminoborate glass is characterized by a highly flexible network structure and upon subjecting the glass to permanent volume densification, the positive effect of humid aging on crack resistance almost vanishes. Our results indicate that the high crack resistance is due to the formation of surface hydroxyl groups, increasing coordination numbers of both Al and B, partial break down of the borate superstructures, and increasing average Cs-O bond distance upon aging. To realize the potential of using such glasses as damage-resistant engineering materials, the plasticity mechanism needs to be transferred to other oxide glass compositions that are suitable for large-scale manufacturing. The hydration layer would need to be formed by a post-treatment process at high relative humidity and/or temperature in order to ensure that the glass does not gradually corrode over time under ambient conditions.

ACKNOWLEDGMENTS

This work was supported by the China Scholarship Council (CSC No. 201806370210). We thank K. Januchta for providing some of the glass samples, and M. S. Bødker and C. Gao for assistance with the FTIR measurements.

- [1] G. Brambilla and D. N. Payne, *Nano Lett.* **9**, 831 (2009).
 [2] E. J. Frankberg, J. Kalikka, F. García Ferré, L. Joly-Pottuz, T. Salminen, J. Hintikka, M. Hokka, S. Koneti, T. Douillard, B.

- Le Saint, P. Kreiml, M. J. Cordill, T. Epicier, D. Stauffer, M. Vanazzi, L. Roiban, J. Akola, F. Di Fonzo, E. Levänen, and K. Masenelli-Varlot, *Science* **366**, 864 (2019).

- [3] L. Wondraczek, J. C. Mauro, J. Eckert, U. Kühn, J. Horbach, J. Deubener, and T. Rouxel, *Adv. Mater.* **23**, 4578 (2011).
- [4] J. E. Ritter and C. L. Sherburne, *J. Am. Ceram. Soc.* **54**, 601 (1971).
- [5] C. R. Kurkjian, P. K. Gupta, and R. K. Brow, *Int. J. Appl. Glas. Sci.* **1**, 27 (2010).
- [6] R. Gardon, Thermal tempering of glass, in *Elasticity and Strength of Glass, Glass: Science and Technology*, edited by D. R. Uhlmann and N. J. Kreidl, Vol. 5 (Academic Press, New York, 1980), pp. 146–217.
- [7] V. M. Sglavo, A. Prezzi, and T. Zandonella, *Adv. Eng. Mater.* **6**, 344 (2004).
- [8] S. Karlsson, B. Jonson, and C. Stålhandske, *Glass Technol.* **51**, 41 (2010).
- [9] Q.-G. Jiang, C. Cao, T.-C. Lin, S. Wu, and X. Li, *Adv. Mater.* **31**, 1901803 (2019).
- [10] Y. Zhang, L. Huang, and Y. Shi, *Nano Lett.* **19**, 5222 (2019).
- [11] C. Moysan, R. Riedel, R. Harshe, T. Rouxel, and F. Augereau, *J. Eur. Ceram. Soc.* **27**, 397 (2007).
- [12] K. Januchta, R. E. Youngman, A. Goel, M. Bauchy, S. L. Logunov, S. J. Rzoska, M. Bockowski, L. R. Jensen, and M. M. Smedskjaer, *Chem. Mater.* **29**, 5865 (2017).
- [13] G. A. Rosales-Sosa, A. Masuno, Y. Higo, and H. Inoue, *Sci. Rep.* **6**, 23620 (2016).
- [14] M. Wada, H. Furukawa, and K. Fujita, Crack resistance of glass on Vickers indentation, in *Proceedings of the 10th International Congress on Glass*, Vol. 11 (Ceramic Society of Japan, Tokyo, 1974), p. 39.
- [15] S. Yoshida, *J. Non-Cryst. Solids X* **1**, 100009 (2019).
- [16] J. Sehgal and S. Ito, *J. Am. Ceram. Soc.* **81**, 2485 (1998).
- [17] T. M. Gross, J. Wu, D. E. Baker, J. J. Price, and R. Yongsunthon, *J. Non-Cryst. Solids* **494**, 13 (2018).
- [18] G. A. Rosales-Sosa, A. Masuno, Y. Higo, H. Inoue, Y. Yanaba, T. Mizoguchi, T. Umada, K. Okamura, K. Kato, and Y. Watanabe, *Sci. Rep.* **5**, 15233 (2015).
- [19] K. Januchta, M. Bauchy, R. E. Youngman, S. J. Rzoska, M. Bockowski, and M. M. Smedskjaer, *Phys. Rev. Mater.* **1**, 063603 (2017).
- [20] K. Januchta and M. M. Smedskjaer, *J. Non-Cryst. Solids X* **1**, 100007 (2019).
- [21] T. M. Gross and J. J. Price, *Front. Mater.* **4**, 4 (2017).
- [22] S. Yoshida, K. Wada, T. Fujimura, A. Yamada, M. Kato, J. Matsuoka, and N. Soga, *Front. Mater.* **3**, 54 (2016).
- [23] T. K. Bechgaard, J. C. Mauro, and M. M. Smedskjaer, *J. Non-Cryst. Solids* **491**, 64 (2018).
- [24] K. Januchta, M. Stepniewska, L. R. Jensen, Y. Zhang, M. A. J. Somers, M. Bauchy, Y. Yue, and M. M. Smedskjaer, *Adv. Sci.* **6**, 1901281 (2019).
- [25] J. Acocella, M. Tomozawa, and E. B. Watson, *J. Non-Cryst. Solids* **65**, 355 (1984).
- [26] J. Luo, S. ichi Amma, L. Chen, D. Ngo, J. C. Mauro, C. G. Pantano, and S. H. Kim, *J. Non-Cryst. Solids* **510**, 179 (2019).
- [27] S. M. Wiederhorn, *J. Am. Ceram. Soc.* **50**, 407 (1967).
- [28] K. Hirao and M. Tomozawa, *J. Am. Ceram. Soc.* **70**, 497 (1987).
- [29] J. M. Rimsza, R. E. Jones, and L. J. Criscenti, *J. Geophys. Res. Solid Earth* **123**, 9341 (2018).
- [30] H. Mei, Y. Yang, A. C. T. van Duin, S. B. Sinnott, J. C. Mauro, L. Liu, and Z. Fu, *Acta Mater.* **178**, 36 (2019).
- [31] S. Striepe, J. Deubener, M. M. Smedskjaer, and M. Potuzak, *J. Non-Cryst. Solids* **379**, 161 (2013).
- [32] S. M. Wiederhorn, T. Fett, G. Rizzi, M. J. Hoffmann, and J. P. Guin, *Metall. Mater. Trans. A: Phys. Metall. Mater. Sci.* **44**, 1164 (2013).
- [33] S. M. Wiederhorn, T. Fett, G. Rizzi, M. J. Hoffmann, and J. P. Guin, *Eng. Fract. Mech.* **100**, 3 (2013).
- [34] M. Tomozawa and E. M. Aaldenberg, *Phys. Chem. Glasses: Eur. J. Glass Sci. Technol., Part B* **58**, 156 (2017).
- [35] J. Luo, H. Huynh, C. G. Pantano, and S. H. Kim, *J. Non-Cryst. Solids* **452**, 93 (2016).
- [36] T. M. Gross and G. M. Guryanov, US Patent No. 015,283,8A1 (2019).
- [37] K. Januchta, R. E. Youngman, A. Goel, M. Bauchy, S. J. Rzoska, M. Bockowski, and M. M. Smedskjaer, *J. Non-Cryst. Solids* **460**, 54 (2017).
- [38] P. Liu, K. Januchta, L. R. Jensen, M. Bauchy, and M. M. Smedskjaer, *J. Am. Ceram. Soc.* **103**, 944 (2020).
- [39] T. Rouxel, *J. Am. Ceram. Soc.* **90**, 3019 (2007).
- [40] K. Januchta, R. Sun, L. Huang, M. Bockowski, S. J. Rzoska, L. R. Jensen, and M. M. Smedskjaer, *J. Non-Cryst. Solids* **494**, 86 (2018).
- [41] M. M. Smedskjaer, S. J. Rzoska, M. Bockowski, and J. C. Mauro, *J. Chem. Phys.* **140**, 054511 (2014).
- [42] X. Wu and R. Dieckmann, *J. Non-Cryst. Solids* **357**, 2846 (2011).
- [43] C. Peuker, W. Bessau, K. W. Brzezinka, A. Kohl, U. Reinholz, and H. Geibler, *Glass Sci. Technol.* **75**, 313 (2002).
- [44] S. Kapoor, L. Wondraczek, and M. M. Smedskjaer, *Front. Mater.* **4**, 1 (2017).
- [45] D. Massiot, F. Fayon, M. Capron, I. King, S. Le Calvé, B. Alonso, J.-O. Durand, B. Bujoli, Z. Gan, and G. Hoatson, *Magn. Reson. Chem.* **40**, 70 (2002).
- [46] S. Yoshida, J.-C. Sanglebœuf, and T. Rouxel, *J. Mater. Res.* **20**, 3404 (2005).
- [47] K. Januchta, P. Liu, S. R. Hansen, T. To, and M. M. Smedskjaer, *J. Am. Ceram. Soc.* **103**, 1656 (2020).
- [48] See Supplemental Material at <http://link.aps.org/supplemental/10.1103/PhysRevMaterials.4.063606> for further details about thermal, structural, and elastic properties of the studied glasses, including XRD spectra, DSC curves, UV-VIS transmittance spectra, FTIR spectra, micro-Raman spectra, ^{11}B triple quantum (3Q) MAS NMR data and deconvolution of the ^{133}Cs , ^{27}Al , ^{11}B MAS NMR spectra, aging time dependence of hardness and water content, and optical micrographs of Vickers indents. Also, it includes the following supplemental references: [S1] H. Li, Y. Su, L. Li, and D. M. Strachan, *J. Non-Cryst. Solids* **292**, 167 (2001); [S2] W. L. Konijnendijk and J. M. Stevels, *ibid.* **20**, 193 (1976); [S3] E. I. Kamitsos and G. D. Chryssikos, *J. Mol. Struct.* **247**, 1 (1991); [S4] B. N. Meera and J. Ramakrishna, *J. Non-Cryst. Solids* **159**, 1 (1993); [S5] K. Vignarooban, P. Boolchand, M. Micoulaut, M. Malki, and W. J. Bresser, *Europhys. Lett.* **108**, 56001 (2014); [S6] J. Krogh-Moe, *J. Non-Cryst. Solids* **1**, 269 (1969); [S7] P. McMillan and B. Piriou, *ibid.* **55**, 221 (1983); [S8] M. Licheron, V. Montouillout, F. Millot, and D. R. Neuville, *ibid.* **357**, 2796 (2011); [S9] T. Yano, N. Kunimine, S. Shibata, and M. Yamane, *ibid.* **321**, 137 (2003); [S10] R. K. Brow, D. R. Tallant, and G. L. Turner, *J. Am. Ceram. Soc.* **80**, 1239 (2005); [S11] A. Anedda, C. M. Carbonaro, F. Clemente, R. Corpino, P. C. Ricci, D. Fisica, V. Uni, and U. Cagliari,

- J. Phys. Chem. B **107**, 13661 (2003); [S12] M. Mercier, A. Di Muro, D. Giordano, N. Métrich, P. Lesne, M. Pichavant, B. Scaillet, R. Clocchiatti, and G. Montagnac, *Geochim. Cosmochim. Acta* **73**, 197 (2009); [S13] N. Ollier, T. Charpentier, B. Boizot, G. Wallez, and D. Ghaleb, *J. Non-Cryst. Solids* **341**, 26 (2004); [S14] K. Januchta, M. Stepniewska, L. R. Jensen, Y. Zhang, M. A. J. Somers, M. Bauchy, Y. Yue, and M. M. Smedskjaer, *Adv. Sci.* **6**, 1901281 (2019).
- [49] T. To, L. R. Jensen, and M. M. Smedskjaer, *J. Non-Cryst. Solids* **534**, 119946 (2020).
- [50] C. Gautam, A. K. Yadav, and A. K. Singh, *ISRN Ceram.* **2012**, 428497 (2012).
- [51] M. M. Smedskjaer, J. C. Mauro, and Y. Yue, *J. Phys. Chem. B* **119**, 7106 (2015).
- [52] N. Mascaraque, K. Januchta, K. F. Frederiksen, R. E. Youngman, M. Bauchy, and M. M. Smedskjaer, *J. Am. Ceram. Soc.* **102**, 1157 (2019).
- [53] R. D. Shannon, *Acta Crystallogr. Sect. A* **32**, 751 (1976).
- [54] K. G. Aakermann, K. Januchta, J. A. L. Pedersen, M. N. Svenson, S. J. Rzoska, M. Bockowski, J. C. Mauro, M. Guerette, L. Huang, and M. M. Smedskjaer, *J. Non-Cryst. Solids* **426**, 175 (2015).
- [55] M. N. Svenson, M. Guerette, L. Huang, N. Lönnroth, J. C. Mauro, S. J. Rzoska, M. Bockowski, and M. M. Smedskjaer, *Chem. Phys. Lett.* **651**, 88 (2016).
- [56] M. B. Østergaard, S. R. Hansen, K. Januchta, T. To, S. J. Rzoska, M. Bockowski, M. Bauchy, and M. M. Smedskjaer, *Materials (Basel)* **12**, 2439 (2019).
- [57] S. Yoshida, M. Kato, A. Yokota, S. Sasaki, A. Yamada, J. Matsuoka, N. Soga, and C. R. Kurkjian, *J. Mater. Res.* **30**, 2291 (2015).
- [58] U. Bauer, H. Behrens, M. Fechtelkord, S. Reinsch, and J. Deubener, *J. Non-Cryst. Solids* **423-424**, 58 (2015).
- [59] A. Anedda, C. M. Carbonaro, F. Clemente, R. Corpino, and P. C. Ricci, *J. Phys. Chem. B* **107**, 13661 (2003).
- [60] T. Tomozawa, W. -T. Han, and W. A. Lanford, *J. Am. Ceram. Soc.* **74**, 2573 (1991).
- [61] R. Gresch, W. Müller-Warmuth, and H. Dutz, *J. Non-Cryst. Solids* **21**, 31 (1976).
- [62] L. Züchner, J. C. C. Chan, W. Müller-Warmuth, and H. Eckert, *J. Phys. Chem. B* **102**, 4495 (1998).
- [63] L.-S. Du and J. F. Stebbins, *Solid State Nucl. Magn. Reson.* **27**, 37 (2005).
- [64] M. N. Svenson, T. K. Bechgaard, S. D. Fuglsang, R. H. Pedersen, A. Ø. Tjell, M. B. Østergaard, R. E. Youngman, J. C. Mauro, S. J. Rzoska, M. Bockowski, and M. M. Smedskjaer, *Phys. Rev. Appl.* **2**, 024006 (2014).
- [65] T. K. Bechgaard, A. Goel, R. E. Youngman, J. C. Mauro, S. J. Rzoska, M. Bockowski, L. R. Jensen, and M. M. Smedskjaer, *J. Non-Cryst. Solids* **441**, 49 (2016).
- [66] R. E. Youngman and J. W. Zwanziger, *J. Non-Cryst. Solids* **168**, 293 (1994).
- [67] R. E. Youngman and J. W. Zwanziger, *J. Phys. Chem.* **100**, 16720 (1996).
- [68] B. R. Cherry, M. Nyman, and T. M. Alam, *J. Solid State Chem.* **177**, 2079 (2004).
- [69] C. A. Weiss, R. J. Kirkpatrick, and S. P. Altaner, *Geochim. Cosmochim. Acta* **54**, 1655 (1990).
- [70] X. Xu, A. G. Kalinichev, and R. James Kirkpatrick, *Geochim. Cosmochim. Acta* **70**, 4319 (2006).
- [71] V. Luca, J. V. Hanna, M. E. Smith, M. James, D. R. G. Mitchell, and J. R. Bartlett, *Microporous Mesoporous Mater.* **55**, 1 (2002).
- [72] H. Liu and C. P. Grey, *Microporous Mesoporous Mater.* **53**, 109 (2002).
- [73] P.-J. Chu, B. C. Gerstein, J. Nunan, and K. Klier, *ChemInform* **18**, 3588 (1987).

SUPPLEMENTAL MATERIAL

Achieving Ultra-High Crack Resistance in Glass through Humid Aging

Pengfei Liu¹, Randall E. Youngman², Lars R. Jensen³, Michal Bockowski⁴, Morten M. Smedskjaer^{1,*}

¹Department of Chemistry and Bioscience, Aalborg University, Aalborg, Denmark

²Science and Technology Division, Corning Incorporated, Corning, New York 14831, United States

³Department of Materials and Production, Aalborg University, 9220 Aalborg, Denmark

⁴Institute of High-Pressure Physics, Polish Academy of Sciences, 01-142 Warsaw, Poland

*Corresponding author. e-mail: mos@bio.aau.dk

Table S1. Boron and aluminum speciation derived from ^{11}B and ^{27}Al magic angle spinning (MAS) nuclear magnetic resonance (NMR) measurements on the CsAlB glasses. The errors of the boron and aluminum speciation do not exceed $\pm 1\%$.

Glass	B^{\square} [%]	$[\text{B}^{\square}_{\text{ring}}]/[\text{B}^{\square}_{\text{non-ring}}]$ [-]	B^{\square} [%]	Al^{\square} [%]	Al^{\square} [%]	Al^{\square} [%]
As-prepared (no aging)	95.4	3.20	4.6	98.1	1.9	0
Compressed (no aging)	94.3	2.18	5.7	94.7	5.3	0
As-prepared (aged for 7 days)	87.4	1.66	12.6	76.1	7.0	16.9
Compressed (aged for 7 days)	92.8	1.90	7.2	88.8	6.6	4.6

Table S2. Raman band assignments with references.

Structural unit	Wavenumber [cm ⁻¹]	Ref
B-O-B stretch & BO ₄ unit	450-570 & 900-1000	[S1]
Al-O-B stretch & aluminate network	480-500 & 700-720	[S1]
Ring metaborate	630 & 1300-1600	[S1-3]
Chain metaborate	730 & 1300-1600	[S1,2]
Di-triborate	755	[S4]
Tri-, Tetra- or Pentaborate	770 & 930	[S2-5]
Boroxol ring	808	[S2,6]
Pyroborate	820 & 1200-1300	[S1-3]
AlO ₄ unit	790 & 900	[S7,8]
Orthoborate	890-940	[S1]
Diborate	1100	[S3]
BO ₃ unit	1260, 1350, 1470, & 1530	[S9]
BO ₂ O- unit	1490 & 1550	[S9]
Al-B network	980	[S10]
M-OH	3200-3700	[S11,12]

Table S3. Caesium speciation derived from ^{133}Cs MAS NMR measurements on the CsAlB glasses. The errors of the caesium speciation do not exceed $\pm 3\%$, respectively.

Glass	Site	Position (ppm)	Area (%)
As-prepared (no age)	□	79	100
1 GPa (no age)	□	87	100
As-prepared (age for 7 day)	□	71	73
	□	54	27
1 GPa (age for 7 day)	□	80	96
	□	49	4

Figure S1. X-ray diffraction (XRD) spectrum for the as-made CsAlB glass. No sharp peaks are observed in the spectrum, confirming the non-crystalline nature of the sample at least within the XRD detection limit.

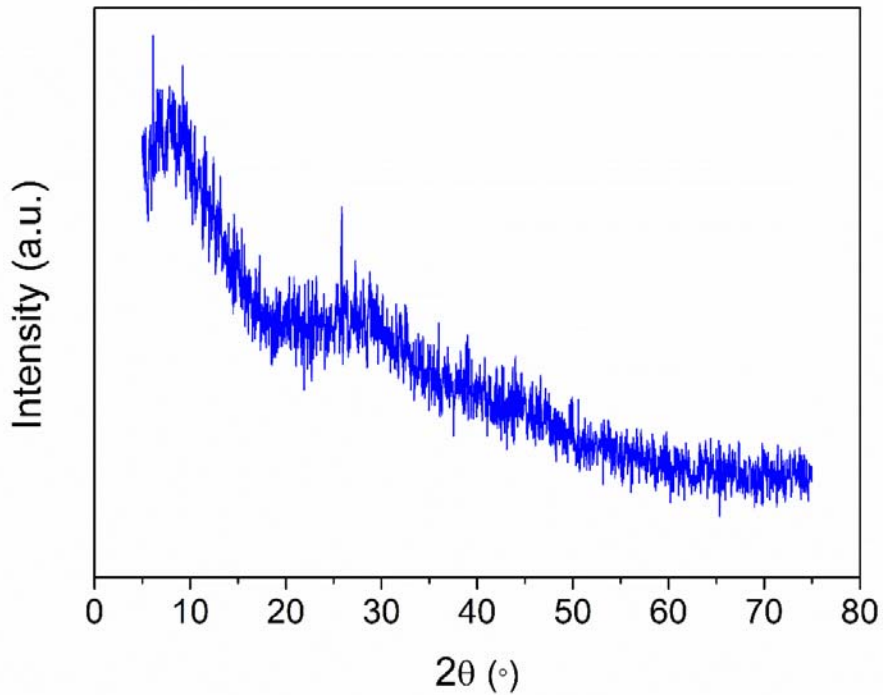


Figure S2. Isobaric heat capacity (C_p) as a function of temperature for the as-prepared CsAlB glass, showing a glass transition temperature (T_g) of 402 °C.

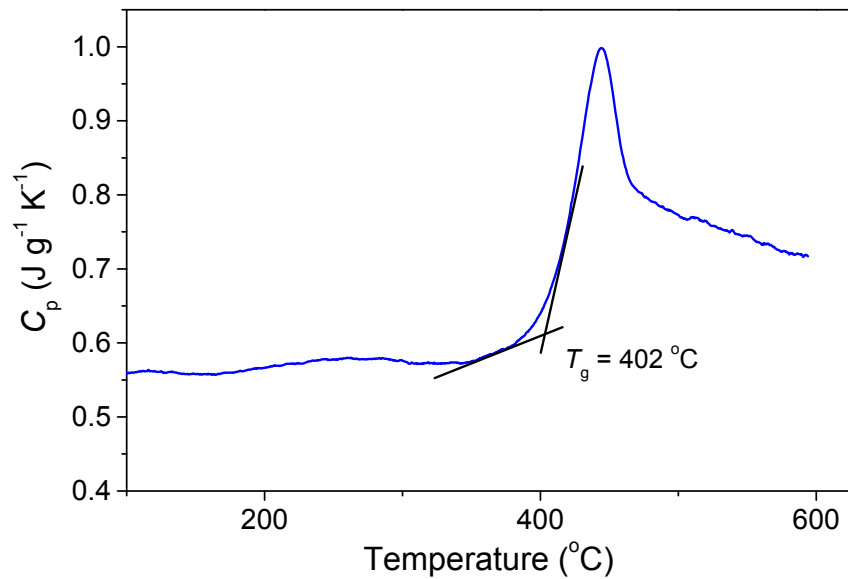


Figure S3. Micro-Raman spectra on the surface of the as-prepared CsAlB glass without aging at five different locations. No significant differences across the sample surface are observed, suggesting that the glass is compositionally homogeneous.

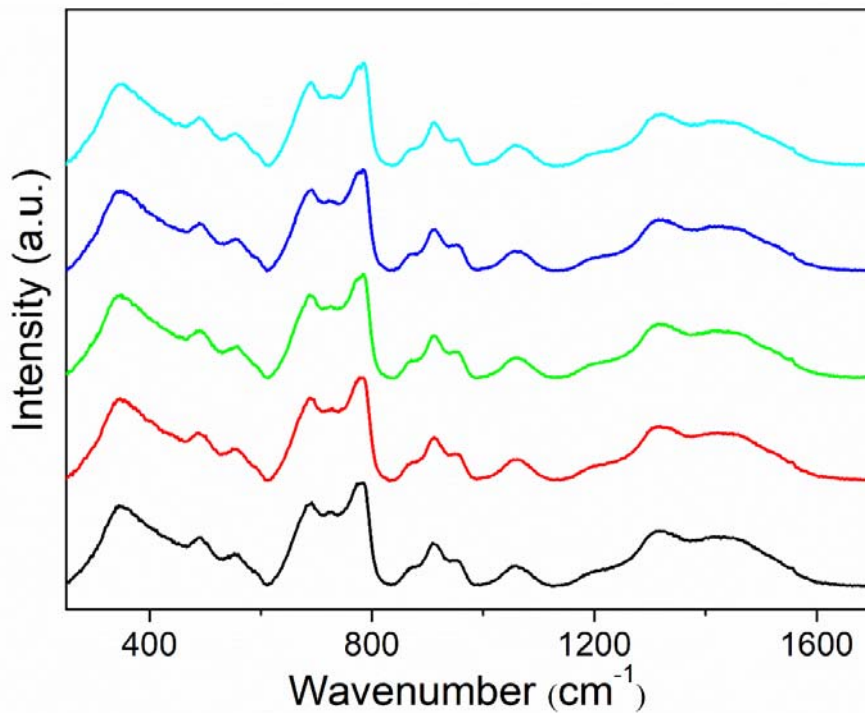


Figure S4. UV-VIS transmittance spectrum of the CsAlB glasses subjected to aging at 45% RH for various durations. The spectra are normalized to 1 mm thickness.

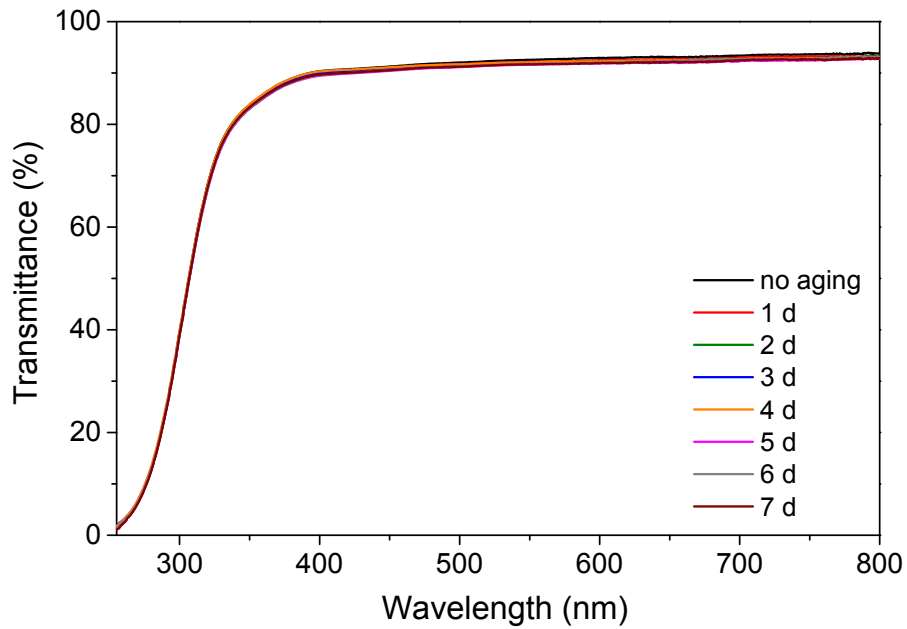


Figure S5. Fourier transform infrared (FT-IR) spectrum of the as-prepared CsAlB glass for different aging times.

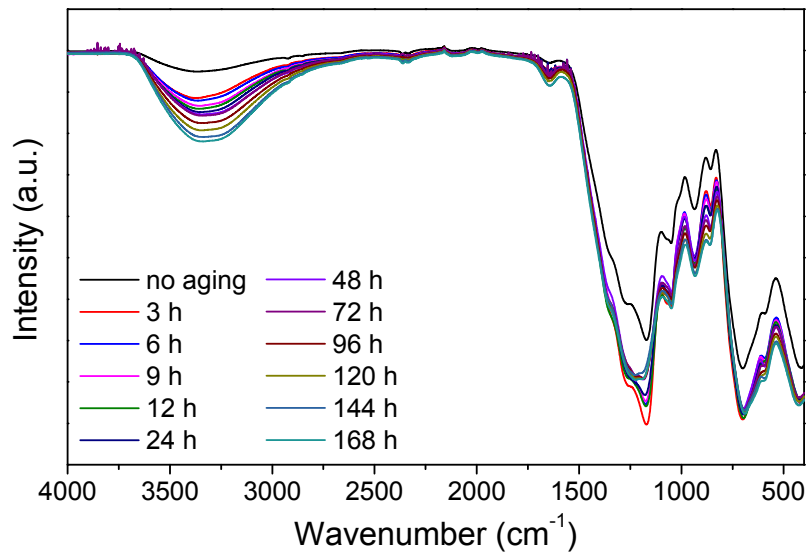


Figure S6. Aging time dependence of $c_{H_2O}\epsilon_{OH}$, which is a measure of the water content, in the CsAlB glass.

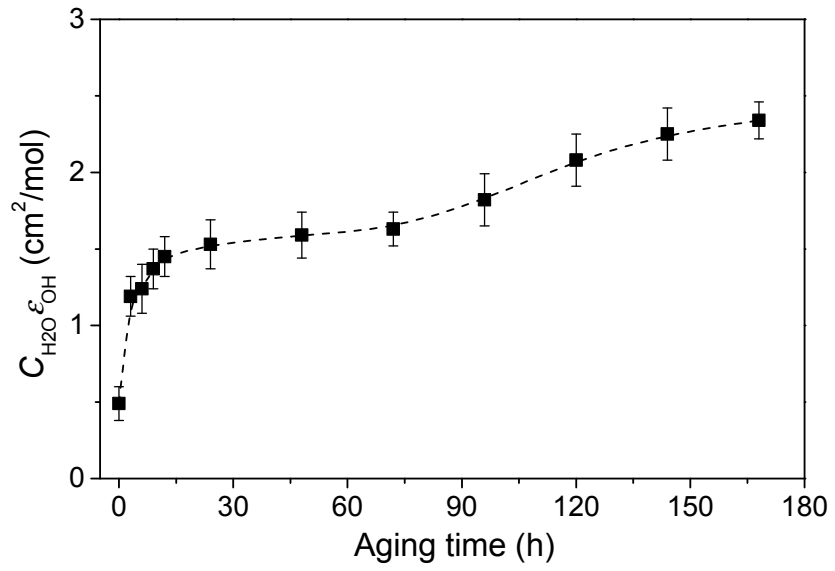


Figure S7. Effect of hot compression on the elastic moduli (Young's (E), shear (G), and bulk (B)) and Poisson's ratio (ν) of the CsAlB glass.

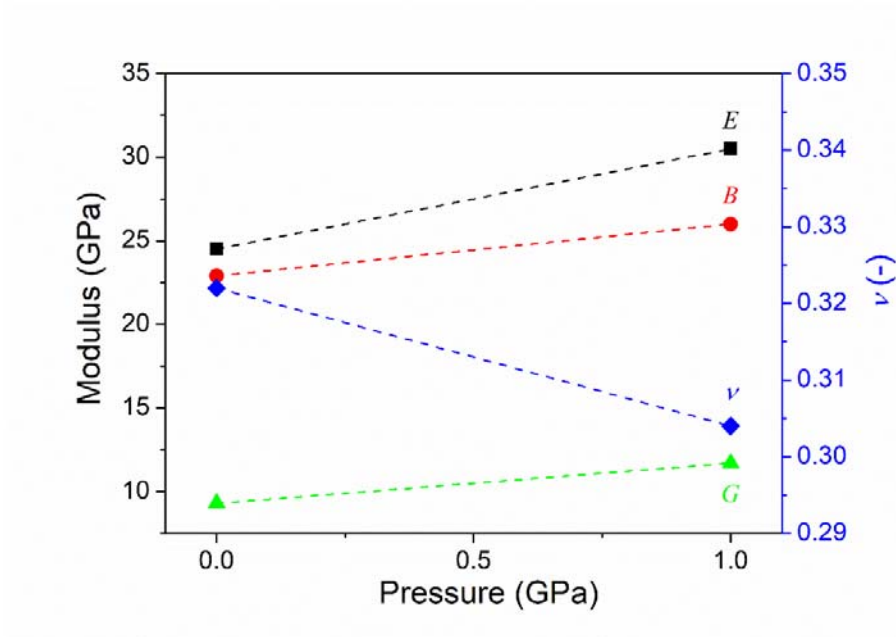


Figure S8. Heat flow (solid line) and mass loss (dashed line) of the as-prepared CsAlB glasses: bulk glass without aging, powdered glass without aging, powdered glass aged in dry desiccator, and powdered glass aged at 45% RH for 7 days in climate chamber.

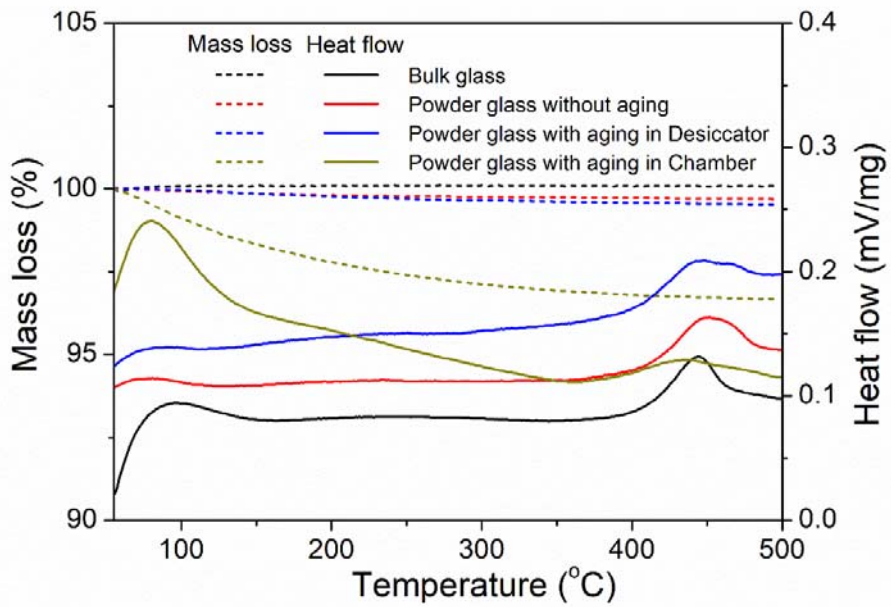


Figure S9. Optical micrographs of a Vickers indents produced at 4.9 N on the freshly polished surface of the CsAlB glass. After indentation, the glass underwent aging for various durations up to 7 days at 45% RH before these images were acquired. That is, the images show the change in size and shape of the same indent as a function of time.

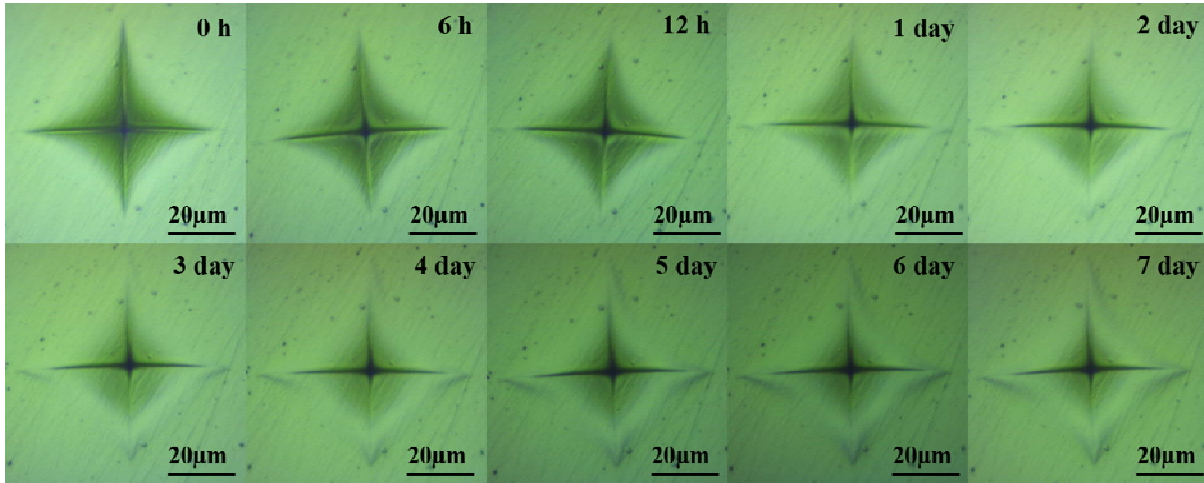


Figure S10. Aging time dependence of the Vickers hardness (H_V) of the the CsAlB glass.

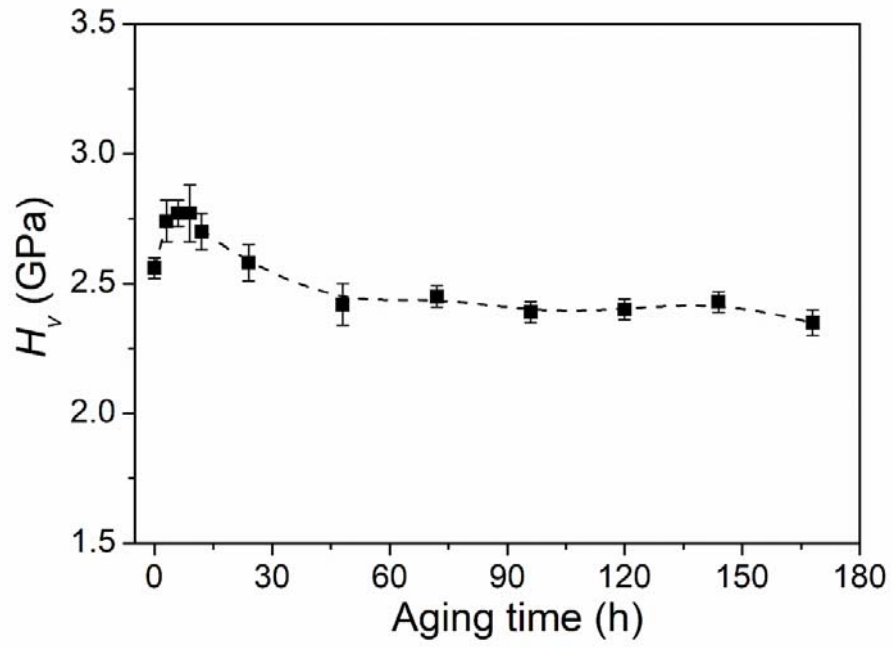


Figure S11. Optical micrographs of Vickers indents produced at 9.8 N on the surfaces of the CsAlB glasses, which have been subjected to humid aging for different durations prior to indentation.

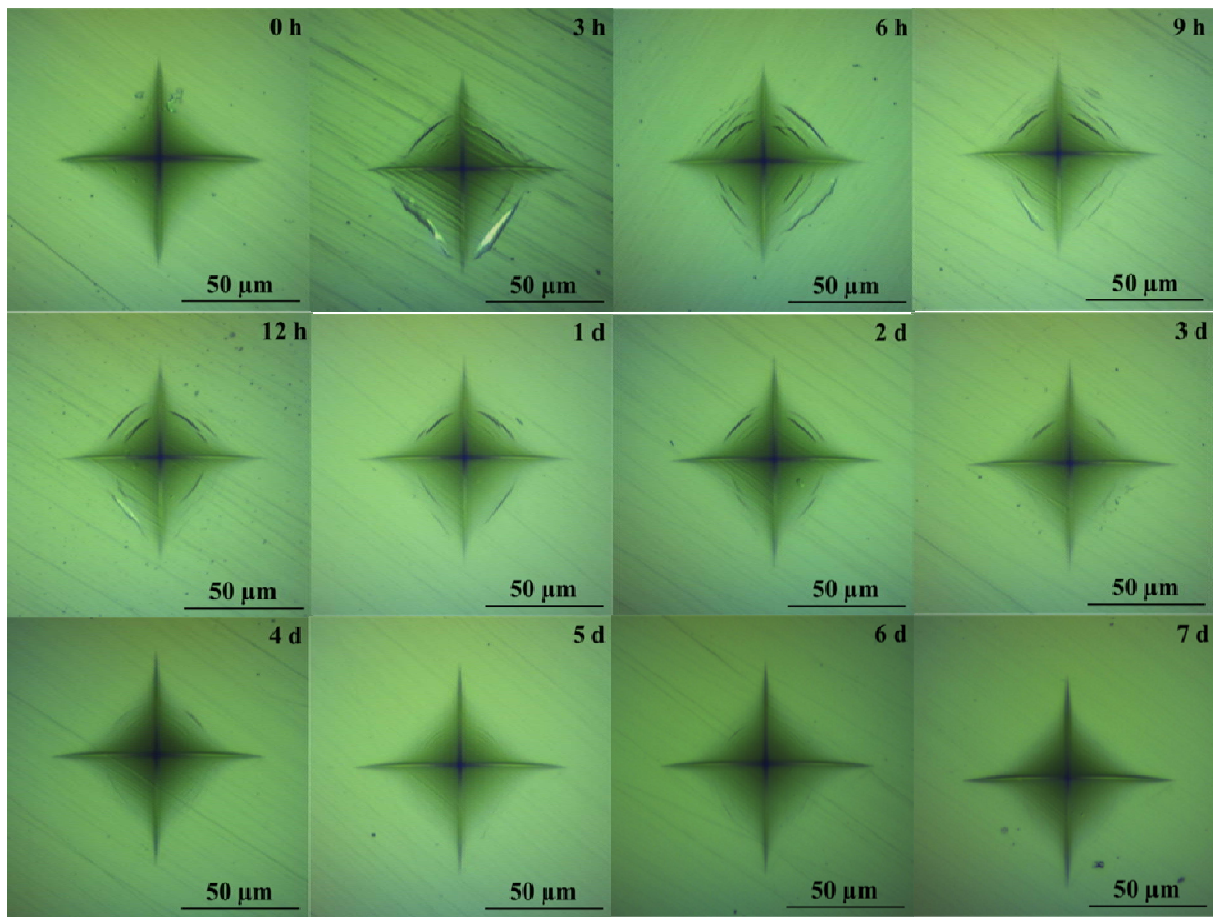


Figure S12. Crack initiation probability (PCI) as a function of applied indentation load for the as-prepared and compressed CsAlB glasses. The experimental data were fit to a sigmoidal function of the form $PCI = A_2 + (A_1 - A_2)/[1 + (x/x_0)^p]$ (solid lines), and the crack resistance (dashed line) was derived from the load at which an average of 2 or 1.5 cracks (PCI =50%) formed at the corners of the residual Vickers and cube corner imprints, respectively.

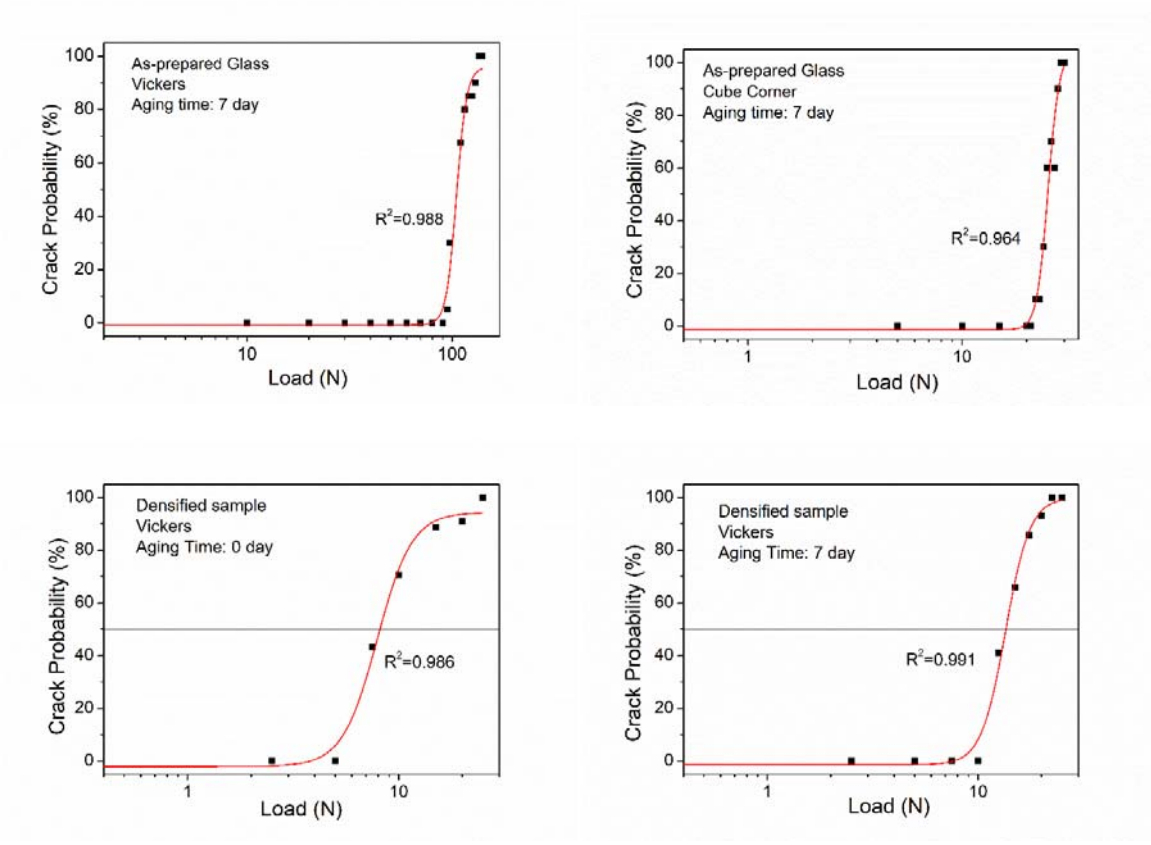
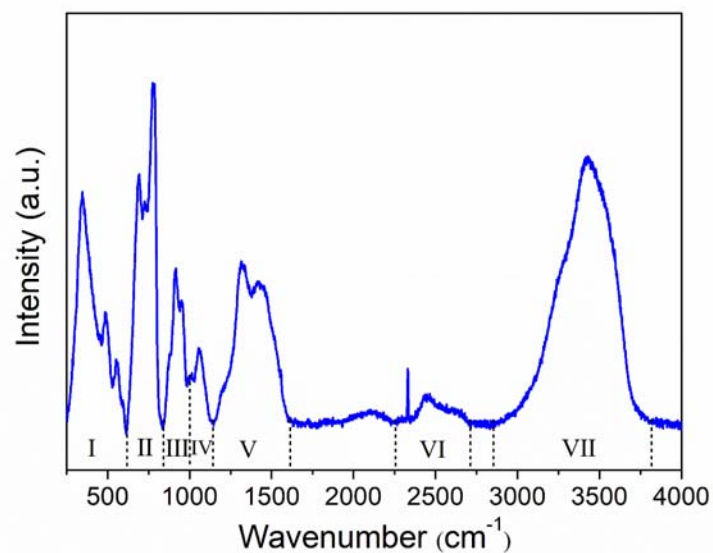


Figure S13. Micro-Raman spectrum of the as-prepared CsAlB glass that has been aged for 7 days at 45% RH. The spectrum is divided into seven main band regions.



The expected band assignments are outlined in the following (see also Table S2). The lowest frequency band region, ranging from ~ 280 to 625 cm^{-1} , is expected to contain contributions from B-O-B, Al-O-Al, and B-O-Al stretching vibrations [S1], in addition to vibrations due to superstructural units such as pentaborates. The second region, ranging from ~ 625 to 815 cm^{-1} , is characteristic for B₂O₃-rich glasses [S1], since peaks in this frequency range are typically assigned to borate superstructures such as chain and ring metaborates [S2,3], di-triborates [S4], and penta-, tetra-, or triborates [S2-5], as well as boroxol rings [S2,6]. In addition, B-O-Al stretching and aluminate network vibrations may be found in this region. The third region, ranging from ~ 815 to 1000 cm^{-1} , is expected to result from vibrations of AlO₄ units ($\sim 900\text{ cm}^{-1}$) [S7,8], Al-B network ($\sim 980\text{ cm}^{-1}$) [S13], and borate superstructures ($\sim 930\text{ cm}^{-1}$) [S1,3]. The fourth region, ranging from ~ 1000 to 1200 cm^{-1} , is usually assigned to other borate superstructural units such as diborates. The fifth region, ranging from ~ 1150 to 1600 cm^{-1} , is expected to be dominated by signal contributions from vibrations of superstructural units such as pyroborate units and chain and ring metaborate units [S9]. The sixth region (containing two small bands), ranging from ~ 2300 to 2400 cm^{-1} , has not yet been assigned [S14]. The last region, ranging from ~ 2850 to 3800 cm^{-1} , is expected to be associated with hydroxyl groups attached to the glass network due to hydration [S11,12].

Figure S14. Micro-Raman spectra on the as-prepared and compressed CsAlB glassed with aging for 0 and 7 days. The spectra are acquired either in the center of Vickers indents produced at 4.9 N or on surfaces without any indents.

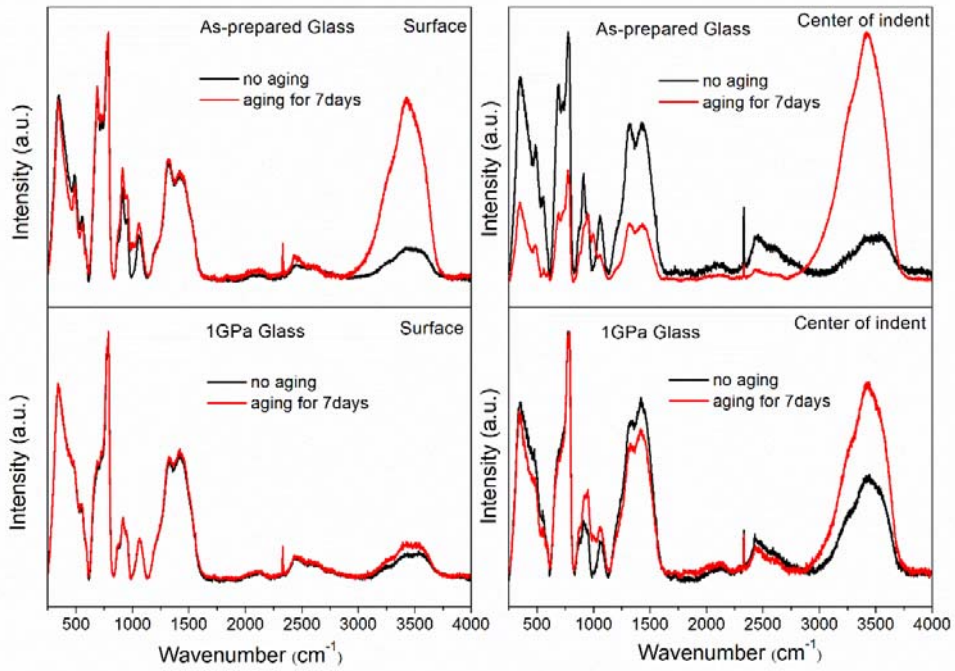


Figure S15. Relative Raman band of the region from ~ 2850 to 3800 cm^{-1} related to OH-groups plotted as a function of the position from the 4.9 N Vickers indent (see Figure 5a) for various as-prepared and compressed CsAIB glasses.

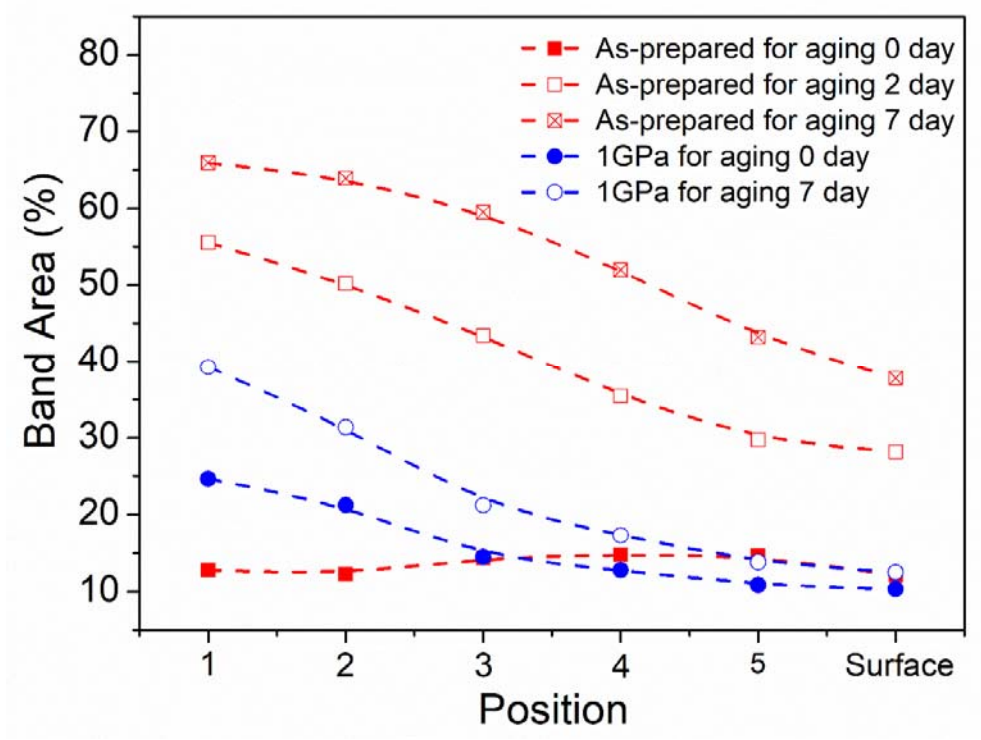


Figure S16. Micro-Raman spectra of the indented as-prepared CsAlB glass prior to aging. The spectra were recorded at increasing distances (about 5 μm) from the center to the edge of a 19.6 N Vickers indent.

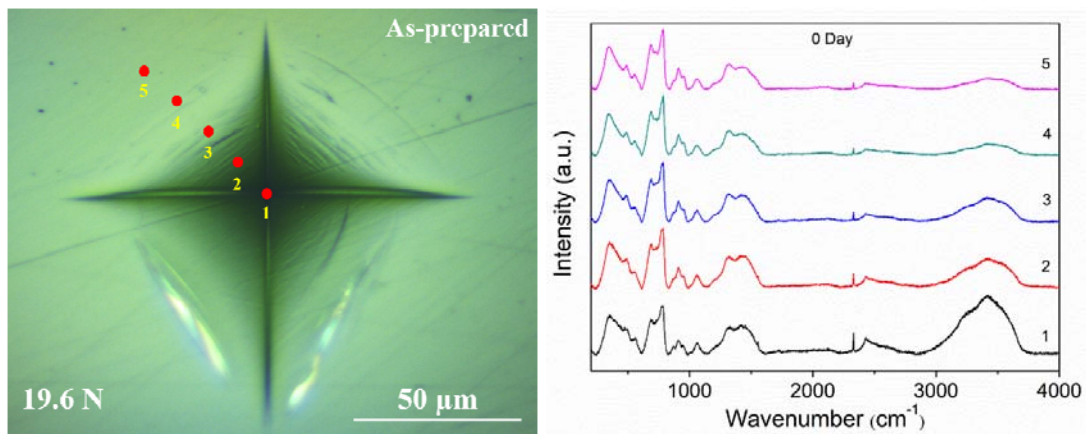


Figure S17. Deconvolution of the ^{11}B MAS NMR spectra for the CsAlB glasses: (a) as-prepared glasses without aging; (b) as-prepared glasses with aging for 7 days; (c) compressed glasses without aging; (d) compressed glasses with aging for 7 days.

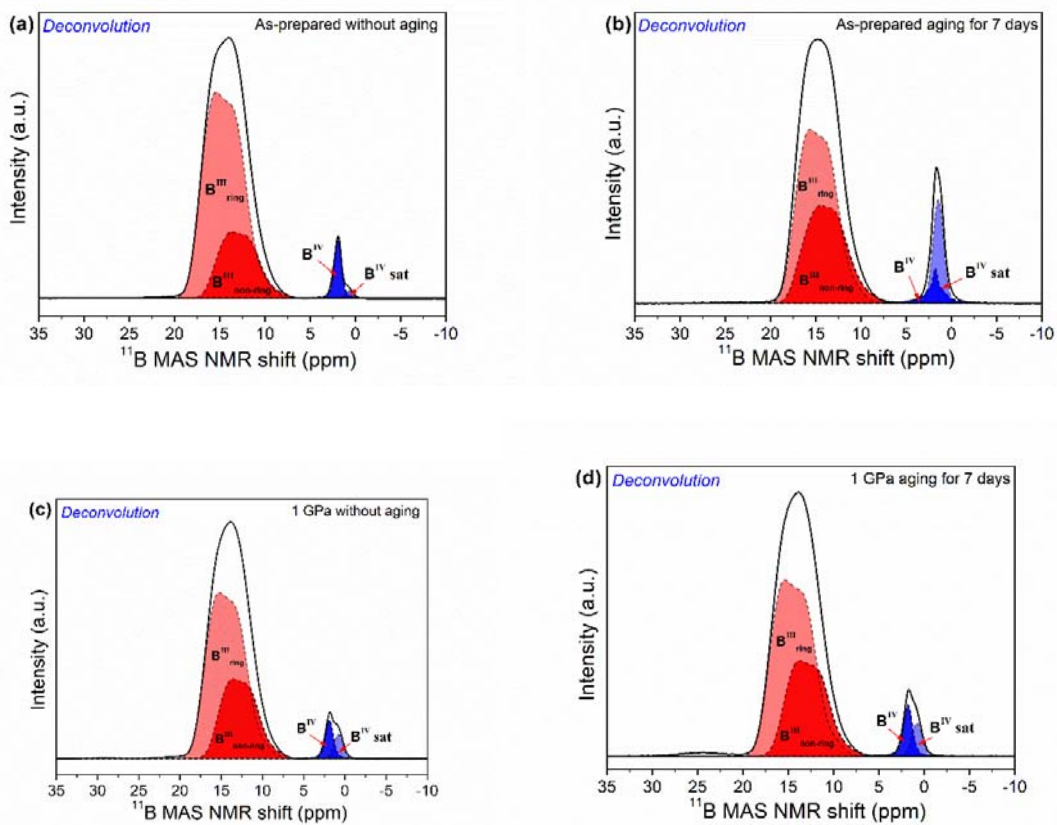


Figure S18. Deconvolution of the ^{27}Al MAS NMR spectra for the CsAlB glasses: (a) as-prepared glasses without aging; (b) as-prepared glasses with aging for 7 days; (c) compressed glasses without aging; (d) compressed glasses with aging for 7 days.

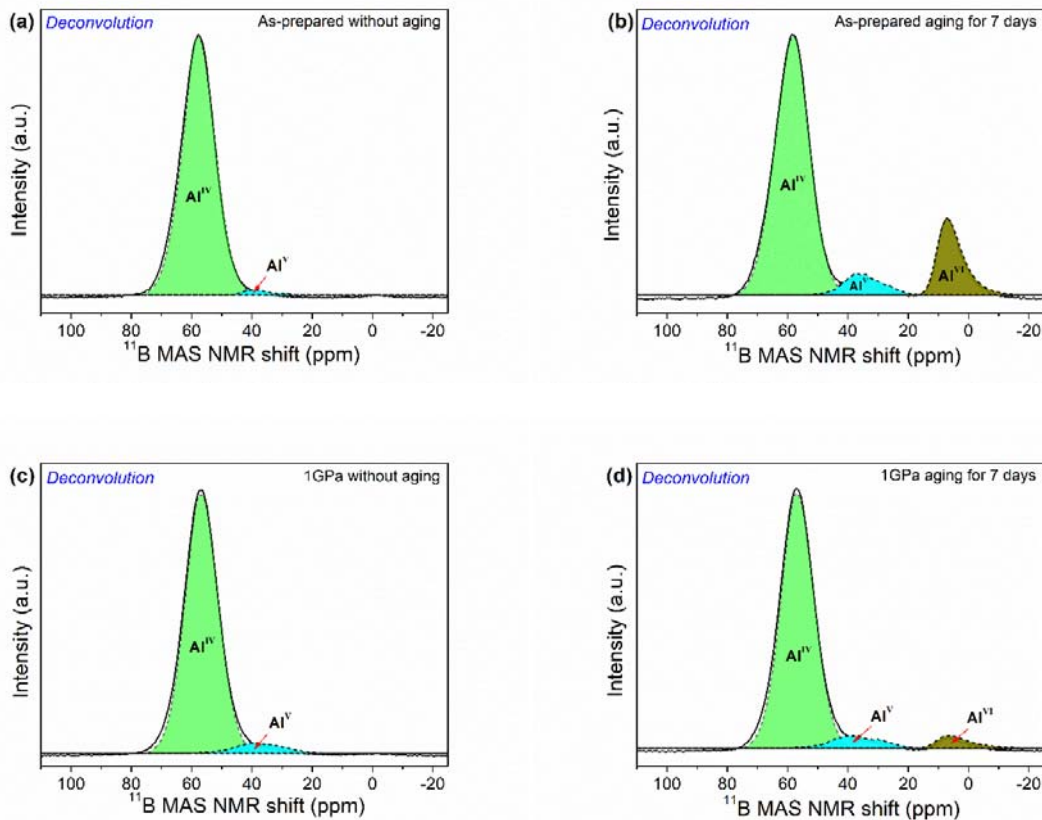


Figure S19. ^{11}B triple quantum (3Q) MAS NMR data for the as-made CsAlB glass without aging. (a) Two-dimensional contour plot, showing trigonal and tetrahedral resonances. (b) Gaussian deconvolution of the isotropic projection of the ^{11}B 3QMAS NMR spectrum for the B^{III} resonances.

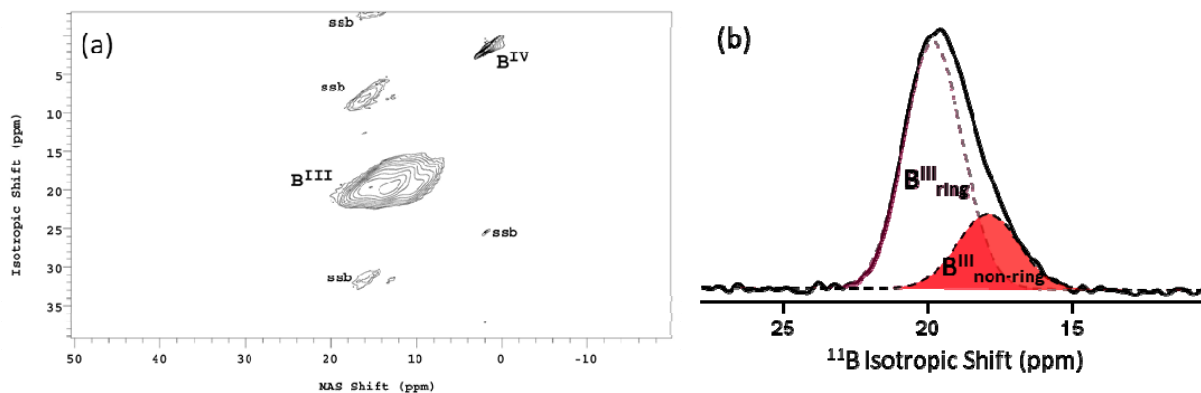
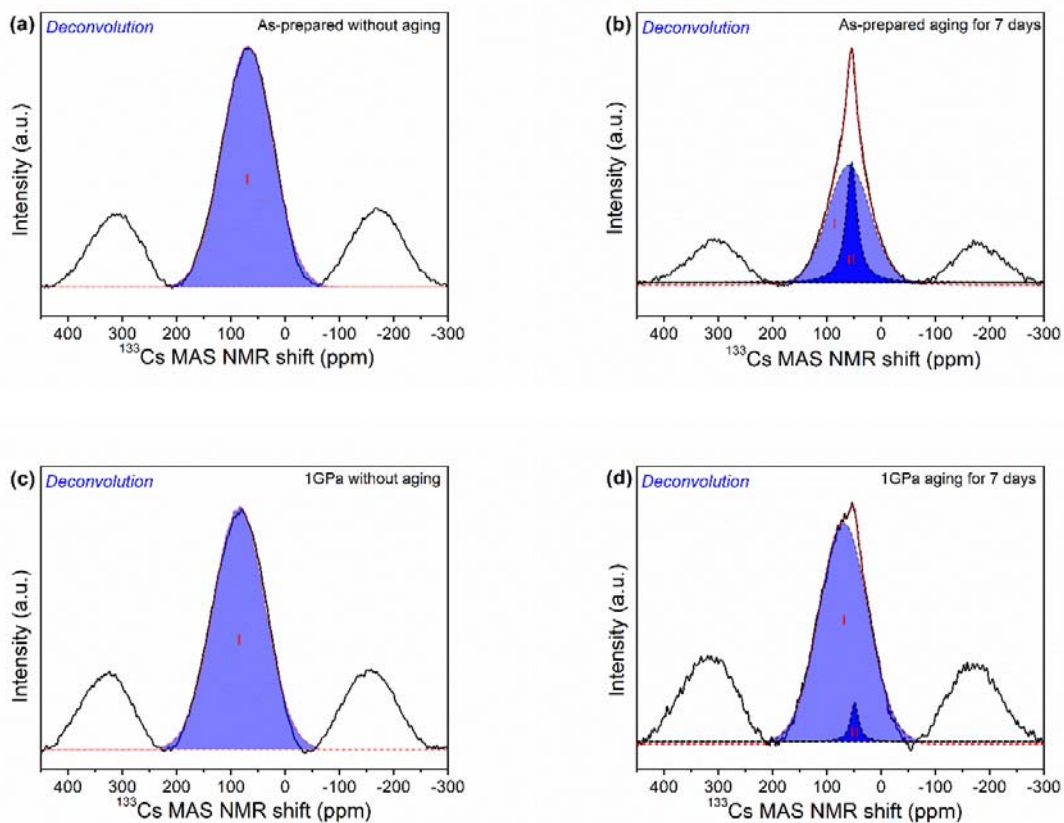


Figure S20. Deconvolution of the ^{133}Cs MAS NMR spectra for the CsAIB glasses: (a) as-prepared glasses without aging; (b) as-prepared glasses with aging for 7 days; (c) compressed glasses without aging; (d) compressed glasses with aging for 7 days.



Supplemental References

- [S1] H. Li, Y. Su, L. Li, and D. M. Strachan, *J. Non. Cryst. Solids* **292**, 167 (2001).
- [S2] W. L. Konijnendijk and J. M. Stevels, *J. Non. Cryst. Solids* **20**, 193 (1976).
- [S3] E. I. Kamitsos and G. D. Chryssikos, *J. Mol. Struct.* **247**, 1 (1991).
- [S4] B. N. Meera and J. Ramakrishna, *J. Non. Cryst. Solids* **159**, 1 (1993).
- [S5] K. Vignarooban, P. Boolchand, M. Micoulaut, M. Malki, and W. J. Bresser, *EPL (Europhysics Lett.)* **108**, 56001 (2014).
- [S6] J. Krogh-Moe, *J. Non. Cryst. Solids* **1**, 269 (1969).
- [S7] P. McMillan and B. Piriou, *J. Non. Cryst. Solids* **55**, 221 (1983).
- [S8] M. Licheron, V. Montouillout, F. Millot, and D. R. Neuville, *J. Non. Cryst. Solids* **357**, 2796 (2011).
- [S9] T. Yano, N. Kunimine, S. Shibata, and M. Yamane, *J. Non. Cryst. Solids* **321**, 137 (2003).
- [S10] R. K. Brow, D. R. Tallant, and G. L. Turner, *J. Am. Ceram. Soc.* **80**, 1239 (2005).
- [S11] A. Anedda, C. M. Carbonaro, F. Clemente, R. Corpino, P. C. Ricci, D. Fisica, V. Uni, and U. Cagliari, 13661 (2003).
- [S12] M. Mercier, A. Di Muro, D. Giordano, N. Métrich, P. Lesne, M. Pichavant, B. Scaillet, R. Clocchiatti, and G. Montagnac, *Geochim. Cosmochim. Acta* **73**, 197 (2009).
- [S13] N. Ollier, T. Charpentier, B. Boizot, G. Wallez, and D. Ghaleb, *J. Non. Cryst. Solids* **341**, 26 (2004).
- [S14] K. Januchta, M. Stepniewska, L. R. Jensen, Y. Zhang, M. A. J. Somers, M. Bauchy, Y. Yue, and M. M. Smedskjaer, *Adv. Sci.* **6**, 1901281 (2019).

ISSN (online): 2446-1636
ISBN (online): 978-87-7210-970-1

AALBORG UNIVERSITY PRESS